Alignment with Kalman filter fitted tracks and reconstruction of $B_s^0 \to J/\psi\phi$ decays

This work is part of the research programme of the Foundation for Fundamental Research on Matter (FOM), which is part of the Netherlands Organisation for Scientific Research (NWO).

VRIJE UNIVERSITEIT

Alignment with Kalman filter fitted tracks and reconstruction of $B_s^0 \to J/\psi\phi$ decays

ACADEMISCH PROEFSCHRIFT

ter verkrijging van de graad Doctor aan
de Vrije Universiteit Amsterdam,
op gezag van de rector magnificus
prof.dr. L.M. Bouter,
in het openbaar te verdedigen
ten overstaan van de promotiecommissie
van de faculteit der Exacte Wetenschappen
op maandag 11 april 2011 om 13.45 uur
in de aula van de universiteit,
De Boelelaan 1105

door

Jan Mennis Amoraal

geboren te Johannesburg, Zuid-Afrika

promotor: prof.dr. M.H.M. Merk
copromotor: dr. W.D. Hulsbergen

Table Of Contents

Introduction

Given its unparallelled centre of mass energy the LHC proton-proton collider at CERN is the new testing ground for the Standard Model of elementary particles. The Standard Model is a theoretical framework based on our current understanding of elementary particles and the interactions between them, and has been very successful in not only describing but also in predicting various phenomena observed at collider experiments. One of its successes is the prediction, which followed from the unification of the electromagnetic and weak forces, and subsequent discovery of the existence of mediators of the weak force: the W and Z bosons. Another success, following from the requirements for CP violation, is its prediction of the existence of the bottom and top quarks to give three generations of quarks.

Despite its successes the Standard Model also has flaws. The values for some fundamental parameters remain unexplained and as such the Standard Model cannot provide answers as to the observed mass hierarchy between fermions or why there exist three generations. Moreover, the Standard Model only incorporates three — the electromagnetic, weak and strong — out of the four fundamental forces — the fourth being gravity. Although the predictions of the Standard Model appear to be consistent with experimental observations, it is clear that it does not paint a full picture of Nature. There are voids that become apparent when considering, for example, cosmological observations. The Standard Model does not quantitatively explain the apparent predominance of matter over anti-matter nor provides answers to the observational existence of cold dark matter.

There are however extensions to the Standard Model, so-called New Physics Models, that do provide answers to these mysteries by introducing new *e.g.* super-symmetric, particles that weakly interact with matter around us. if they exist, these particles will manifest themselves in higher order processes such as loops, *e.g.*, in the oscillations of neutral B_s^0 mesons. However, to distinguish between Standard Model processes and New Physics processes requires being able to measure various observables with a relative precision of a few permille up to a few percent.

A case in point is the weak mixing phase $\phi_s = -2\beta_s$, a key measurement of the LHCb experiment, which can be accessed via $B_s^0 \to J/\psi\phi$ decays. According to the Standard Model this phase is expected to be small, approximately $\phi_s = -0.04\,\mathrm{mrad}$. However, New Physics contributions may augment this CP violating phase, yielding a larger observable value. For this reason the LHCb experiment has been designed to measure ϕ_s with a precision of $0.024\,\mathrm{mrad}$ after one nominal year of data taking. To achieve this sensitivity on ϕ_s requires being able to measure the lifetimes of the neutral B_s^0 mesons with a high precision — approximately $\sigma_t = 30\,\mathrm{fs}$ — and being able to reconstruct and select interesting events with a high signal purity, which in turn depends on the mass and momentum resolution — approximately $\delta p/p = (3-5)‰$. To achieve these resolutions and consequently sensitivity on ϕ_s requires high precision tracking detectors. Furthermore, to determine charged particle trajectories and observables with a high

precision, the positions of the tracking detectors need to be known well within their respective hit resolutions.

To be able to determine the positions of the detectors well within their hit resolutions, a generic track based alignment framework for the LHC*b* detector, the topic of this thesis, has been developed. The novelty of this framework is that it is the first of its kind to use a Kalman filter track model and fit in the so-called *global method of alignment* procedure. In this procedure the alignment offsets are determined through a global least squares method, in which not only the hits themselves are considered but also the correlations between the hits. This has the advantage that only a few iterations are required to determine the alignment offsets. Furthermore, the framework uses the same track model and fit as the standard LHC*b* reconstruction and physics analyses procedures. The obtained alignment offsets are therefore expected to be consistent with the track model and fit procedure used in the reconstruction. Given the design of the LHC*b* reconstruction procedure, an additional advantage of this alignment framework is the possibility to align all of the LHC*b* sub-detectors simultaneously or each sub-detector individually at any granularity.

The remainder of this thesis is outlined as follows: Chapter 1 gives a general overview of CP violation in the Standard Model and its observable manifestation, as well as the implications of New Physics, in $B_s^0 \to J/\psi\phi$ decays.

Chapter 2 gives a general overview of the LHC and LHC*b* experiment followed by Chapter 3 which describes the LHC*b* Outer Tracker simulation and geometry as implemented within the LHC*b* software framework.

Chapter 4 describes the alignment framework for the LHC*b* detector, including the *global method of alignment*, followed by a Monte Carlo validation study. In this study the effects of multiple scattering on the alignment procedure as well as the resulting effects of the obtained alignment offsets on the reconstruction of $J/\psi \to \mu^+\mu^-$ decays are investigated.

Chapter 5 describes the alignment of the LHC*b* Outer Tracker using cosmic ray data that were taken in September 2008. Furthermore, this chapter gives an overview of the LHC*b* Outer Tracker survey at that time and a comparison between the alignment offsets obtained with the alignment framework and the survey.

Chapter 6 describes a Monte Carlo study in which the effects, and implications for physics observables, of random mis-alignments in the LHC*b* Vertex Locater and Tracking stations on the reconstruction of $B_s^0 \to J/\psi\phi$ decays are investigated. Furthermore, it is investigated whether the alignment framework can recover these random mis-alignments and the nominal performance of the LHC*b* experiment with respect to the reconstruction of $B_s^0 \to J/\psi\phi$ decays.

conventions and units:

In this thesis spatial vectors are denoted by bold face letters, *e.g.* $\boldsymbol{x}$, and n parameter vectors by an arrow, *e.g.* $\vec{x}$. Matrices are denoted by capital letters, *e.g.* A. The units used in this thesis are natural units, which implies that $\hbar = c = 1$.

Chapter 1

CP Violation In $B_s^0 \to J/\psi\phi$

In 1972 Kobayashi and Maskawa [1] demonstrated that CP violation is possible within the framework of electroweak interactions. They recognised that a possible source of CP violation resides in the Lagrangian that describes the interactions of quarks with the Higgs boson, the so-called Yukawa interactions. Starting with the assumption that there are only two quark generations, they showed that CP violation is only possible by introducing new additional fields. In particular, they proceeded to demonstrate that if one were to introduce a third generation of quarks, *i.e.* two additional quarks, which was a straightforward extension of the electroweak model, that CP violation is possible through the interaction of the quarks with the Higgs particle. It is through this insight that they did not only give a possible phenomenological explanation for CP violation, but also predicted the existence of the bottom b and top quark t.

In what follows an overview of the Kobayashi-Maskawa mechanism of CP violation in the Standard Model and a possible observable manifestation of CP violation, as well as the implications of New Physics, in $B_s^0 \to J/\psi\phi$ decays are presented. For further theoretical and experimental details on CP violation, as well as the derivations of the equations presented in this chapter, see, *e.g.*, [2, 3]. For a detailed discussion on the analysis of $B_s^0 \to J/\psi\phi$ decays at LHCb, see, *e.g.*, [4, 5].

1.1 CP Violation In The Standard Model

In the Standard Model the single source of CP violation resides, after spontaneous symmetry breaking, in the weak charged current interactions, *i.e.* in the interactions between charged W bosons and quarks [6]. Since W bosons have charge ± 1, they can change the flavour of an up type quark, charge $+2/3$, to a down type quark, charge $-1/3$. The terms in the Standard Model Lagrangian that describes the weak charged interactions are of the following form:

$$\mathcal{L}_W = \frac{g}{\sqrt{2}} \left(\overline{\mathsf{u}_L} \gamma^\mu V_{\text{CKM}} \mathsf{d}_L W_\mu^- + \overline{\mathsf{d}_L} \gamma^\mu V_{\text{CKM}}^\dagger \mathsf{u}_L W_\mu^+ \right), \tag{1.1}$$

where $\mathsf{u} = (u, c, t)$ and $\mathsf{d} = (d, s, b)$ are up-type and down-type multiplets of the up-type and down type quark mass eigenstates, respectively. The (unitary) matrix

$$V_{\text{CKM}} = \begin{pmatrix} V_{ud} & V_{us} & V_{ub} \\ V_{cd} & V_{cs} & V_{cb} \\ V_{td} & V_{ts} & V_{tb} \end{pmatrix} \tag{1.2}$$

is the Cabibbo-Kobayashi-Maskawa quark mixing matrix, where the size of the elements V_{ij} gives the relative strengths of the weak charge couplings between different quark flavours. In the Standard Model, this matrix transforms the quark mass eigenstates to the basis of weak eigenstates, which couple to the W bosons. Furthermore, one can show that Eq. 1.1 is invariant under CP when $V_{ij} = V_{ij}^*$, *i.e.* CP is conserved when the matrix V_{CKM} is real. In other words, the presence of CP violation requires that at least for one element $V_{ij} \neq V_{ij}^*$.

Using the unitarity conditions and the fact that one can redefine the relative phases of the quark fields without affecting the observable physics, it can be shown that, in general, an $N \times N$ unitary matrix, where N is the number of generations, can be parametrised by

$$n_{\text{angles}} = \frac{1}{2}N(N-1) \text{ angles and } n_{\text{phases}} = \frac{1}{2}(N-1)(N-2) \text{ phases.} \tag{1.3}$$

In the case of two generations - there is a single angle and no complex phases - the quark mixing matrix is given by the familiar Cabibbo mixing matrix and the elements of V_{CKM} are real. In the case of three generations V_{CKM} can be parametrised by three (rotation) angles and a single (complex) phase δ. It is this irreducible complex phase that is the source of CP violation. The "standard" representation of V_{CKM} advocated by the Particle Data Group [7] is

$$V_{CKM} = \begin{pmatrix} c_{12}c_{13} & s_{12}c_{13} & s_{13}e^{-i\delta_{13}} \\ -s_{12}c_{23} - c_{12}s_{23}s_{13}e^{+i\delta_{13}} & c_{12}c_{23} - s_{12}s_{23}s_{13}e^{+i\delta_{13}} & s_{23}c_{13} \\ s_{12}s_{23} - c_{12}c_{23}s_{13}e^{+i\delta_{13}} & -c_{12}s_{23} - s_{12}c_{23}s_{13}e^{+i\delta_{13}} & c_{23}c_{13} \end{pmatrix} \tag{1.4}$$

where c_{ij} and s_{ij} are $\cos\theta_{ij}$ and $\sin\theta_{ij}$, respectively. The angles θ_{ij} are the Euler (rotation) angles and $\delta_{13} \equiv \delta_{\text{KM}}$ is the (irreducible) Kobayashi-Maskawa complex phase.

For CP violation to occur in the weak interactions the following eight conditions need to be satisfied [8]:

$$\delta_{\text{KM}} \neq 0, \pi \text{ and } \theta_{ij} \neq 0, \frac{1}{2}\pi \text{ for } i \neq j \in \{1,2,3\}. \tag{1.5}$$

Furthermore, the masses of all quarks with the same charge are required to be non-degenerate, *e.g.* for the up-type quarks one requires that $m_u \neq m_c$, $m_c \neq m_t$ and $m_t \neq m_u$. If they are degenerate there will be no CP violation, since the quarks are indistinguishable. This yields six additional necessary conditions for CP violation to occur. These 14 conditions for CP violation to occur are succinctly unified in the following phase-convention independent relation [8]:

$$\det C = -2J(m_t^2 - m_c^2)(m_c^2 - m_u^2)(m_u^2 - m_t^2)(m_b^2 - m_s^2)(m_s^2 - m_d^2)(m_d^2 - m_b^2) \neq 0, \tag{1.6}$$

where the matrix C is the commutator of the square of the quark mass matrices:

$$iC \equiv \left[m_{\mathsf{u}} m_{\mathsf{u}}^\dagger, m_{\mathsf{d}} m_{\mathsf{d}}^\dagger\right], \tag{1.7}$$

where m_{u} and m_{d} are the mass matrices, originating from the Yukawa couplings, of the up-type and down-type quarks, respectively. The Jacobian

$$J \sum_{m,n=1}^{3} \epsilon_{ikm}\epsilon_{jln} = \Im\left[V_{ij}V_{kl}V_{kj}^*V_{il}^*\right] \text{ for } i,j,k,l \in \{1,2,3\} \tag{1.8}$$

is known as the Jarlskog invariant. It can be shown that this quantity is independent of the phase-

convention used to parametrise $V_{\rm CKM}$ and, because of unitarity, independent of the quarks involved [8].

From current experimental observations, and assuming unitarity and three quark generations, the current allowed ranges of the magnitudes of the CKM elements are

$$|V_{\rm CKM}| = \begin{pmatrix} 0.97428 \pm 0.00015 & 0.2253 \pm 0.0007 & 0.00347^{+0.00016}_{-0.00012} \\ 0.2252 \pm 0.0007 & 0.97345^{+0.00015}_{-0.00016} & 0.0410^{+0.0011}_{-0.0007} \\ 0.00862^{+0.00026}_{-0.00020} & 0.0403^{+0.0011}_{-0.0007} & 0.999152^{+0.000030}_{-0.000045} \end{pmatrix} \quad [7]. \tag{1.9}$$

From this one observes that $V_{\rm CKM}$ is nearly diagonal and that the size of the off-diagonal elements, which are small, decreases for higher generations. Consequently, generation mixing is generally suppressed - a phenomenon known as Cabibbo suppression. This experimentally apparent hierarchy of the magnitudes of the $V_{\rm CKM}$ elements can be conveniently expressed using the Wolfenstein parametrisation [7, 9].

In the Wolfenstein parametrisation, $V_{\rm CKM}$ is parametrised in terms of three real parameters, λ, A and ρ, and an imaginary parameter, $i\eta$. The representation of $V_{\rm CKM}$ in this scheme follows from setting $|V_{us}| \approx 0.23 \equiv \lambda$ and expanding $V_{\rm CKM}$ in powers of λ and exploiting the unitarity of $V_{\rm CKM}$ [10, 11]:

$$V_{CKM} = \begin{pmatrix} 1 - \frac{1}{2}\lambda^2 & \lambda & A\lambda^3 \left[\rho - i\eta\right] \\ -\lambda & 1 - \frac{1}{2}\lambda^2 & A\lambda^2 \\ A\lambda^3 \left[1 - \rho - i\eta\right] & -A\lambda^2 & 1 \end{pmatrix} + \mathcal{O}(\lambda^4), \tag{1.10}$$

where A, ρ and η are of order unity. Experimentally, given the smallness of the off-diagonal elements, the CP violating effect turns out to be small, and from Eq. 1.10 one observes that the CP violating terms are suppressed at the level of λ^3. For the B_s^0 system, the higher order terms of Eq. 1.10 are of particular importance, since they become leading in the B_s^0 mixing process:

$$\mathcal{O}(\lambda^4) \rightarrow \begin{pmatrix} -\frac{1}{8}\lambda^4 & 0 & 0 \\ \frac{1}{2}A^2\lambda^5 \left[1 - 2\left(\rho + i\eta\right)\right] & -\frac{1}{8}\lambda^4 \left[1 + 4A^2\right] & 0 \\ \frac{1}{2}A\lambda^5 \left[\rho + i\eta\right] & \frac{1}{2}A\lambda^4 \left[1 - 2\left(\rho + i\eta\right)\right] & -\frac{1}{2}A^2\lambda^4 \end{pmatrix} + \mathcal{O}(\lambda^6). \tag{1.11}$$

Expressing $V_{\rm CKM}$ in terms of the coupling strengths and the angles of the unitarity angles, discussed below, one obtains the following useful form for $V_{\rm CKM}$ in the Wolfenstein scheme:

$$V_{\rm CKM} = \begin{pmatrix} |V_{ud}| & |V_{us}| & |V_{ub}| \exp[-i\gamma] \\ -|V_{cd}| & |V_{cs}| & |V_{cb}| \\ |V_{td}| \exp[-i\beta] & -|V_{ts}| \exp[+i\beta_s] & |V_{tb}| \end{pmatrix} + \mathcal{O}(\lambda^5). \tag{1.12}$$

1.2 The Unitary Triangles

The unitarity of $V_{\rm CKM}$ leads to nine relations among the elements of the matrix. Two of these contain the couplings of the b quark to an up-type quark and, consequently, are relevant to CP violation in the B-system:

$$\begin{aligned} V_{ud}V_{ub}^* + V_{cd}V_{cb}^* + V_{td}V_{tb}^* = 0 \quad &\text{for the } B_d^0 \text{ system and} \\ V_{us}V_{ub}^* + V_{cs}V_{cb}^* + V_{ts}V_{tb}^* = 0 \quad &\text{for the } B_s^0 \text{ system.} \end{aligned} \tag{1.13}$$

The relations in Eq. 1.13 can be represented as triangles in the complex plane as illustrated in Fig. 1.1, where they have been normalised with respect to $V_{cd}V_{cb}^*$ and $V_{cs}V_{cb}^*$ for the B_d^0 and B_s^0 system, respectively. Consequently, two of the vertices of the triangles are exactly (0,0) and (0,1), such that the bases of the triangles are unity. The remaining vertex, or apex, is

$$\begin{aligned} -\frac{V_{ud}V_{ub}^*}{V_{cd}V_{cb}^*} &= (\overline{\rho},\overline{\eta})_d \text{, with} \quad \overline{\rho}_d = \rho\left[1-\frac{1}{2}\lambda^2\right] \quad \text{and} \quad \overline{\eta}_d = \eta\left[1-\frac{1}{2}\lambda^2\right], \text{ and} \\ -\frac{V_{us}V_{ub}^*}{V_{cs}V_{cb}^*} &= (\overline{\rho},\overline{\eta})_s \text{, with} \quad \overline{\rho}_s = \rho\left[\frac{-\lambda^2}{1-\frac{1}{2}\lambda^2}\right] \quad \text{and} \quad \overline{\eta}_s = \eta\left[\frac{-\lambda^2}{1-\frac{1}{2}\lambda^2}\right], \end{aligned} \tag{1.14}$$

for the B_d^0 and B_s^0 system, respectively. Furthermore, the area of the two (un-normalised) triangles are equal and are given by $|J|/2$ with

$$|J| = \left(2.91^{+0.19}_{-0.11}\right) \times 10^{-5} \quad [7]. \tag{1.15}$$

In addition to the requirement of non-degeneracy of the quark masses, a non-zero area of the unitary triangles, *i.e.* $\eta \neq 0$, is required for the presence of CP violation, see Eq. 1.6.

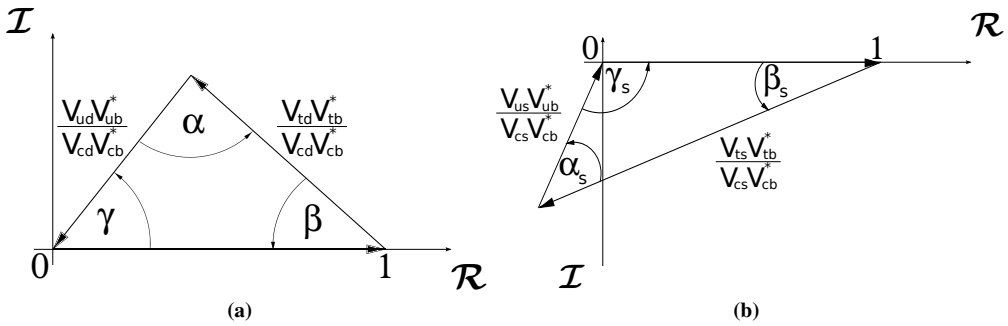

Fig. 1.1: *The unitary triangles for the (a) B_d^0 system and (b) B_s^0 system.*

The internal angles of the B_d^0 triangle, see Fig. 1.1a, are defined as

$$\alpha \equiv \arg\left[-\frac{V_{td}V_{tb}^*}{V_{ud}V_{ub}^*}\right], \beta \equiv \arg\left[-\frac{V_{cd}V_{cb}^*}{V_{td}V_{tb}^*}\right] \text{ and } \gamma \equiv \arg\left[-\frac{V_{ud}V_{ub}^*}{V_{cd}V_{cb}^*}\right], \tag{1.16}$$

and are related through the relation $\alpha+\beta+\gamma = \pi$. Similarly, the internal angles of the B_s^0 triangle, see Fig. 1.1b, are defined as

$$\alpha_s \equiv \arg\left[-\frac{V_{ts}V_{tb}^*}{V_{us}V_{ub}^*}\right], \beta_s \equiv \arg\left[-\frac{V_{cs}V_{cb}^*}{V_{ts}V_{tb}^*}\right] \text{ and } \gamma_s \equiv \arg\left[-\frac{V_{us}V_{ub}^*}{V_{cs}V_{cb}^*}\right], \tag{1.17}$$

and are related through the relation $\alpha_s+\beta_s+\gamma_s = \pi$. These angles can be determined either indirectly from measurements of the sides of the triangles or directly through measuring CP violating effects in certain B decay channels. For further details see, *e.g.*, [12, 13]. The consistency of the (in)-dependent measurements provides an important test of the KM mechanism of CP violation in the Standard Model.

The current (in)-direct measurements [12, 13] of the angles of the unitary triangles are listed in Tab. 1.1 and the constraints on these angles are given in Fig. 1.2. These indirect measurements

follow from constraints imposed by the measurements of the oscillation frequencies Δm_d and Δm_s, respectively, of the B^0_d and B^0_s mesons, the ratio $|V_{ub}/V_{cb}|$ from semi-leptonic decays, and from the observation of CP violation in kaon decays. The angles α, β and γ can be measured directly using, *e.g.*, $B^0_d \to \rho^+\rho^-$, $B^0_d \to J/\psi K_s$ and $B^+ \to D^0 K^+$ decays, respectively. The angle β_s can be measured directly using $B^0_s \to J/\psi\phi$ decays, which is the B^0_s equivalent of the decay $B^0_d \to J/\psi K_s$. From the measurements listed in Tab. 1.1, one observes that the least well known angle is γ. Furthermore, the direct measurement of the angle β_s does not deviate significantly from the indirect measurement of this angle. The main goals of the LHC*b* experiment [4] include the measurement of the angle γ_s and to further constrain the angle γ as well as the angle β_s .

Angle	Indirect Measurements [deg]	Direct Measurements [deg]
α	$97.5^{+1.6}_{-8.1}$	$89.0^{+4.4}_{-4.2}$
β	$28.07^{+0.69}_{-1.69}$	$21.15^{+0.90}_{-0.88}$
γ	$67.2^{+3.9}_{-3.9}$	71^{+21}_{-25}
β_s	$1.041^{+0.050}_{-0.048}$	21^{+6}_{-9} or 68^{+10}_{-7}

Tab. 1.1: *Current experimental values of the angles of the unitary triangles. There are currently no direct or indirect experimental values of α_s and γ_s.*

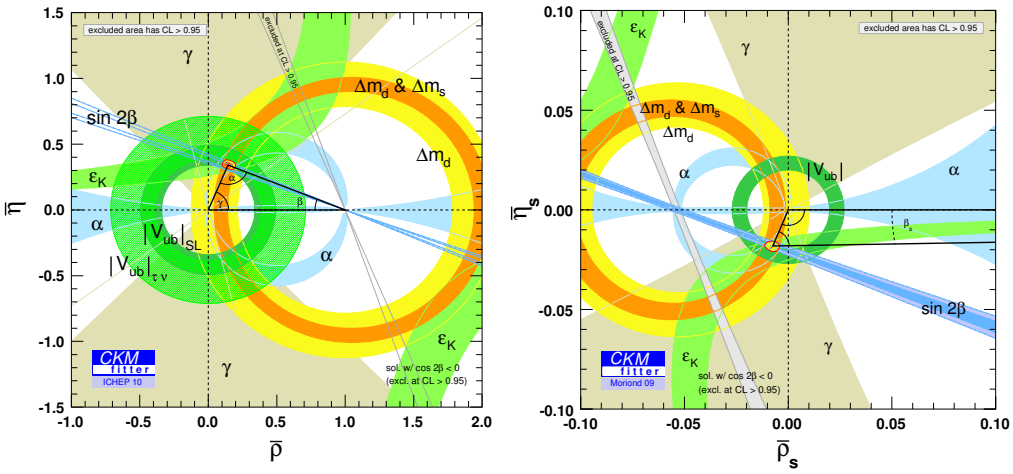

(a) **(b)**

Fig. 1.2: *Constraints on the angles of the unitary triangles of the (a) B^0_d system and (b) B^0_s system.*

1.3 Neutral B Mesons

Neutral B mesons are composed of two quarks of which one of the quarks is a b quark and the other, so-called spectator, quark is either a d quark (B^0_d meson) or an s quark (B^0_s meson). In addition, each neutral B meson has an anti-particle counterpart, which gives a total of four

neutral B mesons:

$$\begin{aligned} |B_d^0\rangle &= |\overline{b}d\rangle \text{ and its anti-particle counterpart } |\overline{B_d^0}\rangle = |b\overline{d}\rangle, \text{ and} \\ |B_s^0\rangle &= |\overline{b}s\rangle \text{ and its anti-particle counterpart } |\overline{B_d^0}\rangle = |b\overline{s}\rangle. \end{aligned} \tag{1.18}$$

These are the, so-called, flavour eigenstates of the B_d^0 and B_s^0, respectively, and according to the *CPT* theorem the $B_d^0(B_s^0)$ and its anti-particle counterpart $\overline{B_d^0}(\overline{B_s^0})$ have the same mass and lifetime.

1.3.1 Mixing

From experimental observations [14, 15] it is known that a neutral B meson, besides directly decaying to a final state, oscillates with time into its anti-particle counterpart through the weak interaction. There are two possible ways in which a neutral B meson can oscillate into its anti-particle counterpart, either via some common intermediate final state f or directly, *i.e.*

$$B \to f \to \overline{B} \text{ versus } B \to \overline{B}, \tag{1.19}$$

and *vice versa* for a neutral $\overline{B}$ meson. This phenomenon is called mixing and is a consequence of the fact that the flavour eigenstates of the B, produced in quark-level strong interactions, are not equal to the mass eigenstates of the weak interactions. Second order weak interactions allow the B to oscillate into its own anti-particle counterpart as illustrated in Fig. 1.3 for the B_s^0 system.

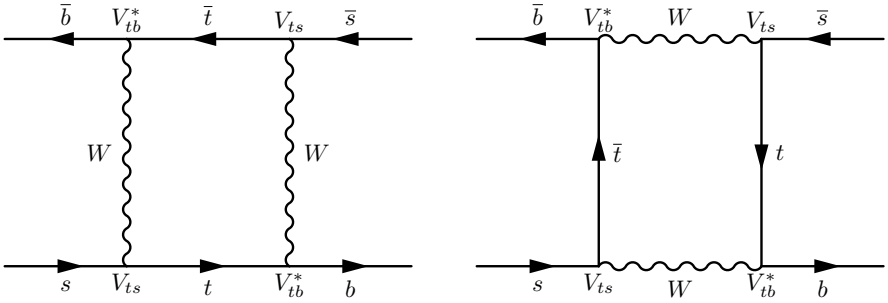

Fig. 1.3: *Feynman box diagrams for B_s^0 mixing. Similar diagrams can be obtained for the B_d^0 system by substituting the d spectator quark for the s spectator quark.*

The currently known values for the decay and oscillation parameters of the B_d^0 and B_s^0 system are listed Tab. 1.2. The third and fourth quantities, Δm_q and $\Delta\Gamma_q$, in Tab. 1.2 are the mass difference and decay width difference of the mass eigenstates, respectively. The former gives the rate in which a B oscillates into its anti-particle counterpart. These quantities are discussed below.

B meson	$M[\text{MeV}]$	$\tau[\text{ps}]$	$\Delta m[\text{ps}^{-1}]$	$\Delta\Gamma[\text{ps}^{-1}]$
B_d^0	5279.50 ± 0.30	1.525 ± 0.009	0.507 ± 0.005	0.005 ± 0.055 at 90% CL
B_s^0	$5366.3 \ \pm 0.6$	1.425 ± 0.041	17.77 ± 0.12	$0.062^{+0.034}_{-0.037}$

Tab. 1.2: *Current experimental values for the mass, lifetime and oscillation frequency for the B_d^0 and B_s^0 [7]. Concerning $\Delta\Gamma_d$ see [16, 17].*

The mass eigenstates can be expressed as a superposition of the flavour eigenstates and *vice versa*. Consider a quantum state that is superposition of the flavour eigenstates

$$|\psi(t)\rangle = \psi_1(t)|B\rangle + \psi_2(t)|\overline{B}\rangle \tag{1.20}$$

of which the time evolution is governed by the Schrödinger equation

$$i\frac{d}{dt}|\psi\rangle = H|\psi\rangle = (M - \frac{i}{2}\Gamma)|\psi\rangle, \tag{1.21}$$

where the mass matrix, M, and the decay width matrix, Γ, are 2×2 hermitian matrices. The eigenvectors of the Hamiltonian H are the mass eigenstates of the B system and can be expressed as a linear combination of the flavour eigenstates, *i.e.*

$$|B_{\rm L}\rangle = p|B\rangle + q|\overline{B}\rangle \text{ and } |B_{\rm H}\rangle = p|B\rangle - q|\overline{B}\rangle, \tag{1.22}$$

where $B_{\rm L}$ and $B_{\rm H}$ are the light and heavy mass eigenstates, respectively. The parameters p and q are normalised complex parameters such that $|p|^2 + |q|^2 = 1$. The real and imaginary parts of the corresponding complex eigenvalues of the Hamiltonian H correspond to the masses and decay widths of the light and heavy mass eigenstates, respectively. Solving the eigenvalue problem of H one can show that the time evolution of these mass eigenstates is given by

$$|B_{\rm H,L}(t)\rangle = \exp\left[-i\left(\mathrm{M}_{\rm H,L} - \frac{1}{2}i\Gamma_{\rm H,L}\right)t\right]|B_{\rm H,L}(0)\rangle, \tag{1.23}$$

where $\mathrm{M}_{\rm H,L} - \frac{1}{2}i\Gamma_{\rm H,L}$ are the eigenvalues of the Hamiltonian H. Here, the real parameters $\mathrm{M}_{\rm H,L}$ and $\Gamma_{\rm H,L}$ are the masses and decay widths of the light and heavy mass eigenstates, respectively.

The time dependent mass eigenstates, Eq. 1.23, can be transformed back to the flavour eigenstate basis which yields the following wave functions for the physical B mesons which are initially produced as either a B or $\overline{B}$

$$\begin{aligned} |B_{\rm phys}(t)\rangle &= g_+(t)|B\rangle + \frac{q}{p}g_-(t)|\overline{B}\rangle \quad (|B\rangle \text{ at } t=0) \quad \text{and} \\ |\overline{B}_{\rm phys}(t)\rangle &= g_+(t)|\overline{B}\rangle + \frac{p}{q}g_-(t)|B\rangle \quad (|\overline{B}\rangle \text{ at } t=0), \end{aligned} \tag{1.24}$$

where $g_\pm(t)$ are the oscillation amplitudes and are given by

$$g_\pm(t) = \frac{1}{2}\left\{\exp\left[-\left(i\,\mathrm{M}_{\rm L} + \frac{1}{2}\Gamma_{\rm L}\right)t\right] \pm \exp\left[-\left(i\,\mathrm{M}_{\rm H} + \frac{1}{2}\Gamma_{\rm H}\right)t\right]\right\}. \tag{1.25}$$

The fraction q/p follows from the eigenvalues of the Hamiltonian H and is given by

$$\frac{q}{p} = \pm\sqrt{\frac{M_{12}^* - \frac{i}{2}\Gamma_{12}^*}{M_{12} - \frac{i}{2}\Gamma_{12}}}, \tag{1.26}$$

where M_{12} and Γ_{12} are the off-diagonal elements of M and Γ. The sign of Eq. 1.26 is convention dependent.

Using Eq. 1.24 one can show that the probability to observe a B or $\overline{B}$, starting from a state

that is initially either a B or $\overline{B}$, at some proper time t is given by:

$$\begin{aligned}
&\left|\langle B|B_{\text{phys}}(t)\rangle\right|^2 = \left|\langle \overline{B}|\overline{B}_{\text{phys}}(t)\rangle\right|^2 = |g_+(t)|^2\,, \\
&\left|\langle \overline{B}|B_{\text{phys}}(t)\rangle\right|^2 = \left|\frac{q}{p}\right|^2 |g_-(t)|^2 \quad \text{and} \quad \left|\langle B|\overline{B}_{\text{phys}}(t)\rangle\right|^2 = \left|\frac{p}{q}\right|^2 |g_-(t)|^2\,,
\end{aligned} \tag{1.27}$$

where

$$|g_\pm(t)|^2 = \frac{1}{2}\exp\left[-\Gamma t\right]\left(\cosh\frac{1}{2}\Delta\Gamma t \pm \cos\Delta m t\right). \tag{1.28}$$

Here $\Delta\Gamma$ and Δm are the decay width difference and mass difference between the heavy and light B_s^0 mass eigenstates, respectively:

$$\Delta\Gamma \equiv \Gamma_L - \Gamma_H \quad \text{and} \quad \Delta m \equiv \mathrm{M}_H - \mathrm{M}_L\,, \tag{1.29}$$

Similarly, the average decay width Γ is defined as

$$\Gamma \equiv \frac{1}{2}\left[\Gamma_L + \Gamma_H\right]. \tag{1.30}$$

Since M_H and M_L are chosen to correspond to the masses of the heavy and light mass eigenstates, respectively, Δm is by convention positive. On the other hand, the sign of $\Delta\Gamma$ needs to be determined experimentally.

1.3.2 Decay rates

Defining the decay amplitude of a neutral B or $\overline{B}$ meson to some final state f as

$$A_f = \langle f|H|B\rangle \quad \text{and} \quad \overline{A}_f = \langle f|H|\bar{B}\rangle, \tag{1.31}$$

one can show, using Eq. 1.24 and Eq. 1.27, that the time dependent decay rates for the physical B or $\overline{B}$ meson, *e.g.* the decay rate of $B \to f$ is defined as

$$\Gamma_{B\to f} = \left|\langle f|H|B_{\text{phys}}\rangle\right|^2, \tag{1.32}$$

are given by

$$\begin{aligned}
\Gamma_{B\to f}(t) =& |A_f|^2\left(1+|\lambda_f|^2\right)\exp\left[-\frac{1}{2}\Gamma t\right]\times \\
&\left(\cosh\frac{1}{2}\Delta\Gamma t - D_f\sinh\frac{1}{2}\Delta\Gamma + C_f\cos\Delta m t - S_f\sin\Delta m t\right) \quad \text{and} \\
\Gamma_{\overline{B}\to f}(t) =& |A_f|^2\left|\frac{p}{q}\right|^2\left(1+|\lambda_f|^2\right)\exp\left[-\frac{1}{2}\Gamma t\right]\times \\
&\left(\cosh\frac{1}{2}\Delta\Gamma t - D_f\sinh\frac{1}{2}\Delta\Gamma - C_f\cos\Delta m t + S_f\sin\Delta m t\right),
\end{aligned} \tag{1.33}$$

where

$$D_f = \frac{2\Re\lambda_f}{1+\lambda_f}, \quad C_f = \frac{1-|\lambda_f|^2}{1+|\lambda_f|^2} \quad \text{and} \quad S_f = \frac{2\Im\lambda_f}{1+\lambda_f}. \tag{1.34}$$

Here, the complex quantity λ_f is the ratio of the amplitude of the decay and the amplitude of the CP conjugated decay defined as

$$\lambda_f \equiv \frac{q}{p}\frac{\overline{A}_f}{A_f} \quad \left(\overline{\lambda}_f = \frac{1}{\lambda_f}\right). \tag{1.35}$$

Similar expressions can be obtained for the decay rates of a B or $\overline{B}$ to a CP conjugated final state $\overline{f}$ by substituting $\overline{f}$ for f and λ_f for

$$\lambda_{\overline{f}} = \frac{q}{p}\frac{\overline{A}_{\overline{f}}}{A_{\overline{f}}} \quad \left(\overline{\lambda}_{\overline{f}} = \frac{1}{\lambda_{\overline{f}}}\right). \tag{1.36}$$

Since the coefficients D_f, C_f, S_f contain real and imaginary parts of the amplitude ratio λ_f, they are sensitive to the complex phases of the amplitudes and, consequently, to CP violation.

1.4 CP Violation In B Decays

Since the amplitudes of the processes that describe B decays contain V_{CKM} elements, they can lead to observable CP violating effects. These CP violating effects can be classified as follows:

- CP violation in decay.
- CP violation in mixing.
- CP violation in the interference between an amplitude without mixing and an amplitude with mixing.

The latter of these apply, *e.g.*, to the decay $B_s^0 \to J/\psi\phi$, which is similar to the B_d^0 golden decay mode $B_d^0 \to J/\psi K_s$, which was studied extensively at the B-factories. The latter gives access to the angle β, while the former gives access to the β_s.

1.4.1 CP violation in decay

Consider the decay $B \to f$ and its CP conjugate $\overline{B} \to \overline{f}$ with amplitudes

$$A_f = \langle f|H_d|B\rangle \quad \text{and} \quad \overline{A}_{\overline{f}} = \langle \overline{f}|H_d|\overline{B}\rangle, \tag{1.37}$$

where H_d is the decay Hamiltonian, and assume that there is more than one possible decay mode to the final state $f(\overline{f})$. In this case the amplitudes can be written as the sum over all possible decay modes k

$$A_f = \sum_{k=1}^{N} |A|_k \exp\left[i\theta_k\right]\exp\left[i\delta_k\right] \quad \text{and} \quad \overline{A}_{\overline{f}} = \sum_{k=1}^{N} |A|_k \exp\left[-i\theta_k\right]\exp\left[i\delta_k\right]. \tag{1.38}$$

Here θ represents a weak phase, which flips its sign under CP, and δ a corresponding strong phase for the amplitudes, which is invariant under CP.

The CP asymmetry between these decay amplitudes are given by

$$\mathcal{A}_{\text{CP}} = \frac{|A_f|^2 - \left|\overline{A}_{\overline{f}}\right|^2}{|A_f|^2 + \left|\overline{A}_{\overline{f}}\right|^2}. \tag{1.39}$$

In the case $k = 1$ there can not be any observable CP asymmetry, *i.e.* CP violation, since $|A_f| =$

$\left|\overline{A}_{\overline{f}}\right| = |A_1|$. However, CP violation may occur for $k \geq 2$. For example, in the case $k = 2$ the numerator of Eq. 1.39 is given by the following interference term

$$|A_f|^2 - \left|\overline{A}_{\overline{f}}\right|^2 = -4\,|A|_1\,|A|_2 \sin\Delta\theta \sin\Delta\delta, \tag{1.40}$$

where $\Delta\theta = \theta_2 - \theta_1$ and $\Delta\delta = \delta_2 - \delta_1$. From this one observes that CP violation is possible if and only if

$$\theta_1 \neq \theta_2 \text{ and } \delta_1 \neq \delta_2. \tag{1.41}$$

In other words, if there are two amplitudes with a different weak and strong phase, respectively, the probability for the decay $B \to f$ is different from the probability for its CP conjugate counterpart, *i.e.*

$$\frac{|A_f|}{\left|\overline{A}_{\overline{f}}\right|} \neq 1. \tag{1.42}$$

This is also referred to as direct CP violation.

An example of an decay with which one can measure direct CP violation, and in particular the angle γ, is $B^+ \to D^0 K^+$. In this case there is an interference between two tree level processes, where one of the processes is Cabibbo and colour suppressed.

1.4.2 CP violation in mixing

CP violation in mixing occurs when the B to $\overline{B}$ mixing probability is different from its CP conjugated, *i.e.* $\overline{B}$ to B, mixing probability. From Eq. 1.27 one observes that this is the case when

$$\left|\frac{q}{p}\right| \neq 1. \tag{1.43}$$

In this case the mass eigenstates of the oscillating mesons are not identical to the CP eigenstates, which is the case, *e.g.*, in the neutral Kaon system. In the Standard Model $|q/p|$ is predicted to be approximately equal to one in the B_d^0 and B_s^0 system, which is consistent with current experimental observations [13].

This type of CP violation can be measured using semi-leptonic B-decays where the asymmetry is given by

$$a_{\text{sl}} = \frac{\Gamma(B^0(t) \to l^- \overline{\nu}_l X) - \Gamma(\overline{B^0}(t) \to l^+ \nu_l X)}{\Gamma(B^0(t) \to l^- \overline{\nu}_l X) + \Gamma(\overline{B^0}(t) \to l^+ \nu_l X)} = \frac{1 - \left|\frac{q}{p}\right|^4}{1 + \left|\frac{q}{p}\right|^4} \tag{1.44}$$

1.4.3 CP violation in the interference between decays with & without mixing

In the absence of direct CP violation and CP violation in mixing, there is a third possible way for CP violation to occur. The observed CP violating effect in this case is due to the interference of the mixing and decay amplitudes of a B that can either decay directly to a final state f or first oscillate into its anti-particle counter part and then decay to the same final state f, *i.e.* f is a final state that is common to both B and $\overline{B}$. This type of CP violation is described by the phase of the complex parameter λ_f (Eq. 1.35). Even though $|\lambda_f| = 1$, the argument of λ_f may be non-zero. In other words, this type of CP violation arises when there is a relative phase difference between the direct decay amplitude and the oscillating decay amplitude of a B into the final state f, *i.e.*

$\arg \lambda_f + \arg \lambda_{\overline{f}} \neq 0$.

A special case, which applies to $B_s^0 \to J/\psi\phi$ and is discussed in the next section, is the case when the final state f is a CP eigenstate $f_{\rm CP}$. In this case λ_f is defined as

$$\lambda_{f_{\rm CP}} \equiv \eta_{f_{\rm CP}} \frac{q}{p} \frac{\overline{A}_{\overline{f_{\rm CP}}}}{A_{f_{\rm CP}}}, \tag{1.45}$$

where $\eta_{\rm CP}$ is the CP eigenvalue of the state $|f_{\rm CP}\rangle$, *i.e.* CP$|f_{\rm CP}\rangle = \eta_{f_{\rm CP}}|f_{\rm CP}\rangle$.

1.5 $B_s^0 \to J/\psi\phi$

The decay of a B_s^0 to a J/ψ and a ϕ, of which the Feynman diagrams are given in Fig. 1.4, is relatively easy to detect and reconstruct, since the J/ψ and ϕ have clear detectable signatures, *i.e.* the J/ψ can decay to a di-muon $(\mu^+\mu^-)$ pair and the ϕ to a di-kaon (K^+K^-) pair. The fact that this decay has a clear signature makes it experimentally attractive to measure CP violation in the B_s^0 system. From a theoretical point of view the decay is also considered an ideal probe for CP violation in the B_s^0 system, since the dominant decay contribution is the first order tree level process, see Fig. 1.4a. The contribution from the second order penguin process, see Fig. 1.4b, is suppressed by a factor λ^2 compared to the tree level process.

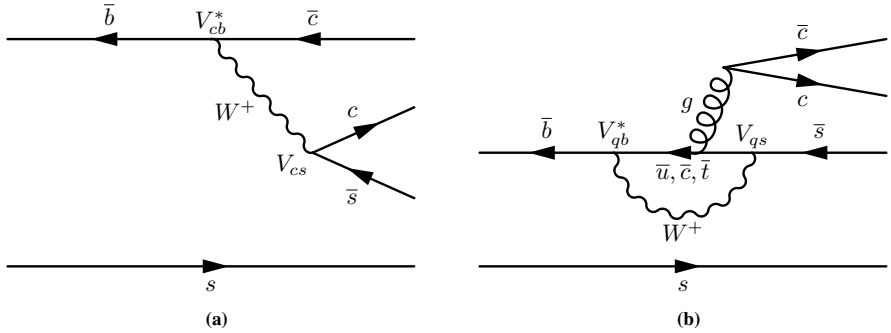

Fig. 1.4: *Feynman diagrams for the decay $B_s^0 \to J/\psi\phi$: (a) the first order tree level process and (b) second order penguin process.*

The CP violating effects in $B_s^0 \to J/\psi\phi$ decays are due to the interference between decays that either decay directly to $J/\psi\phi$ or first oscillate and then decay to $J/\psi\phi$. According to the CKM mechanism the CP asymmetry, using Eq. 1.26, while ignoring $i\Gamma_{12}$ and the second order penguin process, is given by, see Fig. 1.3 and Fig. 1.4a:

$$\lambda_{J/\psi\phi} = \eta_{J/\psi\phi} \left(\frac{q}{p}\right) \left(\frac{\overline{A}_{J/\psi\phi}}{A_{J/\psi\phi}}\right) = \eta_{J/\psi\phi} \left(\frac{V_{tb}^* V_{ts}}{V_{tb} V_{ts}^*}\right) \left(\frac{V_{cb} V_{cs}^*}{V_{cb}^* V_{cs}}\right) = \eta_{J/\psi\phi} \exp\left[i2\beta_s\right], \tag{1.46}$$

where β_s is the unitary angle defined in Eq. 1.17.

Experimentally, the asymmetry can be determined from the decay rates of $B_s^0 \to J/\psi\phi$ and

$\overline{B_s^0} \to J/\psi\phi$. In this case, assuming $|q/p| = 1$, the (time dependent) asymmetry is given by

$$\begin{aligned}\mathcal{A}_{\text{CP}}(t) &= \frac{\Gamma_{B_s^0\to J/\psi\phi}(t) - \Gamma_{\overline{B_s^0}\to J/\psi\phi}(t)}{\Gamma_{B_s^0\to J/\psi\phi}(t) + \Gamma_{\overline{B_s^0}\to J/\psi\phi}(t)} \\ &= \frac{\eta_{J/\psi\phi}\sin 2\beta_s \sin\Delta m_s t}{\cosh\frac{1}{2}\Delta\Gamma_s t - \eta_{J/\psi\phi}\cos 2\beta_s \sinh\frac{1}{2}\Delta\Gamma_s t},\end{aligned} \tag{1.47}$$

which follows directly from the decay rate formulae (Eq. 1.33),

$$\begin{aligned}\Gamma_{B_s^0\to J/\psi\phi}(t) = &\left|A_{J/\psi\phi}\right|^2 \exp\left[-\frac{1}{2}\Gamma_s t\right] \times \\ &\left(\cosh\frac{1}{2}\Delta\Gamma_s t - \eta_{J/\psi\phi}\cos 2\beta_s \sinh\frac{1}{2}\Delta\Gamma_s t - \eta_{J/\psi\phi}\sin 2\beta_s \sin\Delta m_s t\right) \\ \Gamma_{\overline{B_s^0}\to J/\psi\phi}(t) = &\left|A_{J/\psi\phi}\right|^2 \exp\left[-\frac{1}{2}\Gamma_s t\right] \times \\ &\left(\cosh\frac{1}{2}\Delta\Gamma_s t - \eta_{J/\psi\phi}\cos 2\beta_s \sinh\frac{1}{2}\Delta\Gamma_s t + \eta_{J/\psi\phi}\sin 2\beta_s \sin\Delta m_s t\right).\end{aligned} \tag{1.48}$$

Using the Wolfenstein parametrisation and ignoring the $\Delta\Gamma_s$ contribution one can show that

$$\mathcal{A}_{\text{CP}}(t) \propto \Im\lambda_{J/\psi\phi}\sin\Delta m_s t \approx 0.04\eta_{J/\psi\phi}\sin\Delta m_s t. \tag{1.49}$$

Though CP violation in the case of $B_s^0 \to J/\psi\phi$ originates from the interference between decays with and without mixing to the same CP eigenstate, the final states are an admixture of a CP even and CP odd part. The decays consists of a spin zero (pseudo-scalar) meson to two spin one (vector) mesons, in which the total angular momentum $\vec{J} = \vec{L} + \vec{S} = 0$ must be conserved, where $\vec{L}$ and $\vec{S}$ are the orbital momentum and spin of the final state particles. Consequently, the decay can occur with three possible angular momentum states, namely $L = 0$, $L = 1$ and $L = 2$, and the corresponding CP eigenvalues are given by:

$$\eta_{J/\psi\phi} = (-1)^L. \tag{1.50}$$

Furthermore, the CP eigenstates with CP even eigenvalues, *i.e.* $L = 0$ and $L = 2$, are associated with the mass eigenstate B_L and the CP eigenstates with CP odd eigenvalues, *i.e.* $L = 1$, are associated with the mass eigenstate B_H.

Since the CP-even and CP-odd eigenstates contribute, at leading order, with opposite signs to the CP asymmetry, the observable CP asymmetry is effectively diluted. Consequently, to observe the CP violating phase one needs to statistically disentangle the CP-even and CP-odd contributions. This can be done by measuring the decay angles of the final state particles, *e.g.* in the transversity frame [18, 19], from which the polarisation amplitudes associated with the L states follow. The three possible polarisations are the CP-even "longitudinal" $A_0(L = 0)$ and "transverse parallel" $A_\parallel(L = 2)$, and the CP-odd "transverse perpendicular" $A_\perp(L = 1)$.

Using the transversity frame formalism, the differential decay rate of $B_s^0 \to J/\psi\phi$ decays

can be expressed as

$$\frac{d^4\Gamma}{dtd\vec{\Omega}} = \frac{\sum_{i=1}^{6} A_i(t|\vec{\lambda}) f_i(\vec{\Omega})}{\int\int \sum_{j=1}^{6} A_j(t|\vec{\lambda}) f_j(\vec{\Omega})}, \tag{1.51}$$

where the sums run over the product of the time dependent amplitude functions $A_i(t|\vec{\lambda})$ with their corresponding angular distribution functions $f_i(\vec{\Omega})$. These functions are given in Tab. 1.3. Here $\vec{\lambda}$ represents the physics parameters, *e.g.* Δm_s, $\Delta\Gamma_s$ and ϕ_s, and $\vec{\Omega} \equiv (\cos\theta, \cos\psi, \phi)$ the angular observables in the transversity frame, see Fig. 1.5. The infinitesimal $d\vec{\Omega}$ is defined as $d\vec{\Omega} \equiv d\cos\theta d\cos\psi d\phi$.

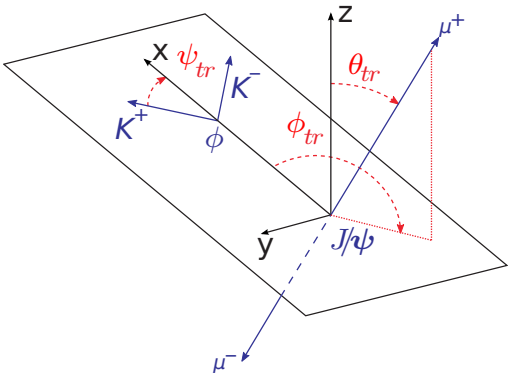

Fig. 1.5: *The decay angles θ_{tr}, ϕ_{tr} and ψ_{tr} of the final state particles in the transversity frame. The xy-plane is given by the plane in which the daughters (K^+K^-) of the ϕ decay. The x-axis is given by the direction of the ϕ momentum vector in the rest frame of the B_s^0 and the y-axis is perpendicular to the x-axis and such that $\mathrm{p}_y(K^+) > 0$. The z-axis is chosen to complete the right-handed coordinate system. The angles θ_{tr} and ϕ_{tr} describe the direction of the μ^+ in the transversity rest frame of the J/ψ, and the angle ψ_{tr} is the helicity angle of the K^+ in the rest frame of the ϕ.*

The current constraints on $\Delta\Gamma_s$ and ϕ_s from the combined measurements of $B_s^0 \to J/\psi\phi$ decays from CDF and DØ are shown in Fig. 1.6. Projecting these constraints on the axes, see Fig. 1.6b, one obtains the following values for $\Delta\Gamma_s$ and ϕ_s:

$$\begin{aligned} \Delta\Gamma_s &= +0.054^{+0.026}_{-0.015}\,\mathrm{ps}^{-1} \text{ or } -0.054^{+0.016}_{-0.026}\,\mathrm{ps}^{-1} \\ &\in [-0.025, +0.097] \cup [-0.099, -0.024]\,\mathrm{ps}^{-1} \text{ at } 90\%\text{ CL and} \\ \Delta\phi_s &= +0.75^{+0.32}_{-0.21}\,\mathrm{rad} \text{ or } -2.38^{+0.25}_{-0.34}\,\mathrm{rad} \\ &\in [-1.19, -0.21] \cup [-2.94, -1.93]\,\mathrm{rad} \text{ at } 90\%\text{ CL}. \end{aligned} \tag{1.52}$$

The predicted smallness of β_s within the Standard Model makes $B_s^0 \to J/\psi\phi$ decays an ideal probe for New Physics. In the presence of New Physics, new particles, are expected to contribute to the off-shell terms in the mixing process [20, 21, 22, 23]. Introducing the complex parameter

$$\Delta_s \equiv |\Delta_s| \exp\phi_s^{\Delta} \tag{1.53}$$

to describe the New Physics contributions, where the norm $|\Delta_s|$ and phase ϕ_s^{Δ} represent the strength and phase of the New Physics coupling, respectively, one can show that the observables Δm_s and $\Delta\Gamma_s$ are affected as follows:

$$\Delta m_s \to 2\,|M_{12}|\,|\Delta_s| \text{ and } \Delta\Gamma_s \to 2\Gamma_{12}\cos\phi_s \quad \text{where} \quad \phi_s = -2\beta_s + \phi_s^{\Delta}. \tag{1.54}$$

i	$f_i\left(\cos\theta, \cos\psi, \phi\right)$	$A_i(t\|\lambda)$
1	$2\cos^2\psi\left[1-\sin^2\theta\cos^2\phi\right]$	$\left\|A_0(t)\right\|^2 = \left\|A_0(0)\right\|^2 \exp\left[-\Gamma_s t\right] \times \left[\cosh\frac{1}{2}\Delta\Gamma_s t - \cos\phi_s \sinh\frac{1}{2}\Delta\Gamma_s t + \sin\phi_s \sin\Delta m_s t\right]$
2	$\sin^2\psi\left[1-\sin^2\theta\sin^2\phi\right]$	$\left\|A_\parallel(t)\right\|^2 = \left\|A_\parallel(0)\right\|^2 \exp\left[-\Gamma_s t\right] \times \left[\cosh\frac{1}{2}\Delta\Gamma_s t - \cos\phi_s \sinh\frac{1}{2}\Delta\Gamma_s t + \sin\phi_s \sin\Delta m_s t\right]$
3	$\sin^2\psi\sin^2\theta$	$\left\|A_\perp(t)\right\|^2 = \left\|A_\perp(0)\right\|^2 \exp\left[-\Gamma_s t\right] \times \left[\cosh\frac{1}{2}\Delta\Gamma_s t + \cos\phi_s \sinh\frac{1}{2}\Delta\Gamma_s t - \sin\phi_s \sin\Delta m_s t\right]$
4	$-\sin^2\psi\sin 2\theta\sin\phi$	$\Im\left(A_\parallel^*(t)A_\perp(t)\right) = \left\|A_\parallel(0)\right\| \left\|A_\perp(0)\right\| \exp\left[-\Gamma_s t\right] \times \left[\sin\left(\delta_\perp-\delta_\parallel\right)\cos\Delta m_s t - \cos\phi_s\cos\left(\delta_\perp-\delta_\parallel\right)\sin\Delta m_s t - \sin\phi_s\cos\left(\delta_\perp-\delta_\parallel\right)\sinh\frac{1}{2}\Delta\Gamma_s t\right]$
5	$\frac{1}{\sqrt{2}}\sin 2\psi\sin^2\theta\sin 2\phi$	$\Re\left(A_\parallel^*(t)A_0(t)\right) = \left\|A_\parallel(0)\right\| \left\|A_0(0)\right\| \cos\left(\delta_\parallel-\delta_0\right) \times \exp\left[-\Gamma_s t\right] \times \left[\cosh\frac{1}{2}\Delta\Gamma_s t - \cos\phi_s\sinh\frac{1}{2}\Delta\Gamma_s + \sin\phi_s\sin\Delta m_s t\right]$
6	$\frac{1}{\sqrt{2}}\sin 2\psi\sin 2\theta\cos\phi$	$\Im\left(A_0^*(t)A_\perp(t)\right) = \left\|A_0(0)\right\| \left\|A_\perp(0)\right\| \times \exp\left[-\Gamma_s t\right] \times \left[\sin(\delta_\perp-\delta_0)\cos\Delta\,\mathrm{m}_s\,t - \cos\phi_s\cos\left(\delta_\perp-\delta_0\right)\sin\Delta m_s t - \sin\phi_s\cos\left(\delta_\perp-\delta_0\right)\sinh\frac{1}{2}\Delta\Gamma_s t\right]$

Tab. 1.3: *The angular dependent functions f_i and time dependent amplitude functions A_i of the differential decay rate for $B_s^0 \to J/\psi\phi$. Here δ_0, $\delta_\parallel$ and $\delta_\perp$ are the strong phases of the polarisation amplitudes A_0, $A_\parallel$ and $A_\perp$, respectively. The CP conjugated time dependent amplitude functions $\overline{A}_i$ follow from the substitution $\phi_s \to -\phi_s$, i.e. $\cos\phi_s \to \cos\phi_s$ and $\sin\phi_s \to -\sin\phi_s$. Note that there exist an two-fold ambiguity in the solutions of these equations, since they are invariant under the following simultaneous substitution $\left[\phi_s, \Delta\Gamma_s, \delta_\parallel, \delta_\perp\right] \leftrightarrow \left[-\phi_s, -\Delta\Gamma_s, 2\pi-\delta_\parallel, \pi-\delta_\perp\right]$.*

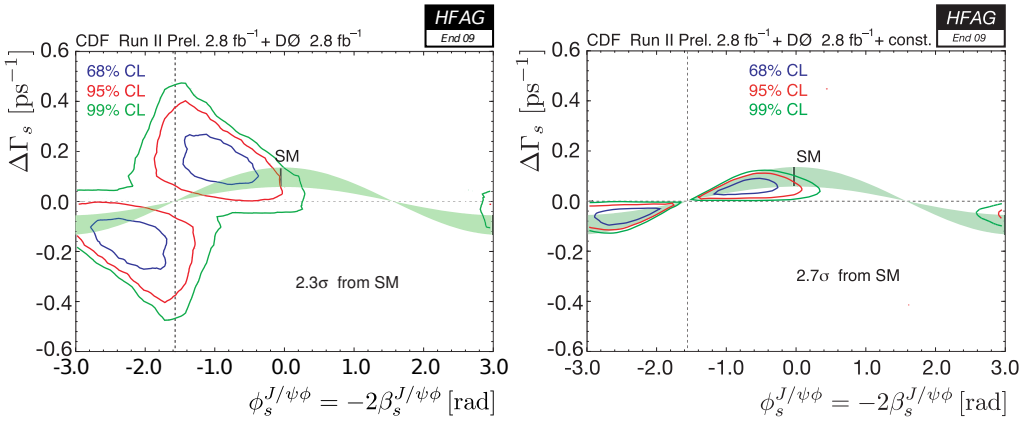

(a) **(b)**

Fig. 1.6: *(a) Current constraints on $\Delta\Gamma_s$ and ϕ_s from the combined measurements of $B_s^0 \to J/\psi\phi$ decays from CDF and DØ [13]. (b) Constraints on $\Delta\Gamma_s$ and ϕ_s when including the lifetimes of flavour specific B_s^0 decays and semi-leptonic asymmetries in B_s^0 decays [13].*

Similarly, the CP asymmetry is also affected by the New Physics phase ϕ_s^{Δ} such that:

$$\lambda_{J/\psi\phi} = \eta_{J/\psi\phi} \exp[-i\phi_s]. \tag{1.55}$$

The current constraints on New Physics is given in Fig. 1.7 which shows that The Standard Model value $\Delta_s = (1, 0)$ is excluded at 2σ.

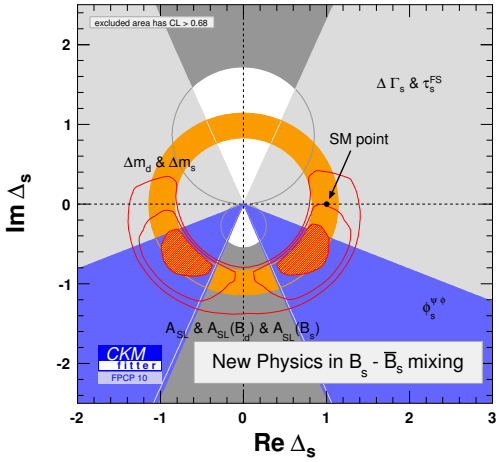

Fig. 1.7: *Current constraints on New Physics from measurements of ϕ_s, decay widths differences, mass differences, lifetimes of flavour specific B_s^0 decays and semi-leptonic asymmetries. The Standard Model value $\Delta_s = (1, 0)$ is excluded at 2σ [12].*

1.6 Enter LHCb

The aim of the LHCb experiment is to determine ϕ_s with a precision of the same order of magnitude as the Standard Model value of β_s after one year of data taking, thereby allowing to confirm either the KM mechanism for CP violation in the B_s^0 system or point at the existence of New Physics. To this end the LHCb detector has been designed to provided an excellent proper

time resolution and momentum resolution for the analyses of B decays. The former is needed to extract the time dependent decay amplitudes of $B_s^0 \to J/\psi\phi$ decays of which the oscillation frequency is given by Δm_s. The latter is needed to kinematically separate the B-decays from the background.

The physics observables are extracted from $B_s^0 \to J/\psi\phi$ candidate events using multi-dimensional likelihood fits [24, 25]. The probability distribution functions used in these fits describe the angular distributions of the final decay products, the time dependent decay amplitudes, and the shape of the mass and proper distributions of the signal and background contributions. The input to these fits are the reconstructed B_s^0 proper time and mass, and the decay angles, the so-called transversity angles, of the final state particles in the transversity frame. These quantities follow from the momenta of the final state particles, which in turn are determined in a track reconstruction procedure.

Monte Carlo studies have shown that in the case of a perfectly aligned LHCb detector the expected sensitivity to ϕ_s is $0.024\,\mathrm{rad}$ with $2\,\mathrm{fb}^{-1}$ at $14\,\mathrm{TeV}$ [5, 24, 25]. However, the observed sensitivity to ϕ_s can be diluted by mis-alignments in the LHCb tracking detectors. Mis-alignments in the VELO will in particular lead to a poor proper time resolution and, similarly, mis-alignments in the T-stations will mainly lead to a poor momentum resolution. In order to achieve the design values for the proper time and momentum resolution the position of the tracking detectors need to be known well within their hit resolution. To this end a track based alignment algorithm using Kalman filter fitted tracks has been developed to simultaneously align all the tracking detectors.

Chapter 2

The LHC*b* Experiment

The Large Hadron Collider beauty (LHC*b*) experiment is one of the main four experiments operating at the Large Hadron Collider (LHC) at CERN. The other three experiments are ATLAS, CMS and ALICE. The common goals of these four experiments are to test the Standard Model of elementary particles and to search for New Physics at the unparallelled centre-of-mass energy of the LHC. The LHC*b* experiment is specifically designed for the precise measurement of beauty and charm hadrons decays, which are expected to be produced copiously at the LHC. The physics goals of the LHC*b* experiment is to search for new physics in CP violation, *e.g.* $B_s^0 \to J/\psi\phi$, and to search for rare decays of beauty and charm hadrons, *e.g.* $B_s^0 \to \mu^+\mu^-$.

This chapter gives a brief overview of the LHC, discussed in Sec. 2.1, and the LHC*b* detector, discussed in Sec. 2.2.

2.1 The LHC

The LHC [26] is a circular proton-proton collider with a circumference of $27\,\mathrm{km}$. Under nominal running conditions, it will be capable of colliding protons at a centre-of-mass energy of $\sqrt{s} = 14\,\mathrm{TeV}$. This is achieved by accelerating two proton beams in opposite directions to an energy of $7\,\mathrm{TeV}$ each. To reach this energy, the beams first pass through several pre-accelerators. In the last stage of the pre-acceleration sequence, the beams are accelerated to an energy of $450\,\mathrm{GeV}$ in the Super Proton Synchrotron (SPS) and, subsequently, injected into the LHC. Here, the beams are then boosted to their final energy of $7\,\mathrm{TeV}$.

The four experiments are each located at one of the four interaction points, where the proton beams cross and collide under a small angle $(150\,\mu\mathrm{rad} - 200\,\mu\mathrm{rad})$. A schematic overview of the LHC and the locations of the four experiments is shown in Fig. 2.1. The protons in a beam are grouped into bunches. Each beam can accommodate 3564 bunches of protons. However, due to the filling procedure, there can only be 2808 filled bunches, each containing 10^{11} protons, per beam. The time spacing between two consecutive bunch crossings is $25\,\mathrm{ns}$, and therefore corresponds to a maximum instantaneous collision rate of $40\,\mathrm{MHz}$. The collision rate of non-empty bunches, which depends on the filling scheme, is on average approximately $30\,\mathrm{MHz}$. Note that the maximum instantaneous collision rate determines the basic clock frequency for the readout electronics.

The number of interactions for a given bunch crossing follows from Poisson statistics, where the probability $P(n, \mu)$ that a bunch crossing contains n interactions with mean μ, *i.e.* the aver-

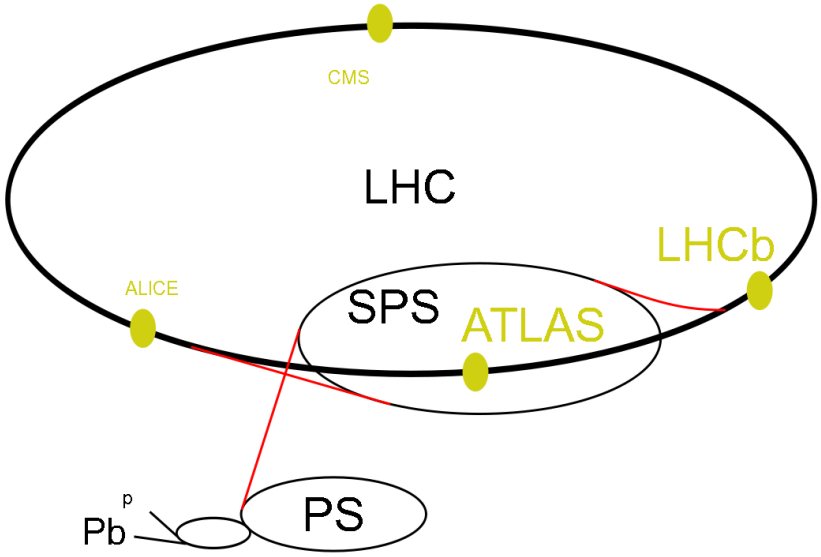

Fig. 2.1: *Schematic overview of the LHC indicating the locations of the four main LHC experiments.*

age number of interactions, is given by

$$P\left(n,\mu\right) = \frac{\mu^n}{n!}e^{-\mu}. \tag{2.1}$$

The average number of interactions μ is given by

$$\mu = \frac{\sigma_{inel}\mathcal{L}}{f}, \tag{2.2}$$

where σ_{inel} is the inelastic cross-section for proton-proton collisions, f the crossing rate for filled bunches and $\mathcal{L}$ the luminosity. The latter depends on the number of bunches and the number of particles per bunch, the bunch crossing rate, the crossing angle of the beams and the beam focus. The design luminosity of the LHC is $\mathcal{L} = 10^{34}\,\text{cm}^{-2}\text{s}^{-1}$ and the estimated inelastic cross-section σ_{inel} for proton-proton collisions at the LHC centre-of-mass energy is $80\,\text{mb}$. Consequently, the average number of inelastic proton-proton collisions is approximately $\mu = 27$ at the LHC design luminosity.

During the start-up of the LHC machine in 2008 a faulty connection between two magnets caused severe damage to a section of the machine and a full year was needed to replace the damaged components. Repairs on the machine were completed by November 2009 and it was decided to operate the machine at moderate energy and luminosity, instead of the design values presented here, to get more experience. Initially, the centre-of-mass energy was $\sqrt{s} = 900\,\text{GeV}$ and by December 2009 the world record breaking centre-of-mass of $\sqrt{s} = 2.36\,\text{TeV}$ was attained. By the end of 2010 the attained centre-of-mass energy was $\sqrt{s} = 7\,\text{TeV}$ and the instantaneous luminosity at LHC*b* was about $\mathcal{L} = 1.6 \times 10^{32}\,\text{cm}^{-2}\text{s}^{-1}$. The number of bunches in a beam was approximately 400.

2.1.1 *b* production at the LHC

The expected cross section for b production at the LHC centre-of-mass energy is $\sigma_{b\bar{b}} = 500\,\mu\mathrm{b}$. Therefore, assuming an inelastic cross-section for proton-proton collision of $\sigma_{\mathrm{inel}} = 80\,\mathrm{mb}$, one in every 160 proton-proton collisions is expected to yield a $b\bar{b}$ hadron pair. The main $b\bar{b}$ production processes [27] that contribute to $\sigma_{b\bar{b}}$ are the leading order process of gluon fusion (14.4%) and the next-to-leading order processes of flavour excitation $(60.3)\%$ and gluon splitting (25.0%). Production via the leading order process of quark - anti-quark annihilation is negligible (0.20%). Examples of Feynman diagrams for these processes are shown in Fig. 2.2. After a $b\bar{b}$ pair has been produced, the b and $\bar{b}$ hadronise independently and incoherently of each other.

In inelastic proton-proton collisions at a centre-of-mass energy of $\sqrt{s} = 14\,\mathrm{TeV}$, B hadrons are expected to be produced uniformly in the rapidity range $[-3, 3]$ — the so-called rapidity plateau [28]. Kinematically, this implies that the the angular distributions of hadrons with a b or $\bar{b}$ peak at polar angles $\theta = 0$ and $\theta = \pi$, as shown in Fig. 2.3a.

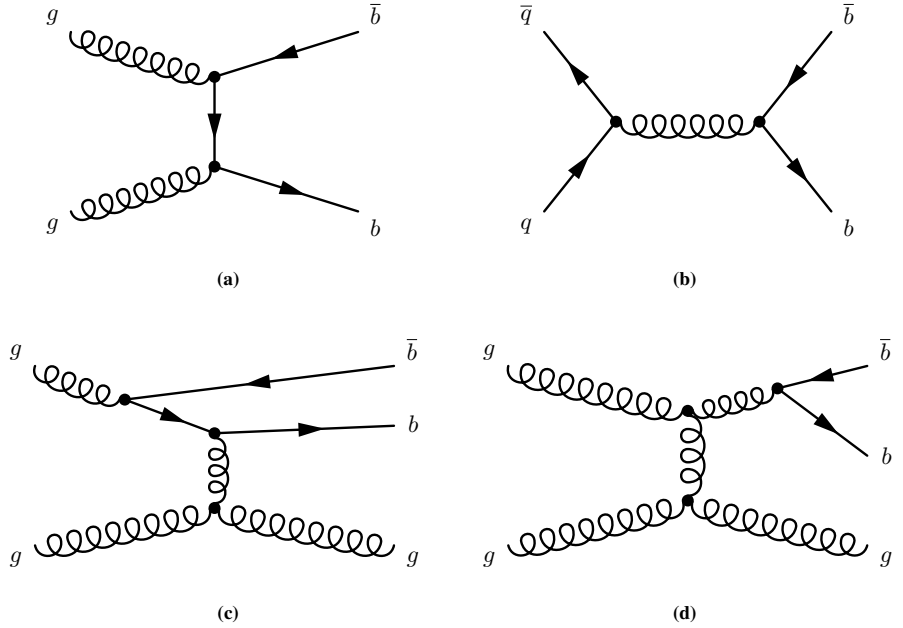

Fig. 2.2: *Examples of Feynman diagrams for B-production. Two leading-order diagrams are: (a) pair creation through gluon fusion and (b) quark–anti-quark annihilation. Examples of important higher order diagrams are: (c) flavour excitations and (d) gluon splitting.*

2.2 The LHC*b* Detector

The LHCb detector [30, 31, 32] is a single arm spectrometer optimised for the detection of forward b and $\bar{b}$ production. A side view of the detector is shown in Fig. 2.4. It consists of various sub-detectors which can be categorised into:

- Tracking detectors: Vertex Locator (VELO), Tracker Turicensis* (TT), Inner Tracker (IT) and Outer Tracker (OT).

*The Tracker Turicensis was formerly known as the Trigger Tracker. Its original purpose was to assign rough momentum estimates to particles in the trigger.

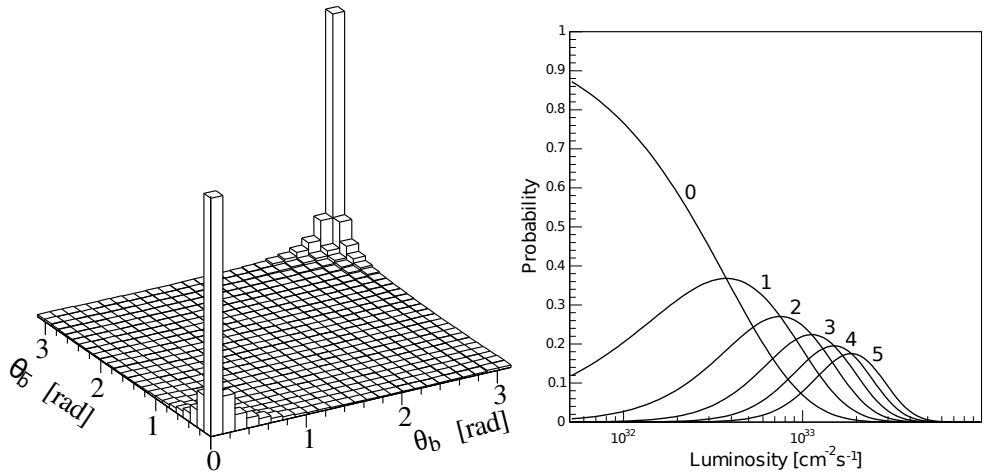

Fig. 2.3: *(a) Production angles of $b\bar{b}$ pairs atLHCb. The $b\bar{b}$ pairs are predominately produced at small angles with respect to the beam pipe in the forward $(0, 0)$ and backward (π, π) direction [29]. (b) Probability distributions for having 0, 1, 2, 3, 4, and 5 interactions per bunch crossing as a function of the LHC luminosity.*

- Particle identification (PID) detectors: Two ring imaging Čerenkov detectors (RICH1 and RICH2), electromagnetic and hadronic calorimeters (ECAL and HCAL), and the muon detector (M1 -M5).

In addition to the sub-detectors, a central component of the LHC*b* detector is the warm dipole magnet [33], which is used to deflect charged particles. Combined with the tracking system it allows to determine the momenta of charged particles. The main component of the magnetic field is along the vertical direction and the total integrated magnetic field is $4.2\,\mathrm{Tm}$.

2.2.1 The LHC*b* coordinate system

The coordinate system of the detector, which is adopted throughout this thesis, is a right handed coordinate system with the positive z-axis pointing from the Vertex Locator, along the beam pipe, towards the muon detector. Looking along the z-axis towards the muon detector, the positive y-axis is pointing upwards and the positive x-axis is pointing to the left, *i.e.* into the page in Fig. 2.4. The origin of this coordinate system is chosen to coincide with the nominal interaction point.

Other nomenclature related to this coordinate system are the terms: “downstream”, “upstream”, “stereo angle”, and “A-side” and “C-side”. Downstream and upstream indicate the direction along the z-axis. The former is the direction of increasing z and the latter is the direction of decreasing z.

The stereo angle is defined as the angle a detector element makes with the y-axis and applies to the TT, IT and OT tracking stations. This angle corresponds to a rotation about the z-axis and the orientation of the detector element with respect to the y-axis is denoted with x, u or v. The x-measurement planes consist of detector elements positioned parallel to the y-axis, *i.e.* $\phi_s = 0°$, while detector elements in the u and v-measurement planes make an angle with the y-axis of $\phi_s = -5°$ and $\phi_s = +5°$, respectively. The VELO detector has a stereo angle built into the silicon wafer geometry.

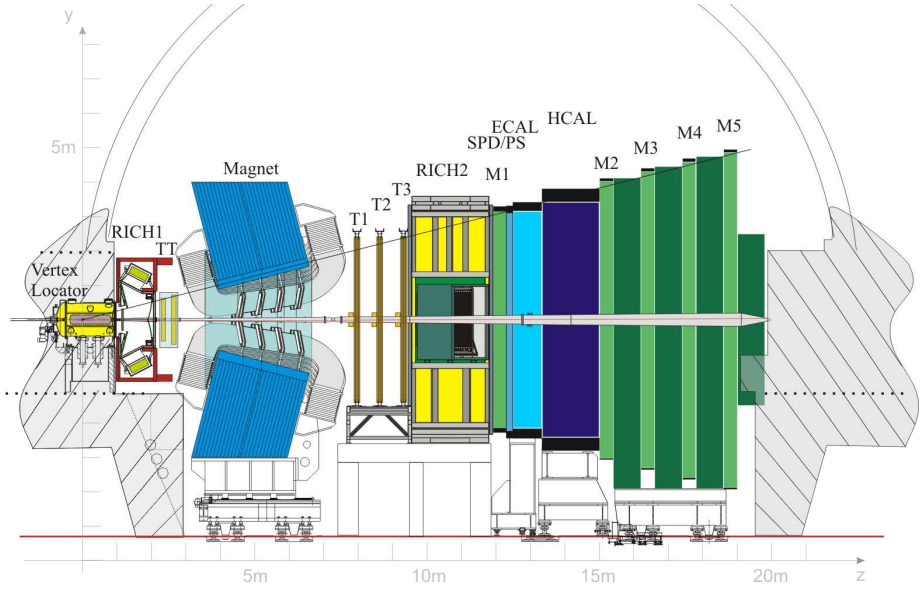

Fig. 2.4: *Side-view of the LHCb detector.*

All of the sub-detectors, except RICH1 and RICH2, are designed to be opened along the x-axis to allow easy access for maintenance. A-side (or Access side) indicates detector halves located at $+x$. C-side (or Cooling side) indicates detector halves at $-x$, close to the cooling installations inside the cavern.

The detector is approximately $20\,\mathrm{m}$ long and its maximum width and height are determined by the last muon station M5. This gives an overall dimension of roughly $6\,\mathrm{m} \times 5\,\mathrm{m} \times 20\,\mathrm{m}$. The acceptance of the detector is defined by the angle with respect to the z-axis and covers the sensitive region in which approximately 15% of the $b\bar{b}$ hadron pairs are emitted. In the horizontal plane, *i.e.* the bending plane, the acceptance is given by the polar angle $15\,\mathrm{mrad} < \theta < 300\,\mathrm{mrad}$. In the vertical plane, *i.e.* the non-bending plane, the acceptance is given by the polar angle $15\,\mathrm{mrad} < \theta < 250\,\mathrm{mrad}$. The latter corresponds to a pseudo rapidity, defined as

$$\eta = -\ln\left[\tan\left(\frac{\theta}{2}\right)\right], \tag{2.3}$$

of $2 < \eta < 5$.

2.2.2 Luminosity at the LHC*b* interaction point

Though the nominal design luminosity of the LHC is $\mathcal{L} = 10^{34}\,\mathrm{cm^{-2}s^{-1}}$, the LHC*b* experiment operates at a moderate luminosity of $\mathcal{L} = 2 \times 10^{32}\,\mathrm{cm^{-2}s^{-1}}$. This is achieved by not focusing the beam as strongly as at the interaction points of the ATLAS and CMS experiments. At this luminosity, as shown in Fig. 2.3b, the probability to have at most one proton-proton interaction per bunch crossing, assuming 2808 bunches, is approximately 0.3. While, the probability to have more than one proton-proton collision per bunch crossing, so-called pile-up events, is $\leqslant 0.1$. Running at this luminosity has several advantages. For example, it greatly simplifies the triggering, reconstruction and flavour tagging procedures, since events are primarily dominated by single proton-proton interactions. In addition, there is less radiation damage to the sub-detectors

and the detector occupancy is moderate. Nonetheless, the sub-detectors have been designed to run at a luminosity of $\mathcal{L} = 5 \times 10^{32}\,\mathrm{cm}^{-2}\mathrm{s}^{-1}$.

2.3 Tracking Detectors

The tracking system of LHC*b* comprises the VELO, TT, IT and OT. The VELO, TT and IT are silicon based detectors: the latter two were developed within a common project called Silicon Tracker (ST). The VELO is primarily used for the reconstruction of primary and secondary vertices, whereas the TT, IT and OT are used in the track reconstruction primarily to determine the momenta of charged particles.

2.3.1 The Vertex Locator (VELO)

The VELO [34] comprises a series of silicon modules positioned along and perpendicular to the beam pipe. Each module consists of two $300\,\mu\mathrm{m}$ thick n-on-n silicon sensors, shown in Fig. 2.5, called r and ϕ-sensors, which allows to reconstruct tracks in 3D.

The r-sensor has circular strips segmented into four $\frac{4}{\pi}$ sectors centred around the beam axis and measure the r-coordinate of a hit. Each sector has 512 readout strips and the strip pitch increases linearly with the radius, from $38\,\mu\mathrm{m}$ at the inner edge to $102\,\mu\mathrm{m}$ at the outer edge.

The ϕ-sensor has almost-radial strips that measure the azimuthal ϕ-coordinate of the hit. The sensor is divided into an inner and outer region. In the inner region the strips make a stereo angle of 20° with the radial, while in the outer region this angle is 10°. The strip pitch of the ϕ-sensor, similar to the r-sensor, increases linearly with the the radius and goes from $38\,\mu\mathrm{m}$ to $78\,\mu\mathrm{m}$ in the inner region and from $39\,\mu\mathrm{m}$ to $97\,\mu\mathrm{m}$ in the outer region.

The corresponding hit resolution for both sensors goes from approximately $8\,\mu\mathrm{m}$ at the inner region to $20\,\mu\mathrm{m}$ at the outer region of a sensor [35].

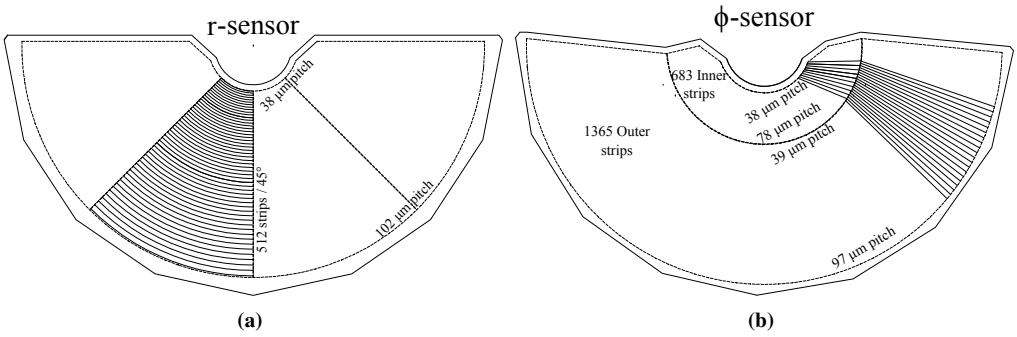

Fig. 2.5: *The VELO r and ϕ sensors: (a) shows the layout of the r-sensor and (b) shows the layout of the ϕ-sensor.*

To fulfil the requirements of high precision reconstruction of primary and secondary vertices, the latter typical of B decays, the VELO sensors need to be as close as possible to the proton beam. To achieve this the modules are housed in two aluminium boxes, 21 modules per box, one at $+x$ and one at $-x$, which in turn are housed in a vessel that is interfaced with the beam pipe. The purposes of these boxes is to separate the detector vacuum from the beam vacuum, and their design is such that the amount of material a particle encounters before being detected is minimal and that the $+x$ and $-x$ modules overlap when they are in a "closed" position. In addition, they also shield the modules and electronics against RF pick-up from the beams and guide the wakefields of the beams.

A cross section of the layout of the modules in the horizontal plane during stable beam and during beam injection are shown in Fig. 2.6. Under stable running conditions, the innermost region of the sensors are $7\,\mathrm{mm}$ away from the beam axis - the innermost active region is $8\,\mathrm{mm}$ away from the beam axis - ensuring that the first measurement is as close to the primary vertex as possible. The VELO modules close to the interaction point allow to reconstruct tracks with polar angles up to $390\,\mathrm{mrad}$ and the modules further downstream allow to reconstruct tracks with polar angles down to $15\,\mathrm{mrad}$. During beam injection the modules are required to be least $3\,\mathrm{cm}$ away from the beam axis, where $3\,\mathrm{cm}$ is the required aperture for the beams when they are kept apart. Therefore, the design of the VELO is such that the boxes can be retracted along the horizontal x-axis direction.

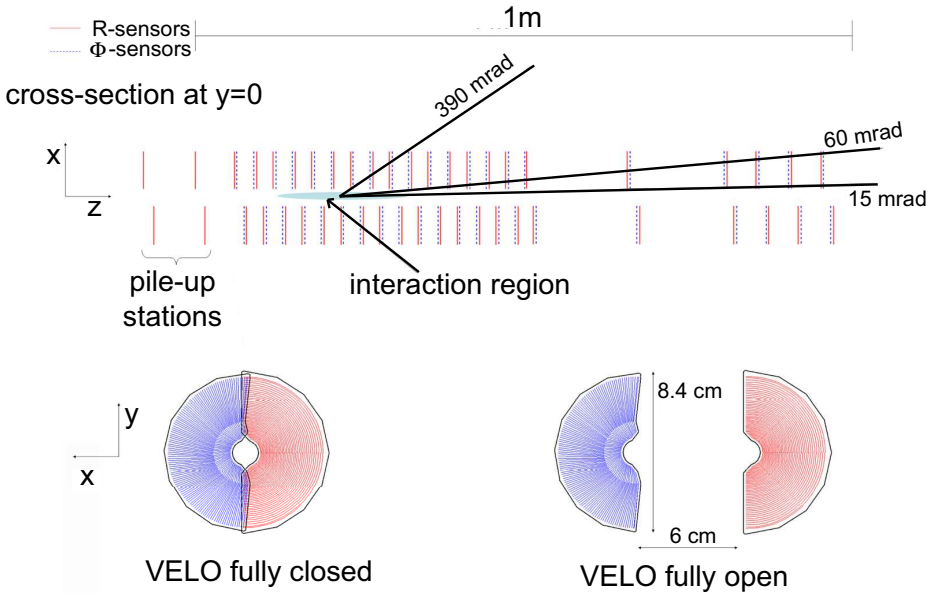

Fig. 2.6: *A cross section of the VELO modules layout in the horizontal plane. Also shown is the position of the modules in the vertical plane during stable beam (left) and beam injection (right).*

Located upstream of the VELO modules are two pile-up stations consisting of r-sensors only. Their purpose is to determine, using upstream tracks originating from the interaction point, the number of interactions in a proton-proton bunch crossing at the lowest trigger level. This information allows the trigger to veto events with multiple collisions.

2.3.2 The Tracker Turicensis (TT) and the Inner Tracker (IT)

The TT [36], located just in front of the magnet, consists of four detection layers of silicon sensor ladders in the following stereo angle configuration along the z axis: x-u-v-x. The dimensions of the TT are such that it covers the full acceptance of the detector. Each sensor is $500\,\mu\mathrm{m}$ thick, $9.64\,\mathrm{cm}$ wide and $9.44\,\mathrm{cm}$ long, and contains 512 readout strips with a strip pitch of $183\,\mu\mathrm{m}$. The corresponding spatial resolution is approximately $50\,\mu\mathrm{m}$.

The IT [36] consists of three stations (IT1, IT2 and IT3), and together with the Outer Tracker (OT) stations form the tracking (T) stations located behind the magnet. The IT covers the inner region where the particle flux is too high to use the gaseous straw tubes of the OT. Each IT

station consists of four boxes arranged in the shape of a cross around the beam pipe as indicated in Fig. 2.7b. A box contains four layers in a similar stereo angle configuration x-u-v-x as the TT. The layout of an IT x layer is shown in the figure. Each layer contains seven ladders. Ladders in the top and bottom layers consist of one silicon sensor each, while modules in the left and right boxes consist of two silicon sensors each. The sensors are $7.6\,\mathrm{cm}$ wide and $11\,\mathrm{cm}$ long and $310\,\mu\mathrm{m}$ (for one-sensor modules) or $410\,\mu\mathrm{m}$ (for two-sensor modules) thick. Each sensor has 384 readout strips with strip pitch of $198\,\mu\mathrm{m}$. The corresponding spatial resolution is approximately $60\,\mu\mathrm{m}$.

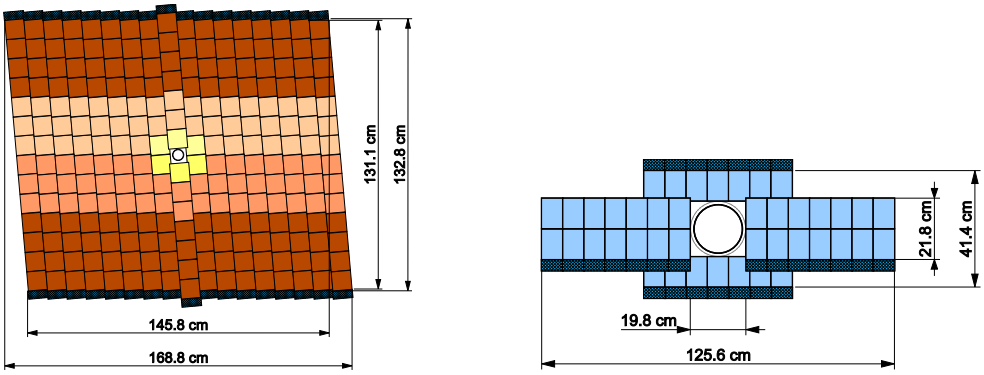

Fig. 2.7: *Layout of (a) a TT u layer and (b) a IT x layer.*

2.3.3 The Outer Tracker (OT)

The OT [37], of which the simulation is described in Chapter 3, uses gaseous straw tube detectors to measure the drift times of ionisation clusters produced by particles traversing the straw tubes. Each straw tube is operated as a proportional counter with a typical drift distance resolution of $200\,\mu\mathrm{m}$.

The detection principle of a straw tube detector is illustrated in Fig. 2.8. When a charged particle traverses the straw tube it transfers energy to the gas molecules through electromagnetic interactions. If the transferred energy exceeds the ionisation potential of the gas molecules, electrons can be liberated. In the presence of an electric field the ions and electrons will not recombine. Instead the electrons and ions will drift in opposite directions along the electric field, *i.e.* the electrons will travel to anode wire and the ions to the cathode straw wall. At high field strengths, the electrons will be accelerated sufficiently to further liberate electrons through collisions with the gas molecules. This leads to an avalanche of electrons near the anode wire, where the electric field is the largest, leaving a behind a large cluster of ions near the cathode wall. This process is referred to as gas amplification.

The arrival of the electrons at the anode wire and ions at the cathode wall induces an detectable electronic signal with a sharp rise time and a long "ion" tail. The elapsed time between particle impact and appearance of the anode signal is dominated by the electron drift, which, given the low mass of the electron, is approximately two orders of magnitude faster than the ion drift. The minimum distance, *i.e.* distance of closest approach, between the particle and the wire is inferred from the timing of the response of the straw tube. In order to obtain a high spatial resolution it is important that the first cluster arriving at the anode wire is detected. For further details on gaseous detectors and the OT hardware design see, *e.g.*, [37, 38, 39, 40, 41].

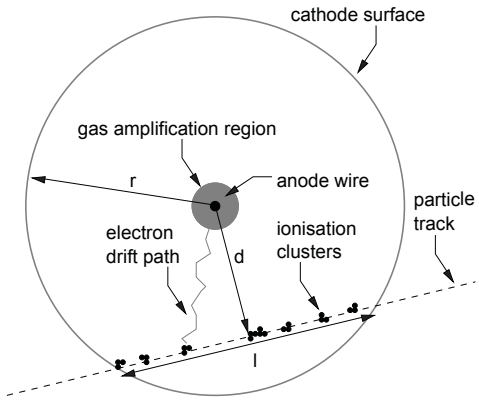

Fig. 2.8: *Illustration of the detection principles of a straw tube. The straw tube inner radius is r, which is $r = 4.9\,\mathrm{mm}$ for the OT. The distance of closest approach, i.e. the drift distance, of the particle to the wire is given by d and l is the path length of the particle in the straw tube.*

The OT consists of three stations (T1, T2 and T3), and covers the region outside the IT where the particle flux is sufficiently low. There is a small overlap between the IT and OT to ensure there are no gaps in the acceptance. Each station consists of four layers of modules in a similar stereo angle configuration x-u-v-x as the TT and IT. Each module contains two staggered layers, so-called mono-layers, of straw tubes. The modules are mounted on the front and rear of aluminium support frames, so-called C-frames, that house the readout electronics and services. There are four C-frames per station, two on the C-side and two on the A-side of a station, as shown Fig. 2.9.

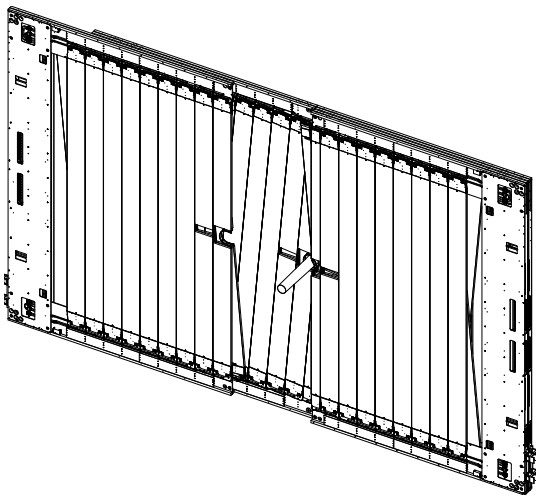

Fig. 2.9: *An OT station, shown with the first A-side C-frame in its open position.*

As illustrated in Fig. 2.9 each C-frame consists of an x and stereo layer, either u or v. Most modules in C-frame cover the whole vertical acceptance of the LHCb detector and are called Full modules or F-modules. There are seven F-modules per layer in a C-frame. While an F-module covers the whole vertical acceptance, the straws in an F-module are segmented into a top and bottom half around $y = 0$. Therefore, an F-module can in principle be considered as two separate modules. Each half of an F-module contains 128 straws, *i.e.* 64 straws per mono-layer.

The inner most modules, *i.e.* in the region around the beam pipe are called Short modules or

S-modules, and covers the region above and below the IT. There are three types of short modules S1, S2 and S3. The S1-modules are located at the side of the beam pipe adjacent to the last F-module and the S2 and S3-modules are located above and and below the beam pipe. There are two S1-modules per layer, one above and one below, per layer in a C-frame. The A-side C-frames contains two S2-modules per layer and the C-side C-frames contains two S3-modules per layer. All short modules, except the S3 modules, contain 64 straws per mono-layer giving a total of 128 straws. The S3 modules contain 32 straws per mono-layer giving a total of 64 straws. The total number of straws of in the OT is 53760.

2.4 Particle Identification Detectors

The particle identification system of LHC*b* comprises two ring imaging Čerenkov detectors (RICH1 and RICH2), the electromagnetic calorimeter (ECAL), the hadronic calorimeter (HCAL) and the muon detector (M1-M5). They are used to identify particles whose trajectories have been reconstructed in the Tracking system.

The primary purpose of the RICH detectors are to identify charged pions and charged kaons. The ECAL is used to identify electrons and photons and determine their energy. Similarly, the HCAL is used to identify hadrons, *i.e.* kaons, pions and protons, and to determine their energy. Finally, the muon detector is used to identify muons and determine their momenta. In addition to the off-line reconstruction, the energy information from the ECAL and HCAL, and the momentum information from the muon detector are used in the trigger system.

2.4.1 The Ring Imaging Čerenkov Detectors (RICH1 and RICH2)

The first RICH [42] detector, RICH1, is located before the magnet, between the VELO and the TT, to identify low momentum particles over an polar angle acceptance from $25\,\mathrm{mrad}$ to $300\,(250)\,\mathrm{mrad}$ in the horizontal (vertical) plane. The second RICH detector, RICH2, is located behind the magnet, just after the T stations, and covers the region, from approximately $15\,\mathrm{mrad}$ to $120\,(100)\,\mathrm{mrad}$ in the horizontal (vertical) plane, where there are mainly high momentum particles. The combined system is designed to identify and separate kaons from pions in the momentum range $2\,\mathrm{GeV} < \mathrm{p} < 100\,\mathrm{GeV}$.

Both RICH detectors exploit the Čerenkov effect - the emission of radiation when a charged particle traverses a dielectric medium at a speed greater than the macroscopic speed of light - to determine a particle's velocity. This, combined with the momentum estimate of the particle, is used to determine the mass of the particle and, therefore, its type. The velocity of a particle is derived by measuring the emission angle θ_C of the Čerenkov radiation, which is emitted in a cone with the respect to the particle's trajectory. The dependence of the emission angle θ_C on the particle's velocity $\beta = v/c$ is given by

$$\cos\theta_C = \frac{1}{n\beta}, \tag{2.4}$$

where n is the refractive index of the dielectric medium. The following can be deduced from Eq. 2.4: first, the emission threshold is given by $\beta_t = 1/n$. Second, a large refractive index allows to identify low momentum particles.

Both RICH detectors use different radiators, *i.e.* dielectric media, to cover different momentum ranges. RICH1 covers the low momentum range $1\,\mathrm{GeV} < \mathrm{p} < 60\,\mathrm{GeV}$ using aerogel and $\mathrm{C_4F_{10}}$, while RICH2 covers the high momentum range $15\,\mathrm{GeV} < \mathrm{p} < 100\,\mathrm{GeV}$ using $\mathrm{CF_4}$.

2.4.2 The Calorimeters (ECAL and HCAL)

The calorimeter system [43] is located downstream of the magnet, between the first muon station M1 and second muon station M2. It comprises an electromagnetic calorimeter, ECAL, followed by a hadronic calorimeter, HCAL. In addition, a scintillator pad detector, SPD, and a pre-shower detector, PS, separated by a thin lead converter, are located in front of the ECAL. The SPD and PS provide additional information on the longitudinal evolution of an electromagnetic shower.

Both electromagnetic and hadronic calorimeters follow the same basic working principle. They consist of alternate layers of absorber and scintillator materials. All incident particles, except muons, that interact with the absorber material produce a cascade of particles, which are subsequently absorbed. The ionisations induced by this cascade excite atoms in the scintillator material, which emit scintillation light as they return to their ground state. This scintillation light is transmitted to a photo-multiplier tube via wavelength-shifting fibres. Ultimately, the energy of the incident particle is directly proportional to the total amount of collected scintillation light.

The scintillator material used in the SPD, PS, and both the calorimeters is doped polystyrene. The SPD and PS consists of $15\,\mathrm{mm}$ thick scintillation pads, and the total area covered by the pads is $7.2\,\mathrm{m} \times 6.2\,\mathrm{m}$. Located between the SPD and PS is a $15\,\mathrm{mm}$ thick lead converter. The SPD is used to identify charged particles before they begin to shower, since they produce ionisation as opposed to neutral particles. The lead converter initiates an electromagnetic shower, which is then detected by the PS. This allows to discriminate between electrons and photons. The SPD is used to separate electrons and photons, while the PS is used to separate electrons/photons versus hadrons.

The ECAL, which covers the whole acceptance of the detector, consists of modules with a "shashlick" layout: alternating layers of $4\,\mathrm{mm}$ thick scintillator material and $2\,\mathrm{mm}$ thick lead absorber. Each module is oriented perpendicular to the beam pipe and has a thickness of approximately $42\,\mathrm{cm}$. The ECAL measures the energy of incident electrons and photons that interact with the lead via electromagnetic processes with a resolution of [43]

$$\frac{\sigma_E}{E} = \frac{10\%}{\sqrt{E\,[\mathrm{GeV}]}} \oplus 1.0\%, \tag{2.5}$$

where $\oplus$ represents addition in quadrature.

Although hadrons may initially shower in the ECAL, they are fully absorbed in the HCAL where they deposit most of their energy. The HCAL consists of modules with a similar layout as the ECAL. Each module consists of alternating layers of $3\,\mathrm{mm}$ thick scintillator material and $10\,\mathrm{mm}$ thick iron absorber. As opposed to the ECAL, the modules are oriented parallel to the beam pipe. The HCAL measures the energy of the hadrons that interact with the iron via nuclear processes, with a resolution of [43]

$$\frac{\sigma_E}{E} = \frac{80\%}{\sqrt{E\,[\mathrm{GeV}]}} \oplus (10)\%. \tag{2.6}$$

2.4.3 The Muon Detector

Muons typically traverse the whole detector. To detect and identify them, the muon detector [44] is located downstream of the calorimeter system. It comprises five stations M1 to M5, each consisting of 276 chambers. In addition to identifying muons, the muon detector is used to provide transverse momentum, $\mathrm{p_T}$, estimates of the muons to the trigger. To obtain a optimal momentum estimate, M1, which is not used for muon identification, is placed in front of the calorimeter sys-

tem to minimise any uncertainties due to multiple scattering in the calorimeter system. The rest of the stations, alternated with $80\,\mathrm{cm}$ iron absorbers, are located behind the calorimeter system.

A station is logically divided into four quarters, which in turn are divided into four regions of chambers. The stations have a projective geometry, *i.e.* their dimensions scale with their distance from the interaction point. Consequently, the dimensions of the chambers increase from the innermost region to the outermost region and from M1 to M5.

Due to the particle flux close to the beam pipe, the chambers in the innermost region have a finer granularity compared to chambers in the outer regions such that the occupancy over a station is uniform. All chambers, except for the innermost chambers of M1, are multi-wire proportional chambers. The chambers in the innermost region of M1, where the particle flux is higher, are triple-GEM detectors.

Chapter 3

The Outer Tracker Simulation

Detector simulations allow to mimic the response of the detector to traversing particles and aid in the development and optimisation of various algorithms needed for reconstruction, particle identification and physics studies. Hence, it is essential that the assumptions on which the simulation is based accurately reflect the actual detector design.

The simulation of the LHC*b* detector is a twofold process:

- Simulation of material interactions of particles traversing the detector: this is done with the LHC*b* simulation application GAUSS [45] which uses a combination of Monte Carlo generators PYTHIA [29] and EVTGEN [46] to simulate particle production and decays, and GEANT4 [47] to simulate their interactions with the detector. In the active detection layers, the passage of a traversing particle is registered as a detector hit. Of importance here is a precise detector description which is used in GEANT4 to simulate the detector geometry and material effects realistically.
- Simulation of the response of active detection layers and conversion to digital data: this is done with the LHC*b* digitisation application BOOLE [48]. Here the detector response to the hits generated in the previous step, including detector traits such as resolution smearing, dead-time, noise and cross-talk, is simulated. As a consequence of the different detection technologies within LHC*b*, each sub-detector implements its own digitisation procedure.

The simulated detector response is encoded in a format identical to real data from the experiment. Consequently, the same reconstruction and physics algorithms used for real data can be used for Monte Carlo data. The reconstruction algorithms are developed within a common reconstruction application called BRUNEL. The physics algorithms, which rely heavily on the BRUNEL algorithms are developed within a common physics analysis application called DAVINCI. There exist various sub-detector specific calibration applications and a common alignment application called ESCHER. At the base of all these applications is the LHC*b* C++ object oriented event processing framework GAUDI. All algorithms developed within the various applications inherit from the base GAUDI algorithms. This facilitates the re-usability of code and consistency in the algorithms. For example, the alignment application ESCHER uses the same reconstruction algorithms as the reconstruction application BRUNEL. For an overview of the LHC*b* simulation and reconstruction programme see [27].

This chapter gives an overview of the Outer Tracker (OT) simulation. First the OT detector description is discussed in Sec. 3.1, followed by the digitisation procedure in Sec. 3.2. Finally the expected detector response to a typical B decay, based on the input to the simulation, is discussed in Sec. 3.3.

3.1 Detector Description

The detector description is an integral component of the LHC*b* framework and mirrors, as closely as possible, the actual constructed detector. GEANT4 uses this description to simulate particle interactions with the detector. In the digitisation process it is used to determine which detector elements have been hit and to retrieve their location. In addition, the reconstruction software uses it to account for the amount of material a particle has encountered along its path to correctly estimate energy loss and multiple scattering corrections. Furthermore, the detector description contains the best estimates of the positions of the detector elements, which are used as input for alignment and reconstruction.

The detector geometry is described using a hierarchical structure of nested volumes. A volume can be composed of any material, and can have any shape, size and orientation [49, 50, 51]. In addition, a volume can either be an abstract representation of a collection of detector elements or represent an actual detector element. There are two primary requirements to consider when describing the detector, namely:

- CPU speed: this is primarily dominated by the number of volumes, their shapes, and how they are structured, *i.e.* their hierarchy. In order to determine the amount of material a particle has encountered, and to simulate or estimate the energy loss and multiple scattering corrections, one needs to determine the intersections of the trajectory of the particle with a given volume. These calculations are generally less CPU intensive for *simple* shapes compared to compound shapes. In addition, an optimised logical hierarchy of volumes, even when there is a great number of volumes, can also improve the speed of the simulation and reconstruction*.
- Realism: the amount of detail in the simulation also affects the CPU speed and needs to be optimised versus the precision with which the detector is simulated. For the reconstruction the amount of material a particle encounters is of importance to correctly estimate the energy loss and multiple scattering corrections. The detector description is also used in the alignment procedure. Therefore, it is essential that the dimensions, orientation, and positions of the volumes correspond to the values of the actual detector elements. This includes the material of the detector elements, location of individual straw tubes and their encoded sequence in the readout electronics. Any deviations from the design values obtained with the alignment procedure are considered mis-alignments. As a cross check, they are compared to the survey measurements, which also use the design values as reference.

To satisfy the first requirement, the LHC*b* detector is split up into five regions: *upstream*, *before magnet*, *magnet*, *after magnet* and *downstream* (see Fig. 3.1a) to speed up the simulation and, ultimately, the track fit during reconstruction. The OT, together with the Inner Tracker (IT), is located in the tracker (T) volume which, together with RICH2, is located in the *after magnet* region.

The actual design and layout of the OT is described in Sec. 2.3.3. In the geometry description, the hierarchy of the OT volumes, as shown in Fig. 3.1b, is as follows: there are three station volumes, each containing four layer volumes which represent the x and stereo layers. Each layer is divided into quarters, representing the readout regions of a layer. These quarters in turn contain nine modules each. The description mirrors the actual design of the detector as described in Sec. 2.3.3, but uses a slightly simplified module description which is discussed in Sec. 3.1.1. The aluminium C-frames, although outside of the acceptance of the detector, are also included

*The most optimal hierarchy is obtained with $e(\approx 3)$ volumes per level of hierarchy.

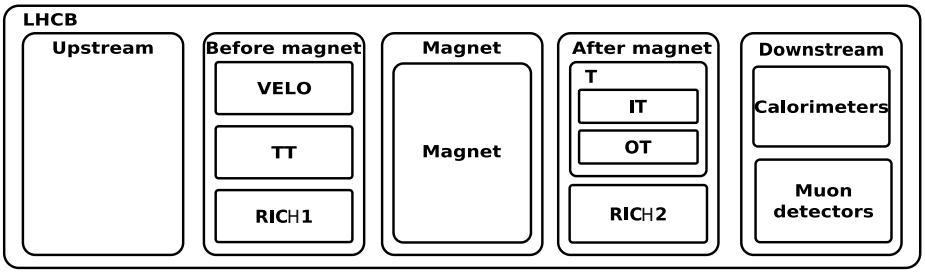

(a)

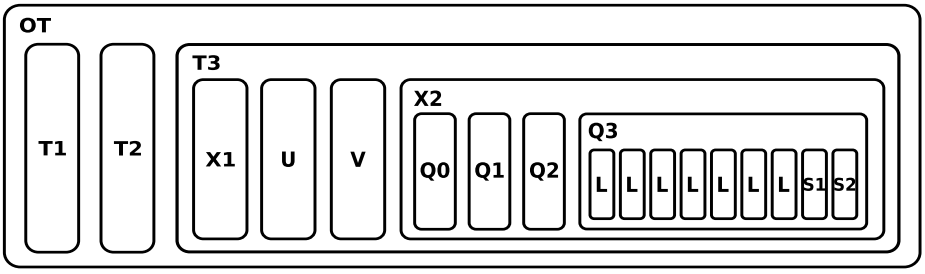

(b)

Fig. 3.1: *LHCb and OT volume hierarchies: (a) shows the LHCb detector hierarchy. The OT, together with the IT, is located in the T volume which, together with RICH2 is located in the after magnet region. (b) shows the OT volume hierarchy. Note that only station T3, layer X2, and quarter Q3 are worked out, but the other stations, layers, and quarters are similar.*

in the description: particle interactions with the C-frames can contribute to the occupancy in sub-detectors downstream of the OT, *e.g.* RICH2, and even in the OT detector layers themselves.

Note that the volumes are nested similar to a babushka doll, which implies that the centre of a daughter volume is positioned with respect to its mother volume. The top most mother volume is the LHCb volume whose coordinate system is equivalent to the LHCb coordinate system defined in Sec. 2.2. The daughter volumes of the LHCb volume are the regions whose centres correspond to the average of the centres of the sub-detectors in the region. In the LHCb geometry framework, daughter volumes are positioned with respect to the coordinate system of their mother volume.

Alignment corrections, *i.e.* the delta translations and rotations, are applied to the nominal coordinate system of the volume itself. Any transformation applied to the mother volume is propagated to the children, *e.g.* if an OT station is displaced in x in the LHCb frame by an amount Δx, the layers are simultaneously displaced by the same amount in the global LHCb frame. Consequently, alignment corrections applied to a station are propagated recursively to all volumes in the station hierarchy: layers, quarters and modules.

3.1.1 The OT module

The OT is an ensemble of gas-tight straw tube modules. Each module contains two staggered layers of straw tubes, so-called mono-layers, sandwiched between two panels. The straws are glued to their panels using a high precision aluminium template to position the straws to better than $50\,\mu\mathrm{m}$ over the whole length of a panel. Since the positions of the anode wires inside a module are known within $50\,\mu\mathrm{m}$ and the typical drift distance resolution is expected to be approximately $200\,\mu\mathrm{m}$, it is not foreseen to align the individual straws. Accordingly, combined with the require-

ments for fast simulation and reconstruction, a module and not a straw is considered the basic building block in the detector description and the straws inside a module are represented by a single sensitive volume. Consequently, the smallest alignable detector element is a module.

Description

It is essential, not only for simulation, digitisation and reconstruction, but also for alignment, that the dimensions of the modules as well as their coordinates in the detector description correspond within errors to the currently known values. In the simulation the point of interaction of a particle with a detector element is encoded in the hit information. This is used in the digitisation to determine which straws have been hit. Their readout locations together with the drift distances and the propagation time of the signals along the anode wire are encoded. The reconstruction uses the detector description to determine a coordinate for a given channel. These coordinates are the input for the pattern recognition and track fit algorithms. The detector description is also used to initialise the alignment procedure, since it contains the best known coordinates of the detector. If the detector is mis-aligned then these mis-alignments will appear as corrections on top of the detector description reference coordinates.

In the detector description a module is composed of five volumes: a straw volume that represents the two mono-layers of straws encased between two panel volumes, and two side wall volumes, see Fig. 3.2a. The straw volume is defined as a sensitive volume, while the panels and side walls are defined as passive volumes. In the simulation, only particle interactions with the sensitive volume are recorded and subsequently considered in the digitisation. The passive volumes are necessary to correctly estimate multiple scattering, energy losses or other physical process that may occur. For this reason it is necessary to include all materials within the acceptance of the detector to accurately simulate the response to charged particles.

The dimensions of a module and the straws are shown in Fig. 3.2. All modules are $32\,\mathrm{mm}$ thick; the straw volume and a panel volume is $10.73\,\mathrm{mm}$ thick and $10.635\,\mathrm{mm}$ thick, respectively. The width of a module is determined by the number of straws in a mono-layer, the straw pitch in x of $5.25\,\mathrm{mm}$, and the thickness of a side wall being $0.6875\,\mathrm{mm}$ *. The length of a module corresponds to the active length of the anode wire.

There are four types of modules that constitute a layer, listed in Tab. 3.1 and illustrated in Fig. 3.3. They differ either in length or the number of straws per mono-layer. Although the F-modules cover the full area of the detector, the straws are separated in two in the horizontal plane $(y = 0)$ with the readout electronics located at the top and bottom of each F-module as shown in Fig. 3.3b. An F-Module can therefore be considered as two separate modules, so-called L-modules, each with a length equal to half an F-module. Similarly, the top and bottom S-modules are read out from above and below, respectively.

Materials

In GEANT4 the material properties of a volume are used to simulate multiple scattering and energy loss of particles traversing the volume. A detailed study [53] of the material of an F-module was performed to determine the weight, thickness, density, and radiation length X_0 of each component in a straw and in a panel. The different materials and their thickness's are shown in Fig. 3.2b. The "fraction-of-radiation-length" X/X_0 for a module was estimated to be 0.79%,

*The width of a module is determined as follows

$$w_m = (\#\text{straws} + 0.5) \times \text{pitch}_x + 2 \times w_{\text{side wall}},$$

where the extra term is due to the staggering of the double layer of straws.

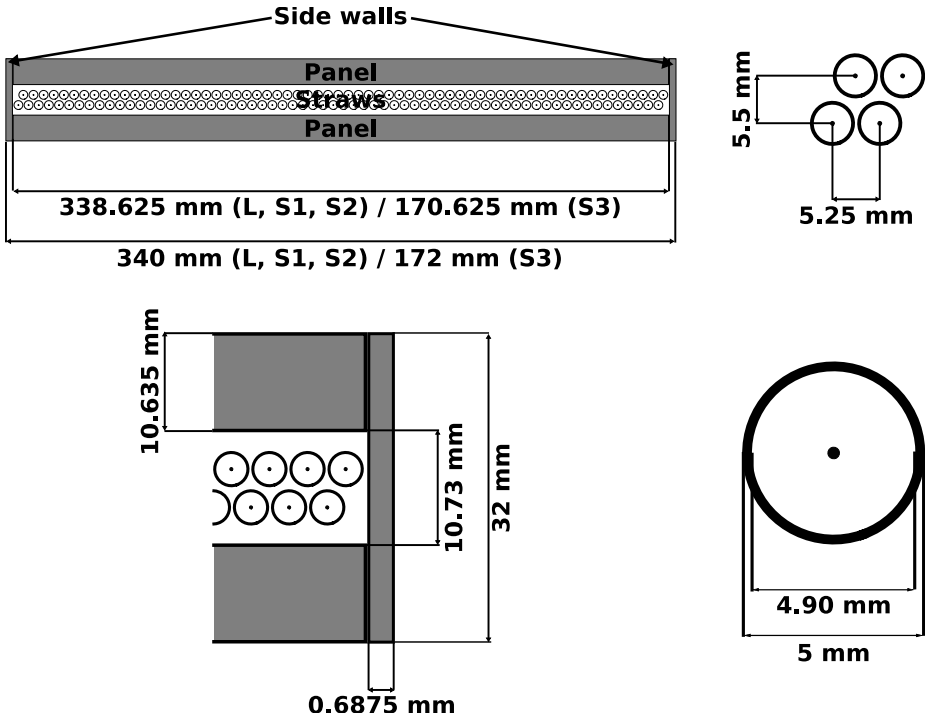

Fig. 3.2: *Properties of an OT module: (a) shows the dimensions of the volumes of the OT module and the dimensions of a straw, as well as the straw pitch in x and z. (b) shows the material composition of the OT module and straw.*

Module	# Straws	Length [mm]	Width[mm]
F	64	4810	340
S1	64	2305	340
S2	64	2213	340
S3	32	2213	172

Tab. 3.1: *The four type of modules that constitute a layer.*

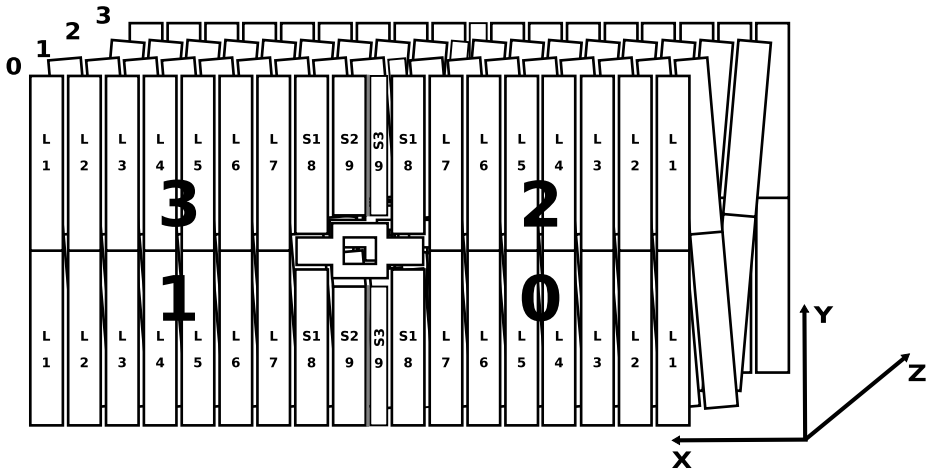

(a)

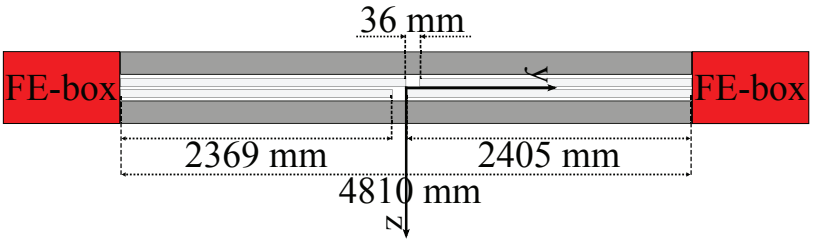

(b)

Fig. 3.3: *The (a) detector description equivalent of an actual OT station and (b) vertical cross section of an F-module. Not shown are the C-Frames which are included in the description. The numbering scheme shown here fully reproduces the readout scheme as described in [52]. The stations are numbered from one to three.*

and for a station, *i.e* four layers of modules, 3.17%. The largest contribution comes from the panels and side walls with $X/X_0 \approx 0.5\%$.

Three homogeneous admixtures, containing mixtures of the individual materials, are defined in the detector description for the three types of volumes that constitute a module as shown in Fig. 3.2b: “side wall”, “panel” and “sensitive”. The densities and composition of these materials are listed in Tab. 3.2. The thickness, expressed as X/X_0, of the tracking station T3, *i.e.* the

third OT and IT station, is shown as a function of y versus x in Fig. 3.4. This is determined by calculating the amount of material, and subsequently the corresponding X/X_0, a particle that traverses the tracking station T3 parallel to the beampipe would encounter. The average X/X_0 for an OT station is 3.1%. This is in good agreement with the $X/X_0 = 3.17\%$ determined for a station by weighing all the materials used in the construction of a module [53]. The C-frames, which are just outside the acceptance at $\eta \approx 2.0$, are clearly visible as a black rectangle. The total material budget for three OT stations inside the acceptance sums up to $X/X_0 = 9.0\%$.

		Epoxy	GTS	Kapton	CFC	Rohacell
Material	Density [g/ cm^3]	Fraction				
Sensitive	0.1067	0.2634	0.4548	0.2818	-	-
Panel	0.0893	0.1765	0.0926	-	0.3465	0.3844
Side wall	0.1236	0.3686	0.0985	-	0.5328	-

Tab. 3.2: *The three materials used in the OT detector description and their corresponding densities. Also listed are the fractions of Epoxy, GTS foil, Kapton, Carbon Fibre Composite (CFC) and Rohacell in each material.*

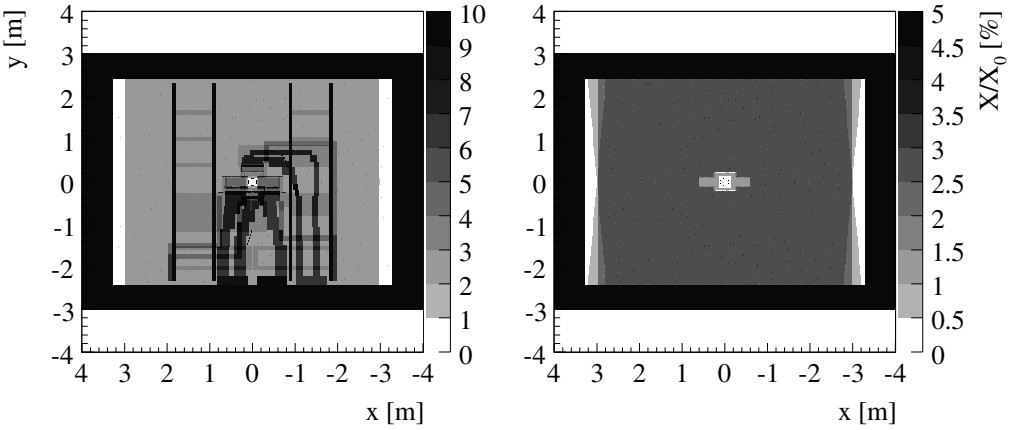

Fig. 3.4: *The thickness, expressed as X/X_0, of the tracking station T3. The left figure shows the thickness, as function of y versus x, of an IT and OT station. The dead material in front of the OT and surrounding the IT are the IT aluminium supports, cabling, cooling and the boxes housing the silicon sensors. The black rectangle surrounding the OT represents the aluminium C-Frames. The right figure shows the thickness of the OT station alone. The grey cross at the centre are the S-module couplings that connect a top S-module to a bottom S-module. The circle is the beam pipe.*

3.1.2 The OT stations, layers and quarters

In the digitisation procedure, discussed in Sec. 3.2, the simulated hits are digitised and encoded. The encoding scheme used in the digitisation follows the readout scheme as described in [52]. The readout electronics provide, in addition to the TDC time of the signal, the location of the

signal, *i.e.* the region from where the signal originates: station, layer, quarter, module and straw ID. Therefore, in order to determine the region a Monte Carlo particle traversed, the hierarchy of the OT volumes follows the encoding scheme of the readout electronics.

The detector description equivalent of an OT station, which is described below, is shown in Fig. 3.3a. As in the encoding, the stations are numbered from one to three. The four layers in a station are numbered from zero to three and each layer is divided into quarters. The quarters are numbered from zero to three. Each quarter contains nine modules numbered from one to nine.

The reference frame used in the OT sub-detector engineering drawings is called the detector frame. This frame is equivalent to the LHCb frame, which is the reference frame used in the detector description, rotated clockwise by $\chi_{\text{beam}} = 3.601\,\text{mrad}$ about its x-axis, where χ_{beam} is the inclination of the beampipe in the detector frame. The detector frame corresponds to the gravitational frame in which the sub-detectors, except the VELO, TT and RICH1, including the Magnet, "hang" vertically. Consequently the sub-detectors appear right slanted in the LHCb frame, except the VELO, TT, RICH1 and the Magnet, which are installed perpendicular to the beampipe. The transformation going from the detector frame to the LHCb frame is given by:

$$\begin{pmatrix} x \\ y \\ z \end{pmatrix}_{\text{LHC}b} = \begin{pmatrix} 1 & 0 & 0 \\ 0 & \cos\chi_{\text{beam}} & -\sin\chi_{\text{beam}} \\ 0 & \sin\chi_{\text{beam}} & \cos\chi_{\text{beam}} \end{pmatrix} \begin{pmatrix} x \\ y \\ z \end{pmatrix}_{\text{DET}} . \tag{3.1}$$

Stations

Each station is simulated as a box of air with a central hole to accommodate the beampipe volume. A station represents the four C-frames of a physical station in their "closed" position. The centre of the station is chosen to lie in the horizontal plane along the z-axis of the detector frame, *i.e.* the centre of the station is $(0, 0, z_T)$. The z coordinate of the centre of a station is given by the average of the z coordinates of the centres of the C-frames in the station. The z-coordinates of the three OT stations are listed in Tab. 3.3.

Station	$z\,[\text{mm}]$
T1	7948
T2	8630
T3	9315

Tab. 3.3: *The z coordinates of the centres of the OT stations in the detector frame. Note that the centres are chosen to lie in the horizontal plane along the z-axis of the detector frame.*

Layers

When the C-frames are in their closed position, an A-side $(+x)$ and C-side $(-x)$ C-frame pair forms two layers of modules, an x and stereo layer, that covers the whole acceptance of the LHCb detector. Each station volume contains four layers of modules in the following stereo angle configuration $x(0°)$, $u(-5°)$, $v(5°)$ and $x(0°)$, respectively. The stereo angle is the angle with respect to the vertical (y) axis in the xy-plane, *i.e.* it corresponds to a rotation about the z-axis.

A layer volume, similar to a station volume, is a box of air with a central hole to accommodate the beampipe volume. The coordinates of the centres of the 12 OT layers are listed in Tab. 3.4. The x coordinate of the centre of a layer is zero. Note that the y coordinate of an x and stereo layer pair corresponds to that of their C-frame and is determined by the inclination of the beampipe in the detector frame. Consequently, since the C-frames are "hanging" vertically in the detector

frame, an x and stereo layer pair will appear right slanted in the LHCb frame, *i.e.* the C-frames are rotated by χ_{beam} about their x-axis.

	T1		T2		T3	
	y [mm]	z [mm]	y [mm]	z [mm]	y [mm]	z [mm]
X1	28.4	7860.75	30.9	8542.75	33.3	9227.75
U	28.4	7915.25	30.9	8597.25	33.3	9282.25
V	28.8	7980.75	31.3	8662.75	33.8	9347.75
X2	28.8	8035.25	31.3	8717.25	33.8	9402.25

Tab. 3.4: *The coordinates of the centres of the* 12 *OT layers in the detector frame. The layer and C-frame pitch in* z *is* $54.5\,\text{mm}$ *and* $120\,\text{mm}$*, respectively.*

Quarters

Quarter volumes are used to determine which quadrant of a layer a Monte Carlo particle traversed. However, unlike the station and layer volumes, a quarter volume has no shape. It is an abstract volume with a frame that represents an ensemble of nine modules: seven half F-modules, so-called L-modules, and two S-modules. The two S-modules are either of the type S1 and S2 or S1 and S3 for A-side and C-side quarters, respectively. Note that due to the smaller width of the S3 module the total width of the C-side quarter differs by half a module width with respect to the A-side quarter. Since a station and consequently a layer is centred around the beampipe at $x = 0$, this implies that the A-side $(1, 3)$ quarters and C-side $(0, 2)$ quarters are shifted by $-83.375\,\text{mm}$ and $-84.625\,\text{mm}$, respectively, within their layer mother volume.

The modules are positioned in x and y with respect to their quarter mother volume coordinate system. The x-coordinate of a module is given by the following general formula:

$$x_{\text{m}} = x_{\text{offset}} - (-1)^q \times \frac{0.5a + (n - m) \times \text{pitch}_x}{\cos\phi_s}, \tag{3.2}$$

where $q = \{0, 1, 2, 3\}$ is the quarter ID, m the module ID, and pitch_x is the module pitch in x. The angle ϕ_s is the stereo angle and is $0°$, $-5°$ or $5°$ for x, u and v-layers, respectively. The offsets in x, x_{offset} and a, and the factor n are given in Tab. 3.5 and depend on whether the module is an A-side or C-side module and its ID.

The y-coordinates of top and bottom L-modules are opposite and chosen such that they "connect" to make full F-modules. The y-coordinates of the S-modules are determined by the diameter of the conical beampipe and lead to a relative offset with respect to the T2 S-modules of $\Delta y = -7\,\text{mm}$ and $\Delta y = +7\,\text{mm}$ for T1 and T3, respectively. To form a stereo layer, a module in a quarter is first translated in y, then rotated by the stereo angle about the z-axis of its quarter and subsequently translated in x.

3.2 Digitisation

The detector description, discussed in Sec. 3.1, is used in GEANT4 to simulate particle interactions with the detector. The particle interactions with the detector are recorded as hits which are subsequently digitised. Digitisation is the procedure in which the detector's response to these hits is simulated. This is done within the LHCb digitisation application BOOLE in which each sub-detector has its own digitisation procedure as the detector technology employed is different.

m	n	x_{offset}	$a[\text{mm}]$	$\text{pitch}_x[\text{mm}]$
A-side ($Q = \{1, 3\}$)				
$\{9, \ldots, 1\}$	9	0	340	341.25
C-side ($Q = \{0, 2\}$)				
9	9	0	172	0
8	9	x_9	0	257.25
$\{7, \ldots, 1\}$	8	x_8	0	341.25

Tab. 3.5: *The parameters to determine the x coordinate of the centre of A-side and C-side modules. Note that x_9 and x_8 denotes the x coordinate of the centre of C-side modules 9 and 8, respectively. The module pitch in x is, in general, $\text{pitch}_x = 340\,\text{mm} + 1.25\,\text{mm}$, where $1.25\,\text{mm}$ is the space between modules. This also means that there is a gap of $1.25\,\text{mm}$ between A-side and C-side C-frames. The global x-coordinates of the modules are given by $x_m^{global} = x_q + x_m$, where $x_q = -83.375\,\text{mm}$ and $x_q = -84.625\,\text{mm}$ for A-side and C-side quarters, respectively.*

In this section the digitisation procedure for the OT, according to the physical processes described in [37, 39, 40], is discussed. This involves determining the drift distance and corresponding drift time for a given hit, and ultimately the time at which the signal was detected. In addition, detector traits such as dead-time, noise and cross-talk, discussed in Sec. 3.2.6, are also simulated. Lastly, the hit channels are encoded. The encoded channels are then stored in the OT data acquisition (DAQ) buffer according to the format described in [52]. The data in the DAQ buffer resembles real data, and is the format expected by the reconstruction application BRUNEL.

The parameters used in the digitisation process were determined from 2005 test beam data [54]. Similarly, the effects described in the digitisation were either measured during the 2005 test beam or during testing of the modules. Note that the parameters used in the digitisation depend on the detector conditions, *e.g.* the high voltage applied to the anode wires, the gas mixture, and the threshold used in the readout electronics. Therefore, in some cases, it was opted to use more conservative, but acceptable, settings. Currently, the values of these parameters are being determined using LHC collision data, such that they match current detector performance.

3.2.1 Radius-to-Time (RT)-relation

The readout electronics of the OT measures the drift times of the ionisation clusters produced by particles traversing the straws with respect to the beam crossing time. The time, relative to the time of the collision, at which a hit is detected in a straw tube, t_{det}, is composed of

$$t_{\text{det}} = t_{\text{tof}} + t_{\text{drift}} + t_{\text{prop}}, \tag{3.3}$$

where t_{tof} is the time-of-flight of a particle that produced the hit, t_{drift} is the drift time, and t_{prop} is the propagation time of the hit signal along the wire. The time-of-flight of a particle t_{tof} is measured with respect to the beam crossing time, and is the time needed for the particle to reach the straw tube. It is obtained from GEANT4. The propagation time t_{prop} is determined from the distance of the hit to the readout electronics, assuming a propagation speed of $0.25\,\text{m/ns}$ [55]. t_{det} is digitised by a time-to-digit converter (TDC), which uses the rising edge of the charge pulse, into a $6\,\text{bit}$ TDC time.

The rising edge of the charge pulse corresponds to the time, t_{drift}, needed for first ionisation clusters to reach the wire, and depends on the drift distance. In the digitisation the drift distance is defined as the distance of closest approach (doca) between a particle and a wire. Apart from tracks passing very close to or through the wire, it is a good approximation of the drift distance of the first ionisation clusters to reach the wire.

The drift distance as function of the drift time is given by a time-to-distance (*rt*-) relation. In the digitisation the inverse of the *rt*-relation is used to determine t_{drift}. For simplicity, a linear *rt*-relation is assumed in the Monte Carlo:

$$d(t) = v_{\text{drift}} t = r \frac{t}{t_{\text{max}}}, \tag{3.4}$$

where $r = 4.90\,\text{mm}$ is the inner straw tube radius and t_{max} the maximum drift time. In the simulation t_{max} is $42\,\text{ns}$, assuming a gas mixture of $70\%\,\text{Ar}$ and $30\%\,\text{CO}_2$. Although the 2005 test beam data show some indications of a higher order *rt*-relation, the linear relation describes the data with a reasonable accuracy. Nonetheless, the actual *rt*-relation has to be determined from real data.

In addition, the hit resolution of the detector, $200\,\mu\text{m}$, is taken into account by smearing t_{det} with a Gaussian with a width of, using Eq. 3.4, $\sigma_t = 3.4\,\text{ns}$.

Drift distance calculation

In GEANT4 only particle interactions with a sensitive volume are recorded. Among the information that is recorded are the entry and exit points of the particles that traverse this volume. As discussed in Sec. 3.1.1 the straws in a module are represented by a single sensitive volume. Consequently, the only way to determine which straws have been hit is to determine the doca d between a particle and a given wire and compare it to the inner radius r of a straw, see Fig. 3.5.

Unfortunately, the procedure described below only works well for particles that go relatively straight through the sensitive volume and not for low momentum particles that curl under influence of the magnetic field, *e.g.* $z_{\text{entry}} \approx z_{\text{exit}}$ (see Fig. 3.5). These are typically low energy particles from secondary interaction processes and are less interesting from a physics point of view. The particles originating from a proton-proton interaction have momenta above $2\,\text{GeV}$. Yet, particles from secondary interactions do contribute to the occupancy in the detector and are therefore digitised.

Consider the following two vectors $\boldsymbol{p}$ and $\boldsymbol{w}$ that represent a particle traversing the sensitive volume and a wire, respectively:

$$\boldsymbol{p} \equiv \boldsymbol{p}^{\text{local}}_{\text{entry}} + \lambda \hat{\boldsymbol{p}} \tag{3.5a}$$

$$\boldsymbol{w} \equiv \boldsymbol{w}^{\text{local}}_{\text{bottom}} + \mu \hat{\boldsymbol{w}} \tag{3.5b}$$

where $\boldsymbol{p}^{\text{local}}_{\text{entry}}$ is the entry point of the particle in the volume and $\boldsymbol{w}^{\text{local}}_{\text{bottom}}$ the bottom point of a wire in a module. The parameters λ and μ are the arc lengths along the particle trajectory and wire trajectory, respectively. Furthermore, $1 - \mu$ and μ give the distance of the hit to the readout electronics for the top and bottom modules, respectively, and are used to determine t_{prop}. The doca between $\boldsymbol{p}$ and $\boldsymbol{w}$ is given by:

$$\boldsymbol{d}(\lambda, \mu) \equiv \boldsymbol{p} - \boldsymbol{w} \tag{3.6}$$

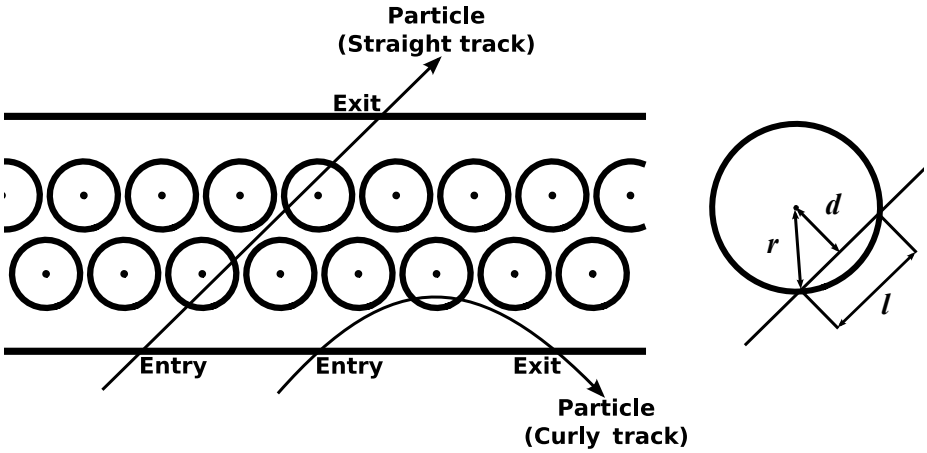

Fig. 3.5: *Particles traversing the sensitive straw volume of a module. The entry and exit points are obtained from GEANT4. The figure on the right shows a particle traversing a straw. The path length of the particle trajectory is given by* $l = 2\sqrt{r^2 - d^2}$*, where* $r = 4.90\,\mathrm{mm}$ *is the inner straw radius and* d *is the distance of closest approach (doca). Note that* d *is perpendicular to* l*.*

where λ and μ are such that the following requirements are satisfied:

$$\boldsymbol{d} \cdot \boldsymbol{p} = 0 \qquad \wedge \qquad \boldsymbol{d} \cdot \boldsymbol{w} = 0, \tag{3.7}$$

which is equivalent to:

$$\frac{\partial d}{\partial \lambda} = 0 \qquad \wedge \qquad \frac{\partial d}{\partial \mu} = 0. \tag{3.8}$$

If $d < r$ for a given straw then that straw can be considered hit. In addition, when a particle traverses an F-module, the inefficient region at $y = 0$ (see Fig. 3.3b) is taken into account.

3.2.2 Cell efficiency

The production of primary ionisation clusters along the path of a particle traversing the straw follows a Poison distribution, since a small number of them are produced independently of each other. Therefore, the probability to observe k primary ionisation clusters is given by

$$p\,(k) = \frac{n_p^k}{k!} e^{-n_p}, \tag{3.9}$$

where $n_p = \rho l$ is the average number of primary ionisation clusters. The latter depends on the path length l and the average number of primary ionisation clusters per unit length ρ. In the case of the OT, the path length l is defined as

$$l = 2\sqrt{r^2 - d^2}, \tag{3.10}$$

where r is the inner radius of the straw tube and d is the drift distance, see Fig. 3.5. The expected average number of primary ionisation clusters per unit length for the OT using a gas mixture of $70\%\,\mathrm{Ar}$ and $30\%\,\mathrm{CO_2}$ is $\rho = 3.05\,\mathrm{mm}^{-1}$. This corresponds to an average ionisation length of $\lambda = \frac{1}{\rho} = 328\,\mu\mathrm{m}$ [38]. Therefore, for a particle that passes close to the anode wire the expected

average number of primary ionisation clusters is approximately 15.

The efficiency to detect a particle that traverses an ideal detection cell is given by

$$\epsilon_{\text{cell}}(l) = 1 - p\,(0) = 1 - e^{-\rho l}. \tag{3.11}$$

Note that $(1 - e^{-\rho l})$ gives the probability for having at least one (efficient) ionisation. Consequently, the probability of primary ionisations being produced when a particle passes close to the straw wall is smaller compared to when it passes close to the wire.

For a real detector there are various effects that can affect the single cell efficiency, such as electron attachment. In the case of electron attachment an electron attaches itself to a CO_2 molecule before reaching the anode wire and is therefore not observed. In addition, the charge collected at the anode wire might be below the threshold of the avalanche gain setting of the amplifier in the readout electronics. These inefficiencies can be accounted for by introducing an additional parameter in Eq. 3.11. A possible parametrisation for the single cell efficiency of a real detector is:

$$\epsilon_{\text{cell}}(l) = \epsilon_{\text{plateau}}(1 - e^{-\rho_{\text{eff}} l}), \tag{3.12}$$

where $\epsilon_{\text{plateau}}$ is the plateau efficiency and $\rho_{\text{eff}} = \alpha\rho$ is the effective number of ionisations per unit length. The plateau efficiency corresponds to an overall detection efficiency and α is the efficiency to detect a given cluster.

The 2005 test beam efficiency profile for the OT fitted for $\epsilon_{\text{plateau}}$ and ρ_{eff} is shown in Fig. 3.6. In the top figure, $\rho_{\text{eff}} = \rho = 3.05\,\text{mm}^{-1}$ is set to the literature value for ρ in the fit which yields $\epsilon_{\text{plateau}} = 0.995$. In the bottom figure, $\epsilon_{\text{plateau}}$ is set to unity in the fit which yields $\rho = 1.18\,\text{mm}^{-1}$.

Though both cases describe the plateau efficiency well for $|d| < 1.6\,\text{mm}$, the latter case does a better job of describing the single cell efficiency for a particle that traverses a straw close to the straw wall. We therefore advise to use the latter case with $\epsilon_{\text{plateau}} = 1$ and $\rho = 1.18\,\text{mm}^{-1}$ in the simulation. Nonetheless, in the current simulation the former case with $\epsilon_{\text{plateau}} = 0.995$ and $\rho = 3.05\,\text{mm}^{-1}$ is used to simulate the single cell efficiency of the OT. The corresponding average single cell efficiency integrated over the straw tube $(d < r)$, is 99.0%. For the case with $\epsilon_{\text{plateau}} = 1.0$ and $\rho = 1.18\,\text{mm}^{-1}$, the corresponding average single cell efficiency is 96.7%.

3.2.3 Dead-time

The readout electronics [40] consists of an amplifier (ASDBLR — Amplifier-Shaper-Discriminator with BaseLine Restoration) and a time-to-digital converter (OTIS — Outer Tracker Time Information System). The former amplifies the (small) signal from the anode wire and discriminates it against a threshold, and the latter measures the arrival time of the hit with respect to the LHC bunch crossing clock. The time it takes the process the signal is called the dead-time of the readout electronics, because during the processing of the signal any subsequent signal is ignored.

First the signal is amplified by the ASDBLR, with an analogue dead-time of 17 ns, depending on the actual pulse height. The digital output of the ASDBLR is then passed on to the OTIS. The OTIS then takes the signal from the ASDBLR and provides a 6 bit TDC time plus 2 bits to identify the spill from which the hit originates within a three bunch crossing readout window. The total dead-time for the TDC conversion of the signal is 25 ns.

The maximal possible drift time is $t_{\text{drift}} = 42\,\text{ns}$. This combined with a maximal signal propagation time of $2.405\,\text{m} \times 4\,\text{ns/m} \approx 10\,\text{ns}$ yields, ignoring the time-of-flight of particle, a maximal detection time of $t_{\text{det}} = 52\,\text{ns}$. This barely falls within a readout window of two bunch crossings. Consequently, to collect as many particles as possible originating from a given bunch

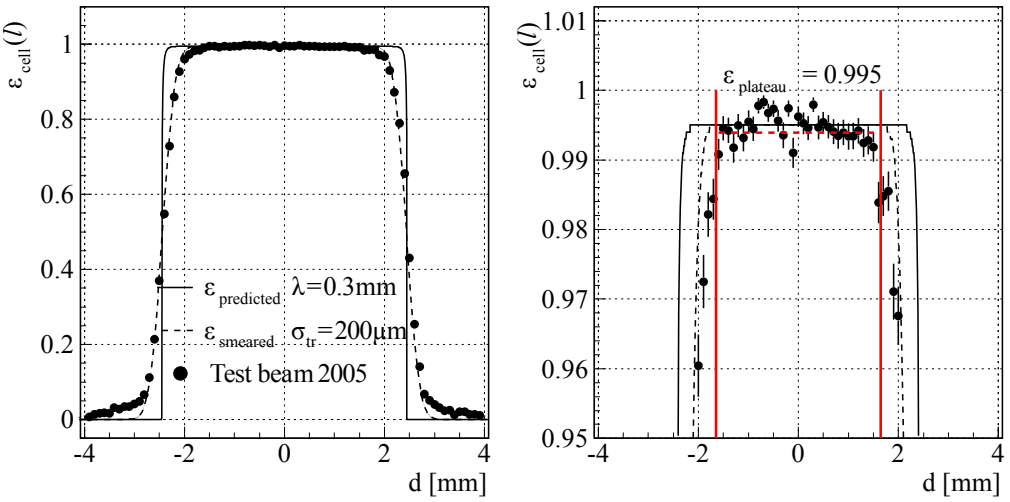

Fig. 3.6: *The 2005 test beam efficiency profile fitted for (a) $\epsilon_{plateau}$ with $\rho_{eff} = \rho = 3.05\,\mathrm{mm}^{-1}$ and (b) ρ_{eff} with $\epsilon_{plateau} = 1$. The solid line is Eq. 3.12 for corresponding values of $\epsilon_{plateau}$ and ρ_{eff}. The dashed line is Eq. 3.12 smeared with the track resolution $\sigma_{tr} = 200\,\mu\mathrm{m}$. The figures on the right show the efficiency profile zoomed in around the plateau. Note that Eq. 3.12 with $\epsilon_{plateau} = 1$ and $\rho_{eff} = \frac{1}{\lambda_{eff}} = 1.18\,\mathrm{mm}^{-1}$ describes the efficiency profile accurately.*

crossing, the maximum width of the readout window of the OTIS is three bunch crossings, *i.e.* it corresponds to $75\,\mathrm{ns}$.

The OTIS can be read out in single-hit mode or multiple-hit mode. In single-hit mode only the first hit in the three bunch crossing readout window is read out. This gives an effective detection "dead-time" of up to $75\,\mathrm{ns}$. In multiple-hit mode a possible hit in each bunch crossing is digitised. The default readout mode of the OTIS, which is also assumed in the simulation, is single-hit mode. Therefore the total effective dead-time of the readout electronics assumed in the simulation is up to $75\,\mathrm{ns}$.

3.2.4 Spill-over

At the LHC bunch crossings will occur every $25\,\mathrm{ns}$. Consequently, for reasons explained in Sec. 3.2.3, a fraction of the particles produced in neighbouring bunch crossings with respect to a given bunch crossing are also digitised in the event. In particular particles with a long drift time from previous bunch crossings and particles with a short drift time from subsequent bunch crossings appear in the TDC spectrum. These particles are called spill-over particles and are considered as background. Taking these spill-over particles into account, Eq. 3.3 becomes

$$t_{\text{det}} = t_{\text{spill}} + t_{\text{tof}} + t_{\text{drift}} + t_{\text{prop}} \tag{3.13}$$

where $t_{\text{spill}} = \{-50\,\mathrm{ns}, -25\,\mathrm{ns}, 0\,\mathrm{ns}, 25\,\mathrm{ns}, 50\,\mathrm{ns}\}$ is the relative time at which the bunch crossing occurred.

3.2.5 Start of the readout window

The start of the readout window, t_0, is defined as the time at which the readout electronics start to collect the signals with respect to the bunch crossing clock. It corresponds to the start of the rising edge of the TDC spectrum. Taking this into account yields a corrected detection time

$$t_{\text{det}}^{\text{cor}} = t_{\text{spill}} + t_{\text{tof}} + t_{\text{drift}} + t_{\text{prop}} - t_0. \tag{3.14}$$

In the digitisation procedure the t_0 time is set to the time-of-flight of a high momentum particle originating from the nominal interaction point and travelling in a straight line to the straw at a position closest to the readout electronics:

$$t_0 \equiv \frac{\sqrt{z_T^2 + (\frac{1}{2} l_m)^2}}{c}, \tag{3.15}$$

where z_T is z coordinate of the centre of a station, l_m is the length of an F-module, and c is the speed of light. This yields a $t_0 = \{28\,\mathrm{ns}, 30\,\mathrm{ns}, 32\,\mathrm{ns}\}$ for T1, T3 and T3, respectively. This corresponds to a shift of the TDC spectrum to the left such that the rising edge of the spectrum starts at $t_{\text{det}}^{\text{corr}} = 0\,\mathrm{ns}$. The actual values for the start of the readout gate will be determined per readout board with real data.

3.2.6 Noise, cross-talk and double pulse

Random (electrical) noise signals are caused by instabilities in a straw tube and by noise in the readout electronics. The noise rate was measured in the 2005 test beam and determined to be less than $10\,\mathrm{kHz}$ per straw. In the digitisation a conservative, but acceptable, noise rate of $10\,\mathrm{kHz}$ is assumed. This yields on average 50 noise hits per event and translates to a noise occupancy of approximately 0.1%.

Cross-talk is the electrical pick-up of signals in neighbouring straws or channels on the ASD-BLR chip. The former is known as analogue cross-talk and the latter as digital cross-talk. While analogue cross-talk can be reduced or eliminated by adjusting the detection threshold of the signal or by increasing the electrical separation of the straws [55], digital cross-talk is always present. In the 2005 test beam the combined analogue and digital cross-talk was determined to be less than 4% per straw tube for straws in the same mono-layer, while cross-talk between the mono-layers was determined to be negligible ($< 1\%$). In the digitisation the fraction of cross-talk hits per straw tube is set to 5% for straws in the same mono-layer.

It is possible to record more than one TDC time for a given particle. This can in principle be due to either reflections of the signal on the wire or a delay in the arrival time between separate ionisation clusters. In both cases a second pulse can be observed if the delay between the first and second signal is greater than the analogue dead-time of $25\,\mathrm{ns}$ [56, 57]. This is called the double pulse effect. Note that from the electronics point of view, the presence of a double pulse effect is the same as the presence of a double hit, *i.e.* two particles traversing a straw tube, since there is no way of distinguishing between them.

It was determined that the majority of double hits is due to the delay in the arrival of ionisation clusters occurring with a probability of 30% and an average delay of $30\,\mathrm{ns}$. These same values are used in the digitisation. Note that this effect is not visible in single-hit mode, since only the first signal with a corresponding dead-time of up to $75\,\mathrm{ns}$ is read out.

3.3 Estimated Detector Response

This section presents an overview of the estimated response of the OT, *i.e.* its occupancy, efficiency, and resolution, based on the input to the simulation and digitisation applications GAUSS and BOOLE, respectively. To do this approximately $1\,\mathrm{k}$ $B_d^0 \to J/\psi K_s$ signal events are used. These events were generated at the nominal LHCb luminosity of $\mathcal{L} = 2 \times 10^{32}\,\mathrm{cm^{-2}s^{-1}}$. The total cross section for proton-proton collisions is assumed to be $\sigma_{pp}^{\text{total}} = 100\,\mathrm{mb}$, which includes elastic and inelastic collisions ($\sigma_{pp}^{\text{inelastic}} = 80\,\mathrm{mb}$). The average number of collisions per beam is therefore, using Eq. 2.2, $\langle n_{pp} \rangle \approx 0.67$. The average number of proton-proton collisions in a bunch crossing that contains a $b\bar{b}$ event is therefore $\left\langle n_{pp}^{b\bar{b}} \right\rangle \approx 1.67$. Here it is assumed that the occurrence of a rare process, such as a B decay, to occur does not alter the much more frequent minimum bias cross section.

3.3.1 OT deposits

The first step in the digitisation procedure is to create the corresponding deposits, *i.e.* an object that contains t_{det} and the corresponding drift distance, for a Monte Carlo particle that traverses the OT. Subsequently, once the deposits have been created, the corresponding TDC times are determined. The deposit spectrum for the OT station T3 corresponding to $1\,\mathrm{k}$ $B_d^0 \to J/\psi K_s$ is shown in Fig. 3.7a, with the contributions from the various spill-over bunch crossings highlighted. The current bunch crossing ($t_{\text{spill}} = 0\,\mathrm{ns}$) contains signal events in addition to pile-up events. The neighbouring bunch crossings ($t_{\text{spill}} = -50\,\mathrm{ns}, -25\,\mathrm{ns}, 25\,\mathrm{ns}, 50\,\mathrm{ns}$) contain particles from minimum bias events. The higher hit multiplicity in the current spill is due to two reasons: firstly, this spill always contains at least one proton-proton collision. Secondly, $b\bar{b}$ events contain on average twice as many final state particles as minimum bias events. Note that most of the current spill is covered by the readout window, indicated in Fig. 3.7a. In addition, substantial fractions of the previous and next spills fall inside the readout window. In the end, only the sum of the TDC spectra of the spills within in the readout window is observed, see Fig. 3.7b. Here the TDC

spectrum is corrected for the start of the readout gate of T3, $t_0 = 32\,\mathrm{ns}$, such that it starts at zero.

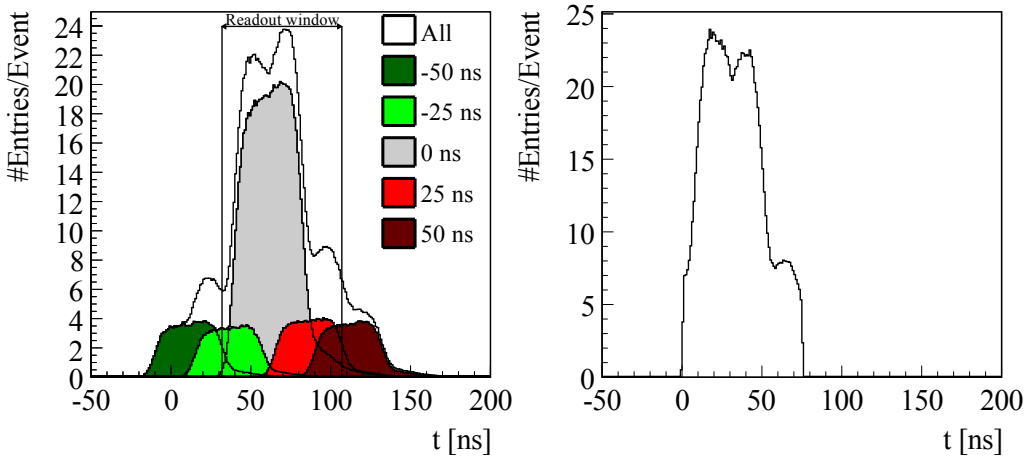

Fig. 3.7: *Spectra for station T3: (a) shows t_{det} for the current and neighbouring spills. The readout window is 75 ns. Note the tails of the neighbouring spill in the readout window. (b) shows the $t_0 = 32\,\mathrm{ns}$ corrected TDC spectrum (see Eq. 3.14). Note that the spectra also contain "noise" deposits.*

Background

In addition to creating deposits that correspond to a Monte Carlo particle, also noise, cross-talk and double pulse background deposits are created in the digitisation procedure. In addition to these detector effects, also deposits corresponding to particles from spill-over collisions are considered as background, since they do not originate from the signal event. The fractions, f^i_{bg}, of the various background contributions to the signal is defined as

$$f^i_{\mathrm{bg}} = \frac{N^i_{\mathrm{bg}}}{N_{\mathrm{sig}} + \sum_i^n N^i_{\mathrm{bg}}}, \tag{3.16}$$

where N_{bg} and N_{sig} are the number of background and signal deposits, respectively.

The various contributions of noise, cross talk and double pulse deposits to the signal deposits are shown in Fig. 3.8a. As can be seen in Fig. 3.8a the greatest source of background is double pulse hits, 23% compared to 1% and 5% for noise and cross talk, respectively. The total background fraction, including spill over deposits, is shown in Fig. 3.8b. The peak at 23% is caused by the double pulse background and the long tail is caused by spill-over particles. Note that in single hit readout mode the double pulse deposits are not observed, since they fall inside the effective detection dead time of up to 75 ns.

3.3.2 Occupancy

The detector occupancy affects the reconstruction. The higher the occupancy in a given event, the more difficult it is to reconstruct the event. A high occupancy leads to an increase in CPU time

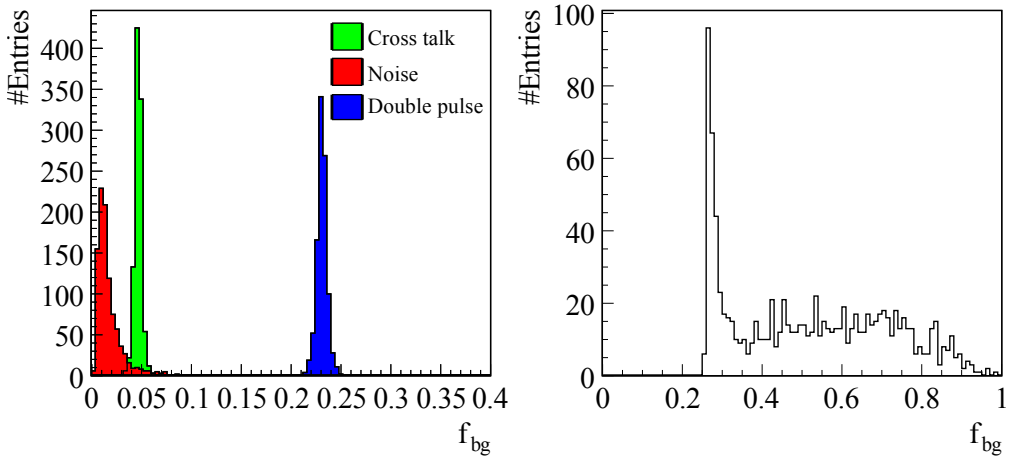

Fig. 3.8: *Noise fractions: (a) shows the background fractions f_{bg} for noise, cross talk, and double pulse. (b) shows the total background fraction including spill-over.*

required by the pattern recognition to reconstruct the event. The occupancy in the OT is defined as the number of hits recorded within the readout window of $75\,\mathrm{ns}$ divided by the number of channels present in a given region of the detector. The total average OT occupancy for $B_d^0 \to J/\psi K_s$ events generated at a luminosity of $\mathcal{L} = 2 \times 10^{32}\,\mathrm{cm}^{-2}\mathrm{s}^{-1}$ is 6%.

The distribution of the particle flux in the first layer in station T3 is shown in Fig. 3.9a. Note that the particle flux is higher around the beampipe region and in the horizontal $(y = 0)$ plane, putting high demands on the detection of particles in this region. Therefore, this region is covered by the silicon detectors of the IT which have a higher granularity than the OT modules. The overall dimensions of the IT in the region around the beampipe were optimised to minimise the occupancy in the OT versus cost of the silicon detector surface [58]. The corresponding occupancy versus x for one half of an OT layer in station T3 is shown in Fig. 3.9b. This reflects the average time integrated occupancy per straw tube. As can be seen in Fig. 3.9b the average occupancy close to the beampipe is approximately 12% and decreases with increasing distance to the beampipe. At the detector edge the average occupancy is approximately 4%.

The various deposit contributions to the TDC spectrum, corresponding to an average total detector occupancy of 6%, are listed in Tab. 3.6. The largest contribution, 68.7%, originates from particles generated in the current spill. Of these, 43.4% are primary interactions, *i.e.* originating directly from proton-proton collisions, and 25.1% are secondary, *i.e.* originating from particle interactions with the detector. The noise and cross-talk fractions, 1.4% and 5% respectively, correspond to the values used in the digitisation. Double pulses are absent, since these fall within the effective dead-time of up to $75\,\mathrm{ns}$ of the single-hit readout mode of the electronics.

3.3.3 Efficiency

Various sources of inefficiencies are introduced in the digitisation. There are geometrical inefficiencies due the layout of the straws and modules (Sec. 3.1), the single cell efficiency (Sec. 3.2.2), and the dead-time and finite width of the readout window of the electronics (Sec. 3.2.3).

The average efficiency, taking all of the above into account, is the probability that a particle

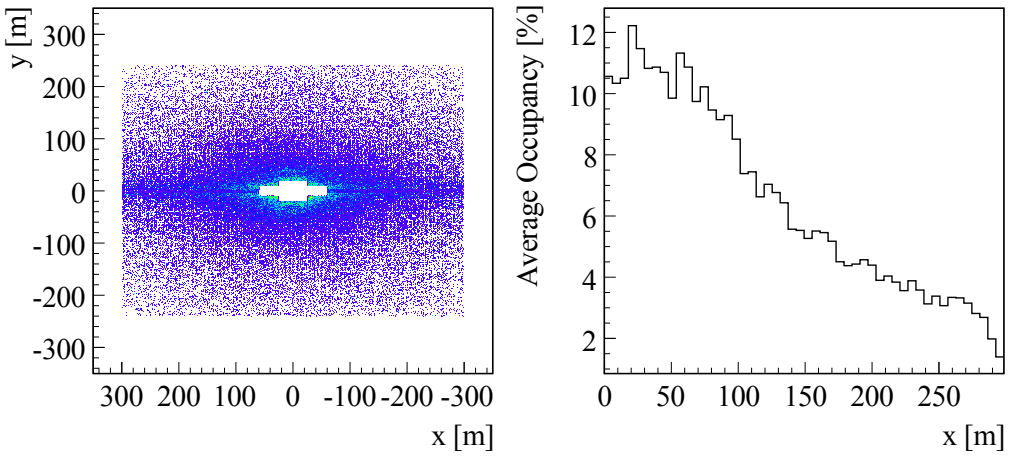

(a) **(b)**

Fig. 3.9: *Particle flux and occupancy in the first layer of station T3: (a) shows the particle flux distribution. Note that the flux is higher around the beam region, i.e. the cross region, and the bending plane. (b) shows the occupancy versus x.*

Deposit			
Origin	Type	Fraction (%)	Sub-total (%)
Current spill (0 ns)	Primary	43.4	
	Secondary	21.1	
	Unknown	0.2	68.7
Spill-over	−25 ns	10.4	
	+25 ns	8.7	
	−50 ns & +50 ns	5.8	24.9
Detector	Noise	1.4	
	Cross-talk	5.0	6.4

Tab. 3.6: *Various deposit contributions to the TDC spectrum.*

is detected by the OT, and is defined as

$$\epsilon_{\text{OT}} = \frac{N_{\text{det}}}{N_{\text{gen}}}, \tag{3.17}$$

where N_{gen} is the number of generated particles that traversed a sensitive volume and N_{det} the number of generated particles that were detected. Other sources, such as cross-talk hits, are not considered, even though they could in principle be associated to a particle. These are considered as background.

The average layer, *i.e.* two mono-layers, efficiency is 96.1% considering all particles. The

inefficiency is primarily due to low momentum particles falling outside the readout window. Requiring that particles have $\mathrm{p} > 2\,\mathrm{GeV}$ the average efficiency increases to 98.8%.

3.3.4 Drift distance resolution

The drift distance resolution σ_r is defined as the width of a Gaussian fit to the drift distance residual distribution δr. Ideally, it should correspond to the drift time resolution, $\sigma_t = 3.4\,\mathrm{ns}$, used as input in the simulation to smear t_{det}.

The drift distance residual is defined as

$$\delta r = s_{\mathrm{gen}} r_{\mathrm{gen}} - s_{\mathrm{obs}} r_{\mathrm{obs}}, \tag{3.18}$$

where r_{gen} is the distance of closest approach (doca) and r_{obs} is the observed drift distance. The latter is obtained from the *rt*-relation for a given calibrated time t_{cal}. The calibrated time t_{cal} is defined as

$$t_{\mathrm{cal}} = t_{\mathrm{det}} + t_0 - t_{\mathrm{tof}} - t_{\mathrm{prop}}, \tag{3.19}$$

where t_{det} is given by Eq. 3.14, t_0 is the start of the readout window of the readout electronics, t_{tof} is the estimated time-of-flight of the particle, and t_{prop} the estimated propagation time of the signal along the wire towards the readout electronics. The coefficients $s_{\mathrm{obs}} = \pm 1$ and $s_{\mathrm{gen}} = \pm 1$ are the corresponding ambiguities for r_{obs} and r_{gen}, respectively. The ambiguity is -1 for particles passing left of the wire and $+1$ for particles passing right of the wire. The parameters t_{tof}, t_{prop} and s_{obs} are determined when the trajectory of the particle or an estimate of the trajectory is known. This information is only available during track reconstruction.

The drift distance residual distribution for all particles is shown in Fig. 3.10a. To disentangle reconstruction effects the simulation values for t_{prop} and $s_{\mathrm{obs}} \equiv s_{\mathrm{gen}}$ are used. The time-of-flight t_{tof} is determined by approximating the flight path of the particle, assumed to originate from the origin, by a straight line. Although the observed distribution does not follow closely the shape of a Gaussian, the width of the best Gaussian fit is used to express the resolution. For all particles the observed resolution, σ_r, is $(291.5 \pm 0.1)\,\mu\mathrm{m}$. For particles with $p > 2\,\mathrm{GeV}$ the drift distance resolution, shown in Fig. 3.10b, is $(197.6 \pm 0.1)\,\mu\mathrm{m}$ which is in agreement with the Monte Carlo input.

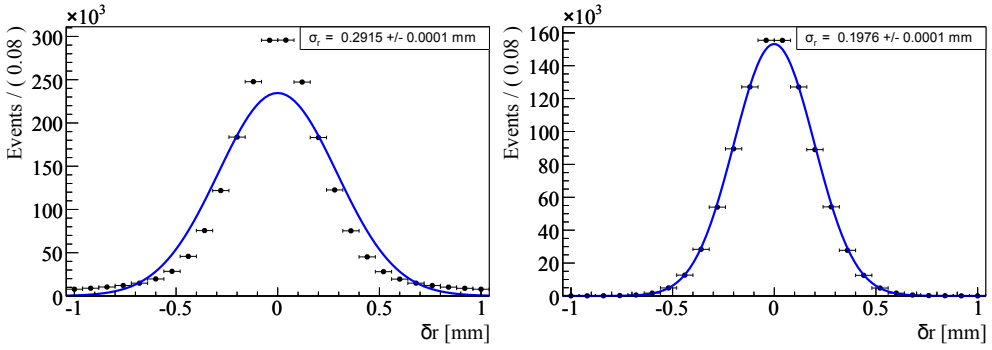

Fig. 3.10: *Drift distance resolutions: (a) shows the drift distance resolution for all Monte Carlo particles. (b) shows the drift distance resolution for Monte Carlo particles with a momentum greater than* $2\,\mathrm{GeV}$.

The non-Gaussian shape of the distribution in Fig. 3.10a is due to the fact that all particles are considered to originate from the nominal interaction point and that their flight paths are straight lines. This is not entirely the case for two reasons: firstly, the flight path of a low momentum particle is not a straight line but a curve through the magnetic field. Secondly, there are also particles from material interactions which, therefore, do not originate from the nominal interaction point. This means that t_{tof} is underestimated for low momentum particles.

3.4 Summary

This chapter described the OT simulation. It involves the simulation of the interactions of the particles with the detector and the digitisation of the detector responses to these particles. The description of the OT mirrors as closely as possible the actual design. This includes the geometry as well as the materials used in the construction of the modules. In order to fulfil the requirements for fast simulation and reconstruction, individual straws are not included in the description. Other detector traits such as the dead-time of the read out electronics and cross talk are also simulated. The values used to simulate these traits were obtained from 2005 test beam data.

Chapter 4

Alignment Of The LHC*b* Detector

Tracking performance studies on Monte Carlo data show that a momentum resolution of $(3 - 5)‰$ can be achieved for tracks that traverse the entire detector [59]. In order to achieve this momentum resolution, and consequently a good mass resolution, the positions of the detectors need to be determined with an accuracy well below the hit resolution for a given detector - 8μm, 60μm and 200μm for the VELO, IT and OT, respectively. To this end an algorithm for a track based alignment for the tracking stations has been developed within the LHC*b* software framework.

This chapter gives an overview of the LHC*b* alignment algorithm. It is based on the same working principles as the Millipede algorithm [60] where not only the hits themselves are considered in the alignment procedure, but also the correlations between the hits on a track are taken into account. This is the so-called *global method of alignment*. The main difference between the Millipede and LHC*b* alignment algorithm is that the former uses a *global least-squares* track model and fit, while the latter uses a Kalman track model and fit. However, in addition to the alignment algorithm discussed here, various stand-alone algorithms based on the actual Millipede formalism do exist in LHC*b* for the alignment of the VELO, TT, IT and OT, and are discussed in [61, 62, 63], respectively.

The Kalman track model and fit is in LHC*b* the standard track fit [27, 59] used in the reconstruction procedure for tracks that either traverse a certain region of the detector or the entire detector. In the LHC*b* Kalman track fit, all sub-detectors are treated in a consistent and generic way. Consequently, it is in principle possible to align the entire LHC*b* detector, *i.e.* all sub-detectors that have hits on a track, with the LHC*b* alignment framework. In addition, since the same track model and fit is used as in the reconstruction procedure and physics analyses, material effects, such as energy loss and multiple scattering, as well as the magnetic field values are consistently taken into account in the alignment procedure. The obtained alignment offsets are therefore expected to be consistent with the track model and fit used in the reconstruction procedure and physics analyses. Moreover, since it is implemented within the LHC*b* software framework, one has direct access to the detector elements and their conditions, tracks and vertices, and the reconstruction tools.

In Sec. 4.1 the master equations of the global alignment method are derived starting from the formalism of the *global least-squares method*. The aim is to extract the necessary ingredients to determine the alignment offsets. In addition, various tracking nomenclature and definitions are introduced in Sec. 4.1 that are used in the subsequent sections and in the given references. Subsequently, in Sec. 4.2 an overview of the Kalman filter track fit method and its use in the global alignment method is given. In Sec. 4.3 the required derivatives for the alignment procedure

are presented. This is followed by an overview of the LHC*b* alignment framework in Sec. 4.4. Finally, in Sec. 4.5, some validation results obtained with Monte Carlo data are presented.

4.1 The Global Or Closed Form Alignment Method

The purpose of any track fitting procedure is to obtain the set of track parameters $\vec{x}$ that optimally describes the trajectory of a charged particle that traverses the detector. In the global least squares method the track parameters that describe the trajectory of a charged particle, given a set of measurements $\vec{m}$ and their covariance matrix V, are determined by minimising the following track χ^2:

$$\chi^2 = \vec{r}^T V^{-1} \vec{r}, \tag{4.1}$$

where $\vec{r}$ is a vector of residuals

$$r_i = m_i - h_i\left(\vec{x}\right). \tag{4.2}$$

The function $h(\vec{x})$ is referred to as the measurement model and expresses the (estimated) measurements in terms of the track parameters $\vec{x}$. The definitions of these depend on the geometry and the magnetic field of the detector, but generally 5 parameters are used to describe the trajectory of a charged particle [64].

In what follows it is assumed that the measurement model $h(\vec{x})$ is linear in terms of the track parameters $\vec{x}$. Note, however, that any measurement model can be linearised using first order Taylor expansion around some initial estimate $\vec{x}_0$ of the track parameters. These estimates are usually obtained from the pattern recognition. In the case that the measurement model is non-linear in $\vec{x}$, iterations are necessary to determine the optimal set of track parameters $\vec{x}$ in the track fitting procedure [59].

The (optimal) set of track parameters that minimises Eq. 4.1 is the set that satisfies the following condition

$$0 \equiv \frac{d\chi^2}{d\vec{x}}, \tag{4.3}$$

and can be obtained from the application of the *Newton-Raphson method** [65] at some initial estimate $\vec{x}_0$ of the track parameters. This yields, using Eq. 4.1 and Eq. 4.2 and considering only terms up to first-order, the following solution for the track parameters $\vec{x}$:

$$\begin{aligned} \vec{x} &= \vec{x}_0 - \left[\frac{d}{d\vec{x}}\left(\frac{d\chi^2}{d\vec{x}}\right)\bigg|_{\vec{x}_0}\right]^{-1} \frac{d\chi^2}{d\vec{x}}\bigg|_{\vec{x}_0}. \\ &= \vec{x}_0 - (H^T V^{-1} H)^{-1} H^T V^{-1} \vec{r} \end{aligned} \tag{4.4}$$

Here, the matrix H is defined as $H \equiv \partial h\left(\vec{x}\right)/\partial\vec{x}$ and is referred to as the projection matrix. The corresponding covariance matrix $C_{\vec{x}}$ for the track parameters $\vec{x}$, which is a 5×5 matrix if there are 5 track parameters, is given by [66]:

$$C_{\vec{x}} = (H^T V^{-1} H)^{-1} = 2\left(\frac{d^2\chi^2}{d\vec{x}^2}\bigg|_{\vec{x}_0}\right)^{-1}, \tag{4.5}$$

*Simply put, this method iteratively determines the root x_i of a function f such that $f(x) = 0$ for x_i, *i.e.* for some value of x, x_i, an improved estimate of the root, x_{i+1}, is given by $x_{i+1} = x_i - f(x_i)/f'(x_i)$.

and Eq. 4.4 can be written in the more compact form:

$$\vec{x} = \vec{x}_0 - C_{\vec{x}} H^T V^{-1} \vec{r}.$$

The residual can be extended to include also the alignment parameters, $\vec{\alpha}$, of the detector via the measurement model*

$$r\left(\vec{x}\right) \rightarrow r\left(\vec{x}, \vec{\alpha}\right) = m - h\left(\vec{\alpha}, \vec{x}\right), \tag{4.6}$$

where the alignment parameters $\vec{\alpha}$ are considered common to all tracks for a given calibration sample. They are referred to as *global* parameters, since they are valid for all tracks in the sample. On the other hand, the track parameters $\vec{x}$ are referred to as *local* parameters, since these are unique per track.

For a given calibration sample containing n tracks, the optimal set of alignment parameters and track parameters can be obtained by minimising the following ensemble χ^2:

$$\chi^2 = \sum_n \chi^2_n, \tag{4.7}$$

where n is the number of tracks and χ^2_n the χ^2 contribution (Eq. 4.1) of track n, simultaneously with respect to the alignment parameters $\vec{\alpha}$ and the n track parameters $\vec{x}$. However, since the alignment parameters are considered common to all tracks in the calibration sample and the track parameters are considered unique per track, the ensemble χ^2 can be effectively minimised in two steps. First, the track parameters $\vec{x}^n$ for each track n are determined by minimising the ensemble χ^2 with respect to these track parameters for an initial estimate of alignment parameters $\vec{\alpha}_0$, *i.e.* the charged particle trajectories are fitted for an initial estimate of alignment parameters $\vec{\alpha}_0$. This yields a set of track parameters $\vec{x}^n_0$ for each track n that satisfies Eq. 4.3 for an initial estimate of alignment parameters $\vec{\alpha}_0$. Subsequently, once the ensemble χ^2 has been minimised with respect to all n track parameters, the corrections to the alignment parameters $\vec{\alpha}_0$ are determined for this set of n track parameters, following the same procedure as described above for the global least squares method, yielding a new set of alignment parameters $\vec{\alpha}_1$. These steps are then iterated until the procedure has converged, *i.e.*

$$\vec{x}^n_0 \text{ for } \vec{\alpha}_0 \rightarrow \vec{\alpha}_1 \text{ for } \vec{x}^n_0 \rightarrow \vec{x}^n_1 \text{ for } \vec{\alpha_1} \rightarrow \vec{\alpha}_2 \text{ for } \vec{x}^n_1 \textit{ etc.}$$

The alignment corrections that minimise the ensemble χ^2 (Eq. 4.7) satisfy the condition

$$0 \equiv \frac{d\chi^2}{d\vec{\alpha}}, \tag{4.8}$$

which, for M alignment parameters, represents a system of M non-linear coupled equations. Here the full derivative with respect to the alignment parameters $\vec{\alpha}$ is given by:

$$\frac{d}{d\vec{\alpha}} = \frac{\partial}{\partial\vec{\alpha}} + \frac{d\vec{x}}{d\vec{\alpha}}\frac{\partial}{\partial\vec{x}}, \tag{4.9}$$

where the second term takes into account the correlations between the track parameters and the alignment parameters.

*Or, alternatively, by extending the measurement, m, to include the alignment parameters $\vec{\alpha}$. Nonetheless, the master alignment equations as derived here remain valid.

The full derivative (Eq. 4.9) can be expressed in terms of the partial derivatives of the residuals with respect to the alignment and track parameters, respectively, the covariance for the measurements V and the covariance for the track parameters as follows: assume that the ensemble χ^2 remains minimal with respect to the n track parameters for a given change in alignment parameters such that

$$\frac{d}{d\vec{\alpha}}\left(\frac{\partial\chi^2}{\partial\vec{x}}\right) = 0. \tag{4.10}$$

Inserting Eq. 4.9 in Eq. 4.10 and using the definition of the track χ^2 (Eq. 4.1), the residual r (Eq. 4.6) and Eq. 4.5 it follows, after ignoring terms of $\mathcal{O}(2)$, that Eq. 4.9 can be expressed as:

$$\frac{d}{d\vec{\alpha}} = \frac{\partial}{\partial\vec{\alpha}} + A^T V^{-1} H C \frac{\partial}{\partial\vec{x}}. \tag{4.11}$$

Here the matrix $A \equiv \partial\vec{r}/\partial\vec{\alpha}$ is defined as the derivative of the set of residuals $\vec{r}$ with respect to the set of alignment parameters $\vec{\alpha}$.

Consequently, given the full derivative with respect to the alignment parameters $\vec{\alpha}$ (Eq. 4.11), the alignment corrections $\Delta\vec{\alpha} = \vec{\alpha} - \vec{\alpha_0}$ now follow from the application of the *Newton-Raphson method*:

$$\left[\frac{d}{d\vec{\alpha}}\left(\frac{d\chi^2}{d\vec{\alpha}}\right)\bigg|_{(\vec{x}_0,\vec{\alpha}_0)}\right]\Delta\vec{\alpha} = -\frac{d\chi^2}{d\vec{\alpha}}\bigg|_{(\vec{x}_0,\vec{\alpha}_0)}, \tag{4.12}$$

which, for M alignment parameters, represents a system of M linear coupled equations that needs to be solved.

For a single track n, the first order derivative in Eq. 4.12, using the definition of the track χ^2 (Eq. 4.1), the residual r (Eq. 4.6) and the full derivative with respect to the alignment parameters $\vec{\alpha}$ (Eq. 4.11), is given by:

$$\begin{aligned}\frac{d\chi^2_n}{d\vec{\alpha}} &= 2A^T V^{-1}\vec{r} + A^T V^{-1} H C\left(-2H^T V^{-1}\vec{r}\right)\\ &= 2A^T V^{-1}\left(V - HCH^T\right)V^{-1}\vec{r}\\ &= 2A^T V^{-1}\vec{r}.\end{aligned} \tag{4.13}$$

The last step follows from the fact that the track parameters $\vec{x}_0^n$ of track n for an initial estimate of alignment parameters $\vec{\alpha}_0$ satisfy the condition given in Eq. 4.3. Or in other words, the track parameters obtained from an estimate of alignment parameters yield a minimum for the track χ^2 (Eq. 4.1) such that:

$$\frac{d\chi^2_n}{d\vec{x}} = H^T V^{-1}\vec{r} = 0,$$

i.e. the second term in the second step of Eq. 4.13 is zero.

Similarly, the second order derivative in Eq. 4.12, for a single track n, follows from applying twice the full derivative with respect to the alignment parameters (Eq. 4.11) to the track χ^2 (Eq. 4.1) with the definition of the residuals r given by Eq. 4.6:

$$\frac{d}{d\vec{\alpha}}\left(\frac{d\chi^2}{d\vec{\alpha}}\right) = 2A^T V^{-1}\left(V - HCH^T\right)V^{-1}A, \tag{4.14}$$

where the matrix

$$R \equiv V - HCH^T \tag{4.15}$$

is the covariance matrix for the residuals. Here V is the covariance matrix for the measurements and the matrix HCH^T is the projection of the covariance matrix for the track parameters onto the measurement space. The off-diagonal elements of R represent the correlations between the residuals, which enter through the covariance matrix of the track parameters C. Taking these correlations into account, the alignment parameters can be estimated with a single pass through the calibration sample. (Note that if h is non-linear then more iterations are necessary.) If these correlations are ignored, *e.g.* by replacing the full derivative $d/d\vec{\alpha}$ with the partial derivative $\partial/\partial\vec{\alpha}$, then each detector element is, effectively, aligned independently of the others and more iterations are necessary to estimate the alignment parameters. This is known as the local method of alignment. Both the local method and global method are implemented within the LHC*b* alignment framework.

In conclusion the master equations to determine the alignment parameters are given by Eq. 4.13 and Eq. 4.14, and for a calibration sample containing n tracks Eq. 4.12 becomes:

$$\Delta\vec{\alpha} = -\left[\sum_n A^T V^{-1}\left(V - HCH^T\right)V^{-1}A\right]^{-1}\left[\sum_n A^T V^{-1}\vec{r}\right]. \tag{4.16}$$

The main ingredients are the residuals r, the covariance matrix for the measurements V, the covariance matrix for the track parameters C, and the partial derivative matrices $H = \partial h\left(\vec{x}\right)/\partial\vec{x}$ and $A = \partial\vec{r}/\partial\vec{\alpha}$. These are presented in the following sections for the LHC*b* reconstruction model.

4.1.1 Convergence

In the case the track model is non-linear, several iterations are required for the procedure to converge to an optimal set of alignment parameters $\vec{\alpha}$. A typical convergence criterion is that the absolute change in the alignment parameters α_i between the current iteration, j, and previous iteration, $j-1$, be less than some small number ϵ:

$$\left|{\alpha^{(i)}}_j - {\alpha^{(i)}}_{j-1}\right| < \epsilon. \tag{4.17}$$

Alternatively, one can look at the change in the ensemble χ^2 (Eq. 4.7) as a result of a change in the alignment parameters $\vec{\alpha}$, which is given by

$$\Delta\chi^2 = \frac{d\chi^2}{d\vec{\alpha}}\Delta\vec{\alpha} + \frac{1}{2}\Delta\vec{\alpha}^T\frac{d^2\chi^2}{d\vec{\alpha}^2}\Delta\vec{\alpha} = -\frac{1}{2}\Delta\vec{\alpha}^T\frac{d^2\chi^2}{d\vec{\alpha}^2}\Delta\vec{\alpha}, \tag{4.18}$$

where in the last step Eq. 4.12 is used. Note that the second order Taylor expansion of the ensemble χ^2 with respect to the alignment parameters is used, since one is interested in the change of the ensemble χ^2 around its minimum. In this case the first order term is approximately zero and the second order term is the deviation from zero. If the change in the ensemble χ^2 per degree of freedom is less than one, then any subsequent improvements in the alignment parameters are statistically insignificant and, consequently, the procedure has converged.

Additional quantities of interest are the average track χ^2 and the number of reconstructed tracks per iteration. These are indicators of the stability of the procedure. An inherent trait of any χ^2 minimisation procedure is that, depending on the initial conditions and the non-linearity

of the problem, one may obtain a different set of parameters corresponding to a different (local) minimum. This is especially true if the system is under-constrained.

4.1.2 Weak modes

Weak modes are linear combinations of alignment parameters that may affect the track parameters, but leave the ensemble χ^2 (Eq. 4.7) invariant. To determine these weak modes one can study the behaviour of the ensemble χ^2 at its minimum, which is given by its second order derivative with respect to the alignment parameters, see Sec. 4.1.1.

One observes from Eq. 4.12 that it has the familiar form for a system of linear equations, *i.e.* "$A\vec{x} = \vec{b}$". Therefore, to simplify the notation, one can rewrite Eq. 4.12 as $Z\vec{c} = \vec{y}$, where the matrix Z and the vectors $\vec{c}$ and $\vec{y}$ are defined as*:

$$Z \equiv \frac{1}{2}\frac{d}{d\vec{\alpha}}\left(\frac{d\chi^2}{d\vec{\alpha}}\right), \quad \vec{c} \equiv \Delta\vec{\alpha} \quad \text{and} \quad \vec{y} \equiv -\frac{1}{2}\frac{d\chi^2}{d\vec{\alpha}}. \tag{4.19}$$

By studying the eigenvalue spectrum of the matrix Z, *i.e.* the second order derivative of the ensemble χ^2 with respect to the alignment parameters $\vec{\alpha}$ in Eq. 4.12, one can determine which linear combination of alignment parameters are poorly constrained as illustrated below.

One can show that any symmetric matrix Z can be decomposed in terms of its eigenvalues and eigenvectors as [67]:

$$Z = UDU^T, \tag{4.20}$$

where D is a diagonal matrix whose elements D_{ii} are the eigenvalues of Z and U is an orthogonal matrix whose columns are the eigenvectors (modes) of Z. If Z is non-singular and its rank is equal to its dimension, then Z is invertible and, subsequently, the solution to the system of linear equations, using Eq. 4.20, is given by:

$$\vec{c} = Z^{-1}\vec{y} = UD^{-1}U^T\vec{y}, \tag{4.21}$$

where the inverse of D and U follows from $DD^{-1} = I$ and $UU^T = I$, respectively. Here the matrix I is the identity matrix.

Furthermore, in the minimisation of the ensemble χ^2 (Eq. 4.12) the inverse of the matrix Z, *i.e.* the second order derivative of the ensemble χ^2 with respect to the alignment parameters $\vec{\alpha}$, is also the covariance matrix for the vector $\vec{c}$, *i.e.* the alignment parameters $\vec{\alpha}$. Using Eq. 4.20 this covariance matrix can be written as:

$$C_{\vec{c}} = UD^{-1}U^T. \tag{4.22}$$

Similarly, given the above definitions (Eq. 4.19 and Eq. 4.22) the change in the ensemble χ^2 as result of a change in the alignment parameters (Eq. 4.18) can be expressed as:

$$\Delta\chi^2 = -\vec{c}^T \left[C_{\vec{c}}\right]^{-1} \vec{c}. \tag{4.23}$$

This quantity, as discussed in Sec. 4.1.1, can be used to determine whether the procedure has converged.

*These symbols are used instead of the familiar symbols to avoid any confusion that my arise with the prior definitions of A and $\vec{x}$.

Using index notation, Eq. 4.21, Eq. 4.22 and Eq. 4.23 can be expressed as

$$c_i = U_{ik} D^{-1}_{kk} U^T_{jk} y_j,\ C_{\vec{c}kl} = U_{ij} D^{-1}_{jj} U^T_{kj} \text{ and } \Delta\chi^2 = -y^T_i U_{ij} D^{-1}_{jj} U^T_{kj} y_k. \tag{4.24}$$

Now the term $U^T_{ij} y_i$ corresponds to the inner product of the j^{th} column of U, *i.e.* the j^{th} eigenmode of Z with eigenvalue D_{jj}, with $\vec{y}$. Similarly, the term $U_{ij} U^T_{kj}$ corresponds to the outer product, or Kronecker product, of the columns of U and U^T. Denoting the eigenmodes j and their corresponding eigenvalues as $\vec{u}^j \equiv U_{ij}$ and $d_j \equiv D_{jj}$, respectively, Eq. 4.21, Eq. 4.22 and Eq. 4.23 can be expressed in terms of the eigenmodes and their eigenvalues as

$$\vec{c} = \sum_j \frac{\langle \vec{u}^j, \vec{y} \rangle}{d_j} \vec{u}^j,\ C_{\vec{c}} = \sum_j \frac{\vec{u}^j \otimes \vec{u}^j}{d_j} \text{ and } \Delta\chi^2 = -\sum_j \frac{\langle \vec{u}^j, \vec{y} \rangle^2}{d_j}, \tag{4.25}$$

where $\langle , \rangle$ denotes the inner product and $\otimes$ the Kronecker product. From this one observes that the eigenmodes of the matrix Z, *i.e.* the second order derivative of the ensemble χ^2 with respect to the alignment parameters $\vec{\alpha}$ in Eq. 4.12, with small eigenvalues will give rise to a large statistical uncertainty in $\vec{c}$, *i.e.* the alignment parameters $\vec{\alpha}$. Furthermore, the change in the ensemble χ^2 for a given change in the alignment parameters is given by the sum over the eigenmodes j.

Eigenmodes with associated small eigenvalues are considered *weak modes*. Examples of weak modes, in the case of a parallel plane geometry, are a shearing, *e.g.* $\Delta x = \beta z$ in the xz-plane, or scaling, *e.g.* $\Delta z = \beta z$, of the system, where β is some scale factor.

4.1.3 Constraints

In the previous section it was shown that modes with small eigenvalues have a large statistically uncertainty. In addition to these weak modes there are the so-called unconstrained modes which have zero eigenvalues. In this case the solution to Eq. 4.16 is degenerate, while in the former case the solution to Eq. 4.16 is almost degenerate, *i.e.* for a given weak mode one can still obtain an unique solution. The unconstrained modes correspond to degrees of freedom that a detector is insensitive to. For example, the OT modules are insensitive to movements along the wire, since these movements are perpendicular to the measurement direction. Note that, ideally, these movements will give rise to zero eigenvalues. However, due to machine accuracy or the Kalman filter fit initialisation these movements will appear to have (very) small eigenvalues.

These weak and unconstrained modes can be removed from the system by introducing constraints. Possible methods of constraining the system is either through explicitly removing certain degrees of freedom from Eq. 4.16 or through using constraints such as *Lagrange* constraints or survey constraints. Alternatively, one could cut on the eigenvalue spectrum of the second order derivative of the ensemble χ^2 with respect to the alignment parameters in Eq. 4.16. For more details on the latter procedure see [68].

In the case of *Lagrange* constraints, so-called exact constraints, the ensemble χ^2 is minimised subject to the constraint that a combination of alignment parameters prescribed by the function $g(\vec{\alpha})$ satisfy some condition $g(\vec{\alpha}) = g_0$, where g_0 is some constant. The estimated alignment parameters in this case are then obtained by introducing a *Lagrange* multiplier λ and minimising the following ensemble χ^2 [66]*:

$$\chi^{2'} = \chi^2 + 2\lambda g(\vec{\alpha}). \tag{4.26}$$

*The factor two serves an aesthetic purpose and in the end cancels against the factor two obtained from differentiating the χ^2, which is a quadratic function. If this factor is omitted then the *Lagrange* multiplier λ is scaled by a factor half.

The parameters which minimises Eq. 4.26 is obtained from the following conditions:

$$\frac{\partial \chi^{2'}}{\partial \vec{\alpha}} \equiv 0 \qquad \wedge \qquad \frac{\partial \chi^{2'}}{\partial \lambda} \equiv 0, \tag{4.27}$$

which leads to the following form for the system of linear equations (using the definitions in Eq. 4.19):

$$\begin{pmatrix} Z & \vec{g} \\ \vec{g}^T & 0 \end{pmatrix} \begin{pmatrix} \vec{c} \\ \lambda \end{pmatrix} = \begin{pmatrix} \vec{y} \\ 0 \end{pmatrix}. \tag{4.28}$$

In other words, the *Lagrange* multiplier λ is added as an additional fit parameter to the alignment parameters. The purpose of these type of constraints is to pull some combination of alignment parameters to some value g_0. For example, to constrain the (global) movement of a set of detector elements in x one could require that the average change in the translation in x of all detectors elements is zero.

Similar to *Lagrange* constrains, certain degrees of freedom can be constrained to their survey values by introducing the following χ^2 penalty term:

$$\chi^2_{\mathrm{s}} = \left(\frac{p - p_s}{\sigma_{p_{\mathrm{s}}}} \right)^2, \tag{4.29}$$

where p_{s} is the survey value of some parameter p and $\sigma_{p_{\mathrm{s}}}$ its associated survey error.

4.2 Global Alignment With Kalman Filter Fitted Tracks

In the LHC*b* experiment charged particle trajectories are fitted using the Kalman filter method [69]. In what follows a brief description of this method and how the information obtained from this method can be used in the global alignment method, discussed in Sec. 4.1, is given. For a derivation of the Kalman filter method see [70]*. For further details on the implementation of the Kalman filter method within the LHC*b* experiment see [27, 59].

The Kalman filter method is a progressive least squares fit which in its final result is equivalent to the global least squares method for linear problems. In contrast to the global least squares method, where a single vector of track parameters $\vec{x}$, a so-called state, at some fixed point is used, the trajectory of a charged particle in the Kalman filter method is modelled as a discrete system of a collection of states. To emphasise this the states have an additional index which represents a "time", where $k-1$, k and $k+1$ represents the past, present and future, respectively. This index corresponds to the points, so-called nodes, where the states are defined. They are typically chosen to coincide with the measurements and are related by a *transport* function f, which describes the motion of the particle through the magnetic field and material of the detector:

$$\vec{x}_k^{k-1} = f\left(\vec{x}_{k-1}\right) = F_{k-1}\vec{x}_{k-1} + \vec{w}_{k-1}. \tag{4.30}$$

In the last step the transport function f is linearised using first order Taylor expansion, which yields the transport matrix F. The second term, w, is called the process noise and represents a random perturbation, such as multiple scattering, with an expectation value of zero and a covariance matrix Q.

In the Kalman filter method each state k is determined progressively using the information gained at state $k-1$ and thereby "improving" the knowledge of the trajectory of the charged

*A heuristic derivation of the Kalman filter method is given in [71].

particle. The procedure to determine the optimal state at node k, as illustrated in Fig. 4.1, consists of three steps: prediction, filtering and smoothing. In the prediction step, the state at node k is estimated from the state at node $k-1$ using the transport function. Subsequently, in the filtering step the estimated state $\vec{x}_k^{k-1}$ is weighted with the information gained from the past up to the present measurements, yielding an improved estimate of the filtered state $\vec{x}_k$ and its covariance C_k at node k. Finally, once all the measurements on a track have been processed with prediction and filtering steps, the information at node $k+1$ is propagated back recursively to the state at node k, yielding an improved estimate of the state at node k. This is the smoothing step and the smoothed state at node k and its covariance matrix are labelled as $\vec{x}_k^n$ and C_k^n, respectively.

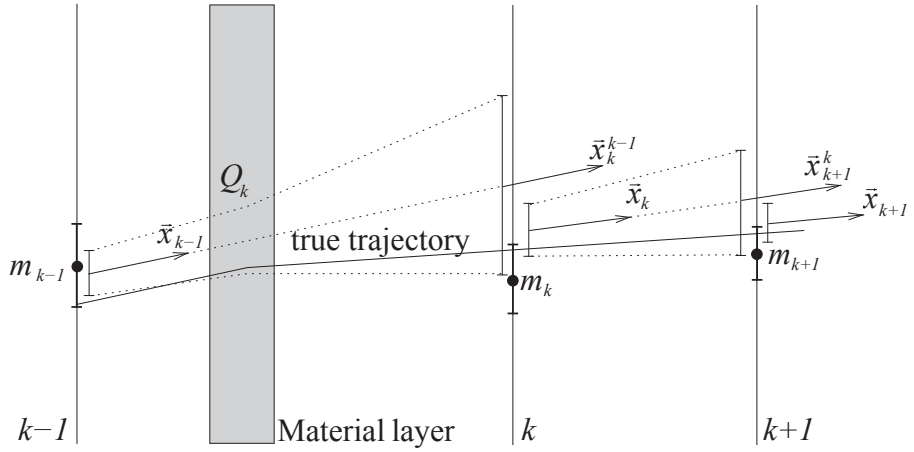

Fig. 4.1: *Schematic drawing of the Kalman Filter method [27] showing the evolution of a track state from prediction to filtering. Note that in the prediction step the error on the state at k, x_k^{k-1}, predicted from the state at $k-1$, is larger, due to (possible) multiple scattering in the material layer. In the filtering step, i.e. when the measurement information is added, the state x_k^{k-1} is pulled towards the measurement at k which yields a filtered state x_k with a smaller error.*

4.2.1 The Kalman filter method global covariance matrix C

The process described above leads to a track represented by a collection of N smoothed states and their corresponding covariance matrices. These states and their covariance matrices can be used to construct a global parameter vector $\vec{x}$ and global covariance matrix C. In essence, one substitutes the Kalman track model for the global least squares track model. However, in contrast to the global least squares method, where $\vec{x}$ is vector of, generally, five parameters and C a 5×5 matrix, $\vec{x}$ is now a vector of $5 \times N$ parameters and C is an $N \times N$ matrix of 5×5 matrices, *i.e.*

$$\vec{x} = \begin{pmatrix} \vec{x}_1^n & \vec{x}_2^n & \vec{x}_3^n & \dots & \vec{x}_N^n \end{pmatrix} \quad \text{and} \quad C = \begin{pmatrix} C_{11} & C_{12} & C_{13} & \dots & C_{1N} \\ C_{21} & C_{22} & C_{23} & \dots & C_{2N} \\ C_{31} & C_{32} & C_{33} & \dots & C_{3N} \\ \vdots & \vdots & \vdots & \ddots & \vdots \\ C_{N1} & C_{N3} & C_{N3} & \dots & C_{NN} \end{pmatrix}, \quad (4.31)$$

where C_{NN} is the smoothed covariance matrix C_N^n of the smoothed state $\vec{x}_N^n$. However, whereas in the global least squares track fit the correlation matrix C is always calculated, in the Kalman filter track fit only the diagonal elements C_{ii} of C are calculated and the off-diagonal elements C_{ij} are either not calculated at all or only implicitly. By design the states and their covariance matrices are determined locally. Consequently, the correlations between the fitted residuals, *i.e.* the off diagonal elements of the residual matrix $R \equiv \left(V - HCH^T\right)$ (Eq. 4.16), where V is the covariance matrix of the measurements and the matrix HCH^T is the projection of the covariance matrix of the state parameters onto the measurement space, which are needed for the global alignment method are missing.

Recently a novel method was developed to determine the global correlation matrix C in the Kalman filter fit [72]. It can be shown that the correlation between state x_i^n and state x_j^n in the Kalman filter method is given by

$$C_{i-1,j}^n = A_{i-1} C_{i,j}^n \quad \forall \quad i \leq j, \tag{4.32}$$

where A is the smoother gain matrix [69]:

$$A_k = C_k F_k^T (C_{k+1}^k)^{-1}. \tag{4.33}$$

Here C_k and C_{k+1}^k are the updated and extrapolated covariance matrices, respectively. Using the definitions of the updated and extrapolated covariance matrices [69], Eq. 4.33 can be expressed as:

$$A_k = F_k^{-1}(C_{k+1}^k - Q_k)(C_{k+1}^k)^{-1}. \tag{4.34}$$

From this one observes that in the absence of multiple scattering smoothing is equivalent to back extrapolation and that the smoothed states are maximally correlated through the transport matrix F, as one would intuitively expect. The latter point can also be illustrated by calculating the covariance, $\mathrm{Cov}(x_{k-1}, x_k^{k-1})$, between the state x_k and the extrapolated state x_k^{k-1}.

Using Eq. 4.32 the correlations between states can be calculated and the Kalman filter method can be used in the global alignment method. Consequently, the LHCb track model and fit, and reconstructions tools can be used in the global alignment method. This has the benefit that the complexities of the LHCb track model, *e.g.* multiple scattering, energy loss corrections and magnetic field, are correctly taken into account. Moreover, the estimated alignment parameters are consistent with the LHCb track model and fit used in the reconstruction and analysis.

Note that an additional advantage of the procedure described in [72] to calculate the correlations between the states, is that it can be used to include vertex or mass constraints in the alignment procedure without refitting the tracks. Instead, the information gained from the vertex or mass fit is propagated back to the track parameters.

4.3 Global Alignment With LHCb Tracks

In LHCb the trajectories of charged particles and the detection elements, *e.g.* the anode wires of the OT and the strips of the silicon detectors (VELO, TT and IT), are represented in the LHCb frame by generic curves, so-called *trajectories*, parametrised as function of their arc length or as a function of z [59, 73]. The advantage of describing the measurements and the particle trajectories as curves in the LHCb frame is that it allows for a uniform and consistent treatment of all the tracking detectors, irrespective of the utilised detection technology. In addition, it introduces an additional layer such that the reconstruction procedure is decoupled from the detector geometry description, *i.e.* no assumptions are made concerning the shape, size or the orientation of the

detector elements, *e.g.* the VELO r-sensors with semi-circular strips compared to the VELO ϕ-sensors or, TT and IT sensors with straight strips.

4.3.1 The hit residual r

The hit residual r, see Fig. 4.2, is defined as the signed distance between the measurement point $\boldsymbol{x}_m(s_m, \vec{\alpha})$ on a measurement trajectory, for a given arc length s_m, and the track point $\boldsymbol{x}_t(s_t, \vec{x})$ on a track trajectory, for a given arc length s_t, and is given by:

$$r = (\boldsymbol{x}_t - \boldsymbol{x}_m) \cdot \hat{\boldsymbol{r}} = (\boldsymbol{x}_t - \boldsymbol{x}_m) \cdot \frac{\boldsymbol{t}_t \times \boldsymbol{t}_m}{|\boldsymbol{t}_t \times \boldsymbol{t}_m|}, \tag{4.35}$$

where $\boldsymbol{t}_m$ and $\boldsymbol{t}_t$ are the direction vectors of the measurement trajectory and track trajectory, respectively. Or in other words the residual is given by the projection of $\boldsymbol{x}_t - \boldsymbol{x}_m$ on the vector that is perpendicular to the measurement and track trajectory. Note that if these points are the points of closest approach (poca), which can be determined by minimising the distance between the measurement point and track point with respect to s_m and s_t, then $\boldsymbol{x}_t - \boldsymbol{x}_m$ is parallel to $\hat{\boldsymbol{r}}$. Or in other words, this distance corresponds to the distance of closest approach (doca) between the measurement and track trajectory.

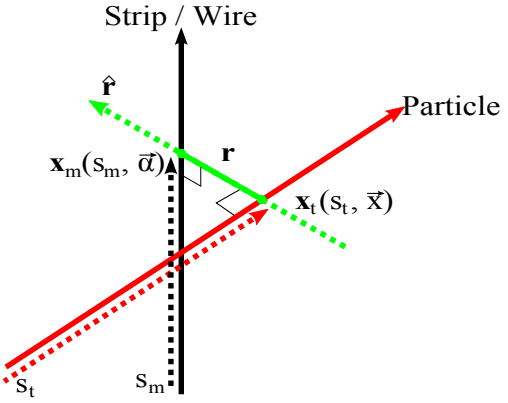

Fig. 4.2: *The distance of closest approach between a measurement trajectory and particle trajectory r is such that $\vec{r}$ is perpendicular to both $\vec{m}$ and $\vec{t}$.*

4.3.2 The partial derivative matrix $H = \partial h(\vec{x})/\partial \vec{x}$

The effect of a small change in the track parameters $\vec{x}$ on the residual r is given by the first order Taylor expansion of r around an initial estimate of of track parameters $\vec{x}_0$:

$$r = r_0 + \left.\frac{\partial r}{\partial \vec{x}}\right|_{\vec{x}_0} \Delta\vec{x}, \tag{4.36}$$

where $\partial r/\partial \vec{x} = H$ is the projection matrix and $\Delta\vec{x} = \vec{x} - \vec{x}_0$. From Eq. 4.35 it follows that the projection matrix is given by:

$$\begin{aligned} H &= \frac{\partial r}{\partial \vec{x}} \\ &= \hat{\boldsymbol{r}}^T \frac{\partial}{\partial \vec{x}} (\boldsymbol{x}_t - \boldsymbol{x}_m) + (\boldsymbol{x}_t - \boldsymbol{x}_m)^T \frac{\partial}{\partial \vec{x}} \hat{\boldsymbol{r}} \\ &\approx -\hat{\boldsymbol{r}}^T D_{\vec{x}}, \end{aligned} \tag{4.37}$$

where in the last step it is assumed that the change in the slope of the track trajectory is negligibly small (of $\mathcal{O}(\Delta s^2)$), *i.e.* one considers only small changes along the track trajectory. Here the matrix $D_{\vec{x}}$ is the derivative matrix of the track point of closest approach with respect to the track parameters. In other words, the change in the residual r as result of a small change in the track parameters $\vec{x}$ is given by the projection of the derivative matrix $D_{\vec{x}}$ onto the direction of the residual r.

In LHCb a charged particle track is modelled as collection of states ordered in z, which is a natural choice given the geometry of the LHCb detector. The track parameters at some z are those that describe the trajectory of the charged particle around this z. These are the position of the charged particle and the tangents to its trajectory in the vertical plane and horizontal plane, and its momentum, respectively:

$$\vec{x} = \begin{pmatrix} x \\ y \\ t_x \\ t_y \\ q/p \end{pmatrix}, \tag{4.38}$$

where x and y are the coordinates in the LHCb frame, and $t_x \equiv dx/dz$ and $t_y \equiv dy/dz$ are the slopes of the trajectory. The last parameter q/p is the signed charge (± 1) divided by the momentum p of the particle.

Given Eq. 4.38 and the track point $\boldsymbol{x}_t = (x_t, y_t, z_t)$, the derivative matrix $D_{\vec{x}}$ is defined as:

$$D_{\vec{x}} \equiv \begin{pmatrix} \frac{\partial x_t}{\partial x} & \frac{\partial x_t}{\partial y} & \frac{\partial x_t}{\partial t_x} & \frac{\partial x_t}{\partial t_y} & \frac{\partial x_t}{\partial q/p} \\ \frac{\partial y_t}{\partial x} & \frac{\partial y_t}{\partial y} & \frac{\partial y_t}{\partial t_x} & \frac{\partial y_t}{\partial t_y} & \frac{\partial y_t}{\partial q/p} \\ \frac{\partial z_t}{\partial x} & \frac{\partial z_t}{\partial y} & \frac{\partial z_t}{\partial t_x} & \frac{\partial z_t}{\partial t_y} & \frac{\partial z_t}{\partial q/p} \end{pmatrix}.$$

For example, assuming one can neglect the magnetic field between z and z_0, *i.e.* the curvature of the track is zero, and that the trajectories are parametrised in z, it follows that

$$\begin{pmatrix} x_t \\ y_t \end{pmatrix} = \begin{pmatrix} x_0 + t_x \Delta z \\ y_0 + t_y \Delta z \end{pmatrix} \quad \text{and} \quad D_{\vec{x}} = \begin{pmatrix} 1 & 0 & \Delta z & 0 & 0 \\ 0 & 1 & 0 & \Delta z & 0 \\ 0 & 0 & 0 & 0 & 0 \end{pmatrix}, \tag{4.39}$$

where $\Delta z = z - z_0$.

4.3.3 The partial derivative matrix $A = \partial r / \partial \alpha$

Similar to the above, the change in the hit residual r as result of a small change in the alignment parameters $\vec{\alpha}$ is given by

$$r = r_0 + \left.\frac{\partial r}{\partial \vec{\alpha}}\right|_{\vec{\alpha}_0} \Delta\vec{\alpha}, \tag{4.40}$$

where $\partial r / \partial \vec{\alpha} = A$ is the matrix of the derivative of the hit residual with respect to the alignment parameters and $\Delta\vec{\alpha} = \vec{\alpha} - \vec{\alpha}_0$. Using the chain rule, the matrix A can be re-written as

$$A = \frac{\partial r}{\partial \vec{\alpha}} = \frac{\partial r}{\partial \boldsymbol{x}_m} \frac{\partial \boldsymbol{x}_m}{\partial \vec{\alpha}} = \hat{\boldsymbol{r}} D_{\vec{\alpha}}, \tag{4.41}$$

where $D_{\vec{\alpha}}$ gives the change in the point of closest approach of the measurement with respect to the track as result of a small change in the alignment parameters.

In LHC*b*, the transformation from local (detector element frame) to global (LHC*b* frame) coordinates is given by

$$\boldsymbol{x}_{\text{global}} = \mathcal{A}^{\text{local}}_{\text{global}} \boldsymbol{x}_{local} = R\boldsymbol{x}_{\text{local}} + T, \tag{4.42}$$

where $\mathcal{A}^{\text{local}}_{\text{global}}$ is the transformation matrix from the local to the global coordinate frame. The matrix R is the rotation matrix from the local to global frame and the vector T the translation vector from the local to global frame. In other words, the transformation from the local frame to the global frame is given by a rotation followed by a translation. In the case of nested volumes, as for example the OT (see Chapter 3), the transform $\mathcal{A}^{\text{module}}_{\text{LHC}b}$ is a composition of transforms and is given by:

$$\mathcal{A}^{\text{module}}_{\text{LHC}b} = \mathcal{A}^{\text{station}}_{\text{LHC}b} \mathcal{A}^{\text{layer}}_{\text{station}} \mathcal{A}^{\text{quarter}}_{\text{layer}} \mathcal{A}^{\text{module}}_{\text{quarter}}. \tag{4.43}$$

In LHC*b* the *Euler 321* co-moving axis convention is used for rotations and is defined as:

$$R = R_x(\alpha) R_y(\beta) R_z(\gamma), \tag{4.44}$$

where α, β and γ are the Euler angles and R_x, R_y and R_z are the usual rotation matrices about the x, y and z-axis, respectively. In other words, a vector is first rotated about the z-axis, followed by a rotation about the y'-axis and subsequently by a rotation about the x''-axis.

The possible degrees of freedom of a detector element in LHC*b*, as illustrated in Fig. 4.3, are the delta translations along the x, y and z-axis and the delta rotations about the x, y and z-axis. In this thesis these degrees of freedom are denoted as Δx, Δy and Δz, and ΔRx, ΔRy and ΔRz for the translations and rotations, respectively.

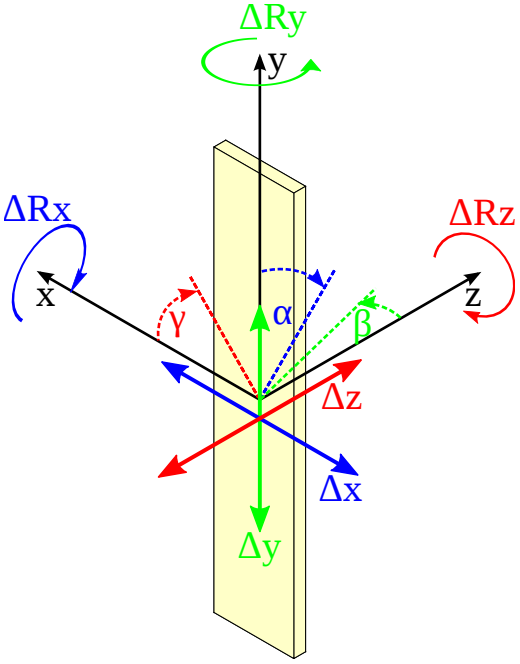

Fig. 4.3: *The six degrees of freedom of a detector element: the delta translations Δx, Δy and Δz along the x, y and z-axis, respectively, and the delta rotations ΔRx, ΔRy and ΔRz about the x, y and z-axis, respectively. The angles α, β and γ are the corresponding Euler angles for ΔRx, ΔRy and ΔRz, respectively.*

Given the three translational and three rotational degrees of freedom and the measurement

point $\boldsymbol{x}_m = (x_m, y_m, z_m)$, the partial derivative matrix $D_{\vec{\alpha}}$ is defined as:

$$D_{\vec{\alpha}} = \begin{pmatrix} \frac{\partial x_m}{\partial x} & \frac{\partial x_m}{\partial y} & \frac{\partial x_m}{\partial z} & \frac{\partial x_m}{\partial \alpha} & \frac{\partial x_m}{\partial \beta} & \frac{\partial x_m}{\partial \gamma} \\ \frac{\partial y_m}{\partial x} & \frac{\partial y_m}{\partial y} & \frac{\partial y_m}{\partial z} & \frac{\partial y_m}{\partial \alpha} & \frac{\partial y_m}{\partial \beta} & \frac{\partial y_m}{\partial \gamma} \\ \frac{\partial z_m}{\partial x} & \frac{\partial z_m}{\partial y} & \frac{\partial z_m}{\partial z} & \frac{\partial z_m}{\partial \alpha} & \frac{\partial z_m}{\partial \beta} & \frac{\partial z_m}{\partial \gamma} \end{pmatrix},$$

Using Eq. 4.42 one can show that the partial derivatives with respect to the translations in x, y and z, *i.e.* the first, second and third columns of $D_{\vec{\alpha}}$, are given by

$$\frac{\partial x_{m_i}}{\partial x_j} = \delta_{ij}, \tag{4.45}$$

where δ_{ij} is the Kronecker delta. Similarly, the partial derivatives with respect to the Euler angles α, β and γ, *i.e.* the fourth, fifth and sixth column of $D_{\vec{\alpha}}$, are given by

$$\frac{\partial R}{\partial \alpha}\boldsymbol{a} = \frac{\partial R_x}{\partial \alpha} R_y R_z \boldsymbol{a}, \quad \frac{\partial R}{\partial \beta}\boldsymbol{a} = R_x \frac{\partial R_y}{\partial \beta} R_z \boldsymbol{a} \quad \text{and} \quad \frac{\partial R}{\partial \gamma}\boldsymbol{a} = R_x R_y \frac{\partial R_z}{\partial \alpha}\boldsymbol{a}, \tag{4.46}$$

where the vector $\boldsymbol{a}$ is the lever arm of the rotation and is defined as $\boldsymbol{a} = \boldsymbol{x}_m - \boldsymbol{p}$. Here $\boldsymbol{p}$ is the pivot point about which the rotations are defined. Since $d\sin\theta/d\theta = \cos\theta = \sin(\pi/2+\theta)$ and $d\cos\theta/d\theta = -\sin\theta = \cos(\pi/2+\theta)$, the derivative with respect to the Euler angle, *e.g* α, can be re-written as

$$\frac{\partial R}{\partial \alpha} = \left[\begin{pmatrix} 1 & 0 & 0 \\ 0 & \cos\alpha & -\sin\alpha \\ 0 & \sin\alpha & \cos\alpha \end{pmatrix} \begin{pmatrix} 0 & 0 & 0 \\ 0 & \cos\frac{1}{2}\pi & -\sin\frac{1}{2}\pi \\ 0 & \sin\frac{1}{2}\pi & \cos\frac{1}{2}\pi \end{pmatrix} \right] R_y(\beta) R_z(\gamma). \tag{4.47}$$

Therefore, it follows that the y and z components of $\partial R/\partial\alpha$ are given by

$$\left[\frac{\partial R}{\partial \alpha}\boldsymbol{a}\right]_{y,z} = \left[\left(R_x(\alpha) R_x(\frac{1}{2}\pi)\right) R_y(\beta) R_z(\gamma)\boldsymbol{a}\right]_{y,z}, \tag{4.48}$$

and the x component is zero, since this is the axis of rotation. Similarly, one obtains for $\partial R/\partial\beta$ (y-axis is the axis of rotation) and $\partial R/\partial\gamma$ (z-axis is the axis of rotation):

$$\left[\frac{\partial R}{\partial \beta}\boldsymbol{a}\right]_{x,z} = \left[R_x(\alpha)\left(R_y(\beta) R_y(\frac{1}{2}\pi)\right) R_z(\gamma)\boldsymbol{a}\right]_{x,z} \tag{4.49}$$

and

$$\left[\frac{\partial R}{\partial \gamma}\boldsymbol{a}\right]_{x,y} = \left[R_x(\alpha) R_y(\beta)\left(R_z(\gamma) R_z(\frac{1}{2}\pi)\right)\boldsymbol{a}\right]_{x,y}. \tag{4.50}$$

Alternatively, since one is considering a linear model and in addition only first order corrections to $\vec{\alpha}_0$, the rotation matrices can be replaced by their infinitesimal counterparts, *e.g.*

$$R_x(\delta\alpha) = \begin{pmatrix} 1 & 0 & 0 \\ 0 & 1 & -\delta\alpha \\ 0 & \delta\alpha & 1 \end{pmatrix}. \tag{4.51}$$

In this case the derivatives with respect to the Euler angles α, β and γ are given by

$$\frac{\partial R}{\partial \alpha}\boldsymbol{a} = \begin{pmatrix} 0 \\ -a_z \\ a_x \end{pmatrix}, \quad \frac{\partial R}{\partial \beta}\boldsymbol{a} = \begin{pmatrix} a_z \\ 0 \\ -a_y \end{pmatrix} \quad \text{and} \quad \frac{\partial R}{\partial \gamma}\boldsymbol{a} = \begin{pmatrix} -a_y \\ a_x \\ 0 \end{pmatrix}. \tag{4.52}$$

Note that the second order terms that follows from the multiplication of the infinitesimal rotation matrices are negligibly small and can be discarded. Consequently, multiplication of infinitesimal matrices is commutative.

One now has all the ingredients to do alignment with "LHC*b*" tracks. Note that the partial derivative matrices H and A are calculated in the LHC*b* frame and consequently the alignment offsets $\Delta\vec{\alpha}$ for a detector element are determined in the LHC*b* frame. Nonetheless, these offsets can be transformed to any frame, as long as one knows the transformation from that frame to the global frame. For example, the offsets in the local frame of a detector element are given by

$$\Delta(\vec{\alpha}_{\text{local}}) = \left(\mathcal{A}^{\text{local}}_{\text{global}}\right)^{-1} \Delta(\vec{\alpha}_{\text{global}})\mathcal{A}^{\text{local}}_{\text{global}} = \mathcal{A}^{\text{global}}_{\text{local}}\Delta(\vec{\alpha}_{\text{global}})\mathcal{A}^{\text{local}}_{\text{global}}, \tag{4.53}$$

where $\Delta(\vec{\alpha}_i)$ is the transform constructed from a set of alignment parameters $\vec{\alpha}$ in frame i.*

4.3.4 The Jacobian for local-to-global transformations

In some cases it may be desirable to calculate the alignment offsets in the local frame, *e.g.* when one is aligning detector elements that have degrees of freedom that are perpendicular to the measurement direction. This can be accomplished by rotating the partial derivative matrix A_{global} with the Jacobian corresponding to the transform of the global alignment parameters to the local alignment parameters $J_{\vec{\alpha}_{\text{local}} \to \vec{\alpha}_{\text{global}}}$ such that:

$$A_{\text{local}} \equiv \frac{\partial r}{\partial \vec{\alpha}_{\text{local}}} = A_{\text{global}} J_{\vec{\alpha}_{\text{local}} \to \vec{\alpha}_{\text{global}}} \equiv \frac{\partial r}{\partial \vec{\alpha}_{\text{global}}} \frac{\partial \vec{\alpha}_{\text{global}}}{\partial \vec{\alpha}_{\text{local}}}. \tag{4.54}$$

The Jacobian $J_{\vec{\alpha}_{\text{local}} \to \vec{\alpha}_{\text{global}}}$ can be determined as follows: given the transform

$$\Delta(\vec{\alpha}_{\text{global}}) = \mathcal{A}^{\text{local}}_{\text{global}}\Delta(\vec{\alpha}_{\text{local}})\mathcal{A}^{\text{global}}_{\text{local}} \tag{4.55}$$

one can show that the global delta rotation is given by

$$R(\alpha_g, \beta_g, \gamma_g) = R^{\text{local}}_{\text{global}} R(\alpha_l, \beta_l, \gamma_l)(R^{\text{local}}_{\text{global}})^T \tag{4.56}$$

and the global delta translation by

$$T(x_g, y_g, z_g) = -R^{\text{local}}_{\text{global}} R(\alpha_l, \beta_l, \gamma_l)(R^{\text{local}}_{\text{global}})^T T^{\text{local}}_{\text{global}} + R^{\text{local}}_{\text{global}} T(x_l, y_l, z_l) + T^{\text{local}}_{\text{global}}. \tag{4.57}$$

Applying the right hand side and left side of Eq. 4.55 to some arbitrary point $\boldsymbol{x}_g$, and assuming that the alignment corrections are small, it follows that for a global delta rotation

*Although the alignment parameters are determined in the global frame, the actual parameters stored in the LHC*b* conditions database are the alignment parameters in the local frame.

$R(\delta\alpha_g, \delta\beta_g, \delta\gamma_g)$:

$$\begin{pmatrix} 0 & -\delta\gamma_g & \delta\beta_g \\ \delta\gamma_g & 0 & -\delta\alpha_g \\ -\delta\beta_g & \delta\alpha_g & 0 \end{pmatrix} = R_g^l D_\alpha (R_g^l)^T \delta\alpha_l + R_g^l D_\beta (R_g^l)^T \delta\beta_l + R_g^l D_\gamma (R_g^l)^T \delta\gamma_l \quad (4.58)$$

and for a global delta translation $T(\delta x_g, \delta y_g, \delta z_g)$:

$$\begin{aligned} \begin{pmatrix} \delta x_g \\ \delta y_g \\ \delta z_g \end{pmatrix} &= -R_g^l D_\alpha (R_g^l)^T T_g^l \delta\alpha_l - R_g^l D_\beta (R_g^l)^T T_g^l \delta\beta_l - R_g^l D_\gamma (R_g^l)^T T_g^l \delta\gamma_l \\ &\quad + R_g^l D_x \delta x_l + R_g^l D_y \delta y_l + R_g^l D_z \delta z_l, \end{aligned} \quad (4.59)$$

where the matrices D_α, D_β and D_γ are defined as

$$D_\alpha = \begin{pmatrix} 0 & 0 & 0 \\ 0 & 0 & -1 \\ 0 & 1 & 0 \end{pmatrix}, \quad D_\beta = \begin{pmatrix} 0 & 0 & 1 \\ 0 & 0 & 0 \\ -1 & 0 & 0 \end{pmatrix} \quad \text{and} \quad D_\gamma = \begin{pmatrix} 0 & -1 & 0 \\ 1 & 0 & 0 \\ 0 & 0 & 0 \end{pmatrix}, \quad (4.60)$$

and the vectors D_x, D_y and D_z are defined as the unit vectors $\hat{\boldsymbol{e}}_x$, $\hat{\boldsymbol{e}}_y$ and $\hat{\boldsymbol{e}}_z$.

All the information necessary to construct $J_{\vec{\alpha}_{\text{local}} \to \vec{\alpha}_{\text{global}}}$ is contained in Eq. 4.58 and Eq. 4.59. By inspection one notices that the derivatives of the global delta rotations to the local delta rotations are generated by $R_g^l D_i (R_g^l)^T$ $(i = \alpha, \beta, \gamma)$ and the derivatives of the global delta rotations to the local delta translations are 0. The derivatives of the global delta translations to the local delta translations are generated by $R_g^l D_j$ $(j = x, y, z)$ and the derivatives of the global delta translations to the local delta rotations are generated by $R_g^l D_i (R_g^l)^T T_g^l$.

4.4 Implementation

The LHC*b* alignment framework [74] is developed within the LHC*b* C++ software framework GAUDI, which is also used by the reconstruction and analysis software. Consequently, the alignment has access to the same information and tools as the reconstruction and analysis software. These include, amongst others, access to the detector elements and their geometry and conditions, and to the tracks and vertices. Furthermore, one has direct access to the various reconstruction, track selection and monitoring tools.

The framework allows for easy and simple configuration via Python [75] and uses the standard reconstruction software to reconstruct tracks and vertices, and to determine the required derivatives. It allows to align for any single detector element or an ensemble of detector elements for the degrees of freedom illustrated in Fig. 4.3. In addition, *Lagrange* and survey constraint methods are implemented to constrain the system.

At the core of the alignment framework is a single generic C++ algorithm. The inputs to the algorithm are the detector elements to be aligned and the tracks to be used for alignment. The former is provided by a tool that gets the detector elements and their conditions, specified by the user, and converts them to generic objects called alignables. The latter is provided by the reconstruction tools and algorithms. The algorithm determines which hits belong to which alignables and gets the corresponding residuals r and measurement covariance matrices V. Subsequently, the global covariance matrix C is calculated. This information is then used to calculate the first

and second derivative in Eq. 4.16. Once all the tracks in a calibration sample have been processed, the first and second order derivatives are passed on to a tool to determine the alignment offsets $\Delta\vec{\alpha}$.

4.5 Validation

By virtue of the fact that it uses the same track model and track fit as the LHC*b* reconstruction framework, the alignment method takes material effects and the magnetic field into account. An example of a material effect that affects the reconstruction of particle trajectories is multiple scattering, *i.e.* the particle is deflected from its path as it traverses and interacts with the material. In what follows a validation study of the LHC*b* alignment framework, with emphasis on the effects of multiple scattering, is presented in which two detectors of different detection technology and with different hit resolutions, namely the IT and the OT, are aligned simultaneously.

In the LHC*b* track fitting procedure [27, 59] multiple scattering is accounted for by introducing terms proportional to the projected scattering angle squared, θ^2, in the processes noise covariance matrix Q and is given by the Highland formula [76]:

$$\theta = \frac{13.6\,\mathrm{MeV}}{\beta p\,\mathrm{c}}\sqrt{\frac{\Delta z\sqrt{1+t_x^2+t_y^2}}{X_0}}\left[1+0.038\ln\left(\frac{\Delta z\sqrt{1+t_x^2+t_y^2}}{X_0}\right)\right], \tag{4.61}$$

where $\beta = v/\,\mathrm{c}$ is the speed of the particle and p its momentum, respectively, and Δz is the distance traversed along z by the particle through a vertical slice of material with radiation length X_0. For example, for a particle with momentum of $13.6\,\mathrm{GeV}$ the projected scattering is approximately $\theta = 1\,\mathrm{mrad}$ per radiation length. In the track fit and alignment procedure multiple scattering competes with the hit resolution in the covariance for the residuals (Eq. 4.15). For low momentum tracks multiple scattering contributions are significant and when ignored lead to an overestimation of the residual and its covariance, and ultimately to a poor track χ^2, while for high momentum tracks the hit resolution dominates and multiple scattering effects can be safely ignored.

Given the above, alignment procedures that do not take material effects into account typically apply momentum cuts ($> 10\,\mathrm{GeV}$), such that the effects of multiple scattering are small and the hit resolution dominates. Here it will be shown, that given that material effects are taken into account in the LHC*b* alignment procedure, it is also possible to align with tracks of lower momenta and that the procedure converges and is stable. For other validation studies of the framework using both Monte Carlo and commissioning data see [72, 77, 41, 78, 79], Chapter 5 and Chapter 6.

4.5.1 Scenario

In this validation study, the IT boxes and OT C-frames are randomly mis-aligned along their primary measurement direction, *i.e.* random Δx translations are introduced. The random Δx translations are picked from a Gaussian with a width $\sigma = 5 \times \sigma_{\text{res}}$, where σ_{res} is the hit resolution of the detector and is $60\,\mu\mathrm{m}$ or $200\,\mu\mathrm{m}$ for the IT or OT, respectively. Note that these misalignments are somewhat extreme compared to the resolution of the survey measurements. The survey resolution is typically a factor two better*.

*Though this scenario is extreme and has a sizeable effect on the track yield, track χ^2 and the $J/\psi \to \mu^+\mu^-$ mass spectrum, the available statistics is sufficient for an alignment procedure at this granularity and does not require re-tuning the default LHC*b* reconstruction procedure.

Station	XU A Δx [mm]	XU C Δx [mm]	VX A Δx [mm]	VX C Δx [mm]
OT1	-0.138	0.410	-1.221	-0.257
OT2	-0.302	-1.675	1.272	1.598
OT3	0.430	-0.315	-0.282	-1.003

Tab. 4.1: *OT C-frame Δx translations picked from a Gaussian with a width $\sigma = 5 \times 200\,\mu$m.*

Station	Top Δx [mm]	Bottom Δx [mm]	A Δx [mm]	C Δx [mm]
IT1	-0.041	0.367	0.077	0.123
IT2	-0.091	-0.382	-0.497	-0.502
IT3	0.129	0.085	0.301	-0.095

Tab. 4.2: *IT boxes Δx translations picked from a Gaussian with a width $\sigma = 5 \times 60\,\mu$m.*

4.5.2 Procedure

A flowchart of a typical alignment procedure is shown in Fig. 4.4. For a given event in a calibration sample, the tracks are first reconstructed, which involves pattern recognition and track fitting. The reconstruction step is then followed by a selection step in which tracks are selected based on certain selection criteria such as momentum, number of hits on a track, track χ^2, *etc.* Subsequently, from the selected tracks, the necessary information to calculate the first and second order derivative of the ensemble χ^2 with respect to the alignment parameters $\vec{\alpha}$ (Eq. 4.16) is accumulated. These steps are repeated for each event in the calibration sample. Once all events have been processed, the solution to Eq. 4.16, *i.e.* the alignment parameters, is determined. If the alignment parameters satisfy some convergence condition, they are stored in the LHC*b* conditions database. Otherwise, the detector elements are updated with the new alignment parameters and the above steps are repeated until the alignment parameters have converged.

In this study the IT boxes and OT C-frames are aligned for two cases. In the first case the particle trajectories are reconstructed taking material effects into account in the alignment procedure. In the second case these material effects are not taken into account in the alignment procedure. To ensure that the initial conditions in the first iteration are identical for both cases, *i.e.* to eliminate pattern recognition and selection effects, an additional step, for reasons given below, is introduced after the track selection step in which the selected tracks are refitted, see Fig. 4.5. In the first case the selected tracks are refitted using the same settings as in the default LHC*b* reconstruction procedure and in the second case the selected tracks are refitted without any additional material corrections.

4.5.3 Track sample and selection

For this study a sample of $10\,$k inclusive $J/\psi \to \mu^+\mu^-$ events, that were generated using the ideal LHC*b* detector geometry, is used. Although the ideal geometry was used to generate these events, mis-alignments can be simulated by reconstructing the particles using a different database from the one used in the generation of these events. Effectively, one displaces the simulated hits in the detector elements with the alignment offsets listed in Tab. 4.1 and Tab. 4.2 for the OT C-frames and IT boxes, respectively. Ultimately, these alignment offsets should converge back to their ideal values in the alignment procedure, which in the ideal case is zero.

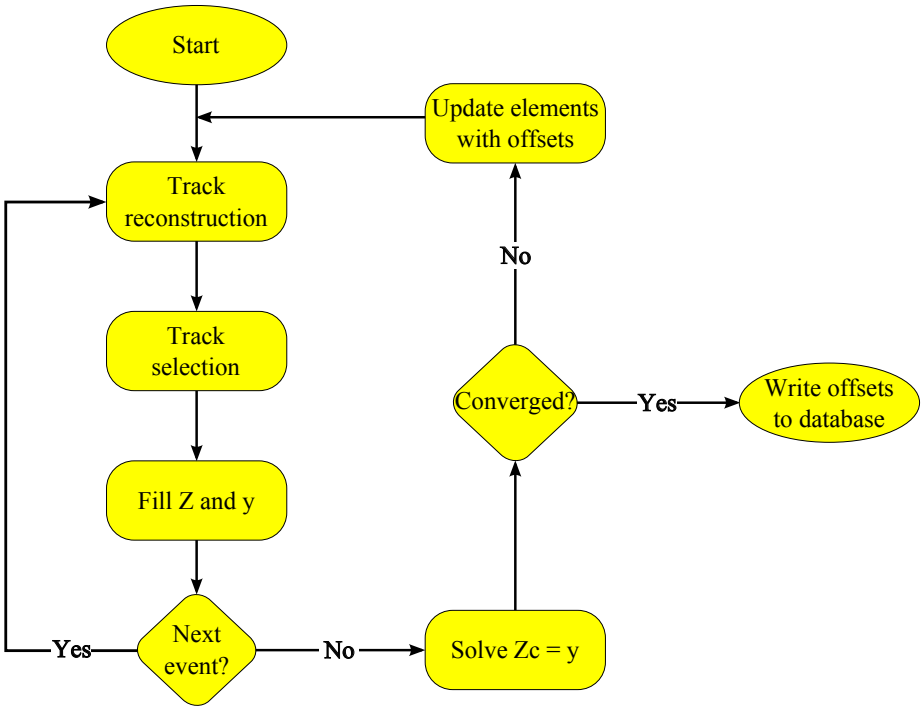

Fig. 4.4: *Flowchart of a typical alignment procedure.*

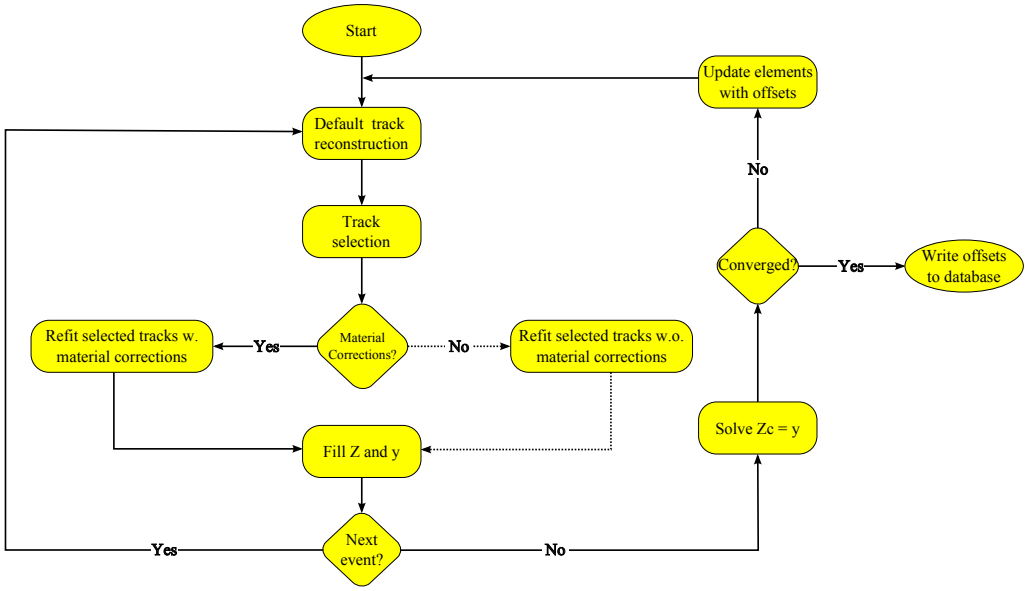

Fig. 4.5: *Flowchart of an alignment procedure to study the effects of multiple scattering.*

The tracks used in this study are tracks that traverse the entire LHCb detector, so-called long tracks. These tracks are formed by matching segments in the VELO to segments in the T-stations and have the advantage, assuming that the VELO is aligned, that the global movements of the IT boxes and OT C-frames are implicitly constrained by the VELO.

Two typical quantities that are used to gauge the quality of a long track are the long track χ^2 and match χ^2. The former is a gauge for the fit quality of the long track, while the latter is a gauge for how well a segment in the T-stations matches with a segment in the VELO at some z. The distributions of the long track χ^2 and the match χ^2 for the ideal and unaligned scenario, each reconstructed for a case where material effects are taken into account and a case where these effects are not taken into account, are shown in Fig. 4.6a and Fig. 4.6b, respectively. It is clear, compared to the ideal scenario, that mis-alignments lead to a poor average χ^2, *i.e.* a shift in the peak and broadening of the distribution. Furthermore, it is clear that the exclusion of material effects in the reconstruction procedure leads to a broader χ^2 distribution and, comparing the tails of the ideal and unaligned scenario χ^2 distributions, to more candidates with a poor χ^2.

Interestingly, see Fig. 4.6c and Fig. 4.6d, long tracks that traverse only the IT ($\approx 15\%$), with a hit resolution of $60\,\mu\mathrm{m}$, are less affected by material effects compared to long tracks that traverse only the OT ($\approx 75\%$), with a hit resolution of $200\,\mu\mathrm{m}$. This is due to the fact that particles that traverse only the IT have on average a higher momentum compared to particles that traverse the OT, approximately $26\,\mathrm{GeV}$ in the IT versus approximately $8\,\mathrm{GeV}$ in the OT. The remainder of the long tracks that traverse both the IT and OT ($\approx 10\%$) have on average a momentum of approximately $14\,\mathrm{GeV}$.

From Fig. 4.6a and Fig. 4.6b it is clear that the long track χ^2 and match χ^2 are not ideal quantities to cut on the in the alignment procedure in the case that material effects are excluded in the reconstruction procedure, compared to the case that these are included. Therefore, to ensure that the initial conditions, specifically the size of the track sample, are the same for both studies and to allow for the ability to apply a unified track selection, the events are first reconstructed with the default LHCb reconstruction procedure and, subsequently, good tracks are selected. The selected tracks are then refitted, depending on the case, either with multiple scattering taken into account or without multiple scattering taken into account, as illustrated in Fig. 4.5.

A track is considered a good candidate if it has a track $\chi^2/d.o.f. < 20$ and a match $\chi^2/d.o.f. < 20$. In addition, the tracks are required to have a momentum of at least $5\,\mathrm{GeV}$. This cut ensures that the long tracks traverse, on average, all three T-stations. Note that due to the momentum cut, a particle that traverses the OT is less affected by multiple scattering.

4.5.4 Weak mode: xz-shearing

Although the VELO and TT implicitly constraint the global movements of the IT and OT there is still a remaining weak mode, namely a shearing in the xz-plane. This weak mode is a consequence of the fact that the momentum fit is under-constrained in the alignment procedure as illustrated in Fig. 4.7.

Although a shearing in the xz-plane leaves the track χ^2 invariant, it does, however, introduce a bias in the momentum resolution for negative and positive charged particles, respectively, and ultimately in the reconstructed mass of, *e.g.* the J/ψ. One can show, in the limit $\mathrm{p}_{\mu^\pm} \gg \mathrm{M}_\mu$, that the biased invariant di-muon mass, $\mathrm{M}'_{\mu^+\mu^-}$, is approximately given by [41]:

$$\mathrm{M}'_{\mu^+\mu^-} = \left[1 + \frac{\left(\mathrm{p}'_{\mu^+} - \mathrm{p}'_{\mu^-}\right)\Delta\omega}{2}\right]\mathrm{M}_{\mu^+\mu^-}\,, \tag{4.62}$$

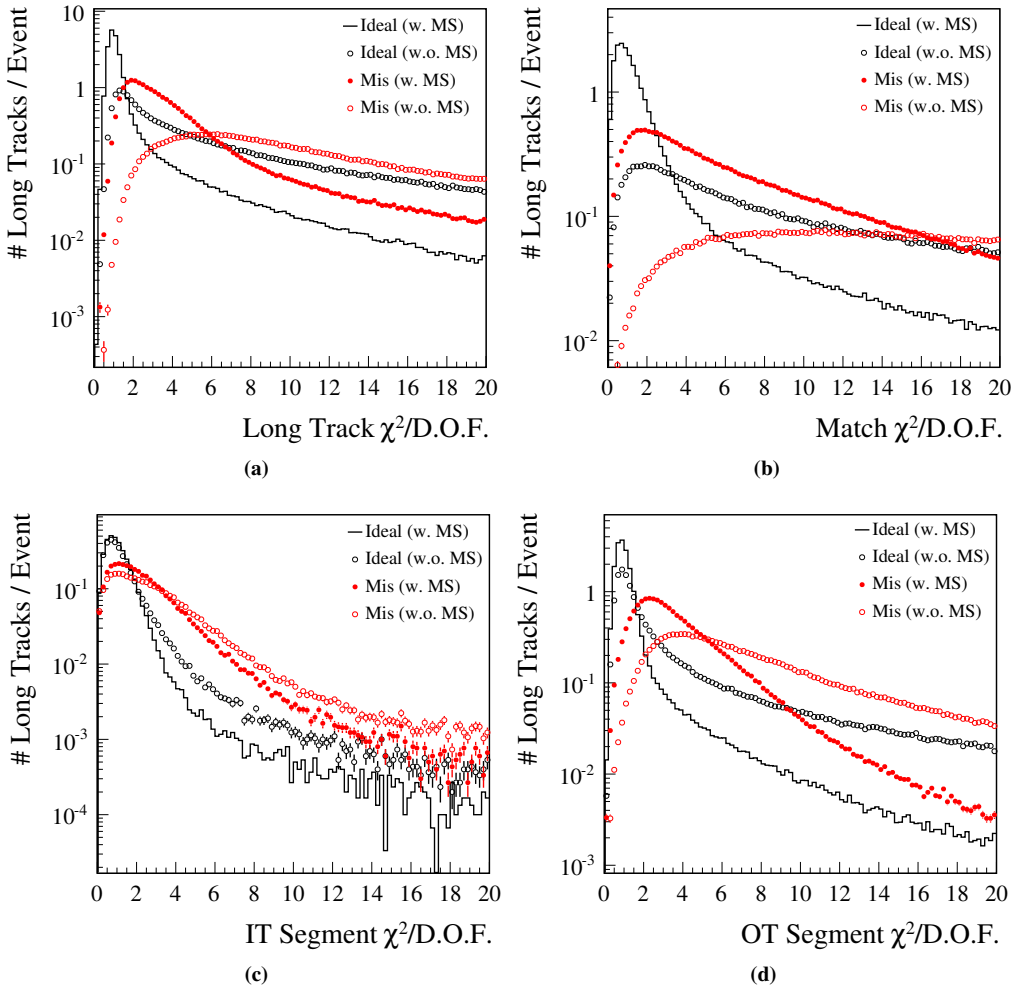

Fig. 4.6: *Distributions of (a) the long track χ^2 and (b) the corresponding matching χ^2 for ideal tracks (reconstructed with and without material corrections) and unaligned tracks (reconstructed with and without material corrections). The χ^2 distributions of IT and OT segments of long tracks are given in (c) and (d), respectively.*

where, $\Delta\omega$ is the curvature bias and $p'_{\mu^\pm} = \pm 1/\omega$, with $\omega = \omega_0 + \Delta\omega$. In other words, the biased di-muon mass is proportional to the difference in the reconstructed momenta of the positive and negative muons. As can be seen in Fig. 4.8a and Fig. 4.8b, the xz-shearing leaves the track χ^2 distribution invariant, while it has a clear effect on the di-muon mass. For further details on weak modes, such as z-scaling and magnetic field scaling, and their effects on $J/\psi \to \mu^+\mu^-$ and $B^0_d \to \pi^+\pi^-$ see [41].

To constrain this weak mode, the combined average translation of T3XU A-side and T3XU C-side is constrained to zero. This is accomplished by setting Δx of T3XU A-side opposite and equal to Δx of T3XU C-side, *i.e.* the combination T3XU A-side and T3XU C-side is required to be centred about the beam pipe. In practice this shearing can be isolated by studying the di-muon

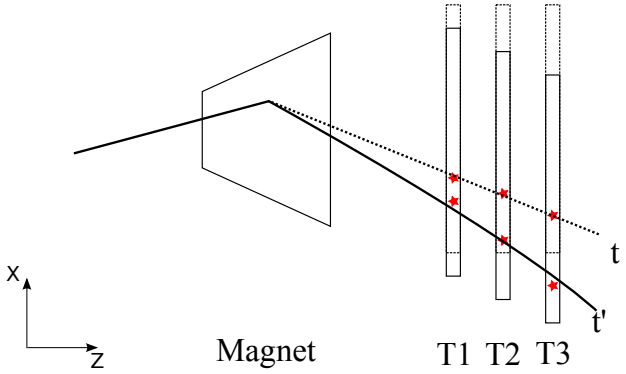

Fig. 4.7: *Two configurations of the T stations that leaves the track χ^2 invariant for the same set of hits (stars): A configuration close to the ideal geometry (dashed lines) and a shearing in the xz-plane (solid lines). Note, however, that the tracks, t (ideal) and t' (shearing), have different curvatures, i.e. momenta.*

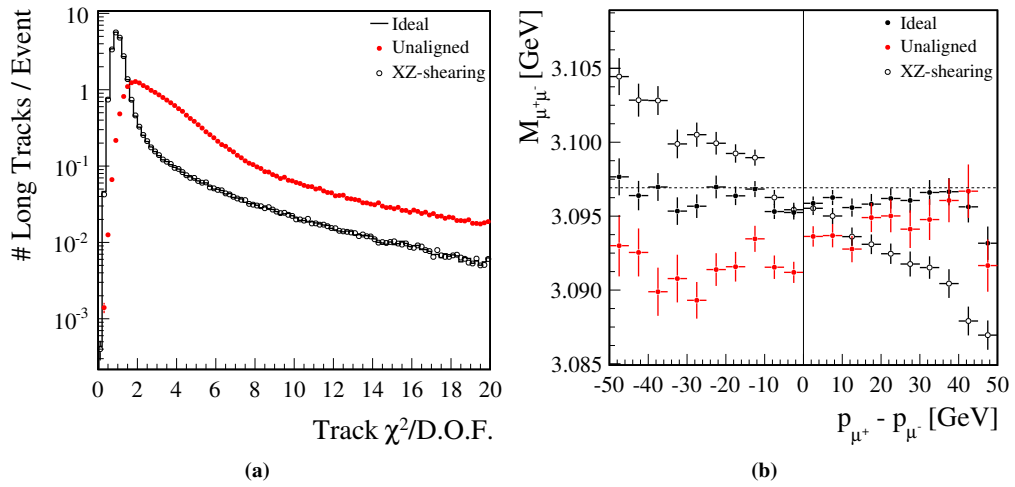

Fig. 4.8: *Distributions of (a) the long track χ^2 and (b) $\mu^+\mu^-$ momentum difference versus the di-muon mass for ideal, xz-shearing and random mis-alignments in x.*

mass as function of the momentum difference between the positive and negative muons as is discussed above.

4.5.5 Convergence

The evolution, as function of iteration, of various parameters that are used to gauge the convergence of the alignment procedure is shown in Fig. 4.9. These parameters are the residual mis-alignment in x, Δx, the change in the alignment χ^2 per degree of freedom (Eq. 4.18), the number of tracks and the average track χ^2 per degree of freedom defined as:

$$\langle \chi^2 \rangle = \frac{1}{N} \sum_{n=1}^{N} \chi^2_n, \tag{4.63}$$

where N is the number of tracks in the sample and χ^2_n the $\chi^2/d.o.f.$ contribution of track n. From these the following conclusions can be drawn:

- The residual mis-alignments in x as function of iteration are shown for two of the 24 detector elements for the two cases in which the selected tracks used for alignment are refitted with and without material correction, respectively. Note that the the vertical scale is magnified around zero, which corresponds to the ideal case. Consequently, the first two iterations are not visible. From Fig. 4.9a one observes that the residual mis-alignments approaches zero (*i.e.* ideal), and is stable after the eight iteration. Any subsequent corrections are of the order of a few microns, and up to $14\,\mu\mathrm{m}$ for the case in which multiple scattering effects are ignored. This convergence is also confirmed in the change in the alignment χ^2 per degree of freedom, see Fig. 4.9b. Starting from the eight iteration onwards, any subsequent corrections are statistically insignificant, *i.e.* the change in the alignment χ^2 is less then one.
- An alignment procedure in which multiple scattering is taken into account converges just as fast as an alignment procedure without multiple scattering taken into account. However, in the latter case the errors on the alignment parameters are underestimated for the given track sample, whereas in the former case the parameters are consistent with zero (see below).
- As the residual mis-alignments approach their ideal values so do the number of selected tracks, see Fig. 4.9c. Initially the pattern recognition, which is tuned on the ideal geometry, finds around $97\,\mathrm{k}$ track candidates for the OT C-frames and IT boxes mis-alignment scenarios listed in Tab. 4.1 and Tab. 4.2, respectively. As the detector elements approach their ideal values the pattern recognition finds more track candidates, and after the fifth iteration the number of tracks in the sample, around $123\,\mathrm{k}$, is stable and compatible with the ideal case.
- Similarly, the average track $\chi^2/d.o.f.$ of the selected tracks that are refitted and used in the alignment procedure, see Fig. 4.9d, improves per iteration and is stable and compatible with the ideal after the fifth iteration. This is due to the fact that the residual mis-alignments are well within the hit resolution for the IT boxes and OT C-frames from the fifth iteration onwards. Note that in the case multiple scattering is not taken into account in the track fit, the track $\chi^2/d.o.f.$ distribution is smeared compared to the case where it is taken into account in the track fit, see Fig. 4.6a.
- One observes from the change in the alignment $\chi^2/d.o.f.$ and the change in the number of tracks per iteration that, once the track sample is statistically stable, at most three iterations are required for the system to converge. Or in other words, the convergence depends on the pattern recognition, which in turn is affected by the size of the initial mis-alignments.

To summarise, an alignment procedure with multiple scattering taken into account converges just as fast as an alignment procedure without multiple scattering taken into account. Nonetheless, in the latter case, as will be shown below, the errors on the alignment parameters are underestimated, while in the former case the alignment parameters are consistent with zero. Ultimately, both procedures lead to an increase in the number of tracks and in an improvement in the average track χ^2. Furthermore, once the procedures have converged, the number of tracks and track χ^2 are compatible with the ideal case.

4.5.6 Residual Δx mis-alignments

The residual Δx mis-alignments for the IT boxes and OT C-frames that remain once the system has converged are shown in Fig. 4.10a for an alignment procedure with multiple scattering taken into account and an alignment procedure without multiple scattering taken into account. Their corresponding significance with respect to the ideal case is shown in Fig. 4.10b.

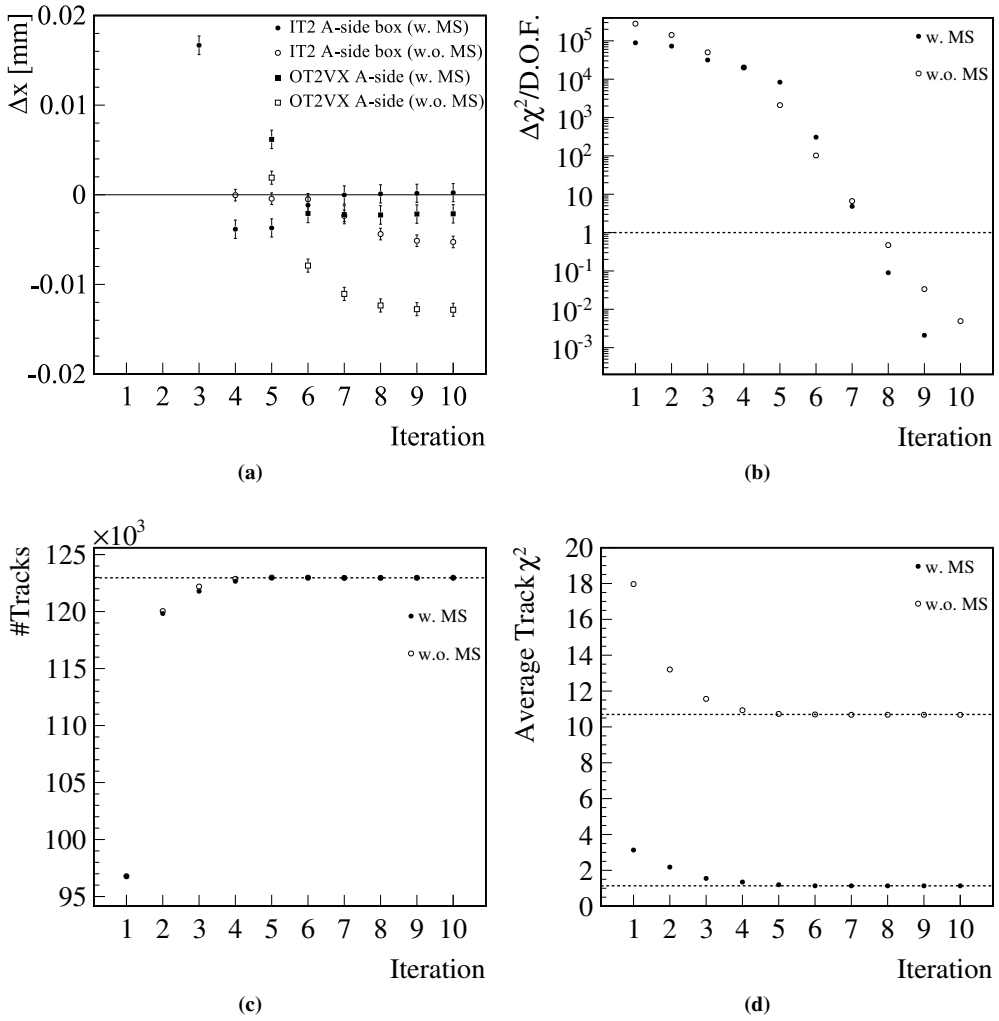

Fig. 4.9: *Evolution, as function of iteration, of (a) Δx, (b) $\Delta\chi^2$, (c) number of tracks and (d) $\langle\chi^2\rangle$ for two cases in which the IT boxes and OT C-frames are aligned with multiple scattering taken into account (dots) and without multiple scattering taken into account (circles), respectively. The dashed lines indicate the ideal values for the two cases.*

In both cases the residual mis-alignments are, in general, well below the hit resolution. In the case where multiple scattering is taken into account in the alignment procedure the residual Δx mis-alignments are all within 3σ from zero, except for the C-frames of the OT station T3, and are therefore considered compatible with ideal. In the case of the C-frames of T3 the errors are clearly underestimated. This is a consequence of the fact that the average of the weighted averages of the alignment parameters of T3XU-A and T3XU-C is required to be zero to constrain the xz-shearing of the T-stations, see Sec. 4.1.3. In addition, the movements of the last two elements, T3XU-A and T3XU-C, are strongly correlated to the movements of the second-to-last elements, T3XU-A and T3XU-C.

However, in the case where multiple scattering is not taken into account in the alignment

procedure, ignoring the last four detector elements, the parameters are $5 - 20\sigma$ from zero indicating that the errors on the parameters are underestimated. Interestingly, the parameters of the OT C-frames follow a similar pattern with increasing z as in the case where multiple scattering is taken into account. The difference between the OT parameters for the two cases is likely due to low momentum tracks that have hits in the IT and OT. Though the effects of multiple scattering in the OT, with a hit resolution of $200\,\mu\mathrm{m}$, is less significant for $5\,\mathrm{GeV}$ tracks, this is not the case for the IT, with a hit resolution of $60\,\mu\mathrm{m}$.

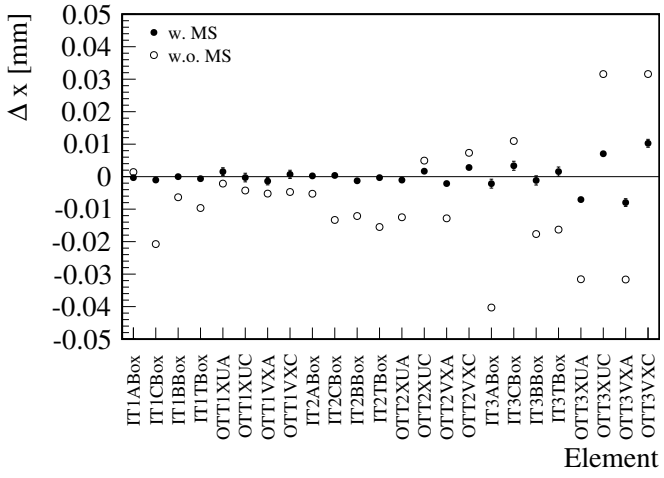

(a)

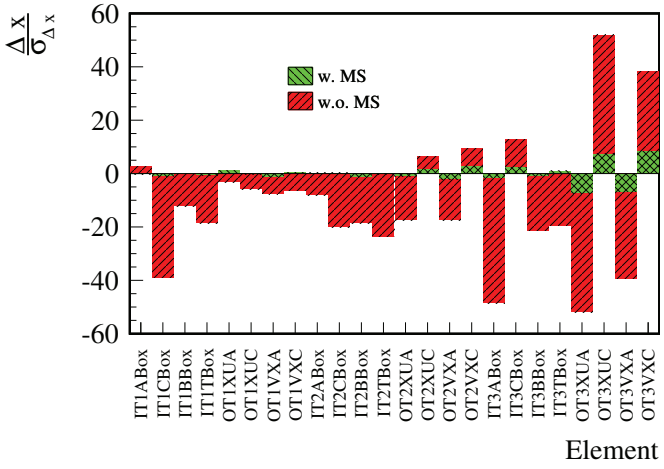

(b)

Fig. 4.10: *(a) Residual Δx mis-alignments for the IT boxes and OT C-frames after the alignment has converged and (b) their corresponding significance with respect to ideal. The statistical errors on the parameters are approximately $1\,\mu\mathrm{m}$. The elements on the x-axis are arranged according to their z-coordinate. Note that the A-side and C-side elements actually have the same z-coordinate.*

4.5.7 Track χ^2 and reconstructed J/ψ mass

Above it is shown that both alignment procedures converge within eight iterations and that the residual Δx mis-alignment are well within the hit resolution. The final test, however, is to study the effects of the obtained alignment parameters on the default LHCb reconstruction procedure. Specifically, to ascertain whether the obtained alignment parameters fully recovers the ideal track χ^2 distribution and the ideal di-muon mass.

For this test inclusive $J/\psi \rightarrow \mu^+\mu^-$ MC events are reconstructed for four different cases, respectively. Each case corresponds to running the default LHCb reconstruction procedure using a different database. The four cases are ideal, unaligned, aligned with material effects taken into account and aligned without material effects taken into account. For the ideal case the default LHCb database is used and for the unaligned case a database containing the Δx offsets listed in Tab. 4.1 and Tab. 4.2 for the OT C-frames and IT boxes, respectively, is used. Similarly for the latter two cases, the databases containing the residual Δx parameters, see Fig. 4.10, obtained from the alignment procedure in which multiple scattering is taken into account and the alignment procedure in which multiple scattering is not taken into account are used, respectively.

Comparing the long track χ^2 distributions, see Fig. 4.11a, it is clear that the ideal long track χ^2 distribution is recovered by both alignment procedures. Although the alignment offsets in the case where multiple scattering effects are excluded in the alignment procedure, are larger, they are still well within the hit resolution of the IT and OT. Note, however, that it is possible that these offsets are masked by the multiple scattering corrections applied in the default track fit.

Judging from the $\mu^+\mu^-$ momentum difference versus the di-muon mass, see Fig. 4.11b, there is no visible shearing in the xz-plane as expected, since this mode is constrained in the alignment procedure. In addition, the distributions of both the aligned cases are compatible with the ideal case and the di-muon mass spectrum is also fully recovered, see Fig. 4.11c.

4.6 Conclusion

This chapter described a global alignment procedure using Kalman filter fitted tracks. Since the Kalman filter fit is the default LHCb fit for tracks that traverse the entire detector or a specific region of the detector, this method is capable of aligning the entire LHCb detector. In other words, all sub-detectors that have hits on a track can be aligned. An additional advantage is that the LHCb alignment framework uses the same track model and track fit as the reconstruction procedure. This means that material effects and the magnetic field values are consistently taken into account with respect to the reconstruction procedure.

To illustrate the above, two sub-detectors of different detection technology and with different hit resolutions, namely the IT boxes and OT C-frames, are mis-aligned along their primary measurement direction and aligned simultaneously for two different cases (using a unified track selection). In the first case these sub-detectors are aligned taking material corrections into account and in the second case these corrections are excluded. It is then shown that both procedures converge equally fast, at most eight iterations are required, and that the ideal number of tracks and ideal average track $\chi^2/d.o.f.$ is recovered. However, in an alignment procedure in which material effects are excluded, the errors on the alignment parameters are underestimated.

Nonetheless, it is shown that the alignment offsets obtained from both procedures yield a track χ^2 and di-muon mass distribution that is compatible with ideal. Although the tracks are refitted using a different track model in the latter case, the alignment offsets are well within the hit resolution. However, it is possible that in this case the residual offsets are masked by the multiple scattering corrections applied in the default LHCb reconstruction procedure.

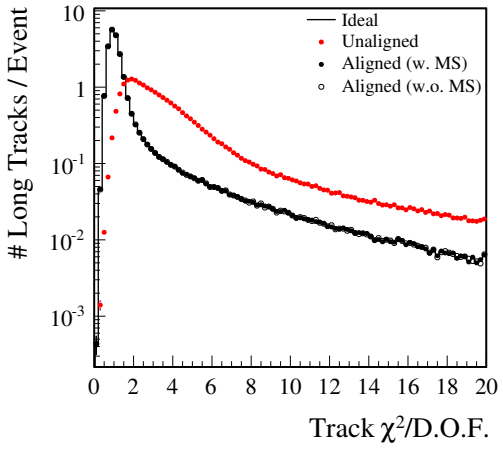

(a)

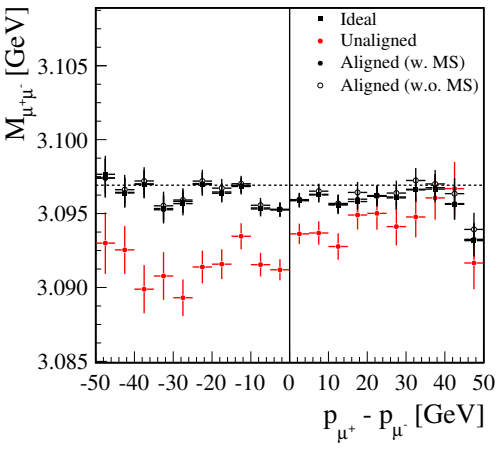

(b)

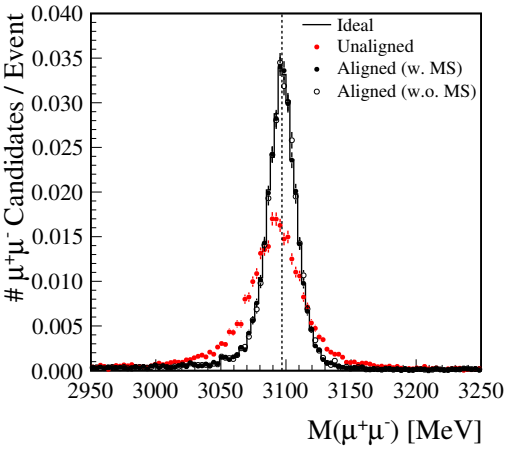

(c)

Case	$M_{\mu^+\mu^-}$ [MeV]	$\sigma_{M_{\mu^+\mu^-}}$ [MeV]
Ideal	3096.56 ± 0.13	12.20 ± 0.12
Unaligned	3092.39 ± 0.26	20.49 ± 0.26
Aligned (w. MS)	3096.62 ± 0.13	12.19 ± 0.12
Aligned (w.o. MS)	3096.93 ± 0.13	12.24 ± 0.13

Fig. 4.11: *Distributions of (a) the long track χ^2, (b) $\mu^+\mu^-$ momentum difference versus the di-muon mass and (c) the di-muon mass for inclusive $J/\psi \to \mu^+\mu^-$ events reconstructed with four different databases, respectively: Ideal, Unaligned, Aligned with multiple scattering taken into account and aligned without multiple scattering taken into account. The di-mass mass and resolution in Fig. 4.11c are determined by fitting the data in the range $\left[M_{J/\psi} - 45\,\mathrm{MeV}, M_{J/\psi} + 45\,\mathrm{MeV}\right]$ to a Gaussian.*

Chapter 5

Alignment Of The OT With Cosmic Rays

In the absence of LHC collision data, comics rays are useful to commission the detector, *i.e.* to test, debug and calibrate the detector, as well as the reconstruction algorithms. Since the LHCb detector is a forward arm spectrometer its acceptance for cosmic rays, which are predominantly vertical, is relatively small compared to the multiple purpose detectors ATLAS and CMS, which have a 4π solid angle coverage. Nonetheless, during the summer of 2008 approximately a million of cosmic rays were observed in the LHCb detector. Part of these cosmic ray events were observed with the whole Outer Tracker (OT) being active and provide an excellent opportunity to test the alignment framework and to determine the alignment offsets ("deltas") to be used for first collision data.

This chapter presents the alignment determination of the OT using cosmic ray data taken in 2008. First, the observed cosmic ray rate and the detector response is presented in Sec. 5.1. This is then followed by a discussion on the properties of the reconstructed cosmic ray tracks in Sec. 5.2. The OT detector geometry as deduced from survey measurements, including some notable deviations from the nominal geometry, are presented in Sec. 5.3. Finally, an alignment procedure using cosmic rays for the OT C-frames and modules is presented and the results are compared to the survey measurements in Sec. 5.4.

5.1 Cosmic Ray Rate

The cosmic ray data used to align the OT are listed in Tab. 5.1. These events were taken during the 20^{th} and 21^{st} of September 2008. The active sub-detectors were the OT, Calorimeters and Muon stations (M2-M5). The cosmic rays were triggered by the calorimeter system, requiring a minimum ionising particle coincidence between the SPD and HCAL detectors.

Run	# Events	Rate [Hz]	# Cosmic in OT
34083	64898	3.69	5959
34117	89754	4.71	7377
34120	101010	4.70	8447

Tab. 5.1: *The cosmic ray commissioning data. The observed lower rate of cosmic rays in run* 34083 *is likely due to different threshold settings of the Calorimeter.*

The event rates listed in Tab. 5.1 are defined as the total number of triggered events divided by the time period for a given run. The corresponding rate of visible cosmic rays, *i.e.* the rate of events that contain one or more reconstructed cosmic ray tracks, in the OT is approximately 8% of the event rate. This is due to the acceptance of the OT and includes the pattern recognition requirements. The latter includes that a cosmic ray traverses all three T stations.

As mentioned above the observed rate of cosmic rays in the OT depends on the acceptance. The acceptance follows from the geometry requirement that a cosmic ray traverses the three OT stations as well as the calorimeter system. This can be translated into a maximal horizontal and vertical track slope limit. The maximal vertical and horizontal track slopes are determined by the active areas of the the OT stations and the SPD, and the distance between them. An OT station and the SPD have an active area of 6.0×4.9 and $7.6 \times 6.2\,\mathrm{m}^2$, respectively, and the first OT station, T1, is located $4.6\,\mathrm{m}$ from the SPD. Therefore, cosmic rays that traverse T1 and are triggered by the calorimeter can have slopes of up to $|t_y| \approx 1.2$ and $|t_x| \approx 1.5$ in the vertical plane and horizontal plane, respectively. Whereas for the third OT station, T3, positioned $3.1\,\mathrm{m}$ from the SPD, these are $|t_y| \approx 1.8$ and $|t_x| \approx 2.2$.

5.1.1 OT response

In the above it is assumed that there are no "holes", *i.e.* inactive modules or channels, in the detector. When there are holes in the detector, the acceptance effectively is smaller. The presence of such inefficient regions, as well as the identification of noisy channels, can be determined by measuring the hit occupancy $\mathcal{O}_c$ defined as:

$$\mathcal{O}_c = \frac{1}{Ns} \sum_{n=1}^{N} h_n, \tag{5.1}$$

where N is the number of calorimeter triggered events, s the number of straws in a group, *e.g* station, layer or module, and h_n the number of hits in the group for a given triggered event.

A sufficient granularity to identify noisy channels or problems in the readout electronics is a group of 32 channels, *i.e.* an OTIS. From the OTIS occupancy profile one can determine which OTISes contain noisy or dead channels, and subsequently which particular channel is noisy in a given OTIS. The occupancy versus OTIS ID is shown in Fig. 5.1 with the OTIS ID defined as:

$$\text{OTIS ID} = o + 4 \times ((m-1) + 9q + 36l + 144 \times (s-1)),$$

where $o = \{0, 1, 2, 3\}$ is the internal ID of an OTIS inside module m, and q, l and s are the quarter, layer and station IDs, respectively. In this definition the OTIS IDs run from the outermost modules to the innermost modules close to the beam pipe along the x-axis of the detector. One clearly sees that the occupancy in T3 is higher compared to T1. This is in agreement with the fact that T3 is closer to the SPD and, therefore, has a higher acceptance to detect cosmic rays triggered by the calorimeter system. The wave like structure of the OTIS occupancy band is due to an acceptance effect. The acceptance for cosmic rays increases as one goes along the x-axis from the outermost region to the innermost region, towards the beam pipe, of the detector. This results in a somewhat higher occupancy for OTISes close to the beam pipe compared to OTISes farther from the beam pipe.

There are also noticeable outliers. The points at zero indicate inactive OTISes, while the points above the occupancy band are OTISes containing noisy channels. There are approximately 12 noisy OTISes and the number of noisy channels with an occupancy greater than 0.04% is 69. Such channels are not used in the reconstruction of the cosmic rays. Some of these noisy channels can be traced back to known problematic channels that were discovered during quality control checks of the modules prior to installation [80]. An example of such a channel is channel 81 in module 3219 with an straw occupancy of approximately 13%. The quality control check of module 3219 revealed that this channel has a relative higher gain compared to the rest of the channels, see Fig. 5.2. The integrated hit-maps for the top and bottom halves of the detector are

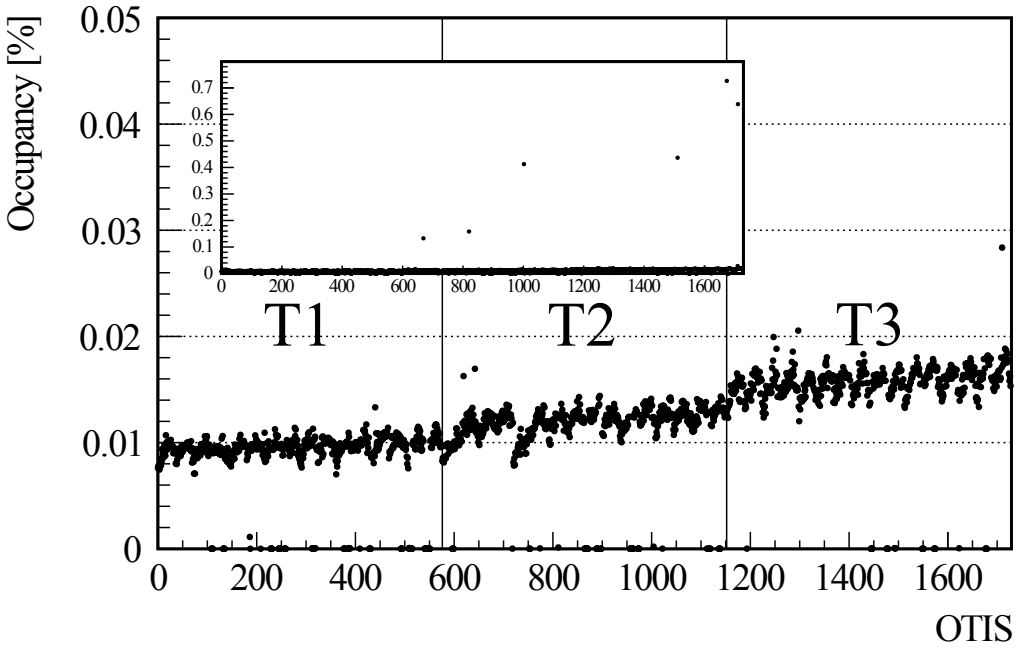

Fig. 5.1: *The occupancy vs OTIS ID, i.e. per group of* 32 *channels. The figure is a zoom in of the insert around the occupancy band. Note that in some cases a noisy OTIS contains a single active (noisy) channel.*

shown in Fig. 5.3a and Fig. 5.3b, respectively. Here the x coordinate vs the z coordinate of the centre of each hit channel is plotted. These clearly show that there are several whole modules and some OTISes missing.

5.2 Cosmic Ray Tracks

The reconstruction of cosmic ray events, similar to beam collision events, is a two step procedure which involves track finding and track fitting. This section gives an overview of the reconstruction of the cosmic ray tracks and their properties.

During the 2008 commissioning run the LHCb magnet was off. Consequently, the momenta of the particles cannot be determined and, therefore, the multiple scattering contribution to the track fit cannot be correctly modelled. A further complication is that, in contrast to beam collision events, cosmic rays can arrive anywhere within the $25\,\mathrm{ns}$ bunch clock timing. Since no precise external timing information is available for the traversing cosmic ray, the "event phase" needs to be extracted from the measured TDC times. At the time of writing the tools to extract the event phase were still in development. It was therefore decided not use the OT drift time measurements in this analysis. Consequently, it is assumed that OT hits have a zero drift distance with a corresponding binary hit resolution of $\sigma_{\mathrm{OT}} = \frac{4.9\,\mathrm{mm}}{\sqrt{12}} = 1.41\,\mathrm{mm}$, where $4.9\,\mathrm{mm}$ is the diameter of a straw tube.

5.2.1 Track finding

In the cosmic ray reconstruction a slightly modified version of the track finding algorithm PatSeeding [81] is used. The original algorithm has been optimised based on the assumption that particles originate from the nominal interaction point. Under this assumption it follows that particles that traverse the top of the first station are expected to traverse the top of the second and

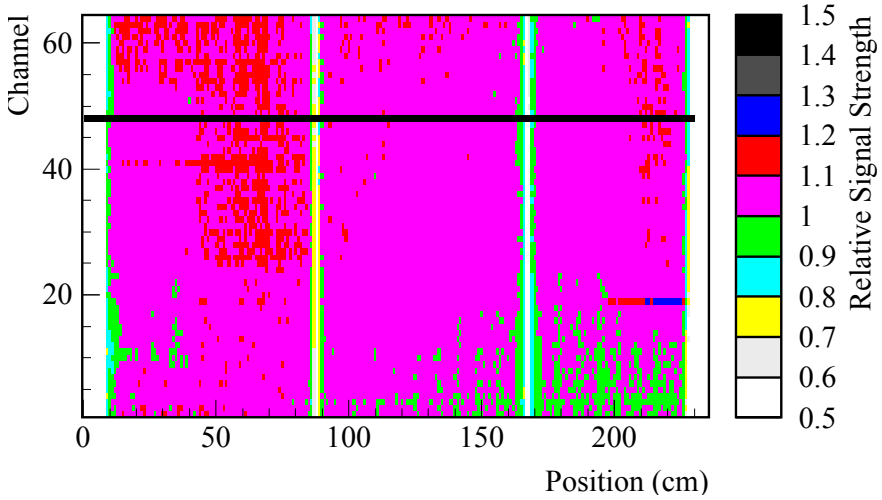

Fig. 5.2: *Radiation scan, i.e. the response of the straws to an ^{90}Sr source, of mono-layer B of module 3219 (S2L-085B) as determined prior to installation of the detector. Here the channels are numbered from $0 - 63$. The black horizontal line indicates that channel 48, which corresponds to channel 81 in the software numbering scheme, has a higher relative signal strength compared to other channels. The white vertical bands are the wire locators which keep the anode wire in place.*

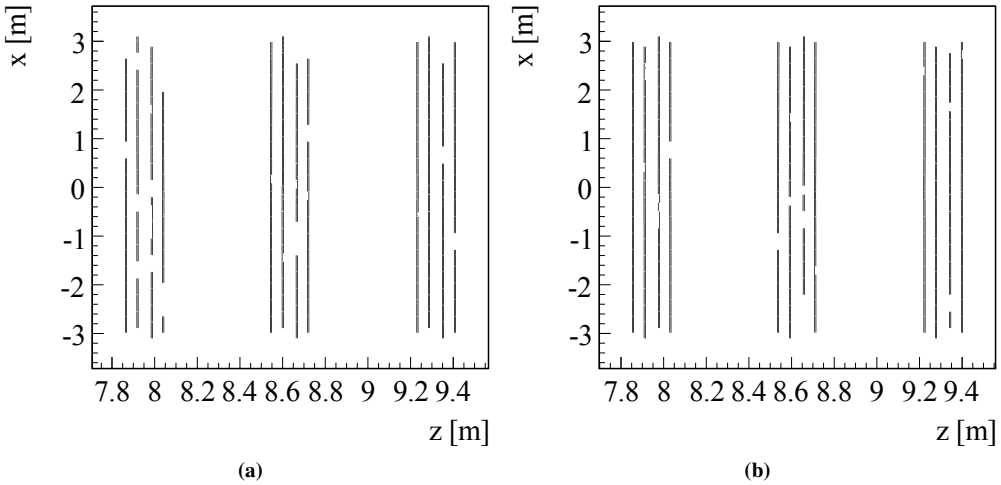

Fig. 5.3: *Hit-maps for (a) the top half and (b) bottom half of the detector.*

third station and *vice versa* for particles that traverse the bottom of the first station. Naturally this is not the case for cosmic rays, which originate anywhere from the sky. A cosmic ray that passes through the top of the first station can either pass through the bottom or top of the second and third station depending on its vertical slope. Nonetheless, by widening the search windows and removing the assumption that the particles originate from the interaction point cosmic ray candidates can be found. The procedure to identify cosmic ray candidates is as follows [81, 82]:

- First, a set of possible track candidates are identified by combining hits in the x-layers of the first tracking station T1 and and the last tracking station T3.
- Second, the possible candidates are further refined by searching for hits in the x-layers of T2 along the trajectory in the xz-plane that connects x-layer hits in T1 to x-layer hits in T3. Here only candidates containing the most number of x layer hits are considered as good candidates.
- Third, the track candidates from the previous step are further refined by searching for stereo hits within a window along the candidate trajectory. Here the candidate with the most number of stereo hits is considered a good candidate.

Once these track candidates have been found, they are fitted with a global least-squares method. The algorithm then returns a list of good track candidates which satisfies the requirements based on the number of hits, outliers and the track χ^2. In addition, it provides a seed state, *i.e.* a starting point to extrapolate from, for the LHCb Kalman track fit.

5.2.2 Track fitting

The track candidates provided by PatSeeding, according to the standard reconstruction procedure, are fitted with the LHCb Kalman track fit. Since there is no magnetic field the cosmic ray trajectory is assumed to be a straight line. This results, effectively, in the same parameters for the particle trajectory as determined in the pattern recognition.

5.2.3 Properties

The combined total number of reconstructed tracks over all runs is approximately $23\,\mathrm{k}$. As shown in Fig. 5.4a, most non-empty events contain a single reconstructed track and there are events that contain up to 16 reconstructed tracks. Nonetheless, the fraction of cosmic ray events with a track multiplicity grater than one is less than one percent.

The normalised track χ^2 of the reconstructed tracks is shown in Fig. 5.4b. As can be seen, the tracks have a pre-alignment $\chi^2/d.o.f.$ of approximately 1.4. This indicates that the C-frames are installed within a mm of their nominal positions. The tracks in the high multiplicity events have a relatively poor χ^2. These are likely busy cosmic showers, or a cosmic muon showering in the Calorimeter or Muon system, containing low momentum particles. Therefore, these high multiplicity events are not considered in the alignment procedure.

The average number of hits per track, shown in Fig. 5.4c, is approximately 20 and is in agreement with what one expects. The number of hits per track depends on a number of factors such as the horizontal slope of the track and the cosmic track properties required in the pattern recognition. For particles perpendicularly incident on the OT the number of hits, due to the staggering of the mono-layers and assuming that all modules are active and efficient, can vary from 12 to 24.

The hit multiplicity per mono-layer is shown in Fig. 5.4d. Note that the stereo mono-layers typically have more hits compared to the x mono-layers. This is due to a difference in the search window size for x and stereo hits in the pattern recognition. In the case of stereo hits, a more conservative window size is used to find the the hits in the stereo layers that belong to a track.

Types

The tracks can be categorised, as shown in Fig. 5.5a, into *crossing* and *side* tracks in the horizontal plane, and *forward* and *backward* tracks in the vertical plane.

Crossing tracks are tracks that have hits in both the C-side and A-side of the detector. While *side* tracks have hits in only one of the sides. These can be categorised as A-side tracks and C-side tracks. For alignment, the *crossing* tracks can be used to align detector elements in both

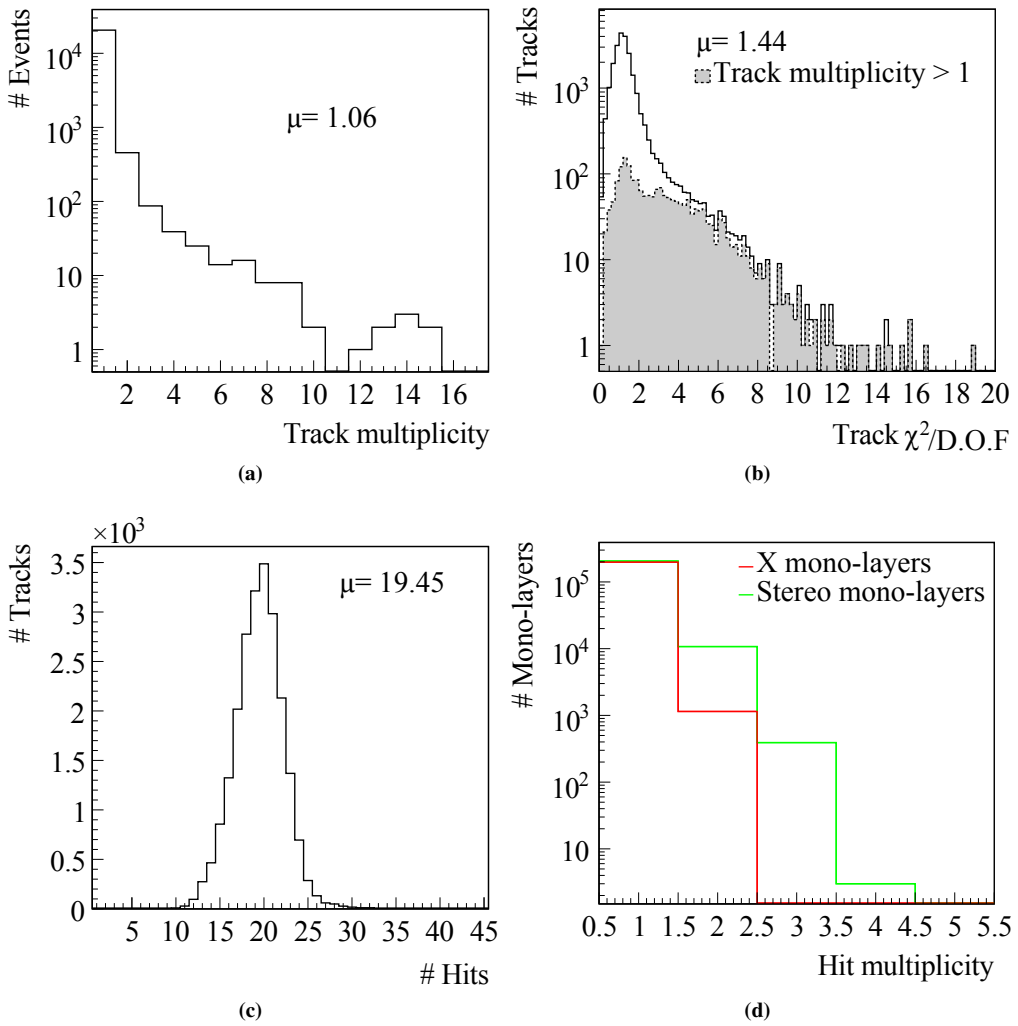

Fig. 5.4: *Cosmic ray track properties: (a) shows the track multiplicity per event. (b) shows the track χ^2 distribution. (c) shows the number of hits per track. (d) shows the hit multiplicity per mono-layer.*

sides with respect to each other. The *side* tracks can be used to align detector elements within a side with respect to each other.

The *crossing* and *side* tracks can be further categorised into *forward* and *backward* tracks. *Forward* tracks are tracks that go downstream from the OT to the calorimeter system and muon stations, while *backward* tracks go in the opposite direction. Since cosmic rays originate from the sky, the *forward* and *backward* tracks have slopes $t_y \equiv dy/dz < 0$ and $t_y \equiv dy/dz > 0$, respectively.

As explained in Sec. 5.1 cosmic rays that traverse the OT and are triggered by the Calorimeter system can have slopes of up to $|t_y| \approx 1.2$ and $|t_x| \approx 1.5$ in the vertical plane and horizontal plane, respectively. The slope distributions for *side* and *crossing* crossing tracks are shown in

Fig. 5.5b. The observed asymmetry, see Fig. 5.5b, is likely due to dead modules. The asymmetry in the t_x slopes due to the geometry of a station, *i.e.* A-side is half a module wider compared to C-side (see Sec. 3.1.2), is negligible. Of the 23 k tracks, there are approximately even fractions of

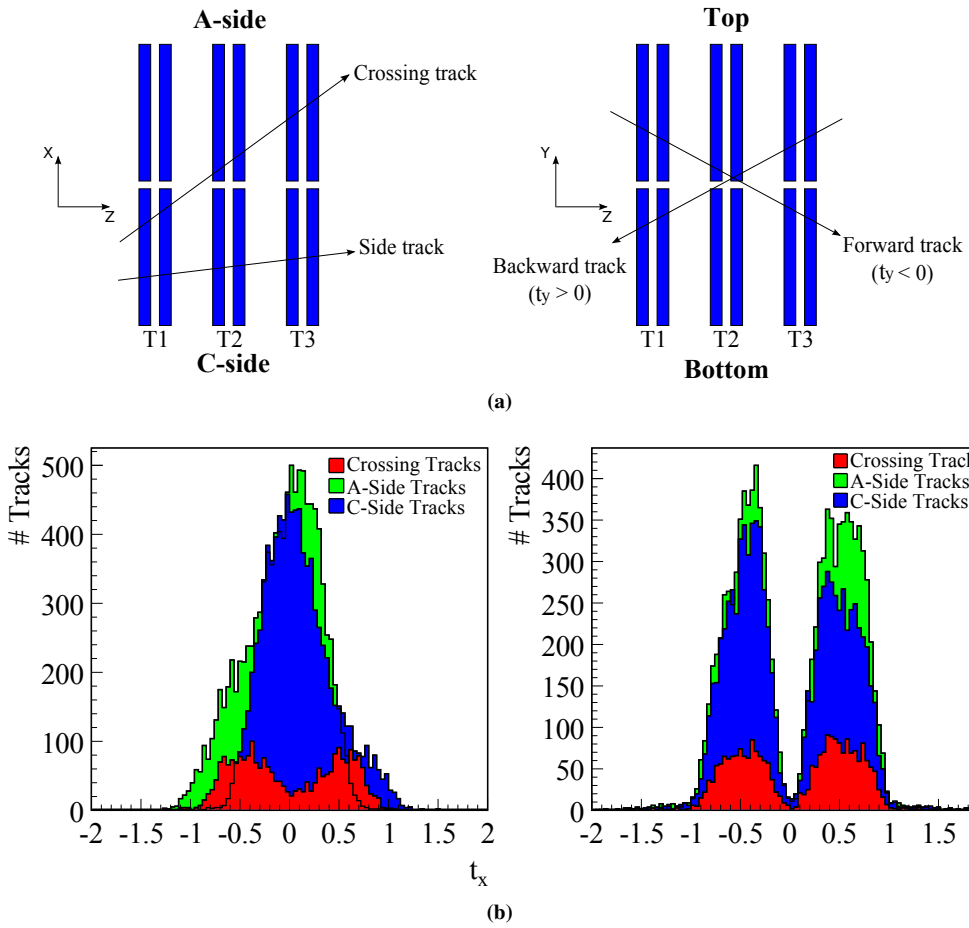

Fig. 5.5: *The cosmic track types (a) and their slopes (b) in the horizontal* (t_x) *and vertical plane* (t_y)*. Each rectangle in the horizontal plane represents a C-frame (one* x *and one stereo layer). In the vertical plane the rectangles represent the top and bottom halves of each C-frame.*

forward and *backward* tracks. This suggests that there are no apparent artefacts in the calorimeter system that can introduce an asymmetry in the trigger for forward or backward cosmic rays. The fractions of A-side, C-side and *crossing* tracks are approximately 0.5, 0.4 and 0.1, respectively.

5.3 OT Survey

An overview of the OT geometry and the corresponding description in the LHC*b* software framework is given in Chapter 3. The description is based on the OT engineering drawings, but some simplifications are introduced to speed up the simulation and reconstruction procedures. The OT geometry description contains materials that lie inside the LHC*b* acceptance, including the aluminium support structures (C-frames) onto which the OT modules are mounted. However, it does

not contain the common IT and OT support structure for the C-frames, because it is considered to lie sufficiently far outside the acceptance as to have a negligible impact on reconstruction and physics performance. Nonetheless, the positions of the OT stations, layers and modules are determined by the common IT and OT support structure and C-frames. In what follows a summary of the OT survey results are presented. The numbers presented here correspond to the detector frame discussed in Sec. 3.1.2.

A drawing of the common support structure for the IT and OT is shown in Fig. 5.6. The main components are the Bridge (top) and the Table (bottom) which determine the IT and OT nominal positions. All C-frames hang vertically from the Bridge rails. Therefore, the y-coordinates of the OT C-frames are essentially determined by the Bridge rails. The z-coordinates of the C-frames are determined at the top by the Bridge rails and at the bottom by the Table rails. In addition, the design of the common IT and OT support is such that the tracking stations can be retracted along the x-axis for maintenance.

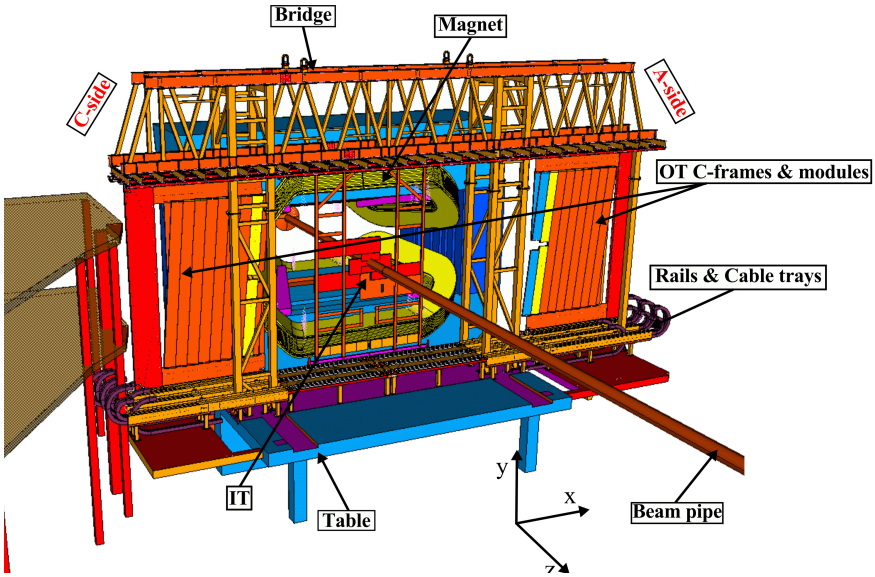

Fig. 5.6: *Drawing of the IT and OT tracking stations and their support structure. Note that only the first IT station and the first two OT C-frames, T1XU-A and T1XU-C, in their open position are shown.*

Located at the four corners of each C-frame are adjustable mechanisms that determine the C-frame position. Threaded rods located at the two top corners of each C-frame allow to adjust the height, *i.e.* the y-coordinate, of a C-frame. The z-coordinate of a C-frame can be adjusted by means of alignment trolleys located at the four corners of each C-frame. The x-coordinates of the C-frames are determined by locks located on the Bridge rails at $x = 0$.

The nominal module coordinates, based on the OT engineering drawings, are listed in Tab. 3.4 and Tab. 3.5. These are determined by the C-frame survey and adjustment, and the module mount points on the C-frame. The survey of the OT involved, in a first step, determining the flatness and straightness of the Bridge and Table rails. These were surveyed extensively during and after installation. The survey of the Bridge and Table revealed that they were level and that the rails were straight and flat within the allowed tolerances of a few millimetres over the full width and length of the Bridge and Table. Once the Bridge and Table were installed and surveyed, the C-frames

were pre-assembled with all straw tube modules and finally hung onto the bridge. Subsequently, in a second step, all 3D coordinates of the module mount points were surveyed. Starting from these, the C-frame positions were adjusted with the mechanisms previously discussed. The goal of this procedure was to iterate until all module mount points were within $\pm 1\,\mathrm{mm}$ from their nominal values. The final survey coordinates provide the corrections to the nominal coordinates of the C-frames and modules.

In what follows, the remaining deviations of the module and C-frame coordinates from their nominal values are presented. The average C-frame deltas will later be used in the comparison with the deltas obtained from the cosmic ray alignment procedure.

Surveyed deviations from nominal

The survey of the OT modules revealed that the x-modules on all C-frames were not hanging vertically, but were slightly rotated about the z-axis. This was traced back to a slight deformation in the shape of the C-frames, namely the vertical arms were not exactly perpendicular to the horizontal arms. Naturally, this also affected the corresponding stereo modules which resulted in a stereo angle different from the design stereo angle of $\phi_s = -5^\circ$ and $\phi_s = +5^\circ$ for u and v, respectively. To correct for this deformation and to ensure that the x-coordinates of the modules, which is also the primary measurement coordinate, correspond to the nominal x-coordinates, the outer threaded rod of each C-frame was lowered in y, such as to introduce a small rotation of the C-frames to compensate for this deformation, as shown in Fig. 5.7. Consequently, the x-coordinates and the stereo angles of the modules are close to nominal (within the survey error of $500\,\mu\mathrm{m}$) but the centres of the modules no longer lie in the same horizontal plane as defined by the engineering drawings. The Δy of the first and last module mount point in a C-frame are listed in Tab. 5.2. The corresponding Δy for the rest of the mount points can be derived from Tab. 5.2 combined with Eq. 3.2 and Tab. 3.5.

Due to external mechanical constraints the nominal z-coordinates of some C-frames had to be re-defined. Consequently, some C-frames are up to a few millimetres closer to the magnet than originally intended. These changes to the nominal z-coordinates are listed in Tab. 5.3.

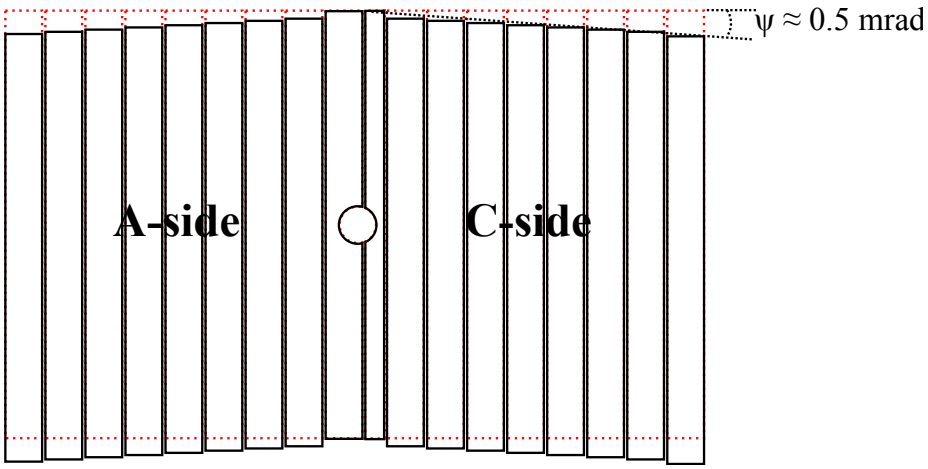

Fig. 5.7: *The resulting, exaggerated, deformation of the internal geometry of the modules in a A-side and C-side C-frame. The dashed volumes indicate the intended design geometry of the module assembly in a C-frame. The actual geometry (continuous lines) leaves the modules hanging vertically, but no longer at their nominal y-coordinates.*

C-frame	$\Delta y_1\,[\mathrm{mm}]$	$\Delta y_9\,[\mathrm{mm}]$	$\Delta y_{9-1}\,[\mathrm{mm}]$	$\psi\,[\times 10^{-3}\,\mathrm{mrad}]$
T1XU-A	-0.5	0.6	1.1	-0.4
T1VX-A	-1.3	0.0	1.3	-0.5
T2XU-A	-0.5	0.6	1.1	-0.4
T2VX-A	-1.7	0.0	1.7	-0.6
T3XU-A	-2.0	-0.5	1.5	-0.5
T3VX-A	-1.8	-0.8	1.0	-0.4
T1XU-C	-0.6	0.5	1.1	-0.4
T1VX-C	-2.0	-1.0	1.0	-0.4
T2XU-C	-1.4	0.0	1.4	-0.5
T2VX-C	-2.4	-1.0	1.4	-0.6
T3XU-C	-1.5	-0.5	1.0	-0.4
T3VX-C	-2.2	-1.2	1.0	-0.4

Tab. 5.2: *Δy for the first and last module mount points and the corresponding rotation $\psi = \frac{\Delta y_{9-1}}{\Delta x_{9-1}}$ in the xy-plane. $\Delta x_{9-1} = x_9 - x_1$ is the difference between the x-coordinates of the first and last mount point and is $\Delta x_{9-1} = -2730\,\mathrm{mm}$ and $\Delta x_{9-1} = -2646\,\mathrm{mm}$ for A-side and C-side, respectively.*

Average C-frames deltas

In the OT detector description the modules are assumed to be rigid bodies to which delta rotations and translations can be applied. This is also true for the C-frames which are represented by an ensemble of x and stereo quarter modules. In reality some combinations of "adjustments" to the four corners of a C-frame may introduce deformations. Nonetheless, if these deformations are small, then the assumption that the C-frames and modules are rigid bodies is valid in first approximation. Assuming that the C-frames are rigid bodies, the ultimate C-frame deltas as determined by the iterative survey and adjustment procedure are those listed in Tab. 5.3. The delta rotations, ΔRx, ΔRy and ΔRz of each C-frame are considered to be negligibly small ($< 1\,\mathrm{mrad}$).

5.4 Alignment

It is clear from the preceding section that the positions of the modules are determined by the C-frames and the internal geometry of the modules inside a C-frame. In addition, since a C-frame supports x and stereo modules, the movements of x and stereo modules are correlated and constrained by the C-frame. Therefore, the C-frames are considered the largest alignable mechanical units. The smallest alignable detector elements, for reasons discussed in Sec. 3.1.1, are the modules.

The OT and its corresponding detector geometry description, see Chapter 3, has an hierarchical structure. The detector geometry description hierarchy follows the readout electronics hierarchy, *i.e.* station, layer, quarter and module, and differs from the mechanical OT hierarchy which is C-frame, layer, and module. There are some differences between these hierarchies. First, the layers in the detector geometry description correspond to the layers formed by the mechanical layers of the A-side and C-side C-frames when they are in their closed position, *i.e.* the two A-side and two C-side C-frames, each consisting of an x and stereo layer, of a station are combined in the detector geometry description to form four layers. Second, the modules in the

C-frame	Δx [mm]	Δy [mm]	Δz [mm]
T1XU-A	-1.43	0.05	-0.0
T1VX-A	-0.47	-0.65	-0.5
T2XU-A	-0.27	0.05	-2.5
T2VX-A	-1.69	-0.85	-3.5
T3XU-A	-1.52	-1.25	-0.0
T3VX-A	-1.49	-1.30	-2.5
T1XU-C	-0.79	-0.05	-0.0
T1VX-C	-0.35	-1.50	-0.5
T2XU-C	-0.98	-0.70	-2.5
T2VX-C	0.04	-1.70	-3.5
T3XU-C	-0.04	-1.00	-0.0
T3VX-C	0.20	-1.70	-2.5

Tab. 5.3: *Average C-frame deltas. The survey uncertainty is approximately* $500\,\mu\mathrm{m}$.

detector geometry description are halves of the mechanical modules, *e.g.* an actual F-module is divided into a top and bottom L-module in the detector description. Nonetheless, it possible to align the elements of the mechanical detector hierarchy in the LHCb alignment framework by combining the detector geometry description elements to form alignable detector elements that matches the mechanical hierarchy of the detector, *e.g.* combining a top and bottom L-module gives an F-module. Note that in this case the coordinate of this new alignable detector element is simply given by the average of the coordinates of the detector geometry description elements it is composed of.

The OT detector hierarchy implies that the coordinates of the modules are determined by the C-frames and the internal geometry of the modules inside a C-frame. The measurement direction of the OT modules, or rather straws, is given by

$$u = x\cos\phi_s + y\sin\phi_s, \tag{5.2}$$

where ϕ_s is the stereo angle and is -5° and $+5^\circ$ for u and v stereo modules, respectively. For x modules, with $\phi_s = 0^\circ$, the measurement direction is $u = x$. Note that the measurement direction is perpendicular to the straw orientation. Consequently, the alignable degrees of freedom for modules are limited, *e.g.* one cannot align the x modules for translations in y, since this degree of freedom is unconstrained, *i.e.* it is perpendicular to the measurement direction. Yet, the combination of x and stereo layers, *i.e.* C-frames, gives xy space points. Therefore, by aligning C-frames one can align for the degrees of freedom that a module alignment would otherwise be insensitive to. In addition, the movements of the modules are constrained by the C-frames. It is therefore, natural to first align the C-frames and subsequently the modules. (Note that the deltas of a C-frame alignment corresponds to the average of the deviations of the modules in a C-frame.)

5.4.1 C-frame alignment

In this section an alignment procedure for the OT C-frames is developed given the cosmic ray track sample described earlier. The aim is to determine the set of delta corrections that describe the coordinates of the OT detector C-frames. The initial assumption is that the C-frames are in their nominal position, *i.e.* the C-frames are aligned with respect to the nominal geometry as described in Chapter 3.

Track and hit selection

It was shown in Sec. 5.2 that a majority of cosmic ray triggered events that contain a track in the OT have a single track, and that events with a higher track multiplicity contained tracks with a poor track χ^2 (see Fig. 5.4b). Therefore, only events with a single track are considered in the alignment procedure. An additional requirement, to avoid outlier hits on a track, is that the hits on a track must have residuals that are smaller than the straw tube radius. The net number of cosmic tracks that pass the selection is approximately $21\,\mathrm{k}$ (out of $23\,\mathrm{k}$).

Constraints

A consequence of considering tracks that only traverse the OT is that there are no external constraints, *e.g.* another sub-detector, to constrain the global movements of the OT C-frames. Therefore the OT C-frames can only be aligned with respect to each other. In practice, this is achieved by constraining the movements of a set of C-frames.

In what follows, the movements of the first XU A-side and C-side C-frames, T1XU-A and T1XU-C, and the last XU A-side and C-side C-frames, T3XU-A and T3XU-C are constrained. These C-frames are chosen for a couple of reasons. First, to disentangle any systematic effects as result of the detector geometry, *i.e.* the XU configuration versus the VX configuration. Secondly, according to the survey these C-frames are, within the survey error, at their nominal z position, see Tab. 5.3. Therefore, allowing a straight forward comparison between the z positions obtained with the alignment procedure with respect to nominal and the survey.

Possible ways of constraining the system are either by explicitly removing the C-frames T1XU-A, T1XU-C, T3XU-A and T3XU-C from the system of linear equations (see Eq. 4.12) or by using Lagrange constraints (see Sec. 4.1.3). Both methods are mathematically identical and, unless specified otherwise, Lagrange constraints are used to constrain the movements of these C-frames.

Aligning for Δx or all degrees of freedom

Since hits in the x and stereo modules of a C-frame can be combined to form xy space points, the degrees of freedom one can align for are, in decreasing order of sensitivity, Δx, Δz, ΔRz, ΔRy, ΔRx and Δy. The sensitivity to these degrees of freedom are determined by the hit resolution of the OT in x and y. The C-frames are most sensitive to Δx, since this the primary measurement direction. The delta translation along z, Δz, is obtained from the tracks under a slope t_x in the xz plane and a slope t_y in the yz plane. The sensitivity to delta rotations about z, ΔRz, depends on the track slopes and on the xy space points. Similarly, delta rotations about x, ΔRx, and y, ΔRy, depend on the track slopes and the yz and xz space points, respectively.

Given the above, there are two (extreme) pragmatic alignment scenarios, without taking the properties of the track sample into consideration. First, one can opt to align only for the degree of freedom the C-frames are most sensitive to, namely, Δx. In this case one takes into account any mis-alignments along the x-axis, *i.e.* along the rails, that may occur as a result of opening and closing the C-frames. Second, one can opt to align for all degrees of freedom taking into account

any deformations and deviations that may occur as a result of the adjustments of the four corners of a C-frame.

These two scenarios form the starting point to determine the required number of iterations necessary for the alignment procedure to converge and to determine what the sufficient set of constraints and degrees of freedom are. They are also used to illustrate the effects, if any, on the track yield and average track χ^2, $\langle\chi^2\rangle$. In addition, to illustrate the differences between ignoring and accounting for the correlations between hits (see Eq. 4.14 and Eq. 4.31), the C-frames are aligned in each scenario for two cases. In the first case, case a, the correlations between the hits are ignored, while in the second case, case b, the correlations between the hits are taken into account. These scenarios are listed in Tab. 5.4.

Scenario	Description
Ia	In this scenario the C-frames aligned for Δx and the correlations between hits are ignored.
Ib	Similar to Scenario Ia, but here the correlations between hits are taken into account.
IIa	In this scenario the C-frames are aligned for all degrees of freedom Δx, Δy, Δz, ΔRx, ΔRy and ΔRz and the correlations between hits are ignored.
IIb	Similar to Scenario IIa, but here the correlations between hits are taken into account.

Tab. 5.4: *The four C-frame alignment scenarios to illustrate the effect of taking the correlations between hits into account as well as the effect of multiple degrees of freedom.*

A typical convergence criterion is to require that the change in alignment parameters between successive iterations approaches zero, *i.e.* the parameters reach a plateau. Another, sufficient but not necessary, test for convergence is the change in the total χ^2 as a result of change in the alignment parameters $\Delta\chi^2 = -\Delta\alpha^T \mathrm{Cov}(\alpha)^{-1}\Delta\alpha$. This is equivalent to the significance of the change of the alignment parameters. Therefore, when $\Delta\chi^2/d.o.f. < 1$ the changes in the alignment parameters are statistically insignificant and no additional iterations are required.

The required number of iterations depends on whether the correlations between hits, *i.e.* the off-diagonal elements in the global covariance matrix C (see Eq. 4.14 and Eq. 4.31), are taken into account as well as the total number of degrees of freedom. Naively, one expects that more iterations are required when the correlations between hits are ignored.

Other convergence criteria are the total number of reconstructed tracks and the average track χ^2, $\langle\chi^2\rangle$, versus iteration. These are indicators of the stability of the procedure and indicate whether the applied alignment corrections approach the correct values. Indeed, if these are incorrect then it would lead to a loss in the total number of tracks. If they are correct then this leads to an improvement in $\langle\chi^2\rangle$ and to an increase in the total number of reconstructed tracks*.

The evolution of the above mentioned criteria versus iteration for the four scenarios listed in Tab. 5.4 is shown in Fig. 5.8. Note that while Δx (Fig. 5.8a), the number of tracks (Fig. 5.8c) and $\langle\chi^2\rangle$ (Fig. 5.8d) are "fair measures" for the performance of the four scenarios, the parameter $\Delta\chi^2$ is not, since the calculation of this measure is different for the scenarios where the correlations

*Note that these tracks could be ghost tracks, but in the case of cosmic ray events, which are relatively clean compared to collision events, this is unlikely.

are not taken into account. (The covariance of the alignment parameters $\mathrm{Cov}(\alpha)$, which includes the global covariance matrix C, is different for the two cases.) Still, the following conclusions can be drawn:

- The number of iterations it takes for Δx to converge depends on the number of degrees of freedom and whether the correlations between hits are taken into account. For the scenarios where the correlations are taken into account, Δx converges within $\mathcal{O}(3)$ and $\mathcal{O}(5)$ iterations for Scenario Ib and IIb, respectively. Otherwise, it takes $\mathcal{O}(20)$ and $\mathcal{O}(40)$ iterations for Scenario Ia and IIa, respectively.
- If the correlations between hits are taken into account, then $\mathcal{O}(5)$ iterations is sufficient. Otherwise, $\mathcal{O}(20)$ iterations are needed. Even though the Δx has not converged, subsequent improvements are insignificant (see Fig. 5.8b) and will not lead to an improvement in the reconstruction or physics performance. This can clearly be seen in the total number of tracks (see Fig. 5.8d) and $\langle \chi^2 \rangle$ (see Fig. 5.8c) versus iteration. Note that it depends weakly on the number of degrees of freedom.
- The total number of tracks and $\langle \chi^2 \rangle$ depends on the constraints on the movements of the C-frames. By aligning only for Δx, *i.e.* Scenarios Ia and Ib, the other translations and rotations of the C-frames are implicitly constrained. By releasing these degrees of freedom one takes any additional mis-alignments into account. This leads to a small increase in the number of tracks and a smaller track χ^2.

Considering the above, at most five iterations are sufficient for the alignment procedure to converge. In addition, judging by the track χ^2 and the number of tracks versus iteration, aligning for more degrees of freedom gives a better estimate of the positions of the C-frames. The obtained deviations from the alignment procedure corresponding to scenario IIb are listed in Tab. 5.5. Comparing the delta translations in Tab. 5.5 to the survey delta translations, Tab. 5.3, one observes that the Δz of the C-frames obtained from the alignment procedure is in good agreement with the survey. A more detailed comparison between the alignment procedure and survey is given below.

C-frame	Δx [mm]	Δy [mm]	Δz [mm]	ΔRx [mrad]	ΔRy [mrad]	ΔRz [mrad]
T1XU-A	–	–	–	–	–	–
T1VX-A	0.76 ± 0.02	0.20 ± 0.27	-0.31 ± 0.08	-0.13 ± 0.03	-0.18 ± 0.05	0.01 ± 0.01
T2XU-A	0.87 ± 0.01	0.63 ± 0.22	-2.31 ± 0.05	0.18 ± 0.02	-0.79 ± 0.04	0.18 ± 0.01
T2VX-A	-0.05 ± 0.01	3.15 ± 0.22	-3.61 ± 0.06	0.02 ± 0.03	-0.63 ± 0.04	0.04 ± 0.01
T3XU-A	–	–	–	–	–	–
T3VX-A	0.41 ± 0.02	2.71 ± 0.27	-2.12 ± 0.08	-0.04 ± 0.04	-0.37 ± 0.06	0.02 ± 0.02
T1XU-C	–	–	–	–	–	–
T1VX-C	1.09 ± 0.02	1.14 ± 0.30	0.43 ± 0.09	0.00 ± 0.03	0.24 ± 0.06	-0.05 ± 0.01
T2XU-C	-0.37 ± 0.02	0.64 ± 0.25	-2.91 ± 0.06	-0.19 ± 0.03	0.37 ± 0.04	-0.06 ± 0.01
T2VX-C	0.57 ± 0.02	0.11 ± 0.25	-3.80 ± 0.07	-0.14 ± 0.03	0.98 ± 0.05	-0.05 ± 0.01
T3XU-C	–	–	–	–	–	–
T3VX-C	0.10 ± 0.02	1.65 ± 0.28	-1.84 ± 0.08	-0.27 ± 0.05	0.87 ± 0.07	-0.15 ± 0.02

Tab. 5.5: *The C-frame deltas corresponding to scenario IIb in Tab. 5.4. The degrees of freedom that are constrained to nominal are denoted with* $-$.

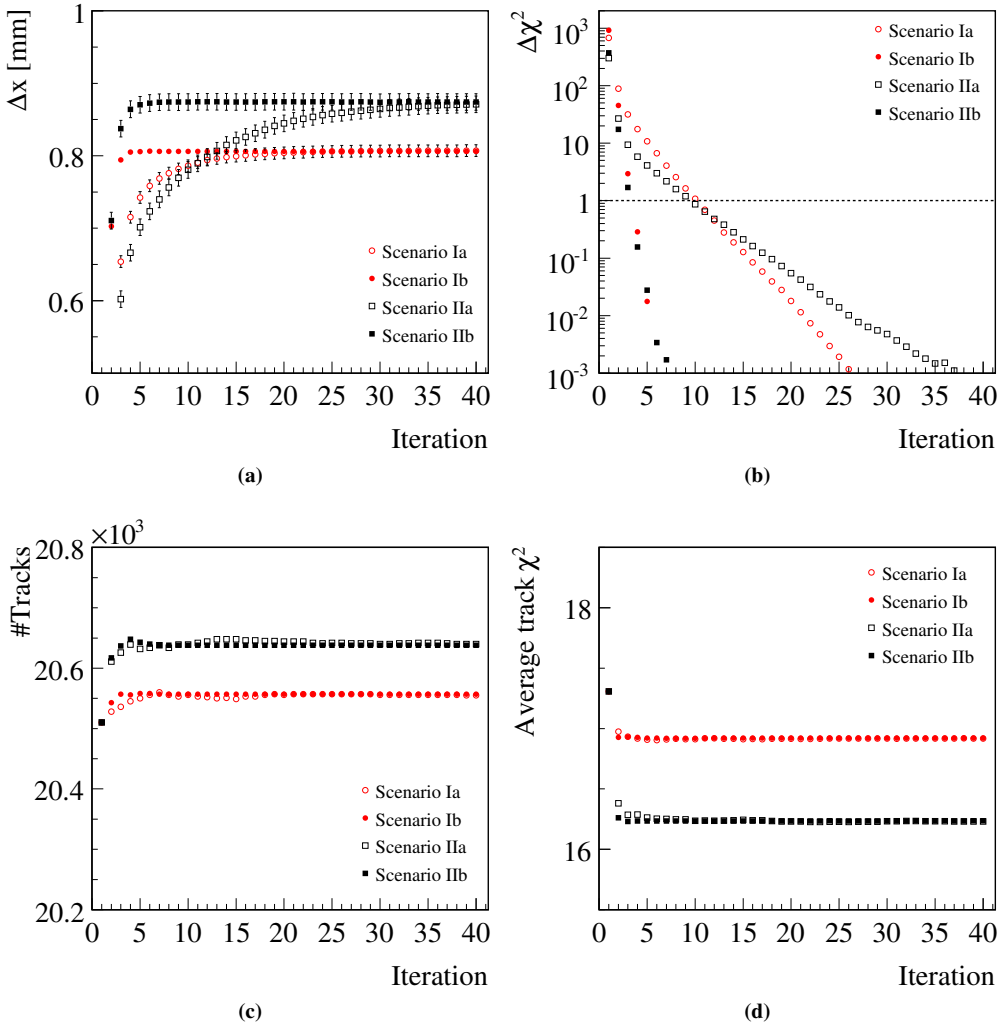

Fig. 5.8: *Evolution, as function of iteration, of (a) Δx, (b) $\Delta\chi^2$, (c) number of tracks and (d) $\langle\chi^2\rangle$ for the C-frame alignment scenarios listed in Tab. 5.4. Note that in Scenarios Ia and IIa the correlations between hits are ignored.*

Weak modes and sufficient set of degrees of freedom

In the previous section it was shown that aligning the C-frames for all degrees of freedom results in more tracks and a relatively better track χ^2. This raises a couple of questions: What is a sufficient set of degrees of freedom that is optimal for reconstruction performance? Is the system perhaps over-constrained for this track sample?

To determine the effect of aligning a set of degrees of freedom on the reconstruction performance, one starts with aligning just for translations in x, the most sensitive measurement direction, and systematically adds additional degrees of freedom to compare the differences in the track yield and the average track χ^2. The track yield and average track χ^2 for various cases are listed in Tab. 5.6. Each scenario follows from the previous by adding an additional degree of

freedom according to decreasing order of sensitivity. It is observed that aligning for Δx and Δz already gives a significant improvement in the reconstruction performance. This can be slightly improved upon by taking ΔRz into account. The other degrees of freedom, ΔRy, ΔRx and Δy have a negligible effect on the performance.

Δx	Δy	Δz	ΔRx	ΔRy	ΔRz	#Tracks	$\langle\chi^2\rangle$
			Initial			20510	17.308
✓	✗	✗	✗	✗	✗	20558	16.922
✓	✗	✓	✗	✗	✗	20649	16.332
✓	✗	✓	✗	✗	✓	20648	16.292
✓	✗	✓	✗	✓	✓	20638	16.257
✓	✗	✓	✓	✓	✓	20646	16.238
✓	✓	✓	✓	✓	✓	20643	16.235

Tab. 5.6: *The total number of tracks and $\langle\chi^2\rangle$ (after five iterations) for various C-frame alignment scenarios. Here ✗ denotes the degrees of freedom that are constrained and ✓ the degrees of freedom the C-frames are aligned for. Since the C-frames are aligned locally, the latter are, in addition, the corresponding constrained degrees of freedom for T1XU A and C-Side, and T3XU A and C-Side.*

It was shown in Sec. 5.2 that approximately 10% of the cosmic tracks are crossing tracks, *i.e.* tracks that go from A-side to C-side and *vice versa*. Since these tracks cross, the movements of A-side and C-side are correlated. Therefore, to constrain the global degrees of freedom of the OT detector, it should be sufficient to constrain the movements of two C-frames, *e.g.* either T1XU-C and T3XU-C or T1XU-A and T3XU-C.

The deltas obtained from an alignment procedure where only the C-side C-frames T1XU-C and T3XU-C are constrained are listed in Tab. 5.7. Judging by these deltas, there seems to be a shearing of the A-side C-frames in the xz-plane. In addition, the A-side C-frames seem to be rotated about the y-axis with respect to the C-side C-frames and the Δz of the A-side C-frames deviate significantly from those as determined by the survey. The latter is unlikely, since the A-side and C-side C-frames share the same rails. In addition, the large relative difference in y between the C-frames are unlikely to be true, since the Bridge and Table are practically flat and level. Apparently, there is an additional (weak) mode, other than the global rotations and translations, that cannot be resolved with this track sample.

Linear combinations of the movements of the system, so-called modes, that have small corresponding eigenvalues will have little or no effect on the total χ^2. An example of such modes are the global translations and rotations of the system. Therefore, to determine whether a set of constraints fully determines a system one can look at the eigenvalue spectrum of the system of linear equations (see Sec. 4.1.2). The eigenvalue spectrum for the case when no constraints are applied and for the case where only the movements of the C-side C-frames T1XU-C and T3XU-C are constrained is shown in Fig. 5.9.

In the case that no constraints are applied one has $N_{\text{d.o.f}} \times N_{\text{detectors}} = 6 \times 6 = 72$ modes. Of these 72 modes there are nine modes with values below 1000 that can be considered small compared to the rest. The first six modes correspond to the global degrees of freedom of the OT and the last three modes to either a twist or shearing. By constraining the movements of the C-side C-frames T1XU-C and T3XU-C the six smallest modes, *i.e.* the global movements of the

C-frame	Δx [mm]	Δy [mm]	Δz [mm]	ΔRx [mrad]	ΔRy [mrad]	ΔRz [mrad]
T1XU-A	0.29 ± 0.07	6.39 ± 0.81	2.48 ± 0.15	0.25 ± 0.08	4.35 ± 0.34	0.39 ± 0.03
T1VX-A	0.57 ± 0.06	5.66 ± 0.80	1.04 ± 0.14	0.05 ± 0.07	3.82 ± 0.34	0.40 ± 0.03
T2XU-A	0.76 ± 0.04	1.38 ± 0.57	-1.68 ± 0.10	0.30 ± 0.06	3.16 ± 0.32	0.61 ± 0.03
T2VX-A	-0.14 ± 0.04	2.11 ± 0.57	-2.64 ± 0.10	0.13 ± 0.06	3.38 ± 0.32	0.49 ± 0.03
T3XU-A	-0.16 ± 0.05	-2.61 ± 0.61	-1.41 ± 0.12	-0.08 ± 0.08	3.42 ± 0.33	0.57 ± 0.03
T3VX-A	-0.15 ± 0.07	1.33 ± 0.64	-2.49 ± 0.13	-0.02 ± 0.09	3.40 ± 0.34	0.59 ± 0.04
T1XU-C	–	–	–	–	–	–
T1VX-C	0.77 ± 0.02	2.58 ± 0.31	0.27 ± 0.10	-0.06 ± 0.04	0.10 ± 0.06	-0.01 ± 0.01
T2XU-C	-0.29 ± 0.02	0.95 ± 0.26	-2.64 ± 0.08	-0.14 ± 0.03	0.39 ± 0.05	-0.06 ± 0.01
T2VX-C	0.39 ± 0.02	1.22 ± 0.27	-3.05 ± 0.08	-0.03 ± 0.03	0.69 ± 0.06	-0.01 ± 0.01
T3XU-C	–	–	–	–	–	–
T3VX-C	0.07 ± 0.02	1.41 ± 0.30	-1.61 ± 0.09	-0.25 ± 0.05	0.87 ± 0.07	-0.09 ± 0.02

Tab. 5.7: *The C-frame deltas corresponding to a scenario where only the C-side C-frames are constrained (denoted with $-$).*

OT, disappear as expected. However, of the remaining three small modes there still remains one mode to which the system is insensitive to. This can either be due to a shearing, rotation or twist in the relative position of the A-side and C-side stack of C-frames. Note that in this case the number of modes is $N_{\text{d.o.f}} \times N_{\text{detectors}} - N_{\text{constraints}} = 72 - 6 \times 2 = 60$.

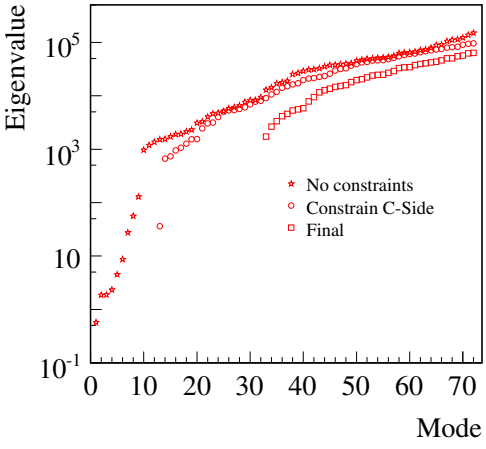

Fig. 5.9: *The eigenvalue spectra for the cases that no constraints are applied, T1XU-C and T3XU-C are constrained, and finally T1XU-C, T1XU-A, T1XU-C and T3XU-C are constrained as well as Δy of the remaining C-frames.*

Since only constraining the movements of T1XU-C and T3XU-C does not sufficiently determine the system, the movements of T1XU-A and T3XU-A are also constrained. In addition, since the relative displacements in y are not compatible with the survey and the fact that the height of the C-frames are mechanically determined by the Bridge, which is flat and level, the translations of all the C-frames along the y-axis are constrained. This gives a total of 32 constraints and 40 alignable degrees of freedom. As can be seen in Fig. 5.9, these set of constraints removes the nine small eigenvalues with values less than 1000. The corresponding deltas in this case are listed in Tab. 5.8. Unless specified otherwise, these set of constraints are used in the rest of this chapter.

C-frame	Δx [mm]	Δy [mm]	Δz [mm]	ΔRx [mrad]	ΔRy [mrad]	ΔRz [mrad]
T1XU-A	–	–	–	–	–	–
T1VX-A	0.71 ± 0.02	–	-0.31 ± 0.08	-0.13 ± 0.03	-0.18 ± 0.05	0.01 ± 0.01
T2XU-A	0.84 ± 0.01	–	-2.34 ± 0.05	0.18 ± 0.02	-0.80 ± 0.04	0.18 ± 0.01
T2VX-A	-0.01 ± 0.01	–	-3.72 ± 0.06	0.04 ± 0.03	-0.73 ± 0.04	0.05 ± 0.01
T3XU-A	–	–	–	–	–	–
T3VX-A	0.38 ± 0.02	–	-2.29 ± 0.08	-0.01 ± 0.04	-0.52 ± 0.06	0.03 ± 0.02
T1XU-C	–	–	–	–	–	–
T1VX-C	1.11 ± 0.02	–	0.45 ± 0.09	-0.00 ± 0.03	0.21 ± 0.06	-0.06 ± 0.01
T2XU-C	-0.39 ± 0.01	–	-2.92 ± 0.06	-0.20 ± 0.03	0.37 ± 0.04	-0.07 ± 0.01
T2VX-C	0.53 ± 0.01	–	-3.81 ± 0.07	-0.14 ± 0.03	0.97 ± 0.05	-0.06 ± 0.01
T3XU-C	–	–	–	–	–	–
T3VX-C	0.09 ± 0.02	–	-1.86 ± 0.08	-0.27 ± 0.05	0.85 ± 0.07	-0.15 ± 0.02

Tab. 5.8: *The C-frame deltas corresponding to the final set of constraints (denoted with −).*

Comparison to survey

Up to this point it is assumed that the C-frames are close to their nominal positions. Accordingly, T1XU-A, T1XU-C, T3XU-A and T3XU-C were constrained to their nominal positions in the scenarios previously presented. As a result, the deltas obtained were with respect to the frame as determined by the constrained C-frames. Nonetheless, comparing Tab. 5.5 or Tab. 5.8 to Tab. 5.3, there is a reasonable agreement with the survey. An alternative approach to obtain a one-to-one correspondence between the alignment and survey deltas, is to align the C-frames by constraining T1XU-A, T1XU-C, T3XU-A and T3XU-C to their survey positions. The obtained values of Δx and Δz for this alignment procedure, in addition to the survey values, are shown in Fig. 5.10. Clearly, the obtained values for the unconstrained degrees of freedom are in good agreement with the survey values. For completeness the deltas obtained from this procedure are listed in Tab. 5.9.

C-frame	Δx [mm]	Δy [mm]	Δz [mm]	ΔRx [mrad]	ΔRy [mrad]	ΔRz [mrad]
T1XU-A	–	–	–	–	–	–
T1VX-A	-0.70 ± 0.02	–	-0.24 ± 0.08	-0.12 ± 0.03	-0.13 ± 0.05	0.02 ± 0.01
T2XU-A	-0.59 ± 0.01	–	-2.13 ± 0.05	0.20 ± 0.02	-0.67 ± 0.04	0.18 ± 0.01
T2VX-A	-1.42 ± 0.01	–	-3.51 ± 0.06	0.05 ± 0.03	-0.61 ± 0.04	0.05 ± 0.01
T3XU-A	–	–	–	–	–	–
T3VX-A	-1.06 ± 0.02	–	-2.37 ± 0.08	-0.02 ± 0.04	-0.59 ± 0.06	0.03 ± 0.02
T1XU-C	–	–	–	–	–	–
T1VX-C	0.40 ± 0.02	–	0.57 ± 0.09	-0.01 ± 0.03	0.13 ± 0.06	-0.06 ± 0.01
T2XU-C	-0.85 ± 0.01	–	-2.76 ± 0.06	-0.20 ± 0.03	0.27 ± 0.04	-0.07 ± 0.01
T2VX-C	0.14 ± 0.01	–	-3.59 ± 0.07	-0.11 ± 0.03	0.83 ± 0.05	-0.06 ± 0.01
T3XU-C	–	–	–	–	–	–
T3VX-C	0.05 ± 0.02	–	-2.14 ± 0.08	-0.25 ± 0.05	1.03 ± 0.07	-0.15 ± 0.02

Tab. 5.9: *The C-frame deltas obtained from the alignment procedure where the C-frames T1XU-A, T1XU-C, T3XU-A and T3XU-C are constrained to their survey values in x and z (denoted with −).*

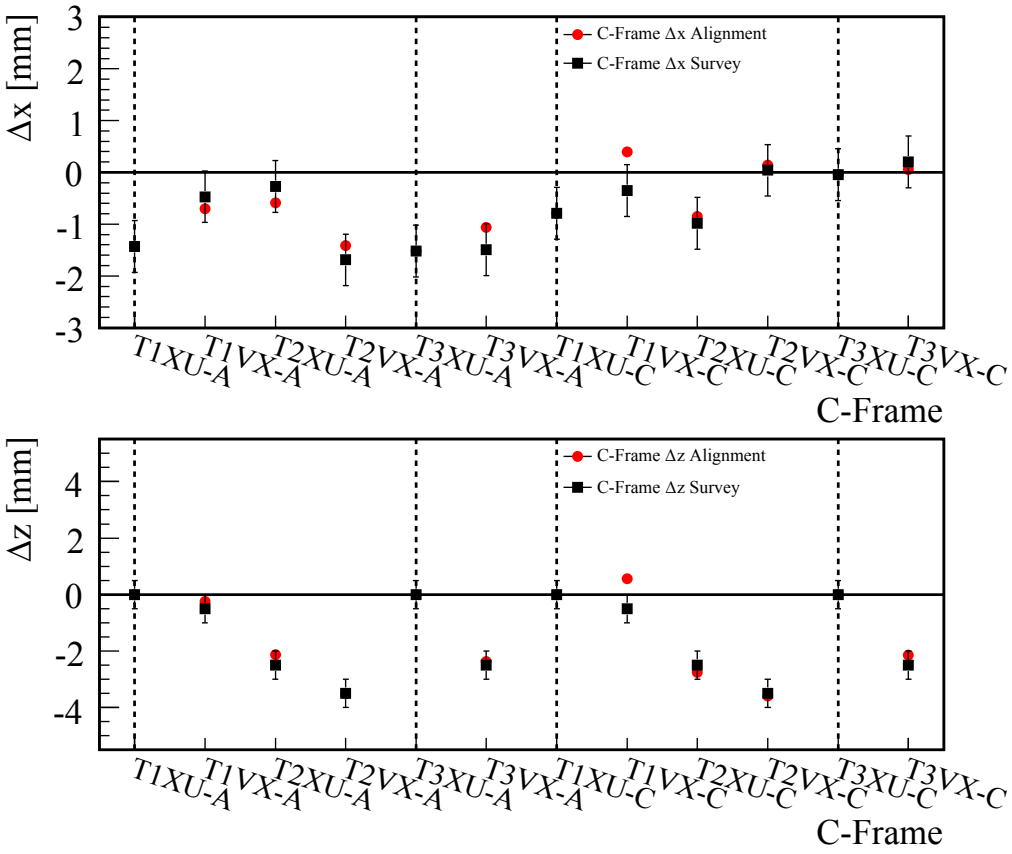

Fig. 5.10: *C-frame Δx and Δz from the alignment procedure and survey, respectively. Here the C-frames were aligned with respect to the survey by constraining the C-frames, indicated with dashed lines, to their survey values. The statistical errors on the alignment deltas are less than* $80\,\mu\mathrm{m}$.

5.4.2 Module alignment

Unlike the C-frames, where a combination of an x and stereo layer gives an xy space point, individual OT modules measure only a single measurement direction. Therefore, the modules are sensitive to delta translations in x and to a certain degree, via the track slopes, to delta rotations about the z axis. Therefore, the alignable degrees of freedom that an x-module is sensitive to are Δx and ΔRz. Note that similar to the C-frame alignment, one could combine an x and its corresponding stereo module to obtain xy space points. This would allow one to align for delta translations in y, and to recover the internal geometry of the modules in a C-frame as depicted in Fig. 5.7. Unfortunately, due to the dead regions in the detector, which affect the acceptance, and given the limited track sample this possibility cannot be explored.

Similar to the C-frame alignment one needs to constrain the movements of a set of modules. A pragmatic approach is to constrain the same movements of the modules of the C-frames that were also constrained in the C-frame alignment procedure, *i.e.* the C-frames T1XU-A, T1XU-C, T3XU-A and T3XU-C. Again, this over-constrains the system, since the movements of the modules are correlated. Ideally one would like to constrain the movements of a limited set modules

that is just sufficient to determine the system. However, such a procedure requires more statistics than is available in the current data.

Given the above and starting from an alignment scenario where the C-frames have been aligned with respect to the survey, the movements of the modules in T1XU-A, T1XU-C, T3XU-A and T3XU-C are constrained and the rest of the modules are aligned for Δx and ΔRz. The obtained module deviations for Δx and ΔRz are shown in Fig. 5.11 and Fig. 5.12, respectively. Here the deltas are plotted against the nominal x-coordinate of the modules to identify any patterns such as x scaling of the modules along the x-axis, or a (remaining) global rotation of the C-frames about the y or z-axis. Since the module deltas appear to be random, one can conclude that there is no visible global rotations or scaling. Furthermore, as can be seen in Fig. 5.13, these deltas are centred about zero and they are significant with respect to alignment resolution. Therefore, these deltas are considered additional corrections on top of the average deviations of the modules as determined by the C-frame alignment procedure.

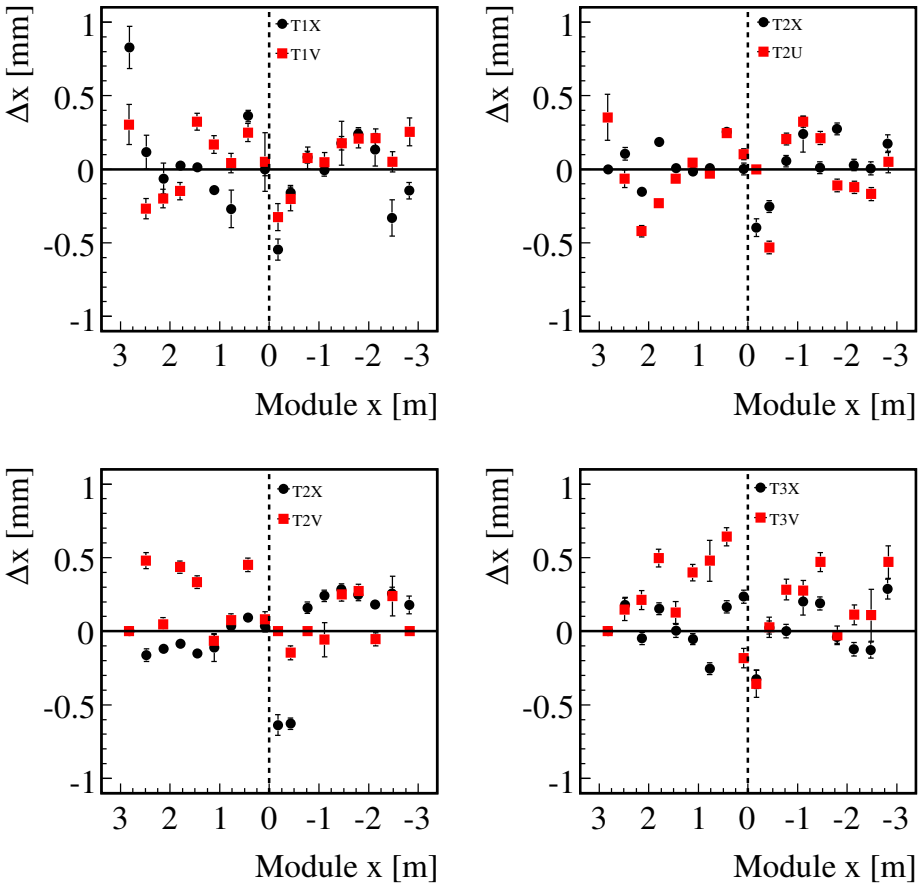

Fig. 5.11: *Module Δx versus nominal module x (in the LHCb frame) for T1VX, T2XU, T2VX and T3VX. The points left of the dashed line correspond to the A-side modules. The points right of the dashed line correspond to C-side modules.*

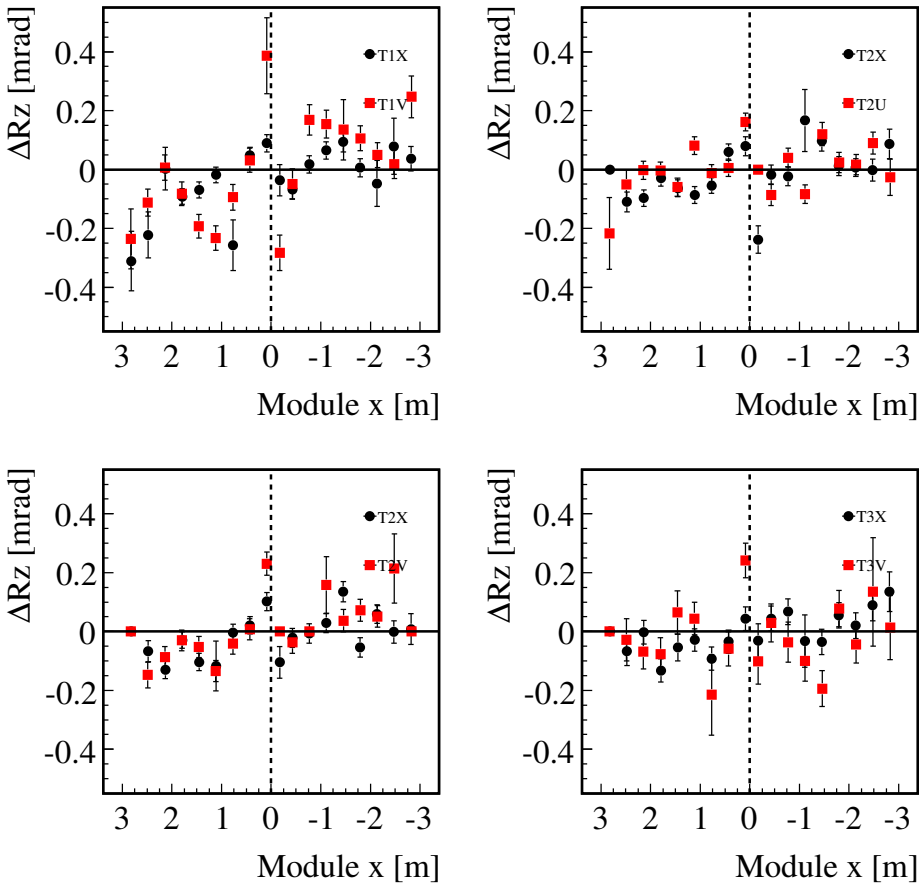

Fig. 5.12: *Module ΔRz versus nominal module x (in the LHCb frame) for T1VX, T2XU, T2VX and T3VX. The points left of the dashed line correspond to the A-side modules. The points right of the dashed line correspond to C-side modules.*

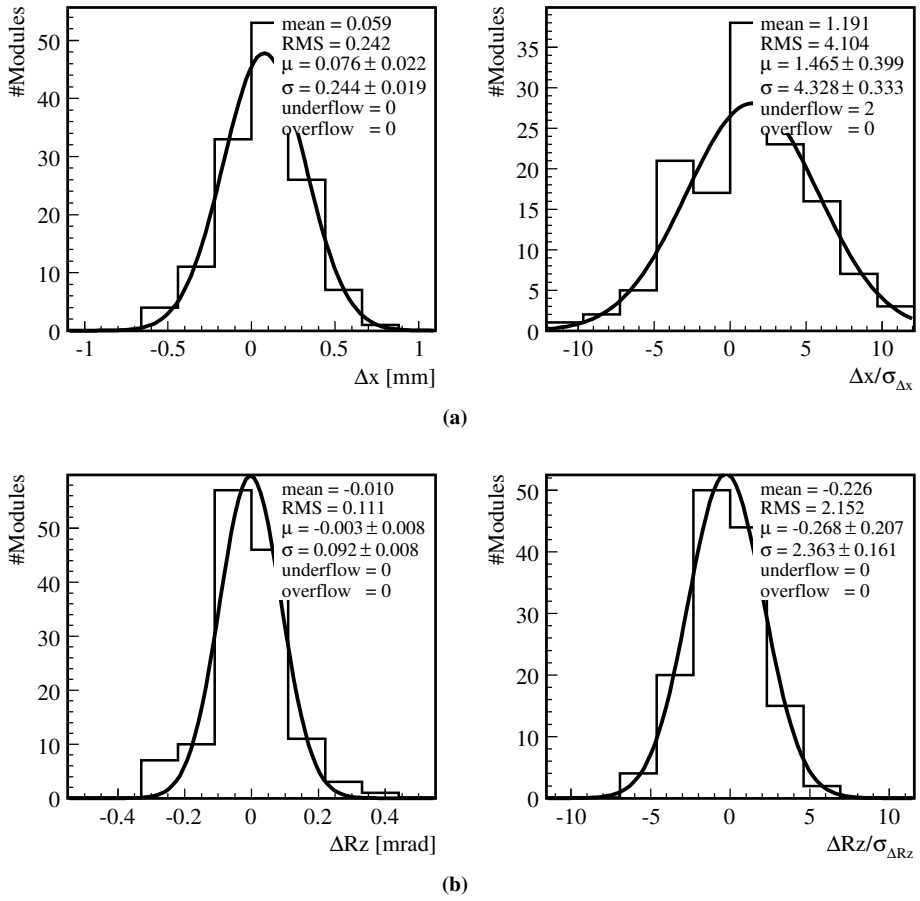

Fig. 5.13: *Distributions of (a) Δx and $\Delta x/\sigma_{\Delta x}$ and (b) ΔRz and $\Delta Rz/\sigma_{\Delta Rz}$ for OT modules.*

5.4.3 Estimating the statistical and systematic errors

In the previous section the additional module alignment corrections, on top of the alignment corrections obtained from the C-frame alignment procedure were presented. It was shown that these corrections were random and significant with respect to the alignment resolution.

To determine the alignment resolution the track sample is divided into two track samples of approximately equal size. Starting from a best estimate for the module positions obtained from the C-frame alignment, the modules are then aligned with one track sample which yields a set of module alignment deltas α_1 and their corresponding statistical error σ_1. Next, these parameters are stored in the geometry database. Note that at this point all information concerning the errors on the deltas for this track sample are lost. Subsequently, starting from the new deltas obtained with the first track sample, α_1, the modules are aligned using the second track sample. This yields a new set of alignment parameters $\alpha_2 = \alpha_1 + \Delta\alpha_2$ and their corresponding statistical errors σ_2. The alignment resolution is then given by the width of the distribution of the residuals $\Delta\alpha_{21} = \alpha_2 - \alpha_1 = \Delta\alpha_2$.

An additional quantity that can be used to determine whether the statistical errors on the alignment parameters are correctly estimated is the pull defined as

$$\text{pull}\,(\Delta\alpha_{ji}) = \frac{\Delta\alpha_{ji}}{\sqrt{\sigma_j^2 + \sigma_i^2}}, \tag{5.3}$$

where $\Delta\alpha_k$ and σ_k are the delta and its corresponding statistical error, respectively, for a track sample k. The numerator in Eq. 5.3 is the residual $\Delta\alpha_{ji} = \Delta\alpha_j - \Delta\alpha_i$. If both track samples are approximately of equal size then Eq. 5.3 is approximately given by

$$\text{pull}\,(\Delta\alpha_{ji}) = \frac{\Delta\alpha_{ji}}{\sqrt{2}\sigma_j}, \tag{5.4}$$

Odd versus even events

An obvious way to divide the track sample is to split it into two samples of even and odd events, respectively. In this case each track sample will have identical properties and one expects the difference between the track samples to be purely statistical. The width of the residual distribution of odd versus even events, $\Delta\alpha_{OE}$, should then correspond to the statistical error in the alignment parameters. The residual and pull distribution of Δx and ΔRz for this case are shown in Fig. 5.14. Note that the pull distributions shown here correspond to the deltas, $\Delta\alpha_j$, divided by their statistical error, σ_j. Therefore, if the statistical errors are correctly estimated, one expects the width of the pull distribution to be approximately $\sqrt{2}$. As can be seen there is no clear bias and the statistical uncertainties are correctly estimated and the statistical errors in Δx and ΔRz are approximately $98\,\mu\text{m}$ and $80\,\text{mrad}$, respectively.

By combining the two samples one obtains the following statistical error for the alignment procedure:

$$\sigma_\Sigma = \frac{1}{\sqrt{2}}\sigma_j = \frac{1}{2}\sigma_\Delta, \tag{5.5}$$

which simply follows from the average of the deltas and error propagation. Therefore, given the statistical errors in Δx and ΔRz above, the statistical error for the combined track sample is approximately $54\,\mu\text{m}$ and $40\,\text{mrad}$ in Δx and ΔRz, respectively.

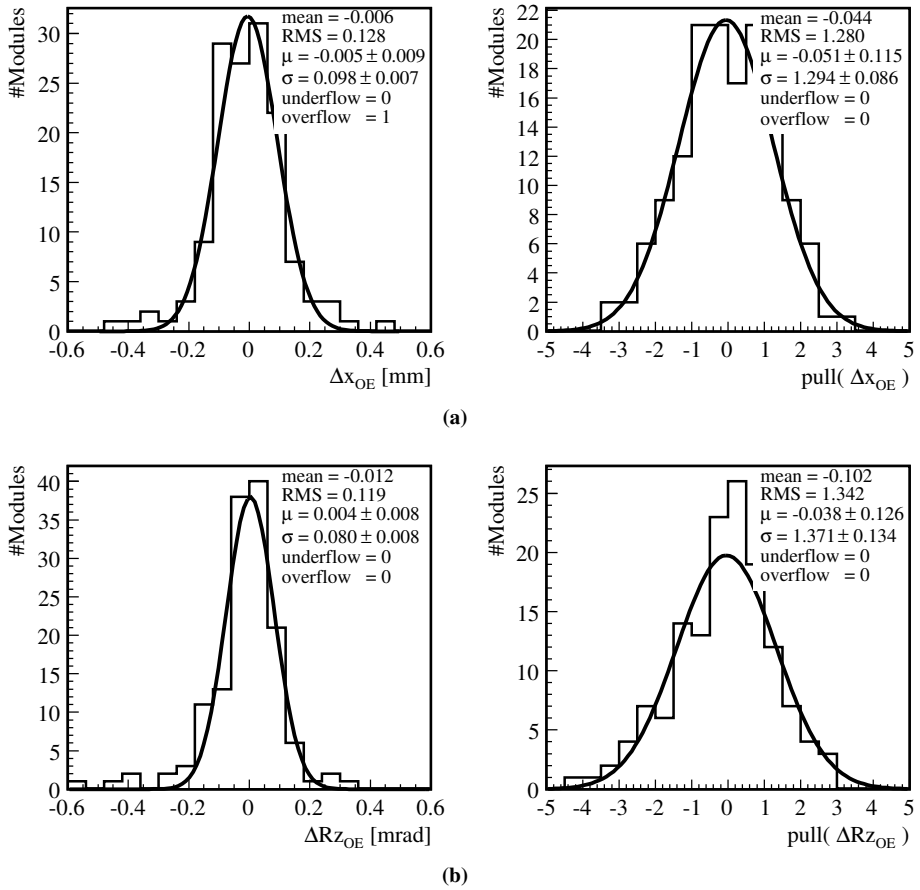

Fig. 5.14: *The resolution and pull distributions for Δx and ΔRx for odd events versus even events. Note that if the statistical errors for Δx for odd events or backward tracks are correctly estimated, the width of the pull distribution is given by $\sqrt{2}$.*

Forward tracks versus backward tracks

To get an estimate of the systematic error one can divide the track sample in a less arbitrary way such that the track samples do not have identical properties. To illustrate this the track sample is divided into two samples of backward and forward tracks, respectively, since there are approximately equal fractions of forward and backward tracks. The residual and pull distributions for Δx and ΔRz for this case are shown in Fig. 5.15. As in the in the case above, if the statistical errors are correctly estimated, one expects the width of the pull distribution to be approximately $\sqrt{2}$. As can be seen there is no bias but the errors are slightly underestimated, judging by the pull distributions and comparing to Fig. 5.14. Knowing the statistical uncertainty, the systematic uncertainty can be estimated from the width of the resolution distributions. Since the alignment resolution is $98\,\mu\mathrm{m}$ and $80\,\mathrm{mrad}$ in Δx and ΔRz, respectively, the systematic error in Δx and ΔRz is approximately $131\,\mu\mathrm{m}$ and $61\,\mathrm{mrad}$, respectively.

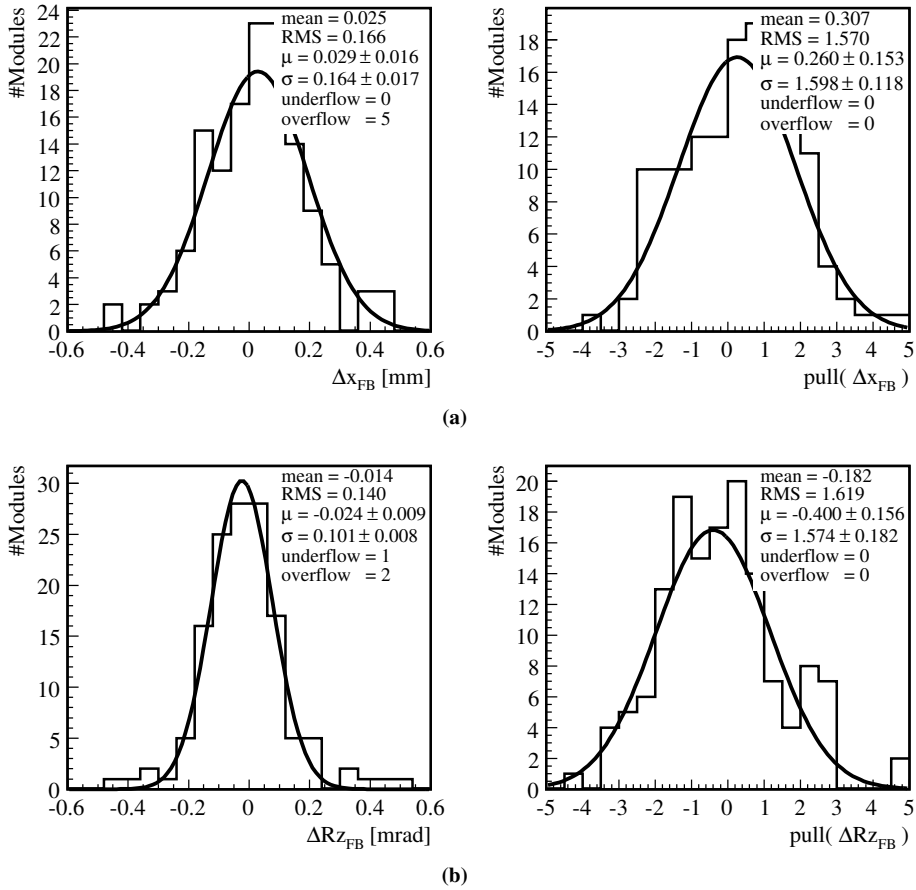

Fig. 5.15: *The resolution and pull distributions for Δx and ΔRx for events containing forward tracks versus events containing backward tracks. Note that if the statistical errors for Δx for odd events or backward tracks are correctly estimated, the width of the pull distribution is given by $\sqrt{2}$.*

5.5 Conclusion

In this chapter an alignment procedure to align the OT C-frames and modules using cosmic rays is presented. This procedure involves the track selection and determination of the optimal set of constraints for the C-frame and module alignment. The aim is to determine a set of alignment deltas that can be used for first beam data.

The study of the cosmic ray tracks shows that events containing a single track typically has a better track χ^2 compared to events containing two or more tracks. Therefore, only events containing a single track is used in the alignment procedure. In addition, the distribution and the characteristics of the tracks, i.e. their slopes, is in good agreement with what one expects from the acceptance of the detector. It also indicates that there is no clear bias for forward or backward tracks.

To determine an alignment procedure for the OT C-frames, the C-frames are first aligned with respect to their nominal geometry with two pragmatic approaches. In the first approach the C-frames are aligned for a single degree of freedom, namely Δx, and in the second approach

for all degrees of freedom. It is shown that in both cases there is an improvement in the number of tracks and the track χ^2. However, aligning for all degrees of freedom, and thereby taking all deformations into account, yields a better performance compared to aligning for a single degree of freedom.

The next step is to determine a sufficient set of constraints. It is shown that ΔRy, ΔRx and Δy has a negligible effect on the performance of the alignment procedure. This is not surprising since these are the degrees of freedom a C-frame is less sensitive to. An attempt is also made to reduce the number of constraints. Since the movements of the C-frames are correlated, it should be sufficient to fix only two C-frames. This study shows that in this case the alignment procedure introduces a shearing in yz. The eigenvalue spectrum of the alignment deltas reveals that by constraining only two C-frames one does remove the global degrees of freedom, but there remains a single (weak) mode that can be attributed to this shearing. In addition, the offsets in y are not in agreement with what one expects from the survey and with what is allowed within the mechanical tolerances, *i.e.* the mechanical constraints imposed by the installation. It is therefore decided to fully constrain two C-frames on each side and Δy movements for all C-frames. Given the above, it is shown that the alignment of the C-frames with respect to survey yields deltas that are consistent with the survey measurements.

As a next step the OT modules are aligned. It is shown that the corrections with respect to their positions inside the C-frames are significant. It is also shown that there is no clear pattern in the deviations, *i.e.* a shearing of the modules inside a C-frame, in the delta corrections. In addition, these deltas are centred around their average displacements inside a C-frame.

As a final result the statistical error in Δx and ΔRz for the total track sample is determined to be $54\,\mu\mathrm{m}$ and $40\,\mathrm{mrad}$, respectively. A less arbitrary division of the track sample reveals that there are systematic uncertainties of approximately $131\,\mu\mathrm{m}$ and $61\,\mathrm{mrad}$ in Δx and ΔRz, respectively.

Chapter 6

Effect Of Mis-Alignments On $B_s^0 \to J/\psi\phi$

One of the main goals of the LHCb experiment is to explore CP violation in the B_s^0 system in which the key measurement is the $B_s^0 - \overline{B_s^0}$ mixing induced CP violating phase ϕ_s [4]. This phase can be determined with $B_s^0 \to J/\psi\phi$ decays, which are attractive from both an experimental and theoretical point of view.

Experimentally, $B_s^0 \to J/\psi\phi$ decays are attractive because they have a clear J/ψ signal, where the J/ψ decays to a di-muon pair, and the reconstruction of these decays is relatively straightforward since the final state contains two oppositely charged muons from the J/ψ combined with two oppositely charged kaons from the ϕ, as illustrated in Fig. 6.1. In addition, these decays have a relatively high branching ratio of approximately B $= \mathcal{O}(10^{-3})$.

Theoretically, $B_s^0 \to J/\psi\phi$ decays are interesting because any deviation from the $B_s^0 - \overline{B_s^0}$ mixing induced CP violating phase as predicted by the CKM mechanism in the Standard Model may be caused by New Physics. In the case of $B_s^0 \to J/\psi\phi$, the observed CP violating effect is due to the interference between B_s^0 decays that decay either directly to $J/\psi\phi$ or via $B_s^0 - \overline{B_s^0}$ mixing. According to the CKM mechanism in the Standard Model this phase is predicted to be $\phi_s = -2\beta_s \approx -0.04\,\mathrm{rad}$, where β_s is the smallest angle of the B_s^0 system CKM unitary triangle, see Chapter 1. However, this phase may be augmented by New Physics [20, 21, 22], which may enter through the off-diagonal mass terms, *i.e.* virtual off-shell contributions, in the mixing Hamiltonian.

Currently, the experimental sensitivity on ϕ_s is $\phi_s \in [-1.18, -0.54] \cup [-2.60, -1.94]\,\mathrm{rad}$ at 68% CL [83]. Given the size of the Standard Model prediction of ϕ_s, which is approximately $0.04\,\mathrm{rad}$, contributions from New Physics are not excluded. However, in the case of LHCb, studies have shown that a sensitivity on ϕ_s of $0.024\,\mathrm{rad}$ can be achieved with $2\,\mathrm{fb}^{-1}$ at $14\,\mathrm{TeV}$ [24, 25].

In LHCb the weak phase ϕ_s is extracted from a multi-dimensional likelihood fit to the reconstructed $B_s^0 \to J/\psi\phi$ decays [24, 25]. The ingredients in the fitting procedure are the reconstructed B_s^0 mass and proper time, and the decay angles of the final state particles in the so-called transversity basis [84] as well as their corresponding resolutions. These quantities all follow from the four momenta of the charged particle tracks, which in turn follow from the reconstructed track parameters.

The optimal set of track parameters that describe the trajectory of a charged particle, for a given collection of detector hits, are determined with a Kalman Filter track fitting procedure [27, 59]. The track parameters of a charged particle that traverses the VELO and T-stations, *i.e.* so-called long tracks, are in general the parameters of the first state closest to beam line. These

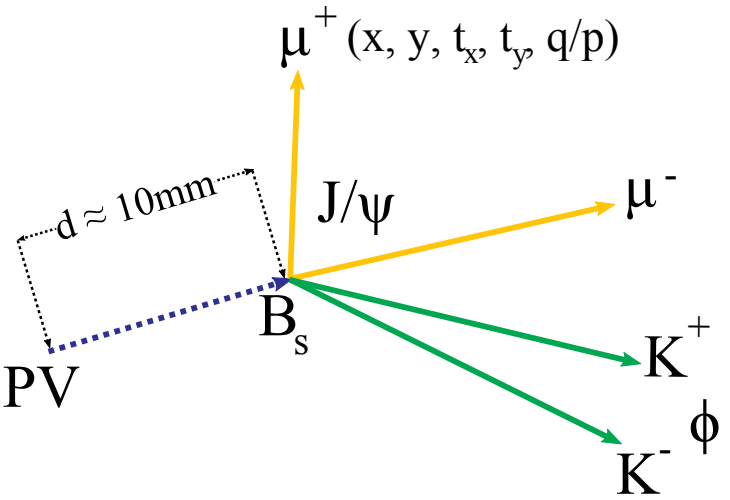

Fig. 6.1: *The topology of the decay $B_s^0 \to J/\psi\phi$. The average decay length d of the B_s^0 is approximately $10\,\mathrm{mm}$ and its average lifetime is approximately $1.5\,\mathrm{ps}$. Due to their short lifetimes, the J/ψ and ϕ practically decay instantaneously into a di-muon and di-kaon pair, respectively.*

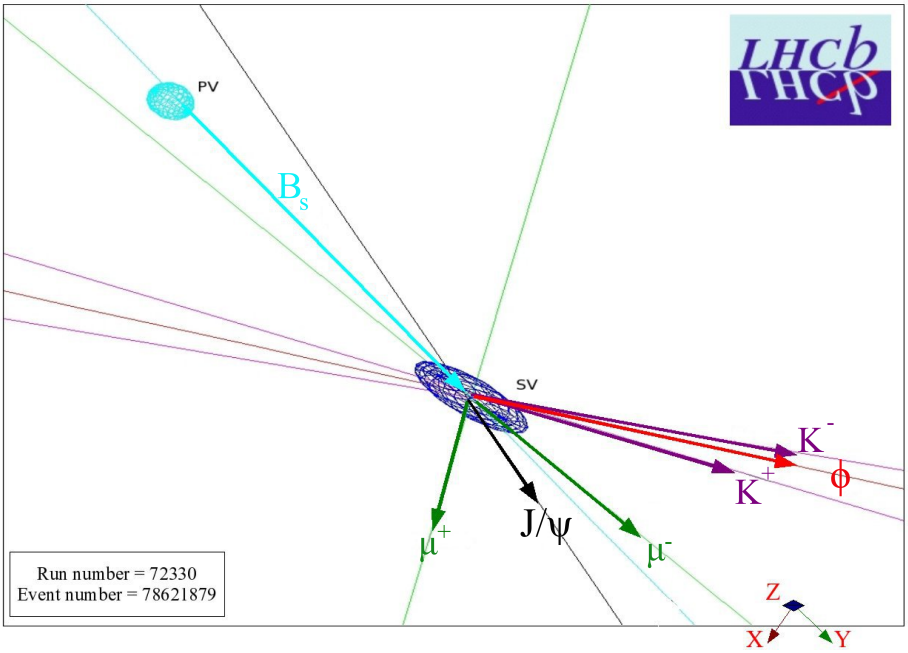

Fig. 6.2: *Event display of a reconstructed $B_s^0 \to J/\psi\phi$ candidate. Here PV denotes the primary vertex location in which the B_s^0 candidate is produced and SV denotes the displaced secondary vertex, which corresponds to the decay vertex of the B_s^0.*

parameters are the coordinates x and y for a given z coordinate, the track slopes t_x and t_y, and the curvature q/p, where $q = \pm 1$ is the charge of the particle.

The coordinates and the track slopes are primarily obtained from the hit information in the VELO. The curvature, and therefore momentum, is inferred from the bending of the charged particle in the magnetic field, which results in a change of the slope of the charged particle between the VELO and the T-Stations. This information is then used in the vertex fit procedures, see, *e.g.*, [72, 85], to determine the position of the primary vertex and secondary vertex and, subsequently, the lifetime of the B_s^0 meson. From the four momenta of the final state particles follows the invariant mass of the B_s^0 particle and similarly the transversity angles in the rest frame of the J/ψ.

In general, mis-alignments in the VELO and T-stations will lead to a degradation in the resolution on the track parameters. Mis-alignments in the VELO are expected to affect the estimation of the coordinates and track slopes, while mis-alignments in the T-stations are mainly expected to affect the estimation of the momenta of the charged particles. Consequently, mis-alignments in the VELO and T-stations will lead to a degradation in the resolution or systematic effects on the reconstructed vertices, lifetime, masses and momenta of the particles. This in turn may lead to a bias or dilution of the sensitivity to the physics parameters, such as ϕ_s, that are extracted from the multi-dimensional likelihood fits.

In this chapter the impact of mis-alignments in the VELO and T-stations on the resolution on the reconstructed quantities that are used in the likelihood fits to extract ϕ_s using $B_s^0 \to J/\psi\phi$ decays are studied. The reconstructed quantities that are studied are the masses of the B_s^0, J/ψ and ϕ particles, the proper time of the B_s^0 and the transversity angles. The mis-alignments scenarios and the procedure used for this study are presented in Sec. 6.1 and Sec. 6.2, respectively. Finally, the results of this study as well as the possible impact on ϕ_s are presented in Sec. 6.3.

6.1 The Scenarios

To get a qualitative impression of how mis-alignments in the tracking detectors affect the reconstruction of $B_s^0 \to J/\psi\phi$ decays, two mis-alignment scenarios are studied independently of each other. The first scenario corresponds to random translational mis-alignments of the VELO modules in the transverse plane, picked from a Gaussian distribution with a width of $5 \times \sigma_{\text{res}}$. A VELO module is composed of a ϕ and r-sensor, with a hit resolution of around $\sigma_{\text{res}} = 8\,\mu\text{m}$ in the innermost region, and the primary measurement directions are r and ϕ.

Similarly, the second scenario corresponds to random translational mis-alignments along the primary measurement direction of the IT detector boxes and OT C-frames. In this scenario, which is the same as the scenario used in the validation study of the alignment algorithm presented in Chapter 4, the IT boxes and OT C-frames are mis-aligned along x. These Δx mis-alignments are picked from a Gaussian with a width of $5 \times \sigma_{\text{res}}$, where the hit resolution σ_{res} is $60\,\mu\text{m}$ and $200\,\mu\text{m}$ for the IT and OT, respectively.

These scenarios are chosen such that the mis-alignment effects are significant with respect to the reconstructed quantities of interest. However, they are conservative compared to the survey resolution, which is typically a factor two better. Nonetheless, as was shown in Chapter 4, mis-alignments of this size can be resolved. Note that these scenarios are studied independently of each other. Therefore, the observed effects can be entirely attributed to either VELO mis-alignments or T-station mis-alignments.

6.2 Procedure

For this study a sample of $100\,\mathrm{k}$ $B_s^0 \to J/\psi\phi$ Monte Carlo signal events is used. Although the ideal geometry was used to generate and reconstruct these events, mis-alignments can be simulated by re-reconstructing the particles using a different geometry from the one used in the generation of these events. Effectively, one displaces the simulated hits in the detector elements with constants offsets corresponding to the scenarios given in Sec. 6.1.

To study the effects of mis-alignments in the tracking stations on the quantities of interest the following procedure is used: first, the tracks are reconstructed using the standard LHC*b* reconstruction procedure and ideal geometry. Subsequently, the reconstructed tracks are matched to the Monte Carlo truth. Finally, the reconstructed tracks that originate from a true Monte Carlo B_s^0 are refitted for a given mis-alignment scenario. The advantage of this procedure is that effects of the pattern recognition and selection procedure, which are both tuned on the ideal geometry, are eliminated. Consequently, the remaining effect is that of the alignment and detector resolution on the quantities of interest.

In addition, since the primary vertex is also affected by mis-alignments, the tracks that contribute to the estimate of the associated primary vertex of a B_s^0 candidate are also refitted. In some cases the tracks that originate from a B_s^0 may have been used to determine the primary vertex position. This introduces a bias in the estimate of the primary vertex. To eliminate such a bias, the tracks of the B_s^0 candidate are removed before refitting the primary vertex.

Note that the only selection criterion used is that the four tracks originating from the Monte Carlo B_s^0 have been reconstructed. Of the $100\,\mathrm{k}$ generated events, approximately $25.6\,\mathrm{k}$ events are reconstructed. This gives an combined detector and reconstruction acceptance in the ideal case of approximately $(25.6 \pm 0.1)\%$. For comparison, the efficiency of the standard selection combined with the trigger efficiency is $(14.5 \pm 0.1)\%$ [4].

6.3 Results

In this section results on the reconstructed mass of the B_s^0, J/ψ and ϕ, lifetime of the B_s^0 and the decay angles are presented for five different cases: *Ideal*, *Unaligned T*, *Aligned T*, *Unaligned V* and *Aligned V*. In the ideal case the particles are reconstructed with the ideal detector geometry, while in the unaligned cases the particles are reconstructed for a given mis-aligned geometry, either *T*-station or *V*ELO mis-alignments, which correspond to the scenarios described in Sec. 6.1. In the aligned cases the particles are reconstructed with the aligned sub-detector, either T-stations or VELO, geometry. These correspond to the geometries containing the residual alignment offsets after aligning the T-stations and VELO, respectively. For reference, the *PDG* values for the masses and lifetimes or decay widths for the B_s^0, J/ψ and ϕ are listed in Tab. 6.1. These correspond to the values used in the LHC*b* simulation.

Particle	$M[\mathrm{MeV}]$	$\tau[\mathrm{ps}]$	$\Gamma[\mathrm{MeV}]$
B_s^0	$5366.3 \quad \pm 0.6$	$1.470 \quad \pm 0.027$	$-$
J/ψ	3096.916 ± 0.011	$-$	0.0932 ± 0.0021
ϕ	1019.455 ± 0.020	$-$	$4.26 \quad \pm 0.04$

Tab. 6.1: *PDG [86] values for the mass, lifetime or decay width of B_s^0, J/ψ and ϕ.*

The primary focus is on the resolution for the quantities of interest for each of the five cases and whether the ideal case resolution is recovered with the alignment algorithm described in

Chapter 4. Since one has access to the Monte Carlo information, the resolution on a quantity of interest q can be determined from the residual distribution

$$\Delta q = q_{\text{rec}} - q_{\text{MC}}, \tag{6.1}$$

where q_{rec} is the reconstructed value and q_{MC} is the Monte Carlo value for q, respectively. In this case the resolution on the quantity q is given by the width of the residual distribution, which in this chapter is denoted as

$$\hat{\sigma}_q \equiv \sigma\left(q_{\text{rec}} - q_{\text{MC}}\right). \tag{6.2}$$

With real data, the resolution can be estimated by introducing a resolution model for a given quantity in a likelihood fit, which is typically described by a Gaussian. In this chapter the estimated resolution on some quantity q using this method is denoted as σ_q. For example, the ϕ resonance signal can be described as a Breit-Wigner convoluted with a Gaussian. By fitting this model to the K^+K^- invariant mass distribution one obtains an estimate for the width Γ_ϕ of the ϕ resonance and an estimate for the detector resolution σ_ϕ. The main difference between this method and the former method is that in the former method the reconstructed K^+K^- invariant mass cancels against the Monte Carlo K^+K^- invariant mass such that the difference is given by the detector resolution. Note that, in principle, $\hat{\sigma}_\phi$ should equal σ_ϕ.

Where appropriate both methods are used to illustrate that the resolution σ_q on some quantity q can be determined with real data and that it is consistent with the resolution $\hat{\sigma}_q$ as determined from the Monte Carlo information.

6.3.1 The reconstructed mass of the B_s^0, J/ψ and ϕ

The lifetimes of the ϕ and J/ψ is in the order of 10^{-22} s and 10^{-20} s, respectively. Consequently, their flight distances are so small that they cannot be observed and $B_s^0 \to J/\psi\phi$ decays can be considered as four prong decays at the decay vertex of the B_s^0. In this case the invariant mass of the B_s^0 is given by the norm of the four vector sum of the momenta of the four charged particle tracks.

To get an impression of the effect of mis-alignments in the tracking stations on the reconstructed invariant mass of a particle, consider a two prong decay, *e.g.*, $J/\psi \to \mu^+\mu^-$. In this case the invariant mass is given by

$$\mathrm{M}^2 = 2\left[\mathrm{M}_\mu^2 + E_+E_- - \mathrm{p}_+\,\mathrm{p}_-\cos\theta\right], \tag{6.3}$$

where $+$ and $-$ denotes the positive muon and negative muon, respectively. Here $E_\pm$ and $p_\pm$ is the energy and reconstructed momentum of the muons. The angle θ is the opening angle between the muons. In the limit $\mathrm{p} \gg \mathrm{M}$, which is assumed for the remainder of this chapter, Eq. 6.3 reduces to

$$\mathrm{M}^2 = 2\,\mathrm{p}_+\,\mathrm{p}_-\left(1 - \cos\theta\right). \tag{6.4}$$

The reconstructed momenta are inferred from the change in the slope of the track between the VELO and T-stations, due to the bending of the track in the magnetic field. The energy $E_\pm$ of the muons are inferred from their reconstructed momentum and the *PDG* value of the muon mass. For example, the four vector for the positive muon is

$$(E_+, \boldsymbol{p}_+) = \left(\sqrt{M_\mu^2 + \mathrm{p}_+^2}, \frac{\mathrm{p}_+}{\sqrt{t_x^2 + t_y^2 + 1}}\left(t_x, t_y, 1\right)\right), \tag{6.5}$$

where M_μ is the *PDG* [86] mass of the muon and p_{μ^+} its measured momentum. Here t_x and t_y are the track slopes.

The initial slope of the tracks and their origin is determined from the VELO hits on the tracks. The angle θ between the particle three momenta $\boldsymbol{p}_+$ and $\boldsymbol{p}_-$ corresponds to the angle between the slopes of tracks of the positive and negative muons and is given by

$$\cos\theta = \frac{t_x^+ t_x^- + t_y^+ t_y^- + 1}{n^+ n^-}, \tag{6.6}$$

where

$$n^i = \sqrt{{t_x^i}^2 + {t_y^i}^2 + 1} \tag{6.7}$$

is the norm of the slope of track i.

Using Eq. 6.4, the variance on the reconstructed mass can be estimated, ignoring the correlations between the momenta and directions of the particles*, as

$$\begin{aligned}\sigma_{\mathrm{M}}^2 &= \sum_n \sigma_{\mathrm{p}_n}^2 \left[\frac{\partial\,\mathrm{M}^2}{\partial\,\mathrm{p}_n}\right]^2 + \sigma_\theta^2 \left[\frac{\partial\,\mathrm{M}^2}{\partial\theta}\right] \\ &= \frac{\mathrm{M}^2}{4}\left[\left(\frac{\sigma_+^2}{\mathrm{p}_+^2} + \frac{\sigma_-^2}{\mathrm{p}_-^2}\right) + \sigma_\theta^2\left(\frac{\sin\theta}{1-\cos\theta}\right)^2\right],\end{aligned} \tag{6.8}$$

where in the last step Eq. 6.4 is used to express the derivatives in terms of the reconstructed invariant mass. In the high momentum limit $\theta \to \epsilon$†, $\cos\epsilon \to 1 - \frac{1}{2}\epsilon^2$, $\sin\epsilon \to \epsilon$ and in the case $\mathrm{p}_+ = \mathrm{p}_- = \frac{1}{2}\,\mathrm{p}$, the estimated variance on the reconstructed mass

$$\mathrm{M} = \frac{1}{2}\,\mathrm{p}\,\theta \tag{6.9}$$

reduces to

$$\sigma_{\mathrm{M}}^2 = \mathrm{M}^2\left[\frac{\sigma_{\mathrm{p}}^2}{\mathrm{p}^2} + \frac{\sigma_\theta^2}{\theta^2}\right], \tag{6.10}$$

where $\sigma_{\mathrm{p}} = \sqrt{\sigma_+^2 + \sigma_-^2}$.

From Eq. 6.10 one observes that for small opening angles that σ_θ is relatively more important than σ_p and *vice versa* for large opening angles. In addition, mis-alignments in the VELO will affect the second term in Eq. 6.8, while mis-alignments in the T-stations will affect the first term in Eq. 6.8.

The $\mu^+\mu^- K^+ K^-$, $\mu^+\mu^-$ and K^+K^- invariant mass distributions for each of the five cases are shown in Fig. 6.3a, Fig. 6.3b and Fig. 6.3c, respectively. Both mis-alignments in the T-Stations and VELO have a considerable effect on the resolution on the B_s^0 and J/ψ mass signal. However, there are no visible effects on the ϕ mass signal.

The mean mass and resolution for B_s^0 and J/ψ for each of the five cases are listed Tab. 6.2. These were determined by fitting a *Crystal Ball* probability distribution function [87], *i.e.* a Gaussian with a radiative tail to account for the energy loss of the muons due to final state radiation, to

*These correlations are sufficiently small that, for the sake of argument, they can be ignored.

†Besides simplifying the calculations considerably, it is also a reasonable assumption given the geometry of the LHC*b* detector.

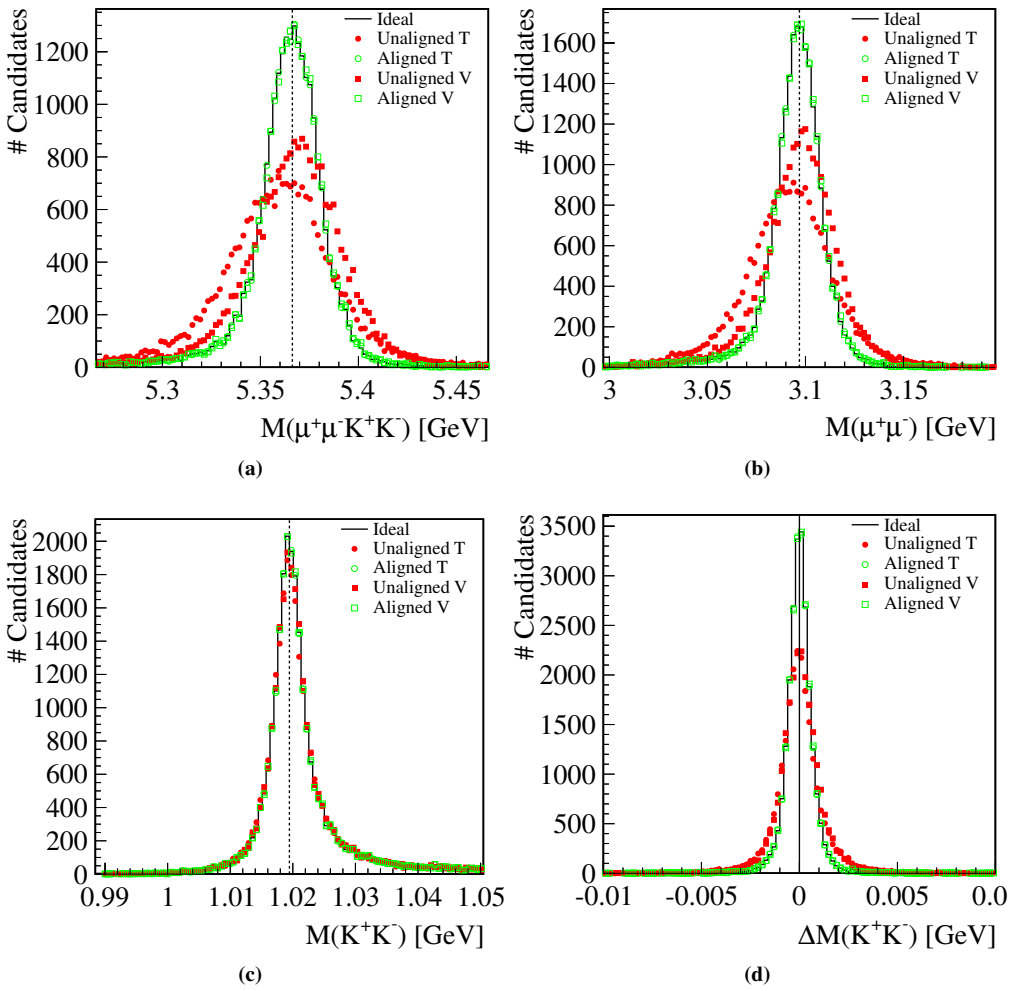

Fig. 6.3: *Invariant mass distributions for (a) B_s^0, (b) J/ψ and (c) ϕ, and (d) the residual mass distribution for the ϕ. The dashed lines indicate the PDG value of the masses for the B_s^0 and J/ψ.*

the distributions in Fig. 6.3a and Fig. 6.3b. For the unaligned V and unaligned T cases, both the central value as well as the resolution are affected. Comparing the values of the aligned cases to the ideal case one observes that they are compatible and therefore one can conclude, as hinted by Fig. 6.3a and Fig. 6.3b, that the nominal resolution is fully recovered by the alignment procedure.

Although there is no visible effect of mis-alignments on the K^+K^- invariant mass distribution, see Fig. 6.3c, this not the case for the residual K^+K^- mass distribution, see Fig. 6.3d, which is defined as the difference between the reconstructed K^+K^- invariant mass and the Monte Carlo K^+K^- invariant mass. The resolution on the K^+K^- invariant mass remains dominated by its natural width as confirmed by fitting a Breit-Wigner convoluted with a Gaussian to the distributions in Fig. 6.3c.

The mean ϕ mass, width and resolution, as determined from the fit and from the residual

Case	$M_{B_s^0}$ [MeV]	$\sigma_{B_s^0}$ [MeV]	$M_{J/\psi}$ [MeV]	$\sigma_{J/\psi}$ [MeV]
Ideal	5366.6 ± 0.1	14.69 ± 0.09	3096.99 ± 0.09	11.18 ± 0.07
Unaligned T	5359.6 ± 0.2	25.4 ± 0.2	3091.9 ± 0.2	19.1 ± 0.1
Aligned T	5366.7 ± 0.1	14.68 ± 0.09	3097.05 ± 0.09	11.19 ± 0.07
Unaligned V	5368.8 ± 0.2	21.6 ± 0.1	3098.4 ± 0.1	15.7 ± 0.1
Aligned V	5366.9 ± 0.1	14.68 ± 0.09	3097.19 ± 0.09	11.20 ± 0.07

Tab. 6.2: *The fitted mass and resolution for B_s^0 and J/ψ, respectively. These are obtained by fitting a Crystal Ball PDF, i.e. a Gaussian with an radiative tail, to the B_s^0 and J/ψ distributions shown in Fig. 6.3a and Fig. 6.3b, respectively.*

distribution, are listed in Tab. 6.3. Again, as for the B_s^0 and J/ψ, the aligned cases are compatible with the nominal (ideal) resolution. In addition, one observes that the dominant contribution to the width of the ϕ signal is its decay width and not the invariant mass resolution.

Case	M_ϕ [MeV]	Γ_ϕ [MeV]	σ_ϕ [MeV]	$\sigma_\phi(\Gamma_\phi^{\text{PDG}})$ [MeV]	$\hat{\sigma}_\phi^{\text{RMS}}$ [MeV]
Ideal	1019.66 ± 0.02	4.27 ± 0.07	0.74 ± 0.08	0.75 ± 0.05	0.767 ± 0.004
Unaligned T	1019.66 ± 0.02	4.37 ± 0.08	1.09 ± 0.07	1.17 ± 0.04	1.176 ± 0.006
Aligned T	1019.66 ± 0.02	4.28 ± 0.07	0.74 ± 0.08	0.75 ± 0.05	0.746 ± 0.004
Unaligned V	1019.72 ± 0.02	4.28 ± 0.07	1.02 ± 0.07	1.04 ± 0.04	1.051 ± 0.005
Aligned V	1019.66 ± 0.02	4.28 ± 0.07	0.74 ± 0.08	0.76 ± 0.05	0.746 ± 0.004

Tab. 6.3: *The fitted mass, width, resolution (without and with Γ_ϕ fixed to its PDG value of $\Gamma_\phi^{PDG} = 4.26\,\text{MeV}$), and width of the residual for ϕ. The first three columns are obtained by fitting a Breit-Wigner convoluted with a Gaussian to the distributions shown in Fig. 6.3c, the fourth column lists the mass resolution in the case Γ_ϕ is constrained to Γ_ϕ^{PDG}, and the fith column lists the RMS of the ϕ mass residual distribution.*

From Tab. 6.2 one observes that mis-alignments in the VELO and in the T-stations lead to a degradation in the $\mu^+\mu^-K^+K^-$ invariant mass resolution compared to the ideal case. This leads to an increase of the observed background and consequently to a dilution of the purity of the signal, *i.e.* the background over signal ratio B/S is diluted by the same amount. This gives a worse sensitivity, *i.e.* the statistical uncertainty on the parameters is proportional to

$$\sigma_{\text{phys}} \propto \frac{\sqrt{S+B}}{S}, \tag{6.11}$$

where S is the number of signal events and B the number of signal like background events.

For $B_s^0 \to J/\psi\phi$ the background remaining after the final selection is relatively small, B/S is approximately 0.5 for long lived background [4], such that the effects of a worse mass resolution are small. However, for the analyses of B decays with a poor S/B, *e.g.* $B_s^0 \to \mu^+\mu^-$, or in which different decays with identical topologically states need to be kinematically separated, *e.g.* $\overline{B_d^0} \to K^-\pi^+$ versus $B_s^0 \to K^-\pi^+$, the effects of mis-alignments on the mass resolution is important [41, 88].

6.3.2 The reconstructed B_s^0 proper time

In the case of $B_s^0 \to J/\psi\phi$, where the background is mostly dominated by combinatorial background, which leads to a peaking background around $t = 0\,\text{ps}$ in the B_s^0 proper time signal, the

effect of mis-alignments in the tracking stations on the proper time resolution and, consequently, on the sensitivity on ϕ_s is of greater importance.

The proper time t of a particle in the lab frame, given its momentum $\boldsymbol{p}$, decay vertex $\boldsymbol{x}_{\mathrm{SV}}$ and the primary vertex $\boldsymbol{x}_{\mathrm{PV}}$, is modelled as follows in the vertex fit [71]:

$$\boldsymbol{x}_{\mathrm{SV}} - \boldsymbol{x}_{\mathrm{PV}} = \frac{\boldsymbol{p}}{\mathrm{p}} d = \frac{\boldsymbol{p}}{m} t, \tag{6.12}$$

where d is the decay length of the particle. The χ^2 of this kinematic constraint is a gauge of how well a reconstructed B_s^0 with momentum $\boldsymbol{p}$ points to a given primary vertex.

Without a vertex fit, a suitable estimate of the proper time is given by

$$t = \frac{m}{\mathrm{p}^2} \boldsymbol{p} \cdot (\boldsymbol{x}_{\mathrm{SV}} - \boldsymbol{x}_{\mathrm{PV}}) = \frac{m}{p} d. \tag{6.13}$$

From this the variance on the proper time can be estimated as

$$\begin{aligned} \sigma_t^2 &= \sigma_p^2 \left[\frac{\partial t}{\partial p}\right]^2 + \sigma_d^2 \left[\frac{\partial t}{\partial d}\right]^2 \\ &= \left[\frac{\sigma_p}{p}\right]^2 t^2 + \left[\frac{M}{p}\right]^2 \sigma_d^2. \end{aligned} \tag{6.14}$$

where σ_p/p and σ_d are the average relative momentum resolution and decay length resolution for the particle, respectively.

As in the case of the estimated variance on the invariant mass of a two prong decay, see Eq. 6.10, one can express Eq. 6.14 in terms of the opening angle θ as follows: using some trigonometry, one can show that

$$\sigma_d \propto \frac{\sigma_{\text{slopes}}}{\sin\theta} L, \tag{6.15}$$

where σ_{slopes} is the variance on the tracks slopes and L is the extrapolation distance. Using the above the estimated variance on the proper time, in the limit $\theta \to \epsilon$, is

$$\sigma_t^2 \propto \left[\frac{\sigma_p}{p}\right]^2 t^2 + \left[\frac{\sigma_{\text{slopes}}}{4} \frac{L}{c}\right]^2, \tag{6.16}$$

where Eq. 6.9 is used to express M in terms of p, leading to the factor $1/4$.

In other words, the second term in Eq. 6.14 is independent of the reconstructed momentum or mass of a particle and is purely given by the resolution on the slopes, which in turn depends on the VELO hit resolution. Furthermore, for short living particles, $t \approx 0\,\mathrm{ps}$,

$$\sigma_t \propto \frac{1}{4} \sigma_{\text{slopes}} \frac{L}{c}, \tag{6.17}$$

i.e. the second term in Eq. 6.14 dominates for short living particles and can be considered a constant. The first term in Eq. 6.14 starts to dominate for long living particles with a proper time

$$t \to \frac{\mathrm{p}}{\sigma_{\mathrm{p}}} \frac{\mathrm{M}}{\mathrm{p}} \sigma_d. \tag{6.18}$$

To get an impression of the sizes of the various contributions involved in the proper time

resolution, consider the following numerical example. The average extrapolation distance, *i.e.* the distance from the first VELO measurement to the primary vertex, is approximately $116\,\mathrm{mm}$ and the average resolution on the reconstructed slopes is approximately of $0.5\,\mathrm{mrad}$. This gives a proper time resolution at $t = 0$, *i.e.* the second term in Eq. 6.14, in the order of $40\,\mathrm{fs}$. In the ideal case the average B_s^0 relative resolution is approximately $\delta p/p = 3‰$. Therefore, the first term in Eq. 6.14 becomes equally important as the second term when t is approximately seven times the mean B_s^0 lifetime.

From Eq. 6.14 and from the example given above one concludes that only for very long lifetimes σ_t is dominated by the momentum resolution, while for shorter lifetimes σ_t is dominated by the decay distance resolution which in turn depends on the resolution on the slopes. In other words, one expects T-station mis-alignments to affect the proper time resolution for long living particles and VELO mis-alignment to affect the proper time resolution for short living particles. This is confirmed in Fig. 6.4, which shows the proper time resolution in bins of true B_s^0 proper time.

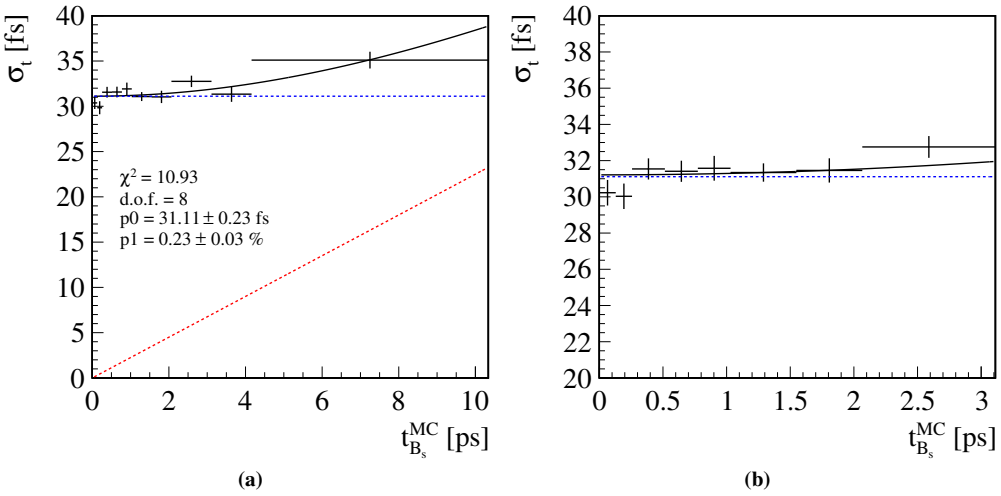

Fig. 6.4: *The proper time resolution $\hat{\sigma}_t$ versus the true proper time of the B_s^0 for the the ideal case up to (a) seven times the B_s^0 lifetime and (b) two times the B_s^0 lifetime. The model fitted to the points is $\sigma_t = \sqrt{p0^2 t^2 + p1^2}$.*

The B_s^0 proper time distribution for each of the five cases is shown in Fig. 6.5a. One observes, as expected, that mis-alignments in T-stations have negligible effect on the lifetime resolution compared to mis-alignments in the VELO for small lifetimes. In other words, the smearing of the lifetime around $t = 0$, as a result of the detector resolution, can be attributed to the decay length resolution, which in turn depends on the VELO measurements.

The width of the proper time residual in bins of proper time for each of the five cases is shown in Fig. 6.5b, and the relative B_s^0 momentum residual distribution and decay length residual distribution are shown in Fig. 6.5c and Fig. 6.5d, respectively. From the latter two one observes that mis-alignments in the VELO have little affect on the momentum resolution and that mis-alignments in the T-Stations have little affect on the decay length resolution. From the former one observes that the lifetime resolution decreases with increasing t. This rise is proportional to the momentum resolution, see Eq. 6.14.

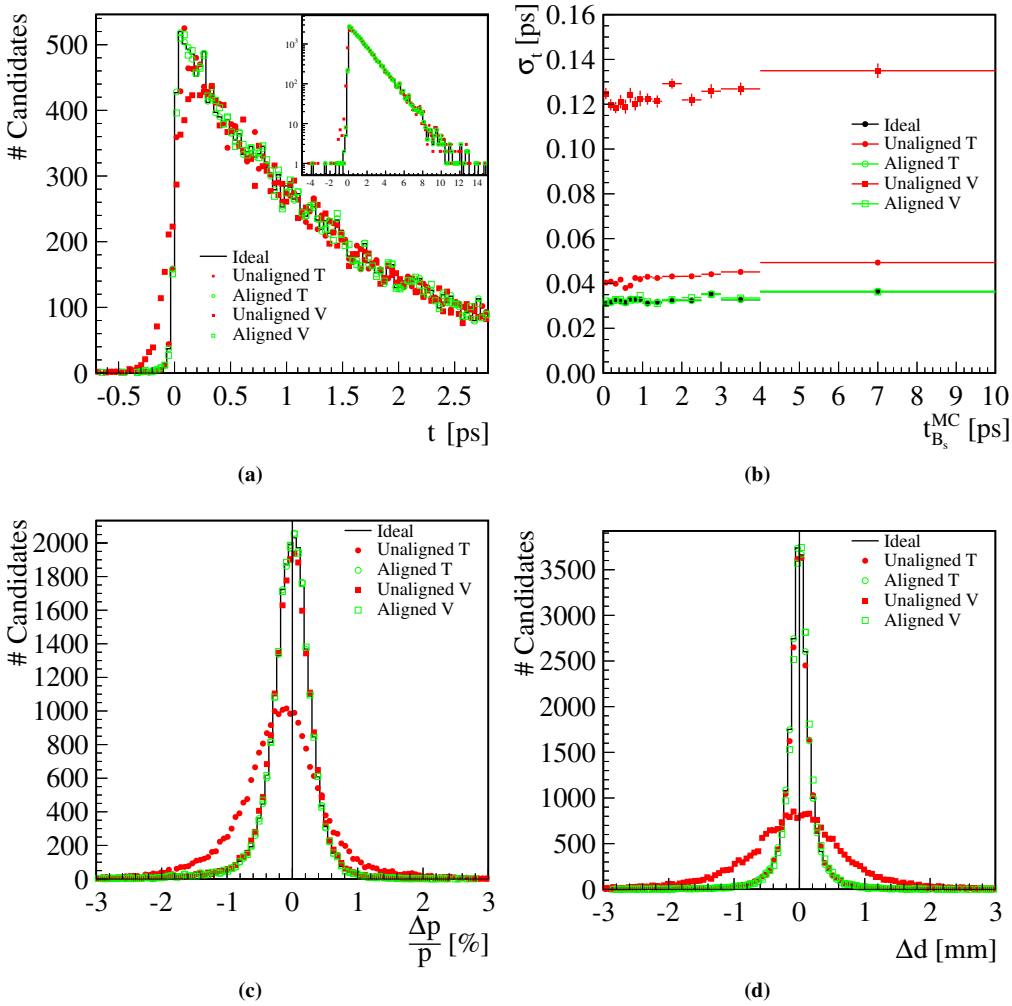

Fig. 6.5: *The (a) reconstructed proper time, (b) proper time resolution versus proper time, (c) momentum residual distribution and (d) decay length residual distribution for the B_s^0 for the five cases.*

Interestingly, see Fig. 6.5b, mis-alignments in the T-stations appear to have a small effect on the proper time resolution at $t = 0$. This is due to the (displaced) measurements in the T-stations pulling on the track slopes in the VELO in the track fitting procedure. Refitting the associated tracks of the particles twice, once to get a momentum estimate using all the hits on the track in the track fitting procedure and subsequently using only the VELO hit information and this estimated momentum, this effect disappears, see Fig. 6.6.

The proper time resolution for each case can be determined by fitting an exponential decay convoluted with a Gaussian to the distributions in Fig. 6.5a. Where the Gaussian describes the smearing of the lifetime due to the detector resolution around $t = 0$, which leads to negative tail. The mean B_s^0 lifetime and resolution, as well as the average B_s^0 momentum resolution and decay length resolution, for each of the five cases are listed Tab. 6.4. The dominant contribution to the

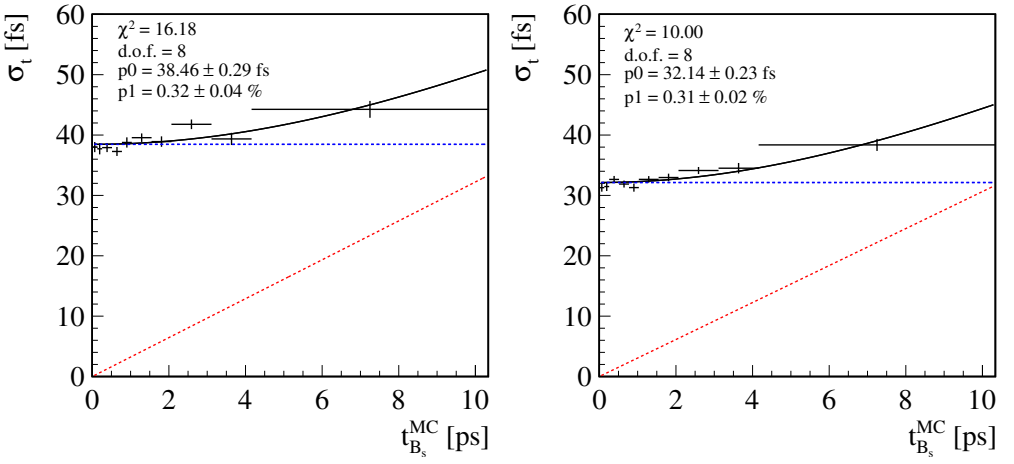

Fig. 6.6: *The width of the proper time residual in bins of proper time in the case of T-station mis-alignments where (a) all the hits on a track are used in the track fitting procedure and (b) only the VELO hits on a track combined with a momentum estimate, which is obtained from first fitting the track using all the hits on the track, are used in the track fitting procedure.*

lifetime resolution is from the decay length resolution. Again, as for the mass resolutions, the aligned cases are compatible with the ideal case.

Case	τ [ps]	σ_t [fs]	$\hat{\sigma}_t$ [fs]	$\frac{\delta p}{p}$ [‰]	$\hat{\sigma}_d$ [μm]	$\frac{M}{p}\hat{\sigma}_d$ [fs]
Ideal	1.455 ± 0.010	29.0 ± 2.0	33.1 ± 0.2	2.97 ± 0.01	159.0 ± 0.8	32.4 ± 0.2
Unaligned T	1.464 ± 0.010	36.0 ± 2.0	39.1 ± 0.2	5.62 ± 0.03	161.2 ± 0.8	33.1 ± 0.2
Aligned T	1.455 ± 0.010	29.0 ± 2.0	33.1 ± 0.2	2.96 ± 0.01	159.0 ± 0.8	32.4 ± 0.2
Unaligned V	1.441 ± 0.010	160.0 ± 3.0	128.5 ± 0.6	3.09 ± 0.01	659.0 ± 3.0	142.6 ± 0.7
Aligned V	1.457 ± 0.010	27.0 ± 2.0	33.3 ± 0.2	2.97 ± 0.01	160.0 ± 0.8	32.6 ± 0.2

Tab. 6.4: *The mean lifetime and resolution, momentum resolution and decay length resolution for B_s^0 for the five cases. The average B_s^0 momentum is approximately* $90\,\mathrm{GeV}$.

From the values in Tab. 6.4 one can estimate the sensitivity to the physics parameters. One can show that the sensitivity to ϕ_s is diluted by a factor [89]

$$D \propto \exp\left[\left(\frac{\Delta m_s}{\sqrt{2}}\sigma_t\right)^2\right], \tag{6.19}$$

where Δm_s is the B_s^0 oscillation frequency. In other words, the sensitivity on ϕ_s decreases as

$$\sigma_t \to \frac{\sqrt{2}}{\Delta m_s} \approx 80\,\mathrm{fs}\,, \tag{6.20}$$

where Δm_s is approximately $18\,\mathrm{ps}^{-1}$ [15]. Therefore, one remains sensitive to ϕ_s as long as

σ_t remains small compared to the effective oscillation period of $80\,\mathrm{fs}$. From the proper time resolutions listed in Tab. 6.4 one can conclude that mis-alignments in the T-stations have little effect on the sensitivity on ϕ_s, whereas mis-alignments in the VELO have a significant effect on the sensitivity on ϕ_s.

6.3.3 Resolutions on the transversity angles

The angular distribution and the corresponding residual distribution for the transversity angle θ_tr are shown in Fig. 6.7a and Fig. 6.7b, respectively. In addition, the residual distributions for the angles ϕ_tr and ψ_tr are shown in Fig. 6.7c and Fig. 6.7d, respectively. The corresponding width of the residual distribution for each of the five cases are listed in Tab. 6.5. One observes that both mis-alignments in the VELO or T-stations lead to a worse resolution on the angles compared to the ideal case. Again, as for the mass and lifetime resolutions, the aligned cases are compatible with the ideal case. In the maximum likelihood fit [24, 25] the transversity amplitudes

Case	$\hat{\sigma}^{\mathrm{RMS}}_{\theta_\mathrm{tr}}$ [mrad]	$\hat{\sigma}^{\mathrm{RMS}}_{\phi_\mathrm{tr}}$ [mrad]	$\hat{\sigma}^{\mathrm{RMS}}_{\psi_\mathrm{tr}}$ [mrad]
Ideal	19.98 ± 0.09	20.31 ± 0.10	15.59 ± 0.07
Unaligned T	23.56 ± 0.11	25.59 ± 0.12	23.74 ± 0.11
Aligned T	20.04 ± 0.09	20.31 ± 0.10	15.59 ± 0.07
Unaligned V	26.67 ± 0.12	26.97 ± 0.13	19.00 ± 0.08
Aligned V	19.97 ± 0.09	20.26 ± 0.10	15.58 ± 0.07

Tab. 6.5: *The resolutions on the transversity angles for each of the five cases.*

are extracted from the transversity angular distributions and the angular resolutions, generally, are ignored. This is valid as long as the angular resolution is small compared to the variation of the PDF that describes the angular distributions. Given that the angular distribution of θ_tr, see Fig. 6.7a, varies smoothly for alignment cases, one may conclude that the effect of a worse angular resolution on the sensitivity on ϕ_s is negligible. Angular resolution sensitivity studies have shown that a degradation of the angular resolution by about a factor three is needed to have an observable effect on the sensitivity on the physics parameters.

6.3.4 Applying a J/ψ mass constraint in the vertex fit

The mis-alignments in the tracking stations lead to a poor estimation of the momenta of the charged particles which in turn affects the mass resolution. To obtain a better estimate of the momenta of the particles and thereby an improved mass resolution on the B^0_s, one can apply a J/ψ mass constraint in the vertex fit. The momentum of the J/ψ, in the case the reconstructed J/ψ mass is constrained to its *PDG* value in the vertex fit, is given by

$$\boldsymbol{p}' = \boldsymbol{p} - \mathrm{Cov}(\mathrm{M}, \boldsymbol{p})\,\mathrm{Var}(\mathrm{M})^{-1}(\mathrm{M} - \mathrm{M}_{\mathrm{PDG}}) \tag{6.21}$$

with variance

$$\mathrm{Var}(\boldsymbol{p}') = \mathrm{Var}(\boldsymbol{p}) - \mathrm{Cov}(\mathrm{M}, \boldsymbol{p})\,\mathrm{Var}(\mathrm{M})^{-1}\,\mathrm{Cov}(\mathrm{M}, \boldsymbol{p}), \tag{6.22}$$

where $\mathrm{Var}(\mathrm{M})$ and $\mathrm{Cov}(\mathrm{M}, \boldsymbol{p})$ is the variance on the reconstructed J/ψ mass and the covariance between the reconstructed J/ψ mass and momentum, respectively.

Though a J/ψ mass constraint improves the resolution on the B^0_s mass, it does not completely eliminate the effects of mis-alignments on the B^0_s mass and resolution. In other words, in the presence of mis-alignments the statistical errors will be underestimated. This is illustrated in

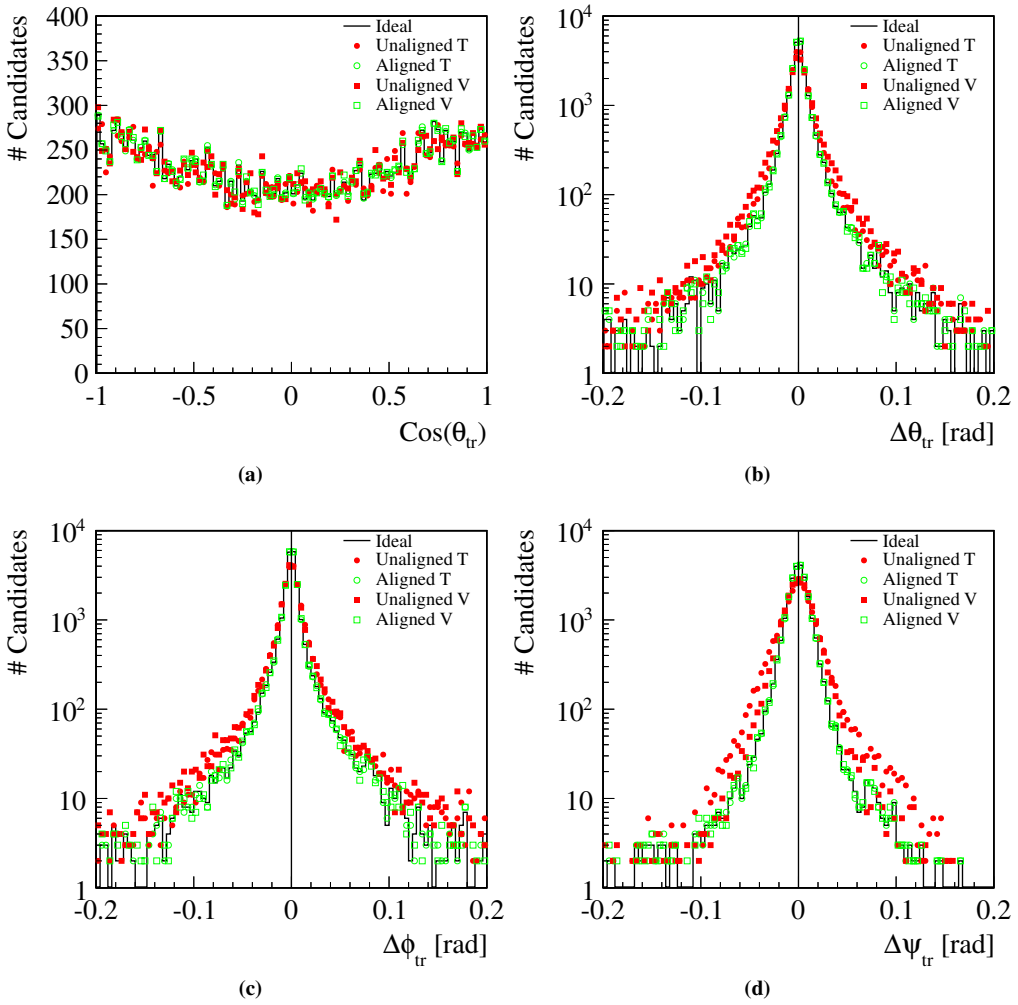

Fig. 6.7: *The (a) angular distribution for θ_{tr} and residual distributions for θ_{tr}, ϕ_{tr}, and ψ_{tr}, respectively, for each of the five cases.*

Fig. 6.8 which shows the pull distribution for the J/ψ mass. Note that also in the ideal case the estimated error on the J/ψ mass is underestimated, which is a consequence of the fact that the error on the momentum is underestimated in the LHC*b* reconstruction procedure [59].

The B_s^0 mass distribution, in the case the J/ψ mass is constrained to its *PDG* value in the vertex fit, is shown in Fig. 6.9a, Fig. 6.9b and Fig. 6.9c for the ideal, unaligned T and unaligned V cases, respectively. One observes that the J/ψ mass constraint leads to a significant improvement on the B_s^0 mass resolution for all three cases. Comparing the mean B_s^0 mass and resolution to the values in Tab. 6.2, which were obtained without a J/ψ mass constraint, one observes that the J/ψ mass constraint improves the resolution by a factor 1.4 in the ideal case, and by a factor 1.9 and 1.7 in the unaligned T and unaligned V cases, respectively. In addition, from Fig. 6.9b and Fig. 6.9b one observes that the J/ψ mass constraint reduces the bias on the B_s^0 mass.

The resolution on the B_s^0 lifetime and transversity angles with a J/ψ mass constraint are

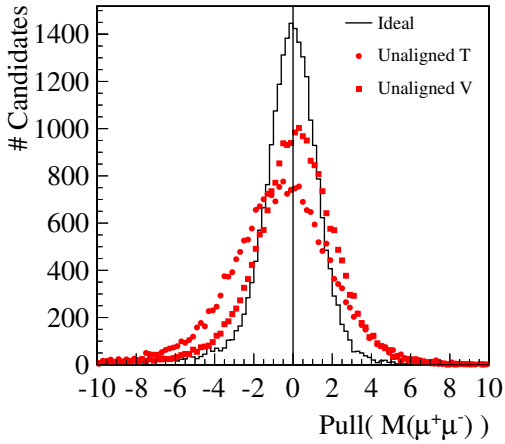

Case	μ	σ
Ideal	-0.054 ± 0.009	1.306 ± 0.007
Unaligned T	0.141 ± 0.013	2.489 ± 0.014
Unaligned V	-0.598 ± 0.017	1.972 ± 0.017

Fig. 6.8: *Pull distribution for the $\mu^+\mu^-$ invariant mass for the ideal, unaligned T-stations and unaligned VELO cases.*

listed in Tab. 6.6. Interestingly, comparing the resolutions in Tab. 6.6 to the resolutions in Tab. 6.4 and Tab. 6.5, applying a J/ψ mass constraint in the vertex fit does not lead to a significant change on the B_s^0 lifetime or on the angular resolutions as compared to the B_s^0 mass resolution.

Case	τ [ps]	σ_t [fs]	$\delta\theta_{\text{tr}}^{\text{RMS}}$ [mrad]	$\delta\phi_{\text{tr}}^{\text{RMS}}$ [mrad]	$\delta\psi_{\text{tr}}^{\text{RMS}}$ [mrad]
Ideal	1.464 ± 0.010	30.0 ± 2.0	20.43 ± 0.09	21.02 ± 0.10	16.33 ± 0.08
Unaligned T	1.472 ± 0.010	33.0 ± 2.0	23.94 ± 0.11	26.06 ± 0.12	24.37 ± 0.11
Unaligned V	1.451 ± 0.009	159.0 ± 3.0	27.07 ± 0.12	27.59 ± 0.13	19.60 ± 0.09

Tab. 6.6: *The mean B_s^0 lifetime and resolution, and resolutions on the transversity angles after applying J/ψ mass constraint in the vertex fit.*

In addition to constraining the J/ψ mass to its *PDG* value in the vertex fit, one may also constrain the B_s^0 mass to its *PDG* value in the vertex fit in the hope of improving the reconstructed B_s^0 momentum. Similarly, as in the case of only constraining the J/ψ mass in the vertex fit, the combination of a J/ψ and B_s^0 mass constraint does not lead to a significant change on the B_s^0 lifetime or on the angular resolutions as compared to the B_s^0 mass resolution, see Tab. 6.7. In some cases it even leads to a slightly worse resolution compared to the unconstrained results, see Tab. 6.4 and Tab. 6.5.

Case	τ [ps]	σ_t [fs]	$\delta\theta_{\text{tr}}^{\text{RMS}}$ [mrad]	$\delta\phi_{\text{tr}}^{\text{RMS}}$ [mrad]	$\delta\psi_{\text{tr}}^{\text{RMS}}$ [mrad]
Ideal	1.473 ± 0.010	29.0 ± 2.0	21.62 ± 0.10	22.54 ± 0.10	18.02 ± 0.08
Unaligned T	1.480 ± 0.010	35.0 ± 2.0	25.11 ± 0.11	26.78 ± 0.12	25.09 ± 0.11
Unaligned V	1.461 ± 0.009	159.0 ± 3.0	27.84 ± 0.13	28.59 ± 0.13	20.84 ± 0.10

Tab. 6.7: *The mean B_s^0 lifetime and resolution, and resolutions on the transversity angles after applying a combined J/ψ and B_s^0 mass constraint in the vertex fit.*

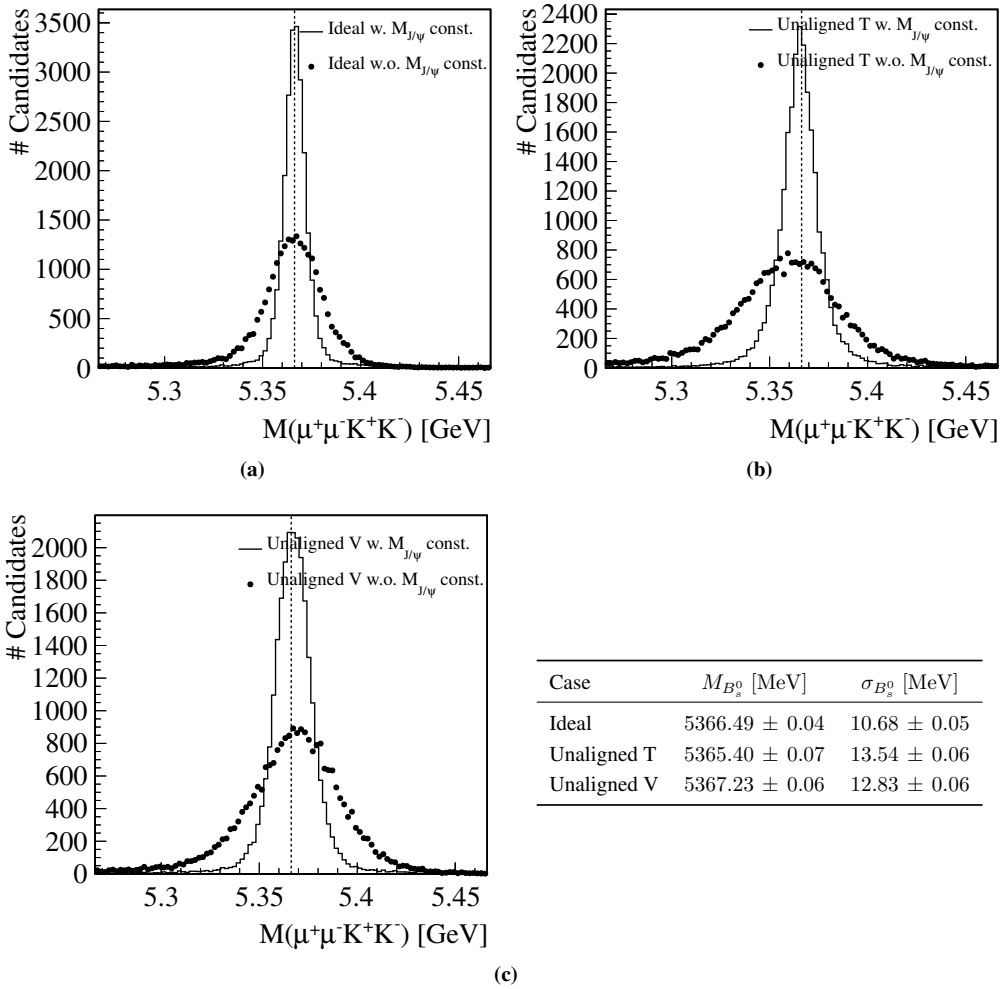

Case	$M_{B_s^0}$ [MeV]	$\sigma_{B_s^0}$ [MeV]
Ideal	5366.49 ± 0.04	10.68 ± 0.05
Unaligned T	5365.40 ± 0.07	13.54 ± 0.06
Unaligned V	5367.23 ± 0.06	12.83 ± 0.06

Fig. 6.9: *The B_s^0 mass distribution before and after applying a J/ψ mass constraint in the vertex fit for (a) ideal, (b) unaligned T and (c) unaligned V cases. The dashed line indicates the PDG value for the B_s^0 mass. The mean B_s^0 mass and resolution without a J/ψ mass constraint are listed in Tab. 6.2*

6.4 Conclusion

In this chapter the effects of mis-alignments in the tracking detectors, *i.e.* the VELO and T-stations, on the reconstruction of the decay $B_s^0 \to J/\psi\phi$ are studied. To get a qualitative impression of how mis-alignments in the VELO or T-stations affect the mass of the B_s^0, J/ψ and ϕ, the lifetime of the B_s^0 and the transversity angles, the VELO modules, the IT boxes and OT C-frames are displaced by $5 \times \sigma_{\text{res}}$ along their primary measurement directions, where σ_{res} is the hit resolution and is typically $8\,\mu\text{m}$, $60\,\mu\text{m}$ and $200\,\mu\text{m}$ for the VELO, IT and OT, respectively. Mis-alignments in the VELO affect the track slopes and consequently the vertex positions, while mis-alignments in the T-station affect the momenta of the tracks. Though these scenarios are conservative compared to the actual survey resolution, which is typically a factor two better, such

mis-alignments can be resolved with the alignment algorithm.

It is shown that both mis-alignments in the VELO and T-stations have an effect on the resolution on the reconstructed $\mu^+\mu^-$ invariant mass distribution and consequently on the resolution on the reconstructed $\mu^+\mu^-K^+K^-$ mass distribution. The resolution on the reconstructed K^+K^- invariant mass is dominated by the natural width of the ϕ resonance. The degradation in the resolution on the reconstructed $\mu^+\mu^-K^+K^-$ invariant mass implies an increase in the number of reconstructed background events, *i.e.* a dilution of the purity of the sample. In the case of $B_s^0 \to J/\psi\phi$, the effects of worse mass resolution is expect to be small, since the background is predominantly (combinatorial) prompt background. However, this may not be the case for analyses of B decays with a poor S/B, *e.g.* $B_s^0 \to \mu^+\mu^-$, or different decays with topologically identical states that need to be kinematically separated, *e.g.* $\overline{B_d^0} \to K^-\pi^+$ versus $B_s^0 \to K^-\pi^+$.

In the case of $B_s^0 \to J/\psi\phi$ the proper time resolution is of greater importance. It is shown that the B_s^0 lifetime resolution is dominated by the decay distance resolution, which in turn depends mostly on the VELO. The effects of T-station mis-alignments on the proper time resolution appear to be negligible compared to the VELO mis-alignments.

Similarly, as for the resolutions on the reconstructed invariant masses, the resolutions on the transversity angles are affected by both VELO and T-station mis-alignments. These are expected to have an negligible effect on the extraction of the transversity amplitudes and ϕ_s, as long as they remain small compared to the variation of the angular distributions.

Though the introduced mis-alignments are large compared to the survey resolution, it is shown that the various resolutions, once the detectors have been aligned, are compatible with the ideal case.

Finally, it is shown that applying a J/ψ mass constraint in the vertex fit leads to an improvement of up to a factor two in the reconstructed $\mu^+\mu^-K^+K^-$ invariant mass resolution. Interestingly, a J/ψ mass constraint has no significant effect, as compared to the $\mu^+\mu^-K^+K^-$ mass resolution, on the resolution on the B_s^0 lifetime and the transversity angles. Furthermore, there is no additional gain by constraining the B_s^0 mass, in addition to the J/ψ mass constraint, in the vertex fit.

Summary

The LHC at CERN provides a new testing ground for the Standard Model of elementary particles as well an opportunity to further explore the mysteries and expand our knowledge of Nature. The Standard Model is a theory based on experimental observations of particle interactions at collider experiments and at cosmic ray experiments. Despite the successes of the Standard Model it does not provide a complete picture of the beautiful intricately woven tapestry called Nature. To further explore the finest threads of this tapestry and to validate or exclude the Standard Model or extensions thereof, so-called New Physics Models, particle physicists at the LHC have built precision instruments to measure fundamental parameters, which may reveal New Physics, with the highest possible precision.

A case in point is the weak mixing phase ϕ_s, a key measurement of the LHCb experiment, which can be accessed via $B_s^0 \to J/\psi\phi$ decays. According to the Standard Model this phase is expected to small, approximately $\phi_s = -0.04\,\mathrm{mrad}$. However, New Physics contributions may augment this phase, yielding a larger value. To be able to attribute the observed magnitude of the phase to New Physics, the LHCb experiment has been designed to measure ϕ_s with a precision of $0.024\,\mathrm{mrad}$ after one nominal year of data taking. To achieve this sensitivity on ϕ_s requires high precision tracking detectors. Furthermore, to determine charged particle trajectories and observables with a high precision, the positions of the tracking detectors need to be known well within their respective hit resolutions.

To determine the positions of the detectors well within their hit resolutions, a generic track based alignment framework for the LHCb detector has been developed. The novelty of this framework is that it uses a Kalman filter track model and fit in the so-called *global method of alignment* procedure. In this procedure alignment offsets are determined through a global least squares method, in which not only the hits themselves are considered but also the correlations between the hits. This has the advantage that only a few iterations are required to determine the alignment offsets. Furthermore, the framework uses the same track model and fit as the standard LHCb reconstruction and physics analyses procedures. The obtained alignment offsets are therefore expected to be consistent with the track model and fit used in these procedures. An additional advantage of this alignment framework is the possibility to align all of the LHCb sub-detectors simultaneously or each sub-detector individually at any granularity.

This thesis presents the implementation and validation of the LHCb alignment framework. In a Monte Carlo validation study the effects of multiple scattering on the alignment procedure are studied. It is shown that it is possible to align two sub-detectors of different detection technology and with different hit resolutions simultaneously without requiring high momentum tracks ($> 10\,\mathrm{GeV}$) to eliminate multiple scattering effects. Furthermore, at most eight iterations are required for the procedure to converge and the obtained alignment offsets are consistent with the input mis-alignments. The obtained offsets also allowed to recover the nominal performance of

the LHCb detector with respect to the reconstruction of $J/\psi \to \mu^+\mu^-$ decays.

Using cosmic ray data from September 2008, various alignment procedures are explored to determine the positions of the OT C-frames and modules. It is shown that the determined alignment offsets are compatible with the OT survey offsets. Furthermore, systematic studies show that the statistical error in Δx is around $54\,\mu\mathrm{m}$ and that the systematic uncertainty is approximately $131\,\mu\mathrm{m}$. In comparison, an OT straw tube has a typical drift distance resolution of $200\,\mu\mathrm{m}$.

In another Monte Carlo study the effects of mis-alignments in the VELO and T-stations, respectively, on the reconstruction of $B_s^0 \to J/\psi\phi$ decays as well is their implications on the sensitivity to ϕ_s are investigated. It is shown that mis-alignments in the VELO and T-stations lead to a degradation in the $\mu^+\mu^-K^+K^-$ invariant mass resolution. This leads to an increase of the observed background and consequently to a dilution of the purity of the signal, which in turn leads to a worse measurement of ϕ_s. Though the effect of this is limited in the case of the analysis of $B_s^0 \to J/\psi\phi$ decays, it can be large in analyses of B decays with either a poor sensitivity, such as $B_s^0 \to \mu^+\mu^-$, or in which different decays with identical topologically states need to be kinematically separated, *e.g.* $\overline{B_d^0} \to K^-\pi^+$ versus $B_s^0 \to K^-\pi^+$. Furthermore, it is shown that the $\mu^+\mu^-K^+K^-$ invariant mass resolution can be improved by applying a J/ψ mass constraint in the vertex reconstruction procedure, even in the presence of mis-alignments in the VELO and T-stations, respectively.

Of importance in the analysis of $B_s^0 \to J/\psi\phi$ decays is the reconstructed B_s^0 proper time resolution, which directly affects the sensitivity to ϕ_s. It is shown that the reconstructed proper time resolution is predominantly affected by mis-alignments in the VELO. This is a consequence of the fact that for short living particles the proper time resolution is practically constant and proportional to the hit resolution of the VELO. Mis-alignments in the T-stations, which have an effect on the momentum resolution of the reconstructed particles, start having an effect on the reconstructed proper time resolution when the reconstructed proper time is approximately seven times the B_s^0 lifetime.

Finally, it is also shown, an initial mis-aligned detector can be recovered using the LHCb alignment framework and that the nominal performance of the LHCb detector with respect to the reconstruction of $B_s^0 \to J/\psi\phi$ decays is fully restored.

Samenvatting

De LHC op CERN brengt zowel een nieuwe mogelijkheid om het Standaard Model van elementaire deeltjes te testen, als een kans om de mysteries en onze kennis van de Natuur verder te onderzoeken. Het Standaard Model is een theorie die is gebaseerd op experimentele observaties van interacties tussen deeltjes in versneller experimenten en in experimenten die metingen doen aan cosmische straling. Ondanks de successen van het Standaard Model geeft het geen compleet beeld van het wonderbaarlijk subtiel gewoven netwerk dat we de Natuur noemen. Om de fijne draden van dit netwerk nog verder te onderzoeken en om het Standaard Model of extenties hierop, genaamd Nieuwe Fysica Modellen, te valideren of juist uit te sluiten, hebben deeltjesfysici in de LHC precisieinstrumenten gebouwd om de fundamentele parameters, die Nieuwe Fysica zouden kunnen blootleggen, te meten met de hoogst mogelijke precisie.

Een zo'n fundamentele parameter is de zwakke interferentie fase ϕ_s. Een preciese meting hiervan met het LHCb experiment kan worden bereikt via $B_s^0 \to J/\psi\phi$ vervallen. Volgens het Standaard Model zou deze fase klein moeten zijn, ongeveer $\phi_s = -0.04\,\mathrm{mrad}$. Echter, contributies van Nieuwe Fysica kunnen deze fase beinvloeden en een grotere waarde teweeg brengen. Om de gemeten grootte van de fase aan Nieuwe Fysica toe te kunnen kennen, is het LHCb experiment ontworpen om ϕ_s te meten met een precisie van $0.024\,\mathrm{mrad}$ binnen een jaar. Om dit gevoeligheid op ϕ_s te bereiken vergt hoge precisie spoor detectoren. Verder is het nodig om de posities van de spoor detectoren wel binnen hun respectievelijke hit-resoluties te kennen.

Om de posities van de detectoren binnen hun hit-resoluties te bepalen, is een generiek, op sporen gebaseerd, aliniering raamwerk ontworpen voor de LHCb detector. Een vernieuwend aspect van dit raamwerk is dat het een Kalman filter spoor model en fit gebruikt in de zogenaamde *global method of alignment* procedure. In deze procedure worden alinierings constanten bepaald met een globale kleinste kwadraten methode, waarin niet alleen de hits zelf worden meegenomen, maar ook de correlaties tussen de hits. Dit heeft het voordeel dat slechts een paar iteraties nodig zijn om de alinierings constanten te bepalen. Daarbij gebruikt het raamwerk hetzelfde sppor en fit model als de standaard LHCb reconstructie en analyse procedures. De verkregen alinierings constanten worden dus verwacht consistent te zijn met het spoor en fit model die in deze procedures worden gebruikt. Een verder voordeel van dit raamwerk is de mogelijkheid om alle LHCb subdetectoren simultaan te alinieren, of elke subdetector individueel, op enige granulariteit.

Dit proefschrift beschrijft de implementatie en validatie van het LHCb alinierings methode. In een Monte Carlo validatie studie worden de effecten van multiple scattering op de procedure bestudeerd. Er wordt aangetoond dat het mogelijk is om twee subdetectoren met verschillende detectie technieken en met verschillende hit resoluties simultaan te alinieren zonder tracks met hoge impuls te vereisen ($> 10\,\mathrm{GeV}$) om multiple scattering effecten te elimineren. Ten hoogste zijn voor de procedure acht iteraties nodig om te convergeren en de verkregen alinierings constanten zijn consistent met de mis-positionerings die in zijn geintroduceerd. De verkregen constanten

staan ook toe de ideale werking van de LHCb detector te bereiken aangaande de reconstructie van $J/\psi \to \mu^+\mu^-$ vervallen.

Met behulp van metingen van cosmische straling in LHCb in September van 2008 worden verscheidene alinierings procedures onderzocht om de posities van de Outer Tracker C-frames en modules te bepalen. Er wordt aangetoond dat de alinierings constanten hiermee verkregen compatibel zijn met de directe meting van de posities van de Outer Track C-frames en modules ter plaatse. Verder laten systemathische studies zien dat de statistische fout in Δx rond de $54\,\mu\mathrm{m}$ is en de systematische fout ongeveer $131\,\mu\mathrm{m}$. Ter vergelijking heeft een OT strootje een typische driftafstandresolutie van $200\,\mu\mathrm{m}$.

In nog een Monte Carlo studie worden de effecten van mispositionering in de VELO en T-stations zowel op de reconstructie van $B_s^0 \to J/\psi\phi$, als hun implicaties op de gevoeligheid voor ϕ_s onderzocht. Er wordt aangetoond dat mispositionering in de VELO en T-stations leiden to een degradatie van de resolutie in de $\mu^+\mu^-K^+K^-$ invariante massa. Dit leidt tot een toename van de gemeten achtergrond en vervolgens tot een vermindering van de puurheid van het signaal, wat op zijn beurt een slechtere meting van ϕ_s tot gevolg heeft. Hoewel het effect hiervan beperkt is in het geval van $B_s^0 \to J/\psi\phi$ vervallen, kan het groot zijn in de analyse van B vervallen met een beperkte gevoeligheid zoals $B_s^0 \to \mu^+\mu^-$, of voor vervallen waarin identieke topologische toestanden kinematisch moeten worden onderscheiden, e.g. $\overline{B_d^0} \to K^-\pi^+$ vs. $B_s^0 \to K^-\pi^+$. Verder wordt aangetoond dat de $\mu^+\mu^-K^+K^-$ invariante massa resolutie verbeterd kan worden door een J/ψ massabeperking toe te passen in de vertex reconstructie procedure, zelfs wanneer er een mispositioneren in de VELO en T-stations is.

Belangrijk in de analyse van $B_s^0 \to J/\psi\phi$ vervallen is de gereconstrueerde B_s^0 eigentijdresolutie, die direct invloed heeft op de gevoeligheid voor ϕ_s. Er wordt aangetoond dat de gereconstrueerde eigentijdresolutie voornamelijk wordt beinvloed door mispositionering in de VELO. Dit is een gevolg van het feit dat voor kortlevende deeltjes de eigentijdresolutie praktisch constant is en evenredig is met de hitresolutie van de VELO. Mispositionering in de T-stations, die de impulsresolutie van gereconstrueerde deeltjes beinvloeden, beginnen een effect te krijgen op de gereconstrueerde eigentijdresolutie als de gereconstrueerde eigentijd ongeveer zeven keer de B_s^0 levensduur is.

Ten slotte wordt ook aangetoond dat een initieel misgepositioneerde detector kan worden hersteld met gebruik van het LHCb aliniering raamwerk en dat de ideal werking van de LHCb detector aangaande de reconstructie van $B_s^0 \to J/\psi\phi$ vervallen volledig wordt gerealiseerd.

Dankbetuigings

As ek dit nie skryf nie dan sal my “baas” weer dink dat dit tipies ek is om tot op die laaste minuut besig te wees om alles perfek te maak, maar nie klaar te maak nie.*

So, laat ek maar eers begin met die liefde van my hart. Silvia, my Italiaanse Skoonhied, baie dankie vir jou ondersteuning en geduld en vir die perfekte omslag. Ek is baie lief vir jou *mio amore*.

’n Halwe mikron verder is my ouers wat die laaste 17 jaar baie geduldig was met my. Die eerste 18 jaar tel nie, want toe was my boude baie geduldig met ma se paplepel. Ek is opreg dankbaar vir julle liefde en ondersteuning en bly dat julle my ouers is.

Een mikron verder is Marcel Merk en Wouter Hulsbergen. Baie dankie vir julle geduld en hulp. Ek weet nie wat ek sou doen sonder julle entoesiastiese en simpatieke aanmoediging en leiding nie. Belangriker is die kanse wat Marcel vir my gegee het, waarsonder ek ook nooit die liefde van my hart sou ontmoet nie. Dus weer baie dankie. Ja, en jy ook Eduard “the |”.

Een en ’n half mikron verder is Antonio Pellegrino, Niels Tuning, Leo Wiggers, Gerhard Raven, Thomas Bauer, Fabian Jansen, Eduard Simioni, Jacopo Nardulli, Stefania Vecchi, Aart Heijboer, Vanya Belyaev, Alexandr Kozlinskiy, Marko Zupan en Gordon Lim. Baie dankie vir die wysheid, kennis, idees, diskussies, suggesties, hulp, geselskap, kursus Italiaans, espresso, vis, pasta, sigare, sigarette, bier, whiskey en Mario Kart.

Tien mikrons verder is Erik van der Kraaij en Maaike Limper. Dit is nie my skuld dat julle so baie van bier hou nie.

Twintig mikrons verder is Serena Oggero. My eerste en beste “student”. Boy, het is ons gesuffer met die pile-up.

Honderd mikrons verder is my proefskrif komittee: Jo van den Brand, Antonio Pellegrino, Thomas Ruf, Thomas Peitzmann en Gerhard Raven. Baie dankie vir julle kommentaar en regstellings.

Sonder hierdie “familie” en hulle bydraes, as ook die nodige kalmerende “ingriëdente”, sou ek lankal moed opgegee het.

Ciao ciao,

Gianni “Die Bielie van die Bosveld” Amoroso

*Die enigste ding wat ek nog mis is ’n Afrikaanse opsomming. Ek dink ek sal dit oorslaan en maar begin aan ’n Afrikaanse Wikipedia oor hoë-energie fisika.

Bibliography

[1] M. Kobayashi *et al.*, "CP Violation in the Renormalizable Theory of Weak Interaction," *Prog. Theor. Phys.*, vol. 49, pp. 652–657, 1973.

[2] G. C. Branco *et al.*, *CP Violation*. Clarendon Press, 1999.

[3] I. I. Bigi *et al.*, *CP Violation*. Cambridge University Press, 2000.

[4] The LHCb Collaboration, B. Adeva *et al.*, "Road map for selected key measurements from LHCb," CERN-LHCb-PUB-2009-029, 2010.

[5] T. Du Pree, "Search for a Strange Phase in Beautiful Oscillations," PhD thesis, Vrije Univ. Amsterdam, 2010.

[6] C. Jarlskog (editor), *CP Violation*. World Scientific, 1989.

[7] Particle Data Group, K. Nakamura *et al.*, "Review of Particle Physics," *J. Phys. G*, vol. 37, 075021, 2010.

[8] C. Jarlskog, "Commutator of the Quark Mass Matrices in the Standard Electroweak Model and a Measure of Maximal CP Violation," *Phys. Rev. Lett.*, vol. 55, p. 1039, 1985.

[9] L. Wolfenstein, "Parametrization of the Kobayashi-Maskawa Matrix," *Phys. Rev. Lett.*, vol. 51, p. 1945, 1983.

[10] A. J. Buras *et al.*, "Waiting for the top quark mass, $K^+ \to \pi^+ \nu\overline{\nu}$, $B_s^0 - \overline{B_s^0}$ mixing, and CP asymmetries in B decays," *Phys. Rev. D*, vol. 50, no. 5, pp. 3433–3446, 1994.

[11] A. J. Buras *et al.*, "Quark mixing, CP violation and rare decays after the top quark discovery," *Adv. Ser. Direct. High Energy Phys.*, vol. 15, pp. 65–238, 1998.

[12] CKMfitter Group, J. Charles *et al.*, "CP violation and the CKM matrix: Assessing the impact of the asymmetric B factories," *Eur. Phys. J.*, vol. C41, pp. 1–131, 2005.

[13] Heavy Flavor Averaging Group, E. Barberio *et al.*, "Averages of $b-$hadron and $c-$hadron properties at the end of 2007," *hep-ex/0808.1297*, 2008.

[14] H. Albrecht *et al.*, "Observation of $B_d^0 - \overline{B_d^0}$ mixing," *Phys. Lett. B*, vol. 192, no. 1-2, pp. 245 – 252, 1987.

[15] A. Abulencia *et al.*, "Observation of $B_s^0 - \overline{B_s^0}$ Oscillations," *Phys. Rev. Lett.*, vol. 97, no. 24, p. 242003, Dec 2006.

[16] B. Aubert *et al.*, "Limits on the decay rate difference of neutral$-B$ mesons and on CP, T, and CPT violation in $B^0\overline{B}^0$ oscillations," *Phys. Rev.*, vol. D70, p. 012007, 2004.

[17] B. Aubert *et al.*, "Search for T, CP and CPT violation in B0 anti-B0 mixing with inclusive dilepton events," *Phys. Rev. Lett.*, vol. 96, p. 251802, 2006.

[18] A. S. Dighe *et al.*, "Angular distributions and lifetime differences in $B_s^0 \to J/\psi\phi$ decays," *Phys. Lett.*, vol. B369, pp. 144–150, 1996.

[19] A. S. Dighe *et al.*, "Extracting CKM phases and $B_s - \overline{B_s}$ mixing parameters from angular distributions of non-leptonic B decays," *Eur. Phys. J.*, vol. C6, pp. 647–662, 1999.

[20] I. Dunietz *et al.*, "In Pursuit of New Physics with B_s Decays," *Phys. Rev. D*, vol. 63, p. 114015. 30 p, 2000.

[21] D. Chang *et al.*, "Neutrino mixing and large CP violation in B physics," *Phys. Rev. D*, vol. 67, no. 7, p. 075013, 2003.

[22] L. V. Barger *et al.*, "$b \to s$ transitions in family-dependent U(1)' models," *Journal of High Energy Physics*, vol. 2009, no. 12, p. 048, 2009.

[23] A. Lenz *et al.*, "Theoretical update of $B_s^0 - \overline{B_s^0}$ mixing," *Journal of High Energy Physics*, vol. 2007, no. 06, p. 072, 2007.

[24] T. Du Pree *et al.*, "Methods for Angular Analyses of $B \to J/\psi X$," CERN-LHCb-2009-024, 2009.

[25] A. Carbone *et al.*, "Systematic studies on the B_s proper time measurement for the determination of the mixing phase ϕ_s in the channel $B_s^0 \to J/\psi\phi$," CERN-LHCb-PUB-2009-021, 2009.

[26] L. Evans and P. Bryant (editors), "LHC Machine," *JINST*, vol. 3, no. 08, 2008.

[27] J. van Tilburg, "Track simulation and reconstruction in LHC*b*," PhD thesis, Vrije Univ. Amsterdam, 2005.

[28] D. Green, *High P_T Physics at Hadron Colliders*. Cambridge University Press, 2005.

[29] T. Sjostrand *et al.*, "High-energy physics event generation with PYTHIA 6.1," *Comput. Phys. Commun.*, vol. 135, pp. 238–259, 2001.

[30] The LHC*b* Collaboration, S. Amato *et al.*, "LHC*b* Technical Proposal," CERN/LHCC-98-4, 1998.

[31] The LHC*b* Collaboration, R. Antunes-Nobrega *et al.*, "LHC*b* Reoptimized Detector Design and Performance: Technical Design Report," CERN/LHCC-2003-030, 2003.

[32] The LHCb Collaboration, A. Augusto Alves Jr *et al.*, "The LHC*b* Detector at the LHC," *JINST*, vol. 3, no. 08, 2008.

[33] The LHC*b* Collaboration, S. Amato *et al.*, "LHC*b* magnet: Technical Design Report," 1999.

[34] The LHC*b* Collaboration, P. R. Barbosa-Marinho *et al.*, "LHC*b* VELO (VErtex LOcator): Technical Design Report," 2001.

[35] A. Papadelis, "Characterisation and commissioning of the LHC*b* VELO detector," PhD thesis, Vrije Univ. Amsterdam, 2009.

[36] The LHC*b* Collaboration, P. R. Barbosa-Marinho *et al.*, "LHC*b* Inner Tracker: Technical Design Report," 2002.

[37] The LHC*b* Collaboration, P. R. Barbosa-Marinho *et al.*, "LHC*b* Outer Tracker: Technical Design Report," 2001.

[38] F. Sauli, "Principles of operation of multiwire proportional and drift chambers," CERN-77-09, 1977.

[39] R. M. van der Eijk, "Track reconstruction in the LHC*b* experiment," PhD thesis, Univ. Amsterdam, 2002.

[40] L. B. A. Hommels, "The Tracker in the Trigger of LHC*b*," PhD thesis, Univ. Amsterdam, 2006.

[41] E. Simioni, "New physics from rare beauty," PhD thesis, Vrije Univ. Amsterdam, 2010.

[42] The LHC*b* Collaboration, S. Amato *et al.*, "LHC*b* RICH: Technical Design Report," 2000.

[43] The LHC*b* Collaboration, S. Amato *et al.*, "LHC*b* Calorimeters: Technical Design Report," 2000.

[44] The LHC*b* Collaboration, P. R. Barbosa-Marinho *et al.*, "LHC*b* Muon System: Technical Design Report," 2001.

[45] S. Miglioranzi *et al.*, "The LHC*b* Simulation Application, Gauss: Design, Evolution and Experience," CERN-LHCb-PROC-2011-006, 2011.

[46] D. J. Lange, "The EvtGen particle decay simulation package," *Nucl. Instr. Meth. A*, vol. 462, no. 1-2, pp. 152 – 155, 2001.

[47] GEANT4 Collaboration, S. Agostinelli *et al.*, "G4–a simulation toolkit," *Nucl. Instr. Meth. A*, vol. 506, no. 3, pp. 250 – 303, 2003.

[48] M. Cattaneo, "Boole: LHCb Digitisation Program." http://lhcb-release-area.web.cern.ch/LHCb-release-area/DOC/boole/

[49] I. Belyaev, "LHCb Detector & Geometry Description: Solids," LHCb-2004-018, 2004.

[50] I. Belyaev, "LHCb Detector & Geometry Description: Optical Properties & Surfaces," LHCb-2004-019, 2004.

[51] I. Belyaev, "LHCb Geometry & Detector Description: Volumes," LHCb-2004-020, 2004.

[52] A. Gong *et al.*, "Outer Tracker DAQ data format," CERN-LHCb-2007-040, 2007.

[53] J. Nardulli *et al.*, "A Study of the Material in an Outer Tracker Module," CERN-LHCb-2004-114, 2005.

[54] G. W. van Apeldoorn *et al.*, "Beam Tests of Final Modules and Electronics of the LHCb Outer Tracker in 2005," CERN-LHCb-2005-076, 2005.

[55] V. Gromov *et al.*, "Electrical properties of various types of straw tubes considered for the LHCb outer tracker," LHCb-2001-001, 2001.

[56] E. Simioni, private communication.

[57] M. Deissenroth, private communication.

[58] R. H. Hierck, "Optimisation of the LHC*b* detector," PhD thesis, Univ. Amsterdam, 2003.

[59] E. Bos, "Reconstruction of charged particles in the LHC*b* experiment," PhD thesis, Vrije Univ. Amsterdam, 2009.

[60] V. Blobel, "Software alignment for tracking detectors," *Nucl. Instr. Meth. A*, vol. A566, pp. 5–13, 2006.

[61] M. Gersabeck, "Alignment of the LHC*b* Vertex Locator and Lifetime Measurements of Two-Body Hadronic Final States," PhD thesis, Univ. Glasgow, 2009.

[62] F. Maciuc, "Software Alignment of the LHC*b* Inner Tracker Sensors," PhD thesis, Univ. Heidelberg, 2009.

[63] M. Deissenroth, "Software Alignment of the LHC*b* Outer Tracker Chambers," PhD thesis, Univ. Heidelberg, 2010.

[64] R. Mankel, "Pattern recognition and event reconstruction in particle physics experiments," *Reports on Progress in Physics*, vol. 67, no. 4, pp. 553–622, 2004.

[65] E. Kreyszig, *Advanced Engineering Mathematics,* 8^{th} *Edition*. John Wiley & Sons, Inc., 1999.

[66] F. James, *Statistical Methods in Experimental Physics,* 2^{nd} *Edition*. World Scientific, 2008.

[67] T. S. Shores, *Applied Linear Algebra and Matrix Analysis*. Springer, 2007.

[68] A. Bocci *et al.*, "TRT Alignment For SR1 Cosmics and Beyond," CERN-ATL-COM-INDET-2007-011, 2007.

[69] R. Fruhwirth, "Application of Kalman filtering to track and vertex fitting," *Nucl. Instr. Meth. A*, vol. A262, pp. 444–450, 1987.

[70] R. E. Kalman, "A New Approach to Linear Filtering and Prediction Problems," *Transactions of the ASME–Journal of Basic Engineering*, vol. 82, no. Series D, pp. 35–45, 1960.

[71] W. D. Hulsbergen, "Decay chain fitting with a Kalman filter," *Nucl. Instr. Meth. A*, vol. 552, no. 3, pp. 566 – 575, 2005.

[72] W. D. Hulsbergen, "The global covariance matrix of tracks fitted with a Kalman filter and an application in detector alignment," *Nucl. Instr. Meth. A*, vol. 600, no. 2, pp. 471 – 477, 2009.

[73] E. Bos *et al.*, "The Trajectory Model for Track Fitting and Alignment," CERN-LHCb-2007-008, 2007.

[74] J. M. Amoraal, "Alignment of the lhcb detector with kalman filter fitted tracks," *Journal of Physics: Conference Series*, vol. 219, no. 3, 2010.

[75] Programming Language. http://www.python.org

[76] V. L. Highland, "Some Practical Remarks on Multiple Scattering," *Nucl. Instr. Meth. A*, vol. 129, p. 497, 1975.

[77] L. Nicolas *et al.*, "First studies of T-station alignment with simulated data," CERN-LHCb-2008-065, 2008.

[78] L. Nicolas *et al.*, "Alignment of the Inner Tracker Stations Using First Data," CERN-LHCb-PUB-2009-012, 2009.

[79] S. Pozzi, "The spatial alignment of the Muon Detector for the LHC*b* experiment," PhD thesis, Univ. degli Studi di Ferrara, 2010.

[80] P. Vankov, "Study of the B-Meson Lifetime and the Performance of the Outer Tracker at LHC*b*," PhD thesis, Vrije Univ. Amsterdam, 2008.

[81] O. Callot *et al.*, "PatSeeding: A Standalone Track Reconstruction Algorithm," CERN-LHCb-2008-042, 2008.

[82] M. Schiller, private communication.

[83] CDF and D$\emptyset$ collaboration, "Combination of D$\emptyset$ and CDF results on $\Delta\Gamma_s$ and the CP violating phase $\beta_s^{J/\psi\phi}$," *CDF/PHYS/BOTTOM/CDFR 9787, D$\emptyset$ note 59-28-CONF*, 2009.

[84] A. S. Dighe *et al.*, "Angular distributions and lifetime differences in $B_s^0 \to J/\psi\phi$ decays," *Phys. Lett. B*, vol. 369, no. 2, pp. 144 – 150, 1996.

[85] P. Billoir *et al.*, "Fast vertex fitting with a local parametrization of tracks," *Nucl. Instr. Meth. A*, vol. 311, no. 1-2, pp. 139 – 150, 1992.

[86] Particle Data Group, C. Amsler *et al.*, "Review of Particle Physics," *Phys. Lett. B*, vol. 667, 2008.

[87] J. E. Gaiser *et al.*, "Charmonium spectroscopy from inclusive ψ' and J/ψ radiative decays," *Phys. Rev. D*, vol. 34, no. 3, pp. 711–721, Aug 1986.

[88] J. Nardulli, "Reconstruction of two-body B decays in LHC*b*," PhD thesis, Vrije Univ. Amsterdam, 2007.

[89] H. Moser *et al.*, "Mathematical methods for $B^0\overline{B^0}$ oscillation analyses," *Nucl. Instr. Meth. A*, vol. 384, no. 2-3, pp. 491 – 505, 1997.